

R-04-01

Äspö Pillar Stability Experiment

Geology and mechanical properties of the rock in TASQ

Isabelle Staub, Golder Associates AB

J Christer Andersson, Björn Magnor
Svensk Kärnbränslehantering AB

March 2004

Svensk Kärnbränslehantering AB

Swedish Nuclear Fuel
and Waste Management Co
Box 5864

SE-102 40 Stockholm Sweden

Tel 08-459 84 00

+46 8 459 84 00

Fax 08-661 57 19

+46 8 661 57 19



ISSN 1402-3091

SKB Rapport R-04-01

Äspö Pillar Stability Experiment

Geology and mechanical properties of the rock in TASQ

Isabelle Staub, Golder Associates AB

J Christer Andersson, Björn Magnor
Svensk Kärnbränslehantering AB

March 2004

Abstract

An extensive characterization programme has been performed in the drift, TASQ, excavated for the Äspö Pillar Stability Experiment, APSE, including the rock volume that will host the experiment pillar between the two deposition holes. The two major objectives with the characterization has been to 1) derive material properties for the final numerical modelling of the experiment and 2) to ensure that the pillar location is suitable from a structural and rock mechanical point of view. In summary the following activities have been performed:

- Geological mapping of the drift, the pilot holes cores and deposition hole DQ0066G01.
- 3D-visualisation of the geological mapping in the experiment (pillar) volume of TASQ.
- Convergence measurements during the excavation and back calculation of the results for determination of the stress tensor and the rock mass Young's modulus.
- Laboratory tests on core samples from the 15 Ø76 mm core boreholes drilled around the pillar volume for determination of: compressive strength, thermal properties and fracture properties.
- P-wave velocity measurements on core samples and between boreholes for estimation of the excavation damaged zone and rock mass properties.

The geological mapping and the 3D-visualisation gives a good description of the TASQ drift in general and the experiment volume in the drift in particular. The fracturing of the drift follows the pattern of the rest of Äspö. Three fracture sets have been mapped in TASQ. The major fracture set is sub-vertical and trending NW, in principle parallel to σ_1 . This set is the most conductive at Äspö and is the only water bearing set in TASQ. A second less pronounced set is trending NE, parallel to TASQ, and is also sub-vertical. The third set is sub-horizontal. It is interesting to note that the third set is the only one that almost completely consists of sealed fractures. The first two sets have mostly open fractures. One unique feature in the drift is a heavily oxidized brittle-ductile shear zone striking along the drift dipping to the south-east. The zone is present in the experiment volume but is less pronounced there than in the rest of the drift. The zone is not assessed to give large enough changes in the geology to hazard the outcome of the experiment. The major concern has been the possibility of shearing along the zone in the pillar that would give stress re-distributions resulting in stresses too low to initiate brittle failure.

The convergence measurements and the back calculation of those resulted in changes of the stress tensor and Young's modulus of the rock mass. The magnitudes and bearings of the principal stresses are in principal the same as the ones compiled from the extensive rock stress measurement made in the vicinity of the drift. However the numerical modelling resulted in changes of the dips. The new tensor has only horizontal and vertical stresses where the second principal stress is vertical. The derived Young's modulus is approximately 20% higher than what earlier has been predicted for the rock mass. The reason in this case is though likely that the convergence measurements were accidentally performed in a rock mass with extremely low fracture frequency. The few fractures likely give a more rigid rock mass than what's generally observed at Äspö. The confirmation of the stress magnitudes by the back calculations is positive for the project. These stresses are concentrated by the drift shape and the large boreholes creating the pillar. A concern in the early part of the project was the risk that the in-situ stresses should be too low to increase the stresses high enough for initiation of spalling. This would have resulted in that very high temperatures would have been needed to expand the rock to initiate spalling which could have been hard to handle.

The extensive laboratory tests are assessed to have given a good data set of the intact rock properties. The uniaxial and triaxial tests give similar results to what's earlier have been derived on the Äspö diorite. Only a few compressive strength tests have been done on rock samples collected close to the shear zone which is mostly due to the lack of representative sections of intact rock in the pillar. The strength of the altered rock is approximately 50–60% of the intact diorite. The results of the testing of the thermal properties are good and lies well within what can be expected of diorite. Nothing in the results from the laboratory programme has indicated that the chosen experiment volume would be unsuitable, it is important to take the heterogeneity in consideration.

The P-wave velocity tests on core samples and between two boreholes perpendicular to the future pillar wall has been performed. The velocities indicate that the excavation disturbed zone is thin. If the dynamic Young's modulus is calculated from the velocities between the two boreholes approximately 3 m apart it is found to be of the same magnitude as the static one measured on intact rock. The reason is probably the low fracturing and that the fractures are either sealed or compressed due to the quite high stress field. It can be concluded that the modulus for the pillar volume should be at least in the same order as the one derived from the convergence measurements. A high modulus in the experiment volume is positive since lower temperatures can be used for the stress increase necessary to initiate brittle spalling.

In Table 4-12 and a selection of the parameters derived from the characterisation to be used in the numerical modelling is presented. The choice of the respective values is discussed in the respective section in this report.

Sammanfattning

Ett omfattande karakteriseringsarbete har genomförts i den ort, TASQ, som byggts för Äspö Pillar Stability Experiment, APSE. Karakteriseringen har genomförts särskilt noggrant i den bergvolym, pelaren, där experimentet skall genomföras. De två viktigaste målsättningarna med karakteriseringsarbetet har varit att: 1) ta fram materialparametrar vilka skall användas i den slutliga numeriska modelleringen och 2) säkerställa att det preliminära läget för pelaren som valts i ett tidigare skede är lämpligt sett ur ett strukturgeologiskt och bergmekaniskt perspektiv. Följande aktiviteter har genomförts under karakteriseringen:

- Geologisk karakterisering av orten TASQ, borrhämnarna från experimentområdet samt deponeringshål DQ0066G01.
- 3D visualisering av den geologiska karteringen i experiment-/pelarområdet i TASQ.
- Tillbakaberäkningar av konvergensmätningar som genomfördes vid byggnationen av orten för att bestämma spänningsfältet och elasticitetsmodulen.
- Laboratoriebestämning av en- och triaxiell tryckhållfasthet, termiska egenskaper samt sprickors egenskaper på kärnprover. Kärnorna var tagna från de totalt 15 kärnborrhål med diametern 76 mm som borrats i anslutning till pelarvolymen.
- Mätningar av P-vågshastigheten på kärnprover samt mellan borrhål för bedömningar av den sprängskadade zonen samt för erhållande av bergmekaniska egenskaper.

Karteringen tillsammans med den tredimensionella visualiseringen av densamma ger en bra beskrivning av TASQ och en synnerligen detaljerad bild av experimentvolymen. Det karterade sprickmönstret i TASQ överensstämmer med de resultat som finns från övriga Äspö. Tre sprickgrupper har identifierats. Den mest framträdande gruppen är subvertikal och stryker åt nordväst, i princip parallellt med riktningen för den största huvudspänningen. Denna grupp är de mest konduktiva sett över hela Äspöanläggningen och i TASQ är det den enda grupp som leder vatten. En mindre omfattande sprickgrupp stryker åt nordost, parallellt med TASQ, och är även den subvertikal. Den tredje sprickgruppen är subhorisontell. Beträffande sprickgrupperna kan man konstatera att den tredje gruppen i princip bara består av läkta sprickor. De andra två grupperna består av öppna sprickor. En geologisk företeelse som gör TASQ unik jämfört med övriga Äspöanläggningen är förekomsten av en kraftigt oxiderad spröd/plastisk skjuvzon som stryker utefter tunnelriktningen och stupar åt sydöst. Zonen påträffas i experimentområdet men är mindre uttalad där än i övriga delar av orten. Den slutliga bedömningen av zonen är att den inte kommer att påverka bergmassan i pelaren på ett sådant sätt att utvärderingen av experimentet äventyras. Vid diskussionerna om hur skjuvzonen kunde påverka pelaren var den största osäkerheten möjligheten för skjuvning utefter zonen i pelaren vilket skulle resultera i att spänningsfältet omfördelades. Denna omfördelning skulle kunna leda till att lasterna inte koncentrerades tillräckligt för att sprött brott skulle kunna initieras.

Konvergensmätningarna och återberäkningen av dessa ledde till att spänningsfältet och elasticitetsmodulen reviderades inför de slutliga numeriska beräkningarna. Storleken och riktningarna på huvudspänningarna är i princip samma som de som togs fram genom en sammanställning av de omfattande bergspänningsmätningar som genomförts i närområdet. Återberäkningarna ledde dock till att stupningen på spänningsfältet ändrades. Det reviderade spänningsfältet består endast av vertikala och horisontella komponenter av vilka den andra huvudspänningen är den vertikala. Den reviderade elasticitetsmodulen är cirka 20 % högre än vad som tidigare har predikerats för bergmassan. Anledningen till detta är troligen att konvergensmätningarna genom en slump genomfördes i en bergvolym med

mycket låg sprickfrekvens vilket ger bergmassan en större styvhet än vad som generellt observerats på Äspö. Att få en verklig bekräftelse på huvudspänningarnas magnituder är viktigt för projektet. Huvudspänningarna koncentreras först genom geometrin på orten och sedan med hjälp av de stora borrhålen/deponeringshålerna som skapar pelaren. En risk i ett tidigt skede av experimentet var att in-situ spänningarna skulle vara för låga för att kunna koncentreras så att sprött brott skulle uppträda vid måttlig uppvärmning. De höga temperaturer som skulle ha blivit nödvändiga i ett sådant scenario skulle ha blivit praktiskt svåra att hantera.

De omfattande laborietester som genomförts bedöms ha givit en bra uppskattning på det intakta bergets egenskaper i experimentområdet. Resultaten från de en- och triaxiella tryckhållfastheterna ligger inom vad som tidigare uppmätts för Äspödiorit. Endast ett fåtal tryckhållfasthetstest har genomförts på kärnor tagna från skjuvzonen. Detta beror på svårigheten att ta fram representativa kärnprover från den delen av bergmassan. Tryckhållfastheten för det omvandlade berget har dock bedömts att vara cirka 50–60 % av den för frisk Äspödiorit. Resultaten från de termiska provningarna är lyckade och ligger inom förväntansramen. Vidare kan konstateras att inga resultat från laboratorieundersökningarna tyder på att den valda experimentvolymen skulle vara olämplig, men heterogeniteten i bergmassan måste beaktas.

Hastigheten för P-vågor har bestämts både på kärnprover och mellan två borrhål som ligger vinkelrätt mot den framtida pelarens vägg har genomförts. Mätningarna indikerar att den sprängskadade zonen är mycket liten. Den dynamiska elasticitetsmodulen har beräknats utifrån P-vågshastigheterna mellan de två borrhålen vinkelrätt pelaren. Resultatet stämmer väl överens med den statiska elasticitetsmodulen som erhöles från tryckhållfasthetstesterna. Detta beror troligen på att sprickfrekvensen är låg mellan hålen samt att sprickorna både är läkta och hoptryckta av spänningsfältet under sulan. Slutsatsen som kan dras av detta är att elasticitetsmodulen i pelaren är i princip i samma storleksordning som den som erhållits vid återberäkningarna av konvergensmätningarna. Detta är bra för experimentet då en hög elasticitetsmodul ger högre spänningar då berget expanderar av värmen, en lägre värmelast behövs således för att initiera sprött brott.

I tabellerna 4-12 och 4-13 redovisas några av de parametrar som erhållits under karakteriseringsprogrammet för att användas som indata i den numeriska modelleringen. Hur de enskilda specifika värdena valts redogörs det för i respektive kapitel.

Contents

1	Introduction	9
2	Geological overview	11
3	Visualisation of experiment volume	15
3.1	The tunnel data	15
3.1.1	Input data	15
3.1.2	3D model of fractures	16
3.1.3	Discussion	18
3.1.4	Conclusions	19
3.2	Borehole data	19
3.2.1	Presentation	19
3.2.2	Analysis of fracture frequency	20
3.2.3	Analysis of fracture orientation	20
3.2.4	Analysis of the shear zone	23
3.3	Model of geological structures	24
3.3.1	Background	24
3.3.2	Assumptions and concepts for interpretation	25
3.3.3	Water-bearing features	25
3.3.4	The mylonite zone in the pillar area	26
3.4	Discussion and conclusion	34
3.4.1	Predictions from the model	34
3.4.2	Mapping observations from the deposition hole DQ0066G01	37
4	Rock mass properties	39
4.1	General information on collected samples	39
4.2	Intact rock properties	40
4.2.1	Density measurements	40
4.2.2	Mechanical properties	41
4.2.3	Thermal properties	46
4.3	Fracture properties	48
4.4	Sonic and ultrasonic velocity measurements	50
4.4.1	P-wave measurements in pilot hole cores	50
4.4.2	Borehole Velocity Profile Survey	52
4.5	Discussions	53
5	Convergence measurements and back analyze	55
5.1	Measuring strategy	56
5.2	Measured results	57
5.3	Numerical modelling	60
5.4	Evaluation of modelled data	62
5.5	Influence of tunnel face geometry	67
5.6	Geology at chainage TASQ0049	68
5.7	Discussion	69

6	Conclusions	71
6.1	Geological structures	71
6.2	In-situ stress	71
6.3	Rock properties	71
6.4	Other Äspö Pillar Stability Experiment reports	72
7	References	73
Appendix A	Tunnel mapping	75
Appendix B	Mechanical testing on samples from KA3376B01	81
Appendix C	Mechanical testing on samples from KQ0064G01, KQ0064G07 and KQ0065G01	101
Appendix D	Laboratory tests report for measurement of coefficient of thermal expansion, density and porosity	127
Appendix E	Laboratory tests report for measurement of heat conductivity and heat capacity	141
Appendix F	Laboratory test report for determination of fracture stiffness, and mode I and mode II fracture toughness	151
Appendix G	Measurement report for sonic velocity in the pilot holes	177
Appendix H	Borehole Velocity Profile Survey – report	191

1 Introduction

The Swedish Nuclear Fuel and Waste Management Company (SKB) is responsible for the disposal of spent nuclear fuel in Sweden. The fuel is to be placed in copper canisters that will be deposited in vertical 8 m deep and 1.8 m diameter shafts at 400–700 m depth in the crystalline Scandinavian shield. The repository will result in the construction of approximately 4,000 rock pillars located between the emplacement holes. During the life span of the repository it is likely that these pillars will be subjected to quite high stresses. At least two stages with stress increase are anticipated. First the thermal expansion of the rock from the decaying nuclear fuel will increase the stresses. The temperature and hence the induced stresses will decrease within a relative short time period. The second anticipated stress increase in the repository is the ice-load from the next ice-age. The ice thickness is assessed to be thousands of metres and the stresses induced from the ice will be larger than from the previous thermal stresses.

Stability of pillars has mainly been a concern for the mining industry and studies have mostly resulted in empirical relationships, some more site specific than others. It is not known how well these relationships can be applied to the crystalline rock of a deep repository in the Scandinavian shield. SKB has therefore initiated a large scale rock mechanics experiment at the Äspö Hard Rock Laboratory Facility named “Äspö Pillar Stability Experiment”, APSE. The following objectives are outlined for the experiment:

- Demonstrate our current capability to predict brittle failure, spalling, in a fractured rock mass.
- Demonstrate the effect of back-fill (confining pressure) on the rock mass response.
- Compare 2D and 3D mechanical and thermal predicting capabilities.

The pillar in the experiment will be created at the 450 m level by boring of two large holes, Ø1.8 m by 6.7 m deep, so that a 1 m thick pillar remains between the holes walls. The in-situ stresses will be concentrated by the choice of the drift geometry and the spacing of the boreholes creating the pillar. The motivation of the localisation of the drift in the underground laboratory has been previously discussed and reviewed /Andersson, 2003; Staub et al. 2003/. The design will be balanced so that the pillar after the excavation of the holes still will respond elastically. Monitoring equipment will be placed in the large holes before the stresses are cranked up by electrical heaters located just outside the pillar volume. The resulting gradual thermal expansion will induce such stresses that spalling is initiated. Preliminary calculations were conducted in order to state the layout of the experiment /Fredriksson et al. 2003/. The experiment is unique since the monitoring programme can follow the rock's response to increased loading from an elastic response through the transitional zone characterised by increased micro-fracturing until brittle failure is initiated.

As mentioned above an objective with the experiment is to demonstrate the numerical modelling predicting capabilities. The numerical models are completely dependent on the properties of the volume to be modelled; hence care has to be taken when the parameters needed are derived. The outcome of the experiment is as can be understood from the previous section strongly dependent on the geology, material properties and the in-situ

stresses in and around the experiment volume. The objectives with the characterization programme reported herein are therefore to:

- finally determine the suitability for the planned experiment in the preliminary target section in the TASQ drift.
- recommend representative input data of intact rock, fractures and rock mass for the numerical modelling to ensure that the modelled results are as good as reasonably could be expected.

All the background reports that have been used in the compilation of the data in this report are included as appendices making this report a comprehensive reference for geology, in-situ stress and rock mechanics properties in the TASQ drift for the Äspö pillar stability experiment and for the Äspö facility as such.

2 Geological overview

The dominating rock types in the Äspö area are the plutonic Äspö diorite and Ävrö granite. They belong to the postorogenic phase of the Transscandinavian Igneous Belt (TIB), their ages are ca 1.8 Ga. The Äspö diorite is a medium-grained, grey to reddish grey rock. It is generally porphyritic, with K-feldspar megacrysts. Its composition does not correspond to a true diorite, but ranges from granite to granodiorite to quartz monzonite /Rhen et al. 1997; Wikman and Kornfält, 1995/. The more felsic Ävrö granite, which is a medium-grained, greyish red rock, is mainly classified as true granite. Transitions between these two rock types are gradual rather than sharp. Chemical relationship between them indicate that they can be considered as two varieties of the Småland granite /Wikman and Kornfält, 1995/. Subordinate rock types intruding the TIB-rocks are mafic rocks, pegmatites and fine-grained granites. 1.4 G.A. anorogenic granite intrusions occur in Götemar and Uthammar 5 km NW and 10 km SSW of Äspö respectively.

Structurally the Äspö area is dominated by regional brittle-ductile shear zones striking NE-SW. Brittle-ductile deformation zones also appear in ENE, E-W and NW-SE /Berglund et al. 2003/. The most pronounced brittle set of deformation structures strikes NW-SE. It is generally associated with high conductivity. Other common orientations for brittle structures are N-S and NE-SW. Generally all of these structural sets dip sub vertically. The NE-SW striking group also contains a sub horizontally dipping set /Berglund et al. 2003/.

Figure 2-1 illustrates the major structures identified and modelled around the experiment volume (200 m side). These are identified as EW1-b, NE2 and HQ3. Their characteristics at that depth and around the experiment volume are presented in detail in /Hansen and Hermanson, 2002/ and /Staub et al. 2003/. As can be seen on the major structures EW-1b and NE2 form an edge and intersect beyond the experiment volume.

The major structures that are intersecting the experiment volume have been truncated against the domain limits and the general illustration is presented in Figure 2-2. The picture illustrates clearly that the modelled major structure NE2 is not encountered so far away from the planned experiment area.

Tunnel TASQ at the -450 m level in the Äspö HRL is dominated by different varieties of Äspö diorite, as seen in the tunnel mapping (Appendix A). The major rock volume consists of unaltered Äspö diorite, but relatively large volumes also consist of oxidized or sheared Äspö diorite. Other rock types present are mafic rocks, pegmatite and fine-grained granite. Rock contacts generally are diffuse, as they are successive transitions from one type of Äspö diorite to another. Contacts between dikes and host rock are sharp. For a more detailed description of the geology in the TASQ, see /Magnor, 2004/.

Regional metamorphism appears absent or of very low grade in the TASQ rock volume. Occasionally a diffuse foliation can be found in the Äspö diorite, which appears to be associated with the regional foliation pattern. Hydrothermal, low grade alteration to some extent appears in association with a shear zone running along the tunnel (see below).

In the Rock Mass Rating (RMR) the rocks in TASQ are characterized as “good” (61–80 in the RMR-system), even though individual structures may be of lower stability.

Q-logging has been performed from section 24 m to the end of the tunnel /Barton, 2004/. Q_{mean} is 110.8 in section 24 to 59 m and 25.1 in section 59 to 80 m.

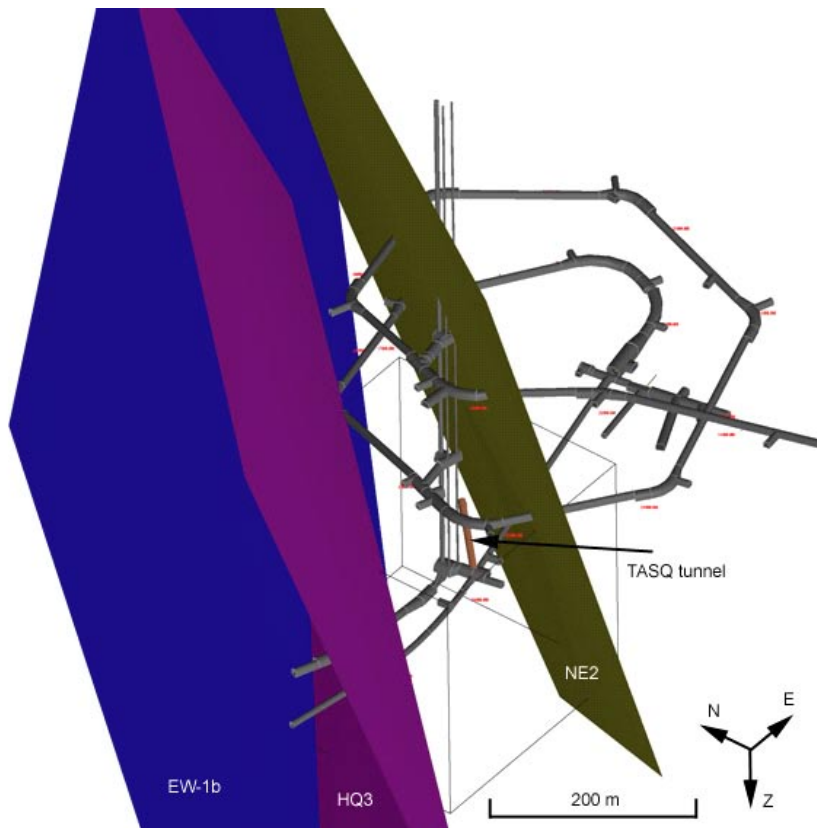


Figure 2-1. Model of the major identified structures in the Äspö area around the experiment volume.

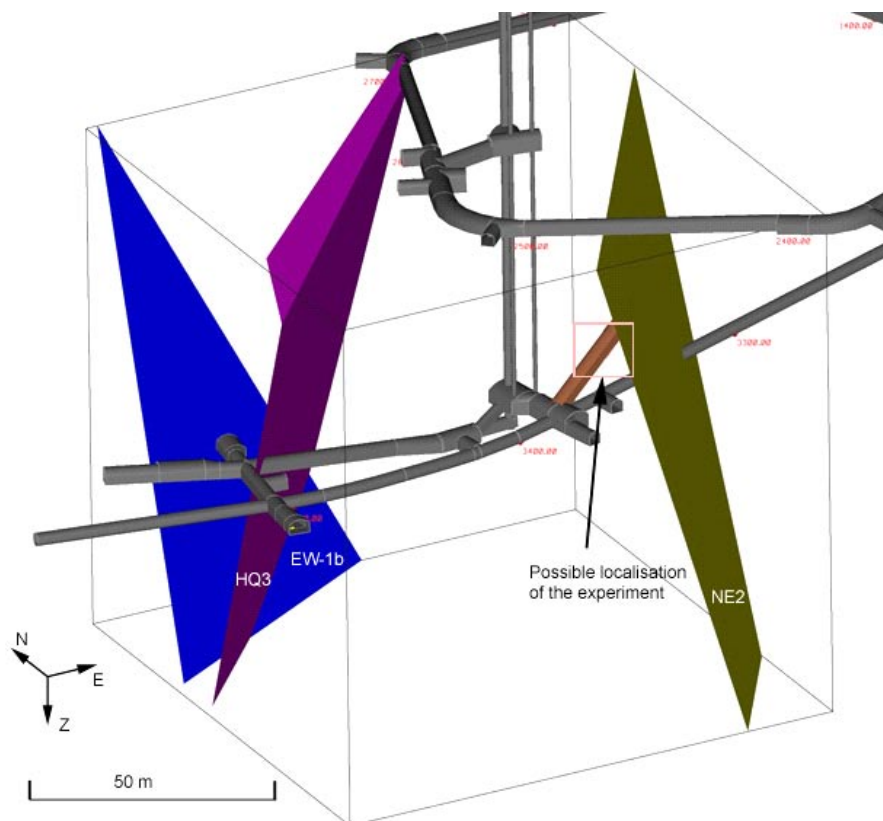


Figure 2-2. Detailed model of the identified major structures in the experiment volume and their localisation towards the possible localisation of the pillar.

Geological structures in TASQ are dominated by three main orientations, all of them related to the regional pattern. In Appendix A all fractures mapped are presented and representative members of each of the three sets are marked out. In Figure 1-2 the three main orientations are presented in stereographic projections. One of the three main sets is striking NW-SE and dipping sub vertically, i.e. perpendicular to the tunnel (set 2 in Figure 2-3). It consists of relatively wide continuous brittle fractures and faults. This set is common in the whole Äspö HRL and is often associated with water leakage, both in TASQ and in the Äspö region in general. Set 1 in Figure 2-3 represents a shear zone parallel set of brittle fractures. It is suggested that these structures are reactivated planes of weakness associated with the shearing. The third main structural set is sub horizontal (set 3 in Figure 2-3). Fracture filling minerals in all these orientations are dominated by chlorite, epidote and calcite.

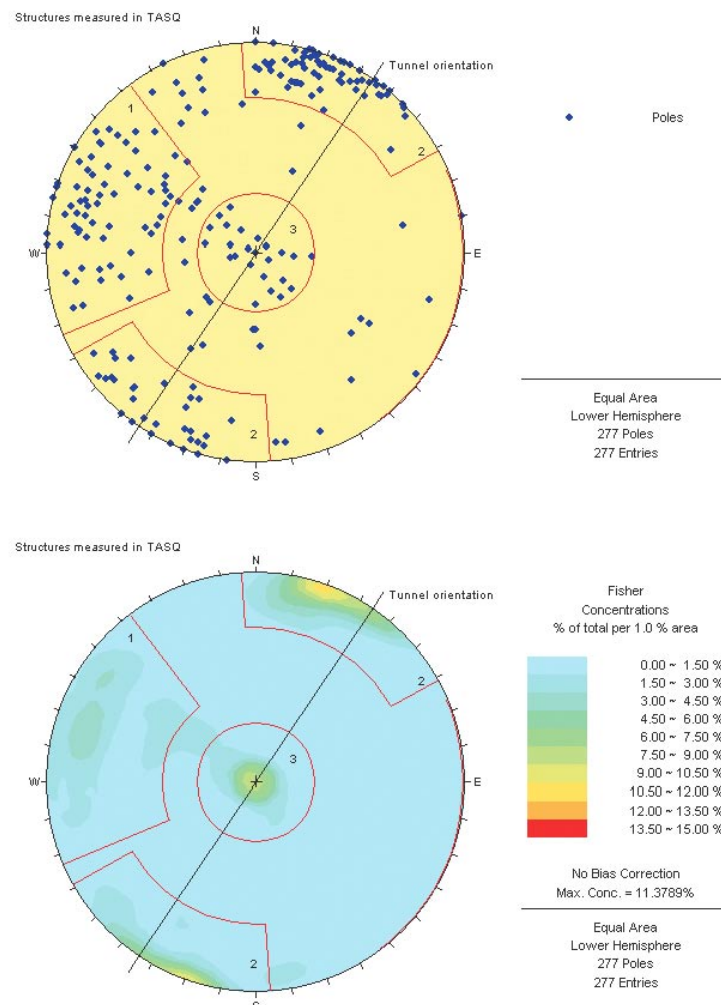


Figure 2-3. Projection of poles to fracture planes to all structures measured in tunnel TASQ. Group 1 includes the shear zone parallel structures. It also contains a set of brittle, steeply dipping structures striking N-NNE. Group 2 consists of a brittle, sub vertical set striking perpendicular to the tunnel. This group includes the majority of the faults in TASQ. Group 3 represents a set of sub horizontal brittle fractures.

The fracture pattern observed in the TASQ tunnel and illustrated in Figure 2-3 can be compared to the pattern obtained on tunnel data in the experiment volume prior to the drilling of the TASQ, Figure 2-4.

A heavily oxidized, brittle-ductile shear zone strikes along the tunnel in 030–035°. It is dipping to the southeast and is present along the major part of the tunnel. In places, this set of structures generates critical surfaces of brittle reactivation with fracture filling of mainly epidote-chlorite. It is, however mainly sealed and not as critical for rock stability as could be expected. The shear zone can be regarded as a mylonite.

The structural set generating most critical zones of weakness is the set of brittle fractures striking perpendicular to the tunnel, in NW-SE and dipping sub vertically (set 2 in Figure 2-3). The planned APSE test area is bordered by two members of this set, in this particular place represented by faults with offset in metre-scale. These faults displaced the tunnel-parallel shear zone, which due to the faulting can not be found in the innermost 12 metres of the tunnel. Except for these faults, displacements in the TASQ are less than 0.3 metres.

Water leakage is mainly associated with the fracture set oriented in NW-SE/sub vertical (set 2 in Figure 2-3). Generally the leakage causes damp surfaces or, at most, seepage. Occasionally, however leakage has been classified as flowing, in these cases exclusively generated in the above mentioned tunnel-perpendicular set. Measurements of the total water-inflow in the first deposition hole indicated 30 litres/minute.

Grating was performed in the inner part of the tunnel and is reported in /Emmelin et al. 2004/.

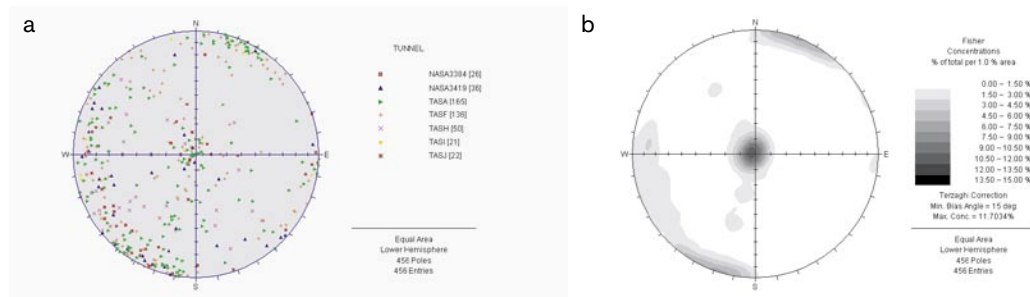


Figure 2-4. Stereoprojection of poles to fractures: Point plot (a) and density plot (b) to all fractures mapped in the tunnel within the experiment volume (200 m side).

3 Visualisation of experiment volume

The localisation of the tunnel and the preliminary target for the experiment had been based on the geological model developed prior to the beginning of the practical issues for the experiment /Staub et al. 2003/. A geological model of structures and conductive features around the TBM tunnel at 450 m depth was the support for decision of the preliminary localisation of the experiment.

This work is a following-up and updating of the geological model based on recently acquired data at a smaller scale. The main aim has been to integrate the results of tunnel mapping in order to confirm the localisation of the pillar stability experiment. Then when the target area has been confirmed 15 boreholes were drilled. The analysis of the cores was used to further confirm the suitability of the target area.

The background data for the development of the model in the experiment volume are provided by the different reports and analyses conducted during the phase 2 of the “Äspö Pillar Stability Experiment”, and can be consulted in /Andersson, 2003/ and /Staub et al. 2003/.

3.1 The tunnel data

The fractures observed in the tunnel have been mapped and the results reported on 2D sheets. In order to better appreciate the structure of the fracture network in the tunnel and determine the area for localisation of the experiment a 3D model of the fracturing in the tunnel TASQ was required.

3.1.1 Input data

The data have been provided by SKB as drawing 2D files and excel files (Figure 3-1).

The drawing files provide the 2D visualisation of mapped fractures, fracture zones and rock contacts. The walls and roof of the tunnel have been mapped from Ch 10 to 80 m. The fractures on the floor have been mapped only in the experiment area, which means between Ch 64 and 69 m.

The 0 m length reference for the TASQ tunnel is located in the centre line of the TBM tunnel.

The excel files gather all data relevant for each mapped fracture, such as orientation, mineralization and occurrence of water seepage or inflow.

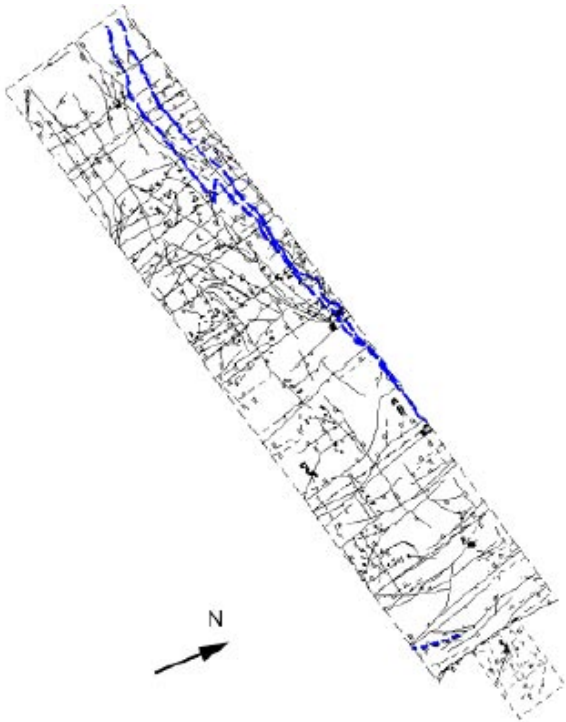


Figure 3-1. 2D digitalised mapping of the TASQ tunnel. The blue lines represent the traces of a deformation zone.

3.1.2 3D model of fractures

The aim of this activity was to transform the 2D fracture traces as digitalised to fit the 3D realistic tunnel geometry. The geometrical data used for the 3D construction of the TASQ frame for fracture projection are presented in Figure 3-2 and Table 3-1.

Fracture traces from the walls are simply rotated and projected at 90° from the 2D trace map. Fractures mapped as “on the roof” are projected on the curved surface representing the tunnel roof.

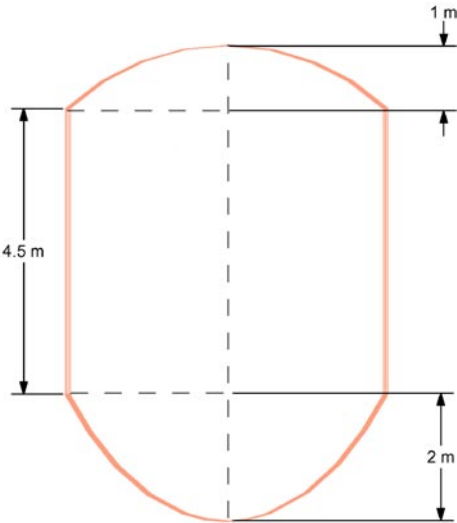


Figure 3-2. Vertical section of the tunnel.

Table 3-1. Planned coordinates of the TASQ tunnel (Äspö96).

	East (m)	North (m)	Depth (m)	Comment
Centre line of the TBM tunnel	2,080.623	7,275.057	447.7	Ch 0
"Start" point	2,088.597	7,282.757	446.47	Ch 10
End point	2,138.065	7,330.528	445.77	Ch 80

Note: the depth coordinates are taken at the middle of the floor.

The 3D visualisation of fractures on TASQ is presented in Figure 3-3 and Figure 3-4.

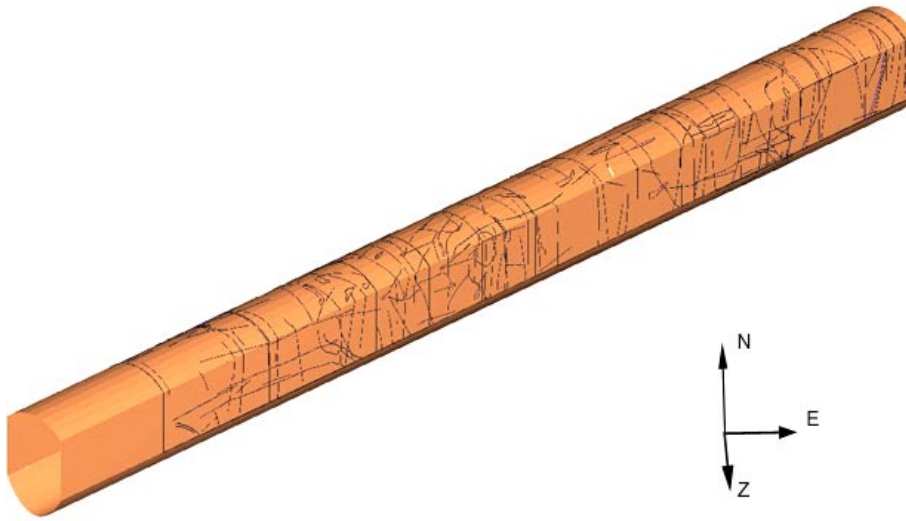


Figure 3-3. 3D visualisation of fractures in the TASQ tunnel. The first 10 metres are not mapped.

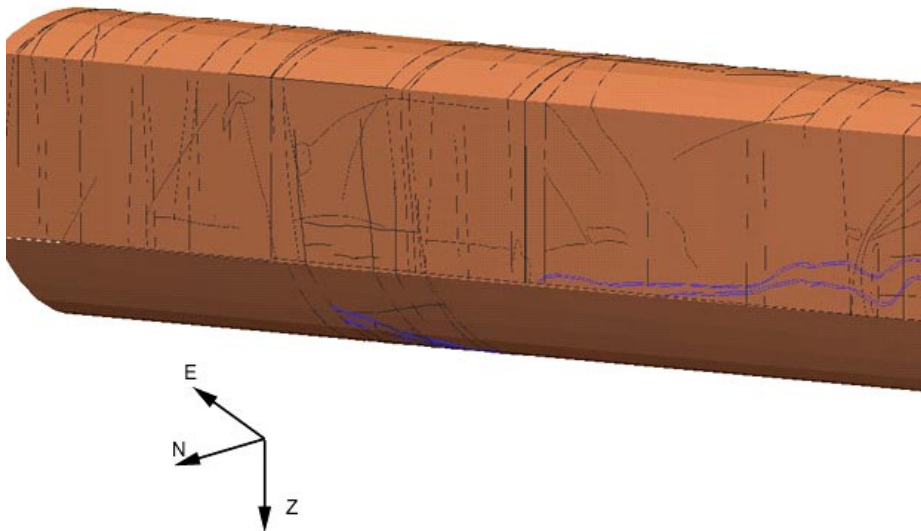


Figure 3-4. 3D visualisation of fractures in the TASQ tunnel, target area. The blue traces correspond to the mapping of a shear zone.

3.1.3 Discussion

The 3D visualisation of the fractures in the tunnel is a good tool for appreciating the fracture network in the rock mass. The presence of WNW conductive features (predicted in the geological model, see /Staub et al. 2003/) was confirmed by mapping especially beyond Ch 50 m in the tunnel.

The dominant rock type in the tunnel is Äspö diorite.

The fracture pattern “exhibits some changes” at about 50 m in the tunnel. Two major conductive WNW subvertical features located at Ch 59 and 69 m are delimiting the experiment area. This designs a potential target area which is quite narrow.

A consistent shear zone has been mapped on the west wall of the tunnel from Ch 10 to 60 m. The zone can be characterised as a mylonite. Even if the zone is sealed and old the influence of the deformation on the rock mass properties and behaviour are observed in the “chippings” pattern on the wall at the occurrence of the zone (see Figure 3-5). This is though very close to the corner of the floor in the pilot drift. The chipping of the rock is probably more intense due to blasting damage in this corner and would be less pronounced if the contact was in the middle of the wall.

The zone is not observed on the wall beyond Ch 60 m and never mapped on the roof. A similar shear zone is mapped on the floor between Ch 64 and 69 m, and two minor features that can be associated to the zone are also mapped on the floor, fracture 7 between Ch 64 and 69 m, and a fracture on the eastern side of the floor between Ch 60 and 64 m.

The orientations of the shear zone as mapped in the tunnel are summarised in Table 3-2. Considering the location of the trace on the floor and the orientation of the zone the probability for the zone to cross the pillar is high.



Figure 3-5. Overview of the “chippings” on the west wall of the tunnel. The chipping is intensified due to blasting damage in the floor of the pilot drift which was located at the approximate same depth.

Table 3-2. Occurrence of the shear zone in the TASQ tunnel.

Location	Chainage	Strike (°)	Dip (°)
West wall	10–59 m	14	58
Floor	64–69 m	12	45

3.1.4 Conclusions

Despite the highly probable occurrence of the shear zone in the pillar the target area for the experiment has been retained. This is partly due to the overall structures and conductive features observed in the tunnel when coming further away from the TBM tunnel. Locations closer to the TBM tunnel might be more suitable on a geological and structural basis but their proximity to the access tunnel and the shaft would have a too strong impact on the stress field.

3.2 Borehole data

3.2.1 Presentation

The next step was to drill fifteen 56 mm diameter boreholes in the experiment area. The number and localisation of boreholes account for the set-up of the experiment /Fredriksson et al. 2003/.

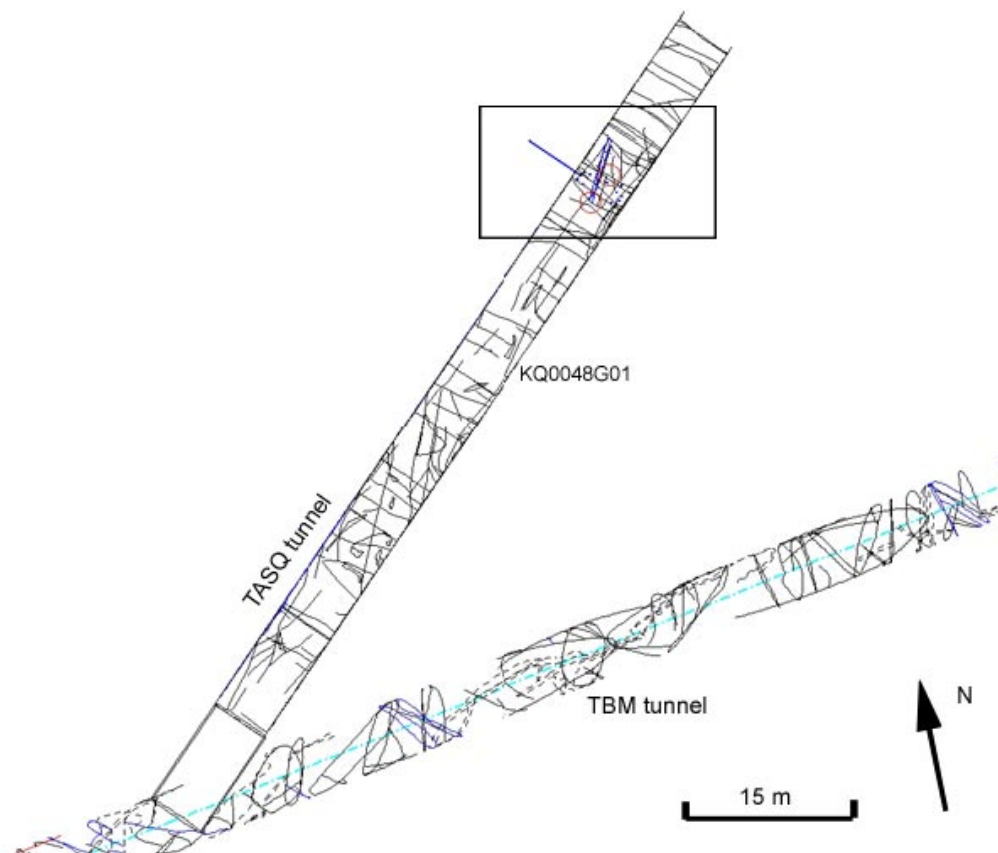


Figure 3-6. Localisation of the target area in the tunnel system and identification of the one borehole located outside of the target area. The box underlines the target area.

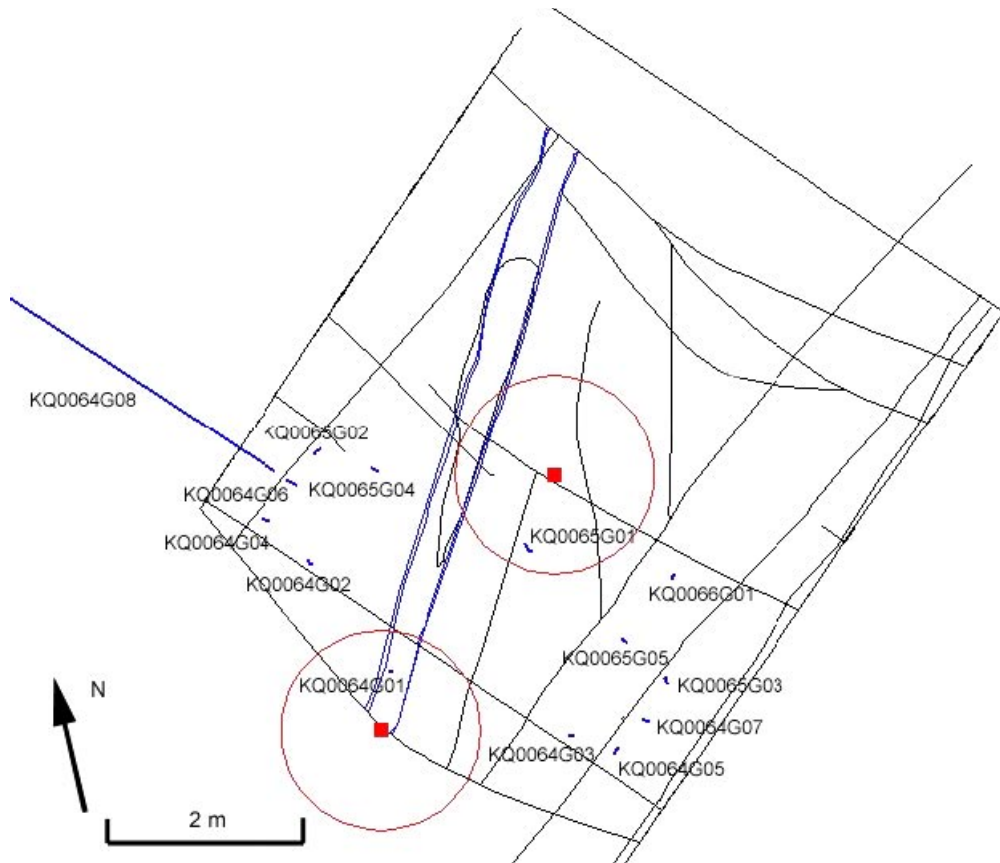


Figure 3-7. Identification and localisation of the boreholes in the target area. The red cylinders represent the planned 1.8 m diameter large holes.

15 pilot boreholes were drilled for the purpose of the experiment and their geometry and the status of data available is summarised in Table 3-3. All boreholes except KQ0064G08 are vertical. Data available for these boreholes are fracture characteristics (orientation, mineral fillings, width, and aperture) and rock occurrence.

3.2.2 Analysis of fracture frequency

The average fracture frequency of natural fractures in all the boreholes is 1.03 fractures/m, with a range of values from 0.26 (borehole KQ0064G04) to 1.96 (borehole KQ0065G05), see Table 3-4.

3.2.3 Analysis of fracture orientation

Fracture data from the boreholes have been plotted on an equal area lower hemisphere projection. A Terzaghi correction is applied for the estimation of fracture density distribution. The correction takes into account the orientation of the boreholes to adjust the representativity of fractures almost parallel to the trace line.

The poles of natural fractures mapped in all the boreholes have been plotted in a stereoplot (Figure 3-8). Based on the density contour plot four fracture sets can be identified of which one is strongly dominant. This is represented by subvertical fractures which are striking 115° and dipping 75° . Three subordinate sets of fractures are observed that possess the mean following orientation (strike/dip): $135/85^\circ$, $000/05^\circ$ and $340/25^\circ$.

Table 3-3. Data for the boreholes drilled in the experiment area.

	Bearing	Inclination	Length	Fracture orientation	Rock occurrence
KQ0048G01	283	89.9	7.05	No	X
KQ0064G01	170	89.9	7.17	X	X
KQ0064G02	163.5	89.6	7.47	X	X
KQ0064G03	99.9	89.8	7.57	X	X
KQ0064G04	275.9	89.4	7.9	X	X
KQ0064G05	18.4	89.7	7.93	X	X
KQ0064G06	291.3	89.3	7.87	X	X
KQ0064G07	111.2	89.6	7.93	X	X
KQ0064G08	303.3	59.4	10	X	X
KQ0065G01	146.1	89.3	7.14	X	X
KQ0065G02	230.9	89.5	7.85	X	X
KQ0065G03	339	89.7	7.92	X	X
KQ0065G04	129.1	89.5	7.43	X	X
KQ0065G05	297.1	89.6	7.5	X	X
KQ0066G01	358	89.8	7.41	X	X

Table 3-4. Fracture frequency in the boreholes.

Hole ID	Amount of natural fractures	Fracture frequency
KQ0048G01	9	1.28
KQ0064G01	6	0.84
KQ0064G02	9	1.20
KQ0064G03	4	0.53
KQ0064G04	2	0.25
KQ0064G05	4	0.50
KQ0064G06	6	0.76
KQ0064G07	5	0.63
KQ0064G08	7	0.70
KQ0065G01	7	0.98
KQ0065G02	13	1.66
KQ0065G03	12	1.52
KQ0065G04	8	1.08
KQ0065G05	14	1.87
KQ0066G01	12	1.62
Average		1.03
Std deviation		0.48

The analysis of sealed fractures in the same boreholes enhance the presence of one dominant fracture set (gently dipping fractures) which is striking 350° and dipping 5°, and two subordinate sets of orientation (strike/dip): 040/60° and 045/70°.

Fracturing has been studied in detail and plots of natural fractures in the two central boreholes have been drawn (Figure 3-10). The fracture data are quite dispersed when comparing both holes.

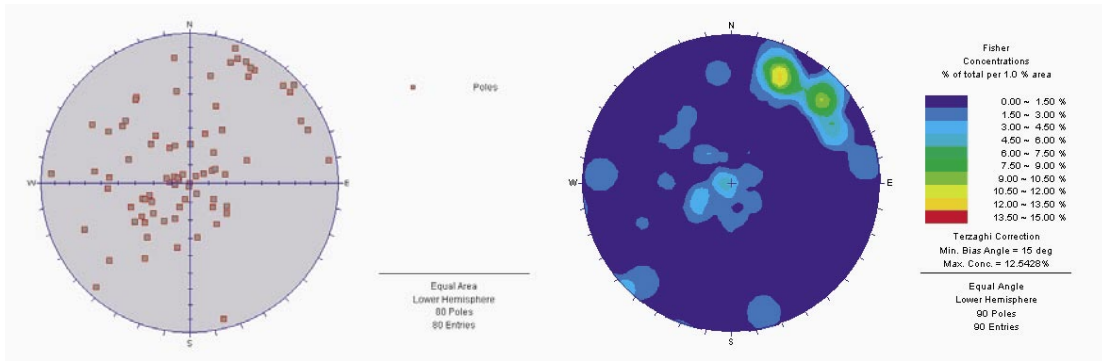


Figure 3-8. Stereoprojection (equal area, lower hemisphere) of natural fractures in all boreholes in the target area.

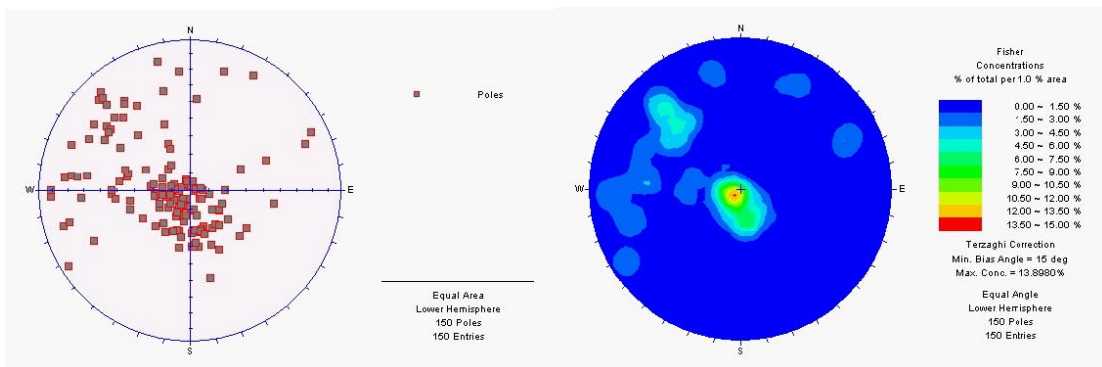


Figure 3-9. Stereoprojection (equal area, lower hemisphere) of sealed fractures in all boreholes in the target area.

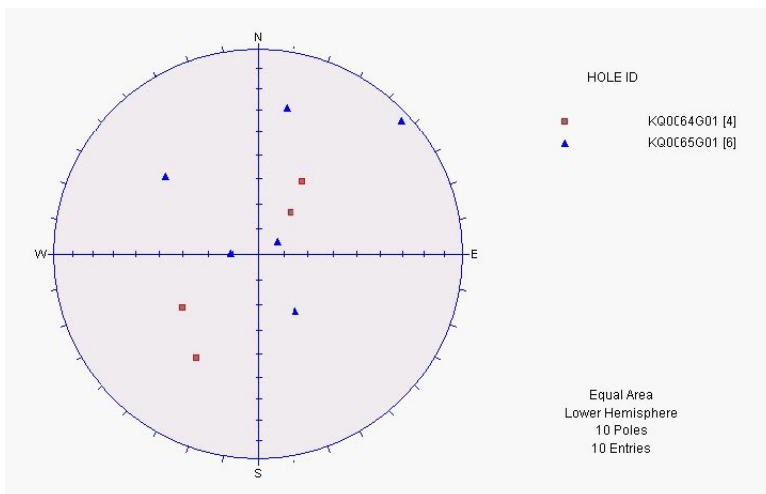


Figure 3-10. Stereoprojection (equal area, lower hemisphere) of natural fractures in the two boreholes located in the deposition holes of the experiment.

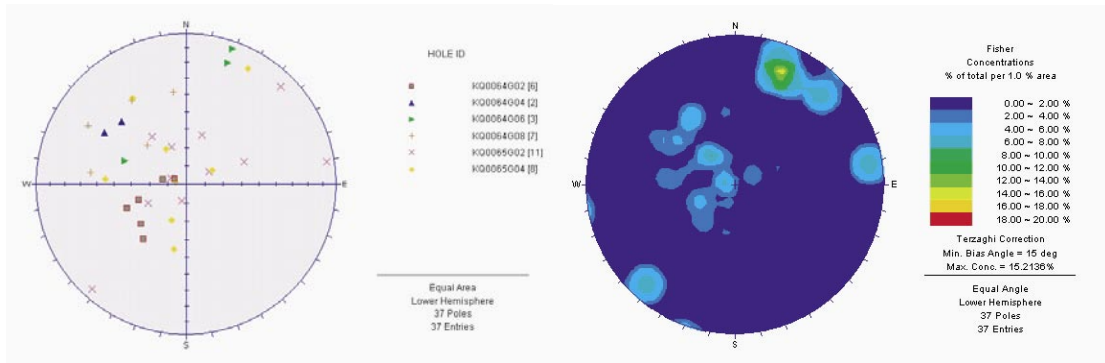


Figure 3-11. Stereoprojection (equal area, lower hemisphere) of natural fractures in the boreholes located on the western side of the tunnel in the target area.

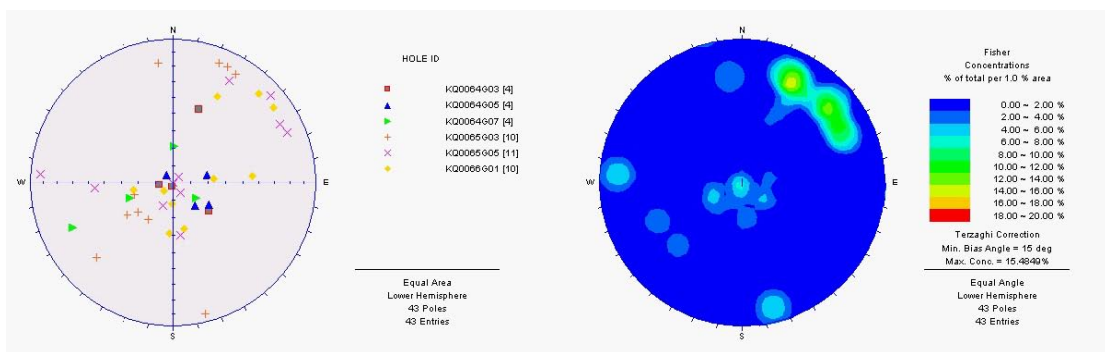


Figure 3-12. Stereoprojection (equal area, lower hemisphere) of natural fractures in the boreholes located on the eastern side of the tunnel in the target area.

Fracture data on both sides of the pillar have been plotted, plots of poles to natural fractures on the western side of the pillar are illustrated in Figure 3-11 and plots of poles to natural fractures on the eastern side of the pillar are presented in Figure 3-12.

The dominant set of natural fractures is identified in pilot holes on both sides of the pillar. Some specific minor sets of natural fractures are identified at both locations.

3.2.4 Analysis of the shear zone

Indications of the mylonite zone have been identified in most of the boreholes. Based on the pattern and the intensity of the deformation the occurrences have been distributed in two different classes (Table 3-5):

- Central zone: sections of the boreholes that can be associated to a fully developed mylonite, where the deformation has been most intense.
- Foliation zone: associated to the zone, but the deformation is less intense than in the central zone and the mylonite is not fully developed. The foliation is an indication of the width of the rock mass which has been influenced by the deformation.

Some narrow shear bands are also observed in some boreholes (KQ0064G08, KQ0066G01).

There is no crush zone or open fractures associated to the shear zone which appears quite old and sealed. A mylonite and epidote filled breccia are characteristics of the zone. The structures are both brittle and ductile.

Table 3-5. Occurrences of the shear zone in the boreholes.

	Foliation zone		Central zone	
		Depth (m)		Depth (m)
KQ0048G01	X	0.1–0.85	X	0.25–0.45
			X	0.55–0.7
KQ0064G01	X	0.3–0.55	X	0.3–0.35
KQ0064G02	X	0–0.15	X	0–0.07
KQ0064G03	X	2.6–3.15	X	2.6–2.7
KQ0064G04	X	0.4–0.55	–	
KQ0064G05	X	4–4.55	X	4.05–4.2
KQ0064G06	X	0.8–0.9	X	0.87–0.9
KQ0064G07	X	4.4–4.8	X	4.45–4.55
KQ0064G08	X	1.8–2.2	X	5–5.05
	X	5–5.1		
KQ0065G01	X	0.85–1.25	X	1.15–1.25
KQ0065G02	X	1.1–1.15	X	1.12–1.15
KQ0065G03	X	0.9–1.05		
	X	4.45–5.1	X	4.5–4.65
	X	5.37–5.55	X	5.37–5.45
KQ0065G04	X	1.1–1.13	X	1.12–1.13
KQ0065G05	X	2.6–2.95	X	2.65–2.85
KQ0066G01	X	2.25–2.6	X	3.25–3.35
	X	3.1–3.5	X	3.47–3.5
	X	3.95–4	X	6.9–7.05
	X	4.55–4.65		

As can be observed in Table 3-5 the sections of cores mapped as zone (central zone and foliation zone) are rather thin, most often less than 50 cm thick. The central zone itself is in most of the boreholes of the order of centimetres.

The zone is identified on both sides of the pillar, and occurrences in all boreholes on the eastern side of the tunnel confirmed the identification of the zone on the floor of the tunnel.

Based both on tunnel and core observations the identification and modelling of the shear zone is required in order to establish its potential influence on the stability of the pillar.

3.3 Model of geological structures

3.3.1 Background

The stability of the pillar and its behaviour during the experiment (drilling and heating) is related to the geometrical and mechanical characteristics of the pillar.

The occurrence of deformation/fracture zones or intense alteration of the rock might alter the mechanical and thermal properties of the rock mass and decrease the stability of the pillar. The fracture pattern inside the pillar is also a factor of influence for spalling risks at the border of the pillar.

The geological model developed during the phase 2 of this project focused on regional and local structures and conductive features in relation to the geology and structure of the Äspö region /Staub et al. 2003/.

The model developed in this stage of the project is mainly focusing on local structures at the experiment area, mainly looking at fracture data in the TASQ tunnel, and especially between Ch 50 and 70 m, and at borehole data. Fractures, conductive features and shear zones have been identified and modelled.

3.3.2 Assumptions and concepts for interpretation

The following assumptions have been made for the interpretation of geological structures:

- Mapping observations in the tunnel represent a much larger exposed fracture trace or trace of a structure than borehole logs do. These observations are therefore primary used to determine the definition and persistence of structures.
- Based on the depth of both 2D levels used for numerical simulations (0.5 and 1.5 m below the tunnel floor) the horizontal fractures mapped in the boreholes have been observed in detail from the top of the boreholes down to 2 metre depth. For open and subvertical or steeply dipping fractures the whole cores for all boreholes have been observed.
- Zones featuring shear characteristics are generally regarded as more continuous than other structures. The whole cores for all boreholes have been analysed to identify the occurrence of such zones.
- Two or more discontinuity indications that can be related between different boreholes have been considered as indications of the same structure. The closer these indications are the more probable the potential structure is.
- Discontinuity indications with the same direction indicate that these joints may not just be more frequent but also more persistent than random indications, therefore they have been interpreted to persist until they meet another structure.

The model has been developed on data provided by the pilot boreholes and the tunnel mapping. None of the large holes was drilled at that stage. Nevertheless the interpretation of intersection of the modelled structures has been based on the projected large holes and pillar, which have for this purpose been visualised (the pillar being the space between the two large holes).

3.3.3 Water-bearing features

Three main subvertical fractures show the characteristics of the WNW water-bearing fractures. These are identified as fracture 19 in the tunnel mapping Ch 45–60 m, and fractures 1 and 6 on the tunnel floor mapping (Appendix A). These two last fractures can be related to similar structures observed on the tunnel walls and roof, see Table 3-6. A 3D visualisation of these objects is presented in Figure 3-13. The orientations of the modelled WNW features are given in Table 3-6.

Water inflow have been observed and reported in fractures 19, 6, 5 and 25.

Table 3-6. Identification of the WNW subvertical features.

	Mapped indications of the structure		Modelled structure	
	Tunnel floor	Tunnel “body”	Strike (°)	Dip (°)
Fracture 19	Not mapped	Fracture 19 (Ch 45–60 m)	283.4	89.5
NW_struct_1	Fracture 1	Fracture 5 (Ch 60–70 m)	126.9	81.3
NW_struct_2	Fracture 6	Fractures 19 and 25 (Ch 60–70 m)	126.7	80.8

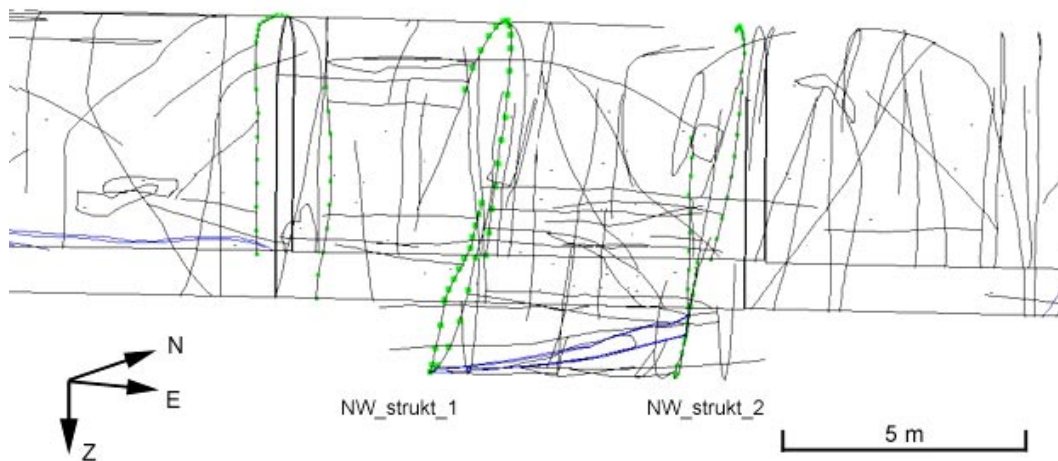


Figure 3-13. Identification of the points used for modelling the WNW subvertical features.

3.3.4 The mylonite zone in the pillar area

The mylonite zone has been modelled based on observations made in the TASQ tunnel and on the borehole cores. According to these observations two main branches of what is assumed to be the same zone considering the deformation properties have been modelled, which might be called SZ_W and SZ_S. The “pivot point” of the SZ_W is the observations on the tunnel wall and the “pivot point” of SZ_S are the observations on the tunnel floor.

Identification of the SZ_W branch of the zone

The identification of the points used for modelling the structure SZ_W are reviewed in Table 3-7 and their localisation is illustrated in Figure 3-14.

As mentioned in Section 3.1.3 no observation of the zone is made on the west wall between Ch 59 and 64 m. However a fracture presenting shear characteristics has been mapped on the eastern side of the tunnel between Ch 59 and 64 m (see Table 3-7).

Based on these observations we could with good confidence identify a block that has been displaced between Ch 59 and 64 m and which is delimited by 2 subvertical fractures, identified as NW_strukt_1 and fracture 19 (Table 3-6). The fracture observed between Ch 59 and 64 m has not been precisely measured but its observation and drawing illustrates a fracture which is parallel to observations of the zone on the wall (measured strike and dip: 14/58°). As a consequence the structure is dislocated and displaced to the east in the section 59–64 m. Identification of the shear zone in the prolongation of the structure as observed between Ch 10 and 59 m is made in fracture 7 on the floor of the tunnel (Ch 64–69).

Table 3-7. Identification of the structure SZ_W.

ID	Mapped occurrences	Location	Remarks
TASQ	Western wall, 14/58°	Ch 10–59 m	2 branches, max width 1 m
TASQ	Base of the eastern wall	Ch 59–64 m	sealed fracture
TASQ	Floor, 12/45°	Ch 64–69 m	sealed fracture (#7)
KQ0064G02	Central zone and foliation zone	L = 0–0.15 m	
KQ0065G02	Central zone and foliation zone	L = 1.1–1.15 m	
KQ0048G01	Central zone and foliation zone	L = 0.1–0.85 m	

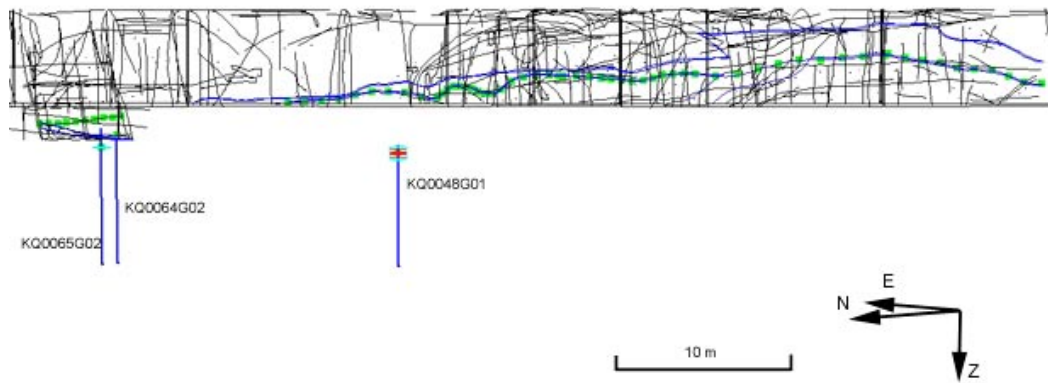


Figure 3-14. Visualisation of the points used for modelling the structure SZ_W.

No trace of the same deformation structure is found beyond Ch 69 m. Another subvertical structure at 69 m (observed on the floor, on the roof and the wall) identified as NW_struct_2 in Section 3.3.3 seems to end the shear zone.

The interpreted SZ_W branch of the shear zone is illustrated in Figure 3-15.

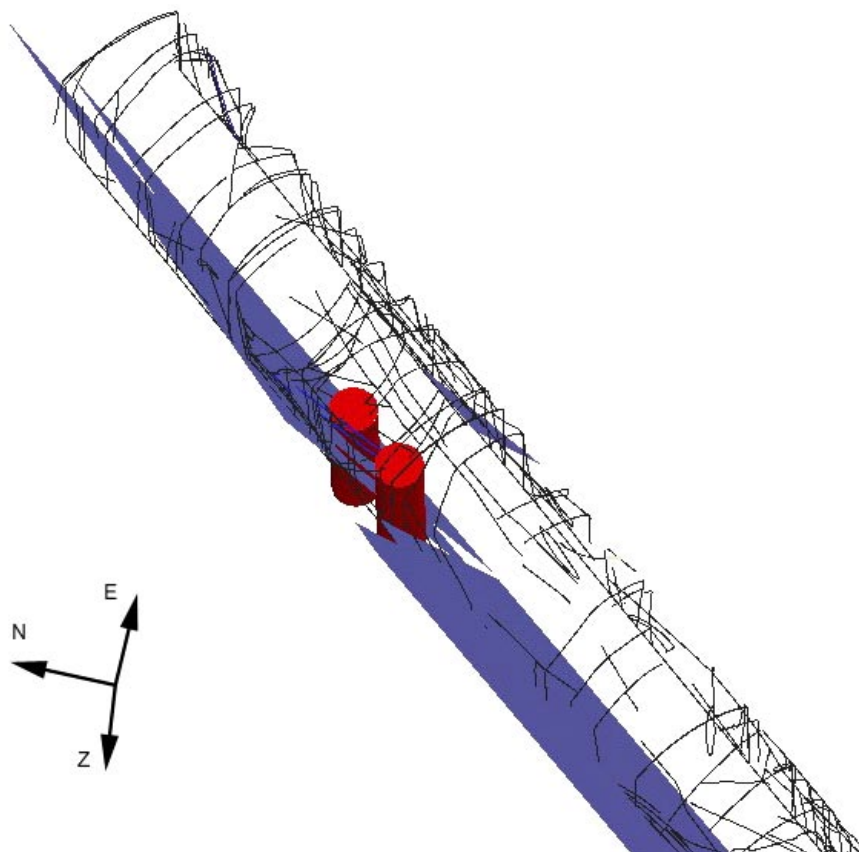


Figure 3-15. 3D visualisation of the SZ_W branch of the shear zone. Obs: the localisation of the displaced section of the SZ_W branch is uncertain as the fracture coordinates have not been exactly measured. The red cylinders represent the planned large holes.

Identification of the SZ_S branch of the zone

The identification of the points used for modelling the structure SZ_S are reviewed in and their localisation is illustrated in Figure 3-16.

Table 3-8. Identification of the structure SZ_S.

ID	Mapped occurrences	Location	Remarks
TASQ	Floor, 12/45°	Ch 64–69 m	About 50 cm wide
KQ0064G01	Central zone and foliation zone	L = 0.3–0.4 m	
KQ0064G03	Central zone and foliation zone	L = 2.6–3 m	
KQ0064G05	Central zone and foliation zone	L = 4–4.55 m	
KQ0064G07	Central zone and foliation zone	L = 4.4–4.8 m	
KQ0065G01	Central zone and foliation zone	L = 0.85–1.25 m	
KQ0065G03	Central zone and foliation zone	L = 4.5–5 m	
KQ0065G05	Central zone and foliation zone	L = 2.6–2.95 m	
KQ0066G01	Central zone and foliation zone	L = 3.1–3.5 m	

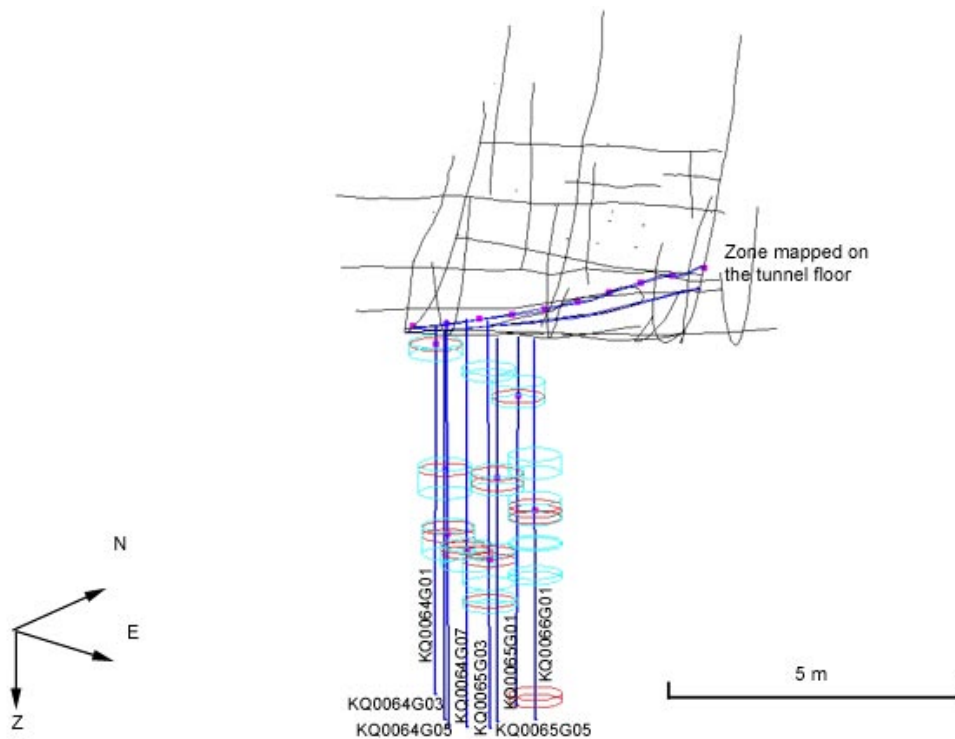


Figure 3-16. Visualisation of the points used for modelling the structure SZ_S.

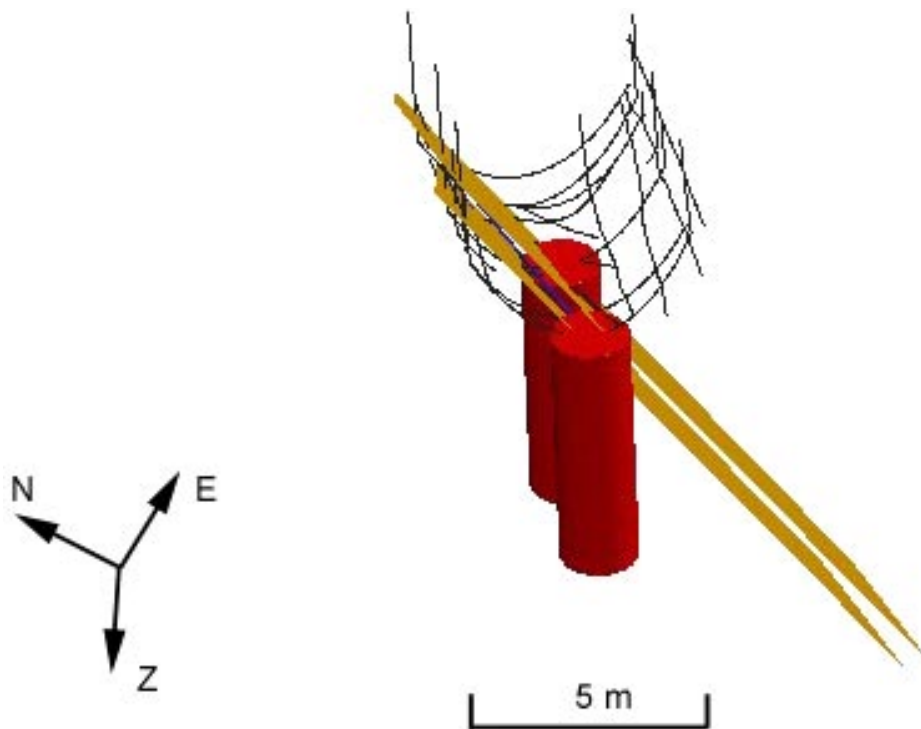


Figure 3-17. 3D visualisation of the SZ_S branch of the shear zone. The red cylinders are a visualisation of the planned large holes.

Indications of the shear structure are found in all the pilot boreholes located on the east side of the tunnel and in both “central” pilot boreholes. The interpreted branch of the zone is visualised in Figure 3-17.

Modelling of the shear zone in the pillar area

According to the geometrical characteristics of the zones and the observations in the field it appears that the structure SZ_W terminates against SZ_S which terminates itself against the subvertical feature NW_strukt_2 (identified as fracture 6 at Ch 69 m).

The displaced section of the structure SZ_W has been modelled with the same characteristics as the overall structure and the fracture mapped on the tunnel floor between Ch 59 and 64 m is used as basis for the localisation of the displaced structure (Table 3-9).

The 3D model of the shear zone is illustrated in Figure 3-18.

Table 3-9. Characteristics of the modelled shear zone.

	Strike (°)	Dip (°)	Remarks
SZ_W_S	33.3	68	Main part of the SZ_W branch, based on observations on the wall and boreholes.
SZ_W_E			Displaced section, based on the fracture between Ch 59 and 64 m.
SZ_W_N			Northern part of the SZ_W branch based on fracture 7, Ch 64–69 m.
SZ_S	23.6	56.2	

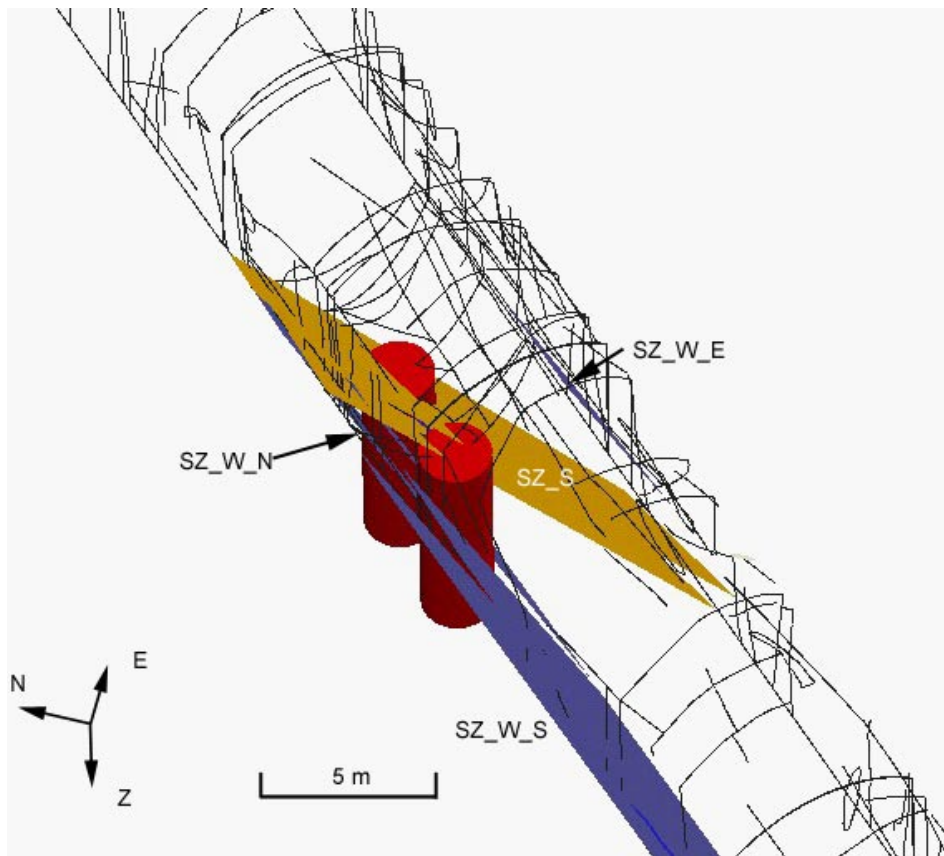


Figure 3-18. 3D visualisation of both branches of the shear zone. The red cylinders are a visualisation of the planned large holes.

Minor fractures in the pillar

A detailed analysis of the borehole cores has been conducted in order to identify potential continuous fractures between different boreholes. Special features identified in one borehole are looked for in the other boreholes. If several occurrences of a similar feature are mapped in different boreholes their depth of occurrence and orientation is imported in RVS for modelling. The 3D visualisation is a support tool for determining the existence of a continuous feature.

This is a time-consuming operation and the analysis has been focused for horizontal fractures on the target depth in the pillar that means between 0 down to around 2 metres. However subvertical fractures have been observed from the tunnel floor down to 6 metres. Some wide recurrent and characteristics features have also been identified and studied.

The analysis resulted in the identification of three main features in the pillar area.

The subvertical open feature

Subvertical open fractures have been identified in several boreholes (Table 3-10). Their localisation in space and orientation indicates that they might be indications of the same structure. The individual fractures and the points used for the interpretation of the structures are illustrated in Figure 3-19.

The modelled fracture is striking 109.8° and dipping 78° and is visualised in Figure 3-20.

Table 3-10. Identification of the subvertical open feature.

	Depth (m)	Strike/Dip (°) – measured	Width (mm)
KQ0065G01	2.1	137.7/85.1	0.6
KQ0065G03	6.23	111.7/78.8	0.7
KQ0065G04	4.97	138.7/80	0
KQ0065G05	1.43	118.2/76.9	1

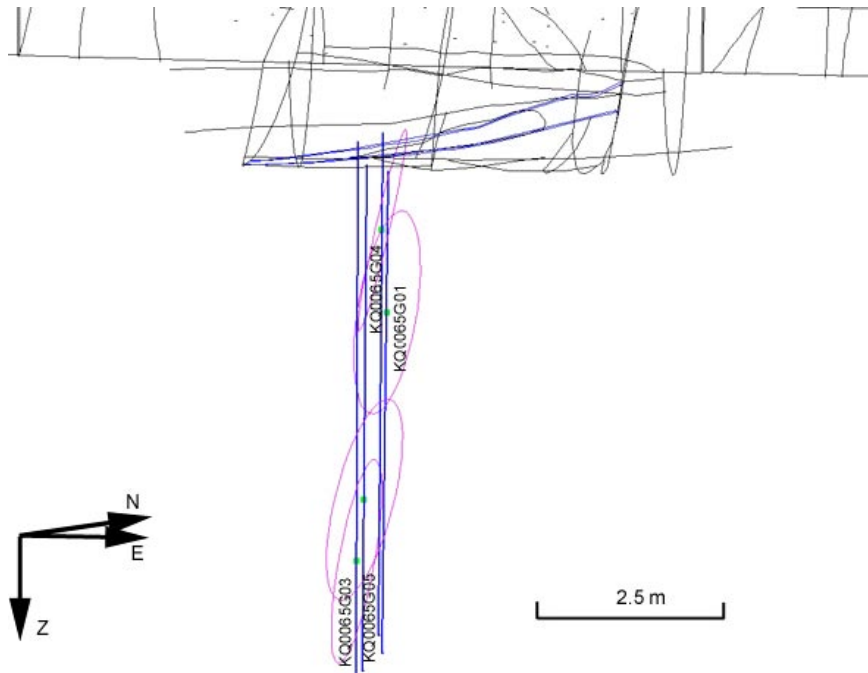


Figure 3-19. Identification of the points used for the modelling of fract_1.

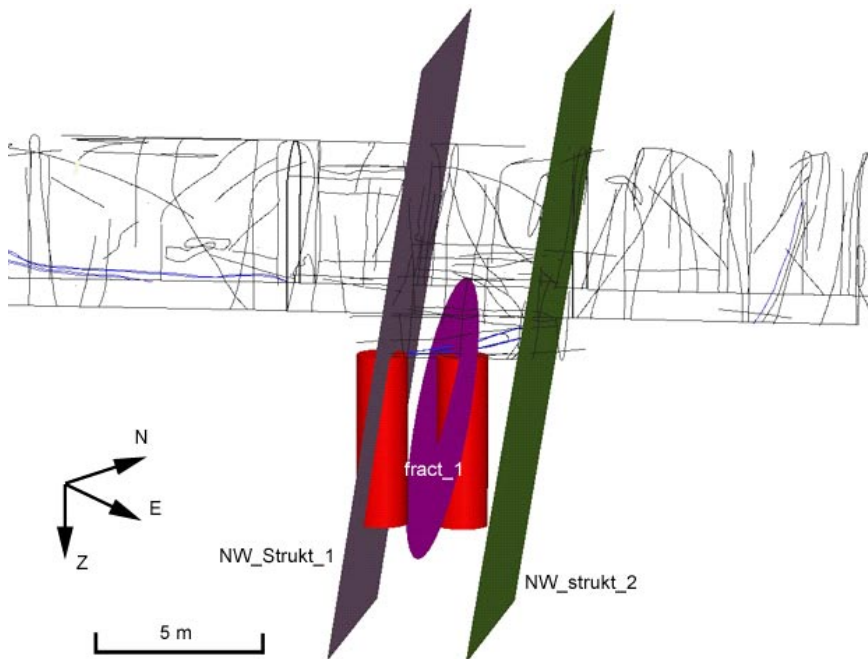


Figure 3-20. Interpreted subvertical structure “fract_1” in the pillar area. The red cylinders are a visualisation of the planned large holes, the pillar being the space in between.

The subhorizontal features

Two recurrent features have been observed in most of the boreholes mapped as a wide breccia or thinner epidote filled fractures. While the breccia mostly occurs at one depth level the epidote filled fractures occur at two depth levels. Two distinct features have been identified and modelled from the observations made on the core. The points for modelling the “breccia” are listed in and the points for the “epidote” are listed in Table 3-12. The first structure is called “breccia” because most of the features fit a breccia but some of the features used for modelling are closer to epidote filled fractures.

The breccia is identified on boreholes located on both sides of the pillar and of the shear zone.

The visualisation of the individual fractures in the boreholes and the points used for the interpretation of the structures are illustrated in Figure 3-21 for the “breccia” and in Figure 3-22 for the “epidote”.

The structures interpreted from the presented data are illustrated in Figure 3-23 and their orientation is reviewed in Table 3-13.

Table 3-11. Identification of the “breccia”.

	Depth (m)	Strike/Dip (°) – measured	Width (mm)	Remarks
KQ0064G01	2.6	13/22	14	Breccia
KQ0064G02	2.7	0/0	5	Epidote
KQ0064G03	2.4	323/2	1	Epidote
KQ0064G04	3	169/2	4	Epidote
KQ0064G05	2.7	265/22	39	Breccia
KQ0064G06	2.9	315/12	70	Breccia
KQ0064G07	2.8	277/8	30	Breccia
KQ0065G02	3	228/8	70	Breccia
KQ0065G03	2.8	219/6	40	Breccia
KQ0065G05	2.4	351/5	7	Breccia

Table 3-12. Identification of the epidote filled fracture.

	Depth (m)	Strike/Dip (°) – measured	Width (mm)	Remarks
KQ0064G02	5.2	140/6	4	Epidote
KQ0064G05	5.4	123/4	5	Epidote
KQ0064G06	5.4	111/4	2	Epidote
KQ0065G01	4.7	144/6	7	Epidote
KQ0065G05	5	209/3	2	Epidote

Table 3-13. Orientation of the interpreted subhorizontal structures in the pillar.

	Strike (°)	Dip (°)
Breccia	170.4	7.5
Epidote	140.3	6.1

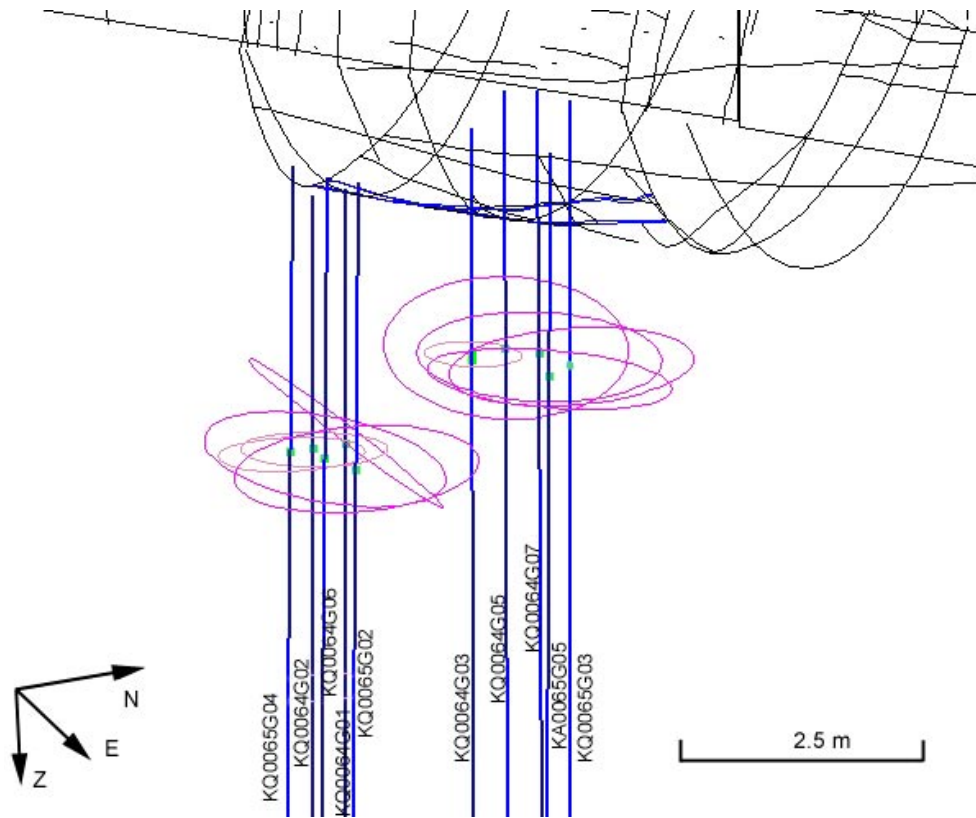


Figure 3-21. Identification of the points used for the modelling of the "breccia".

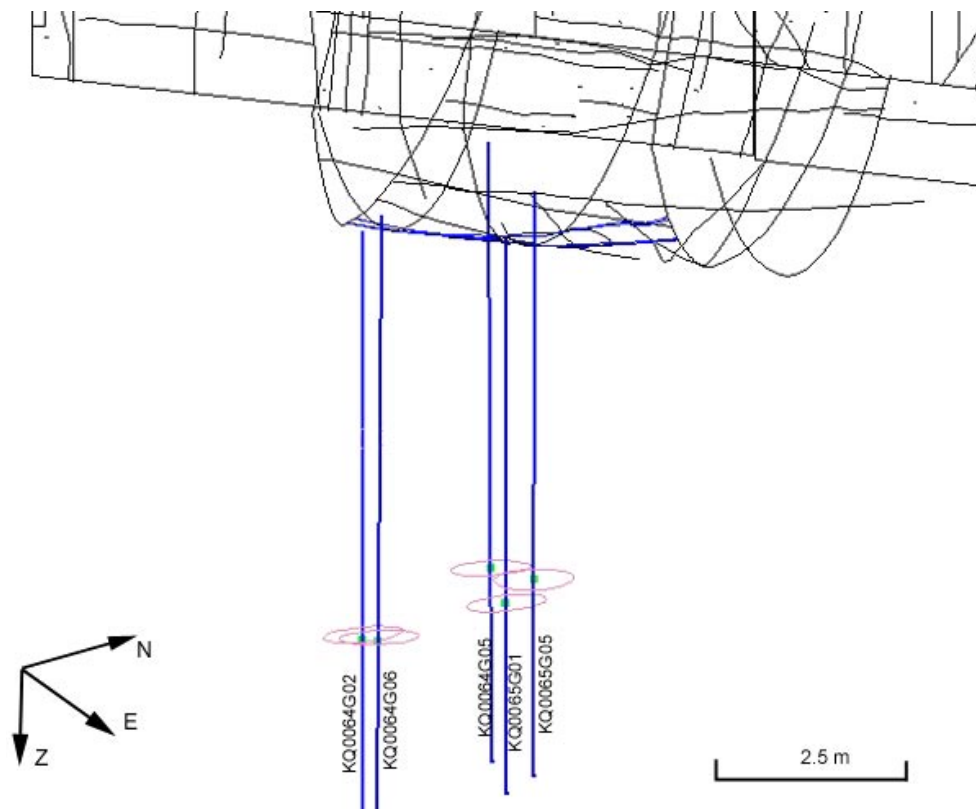


Figure 3-22. Identification of the points used for the modelling of the epidote filled fracture.

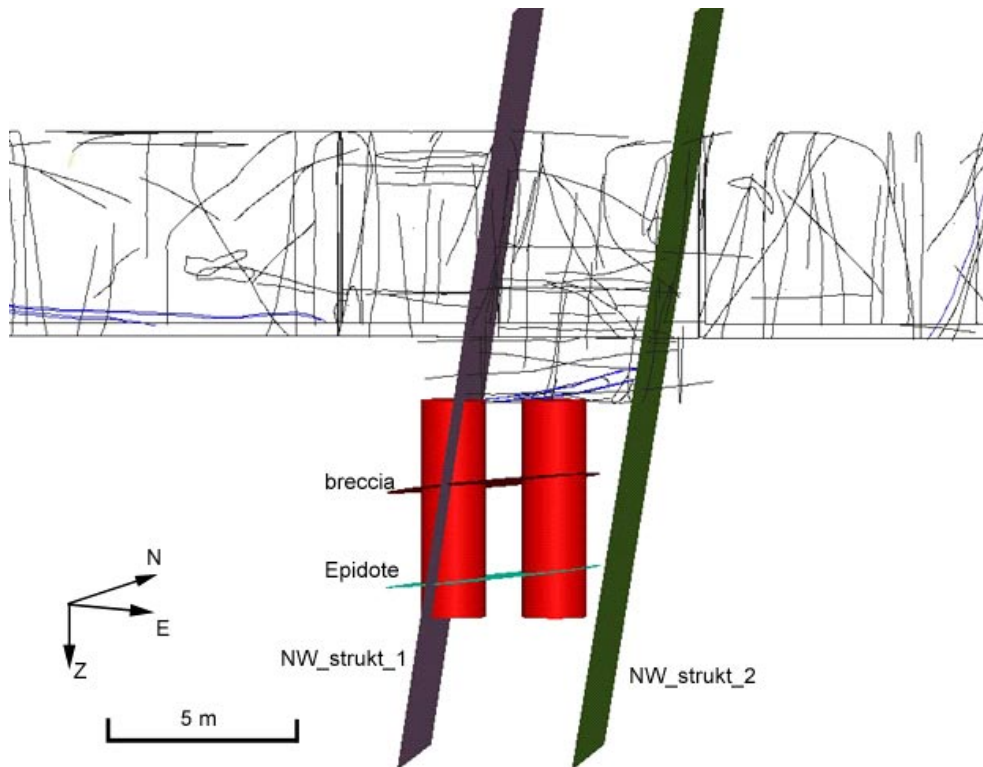


Figure 3-23. Interpreted “breccia” and “epidote” structures in the pillar area. The red cylinders are a visualisation of the planned large holes, the pillar being the space in between.

3.4 Discussion and conclusion

3.4.1 Predictions from the model

A detailed model of structures and fractures in the pillar experiment area has been developed. The interaction between the different interpreted structures is illustrated in Figure 3-24 and in Figure 3-25.

Based on the model of geological structures sections of the pillar could be extracted at 0.5 and 1.5 m below the tunnel floor. These sections show the intersections of the main structures and fractures identified in the experiment area with the large holes and the pillar itself.

These figures illustrate that the main structure of influence for the pillar stability experiment is the SZ_S branch of the shear zone. The subvertical feature fract_1 identified in the northern deposition hole is intersecting the pillar at 5 m depth, far below the target levels. The breccia and epidote features identified in the pillar are also located below the target levels (respectively 2.2 m and 4.8 m).

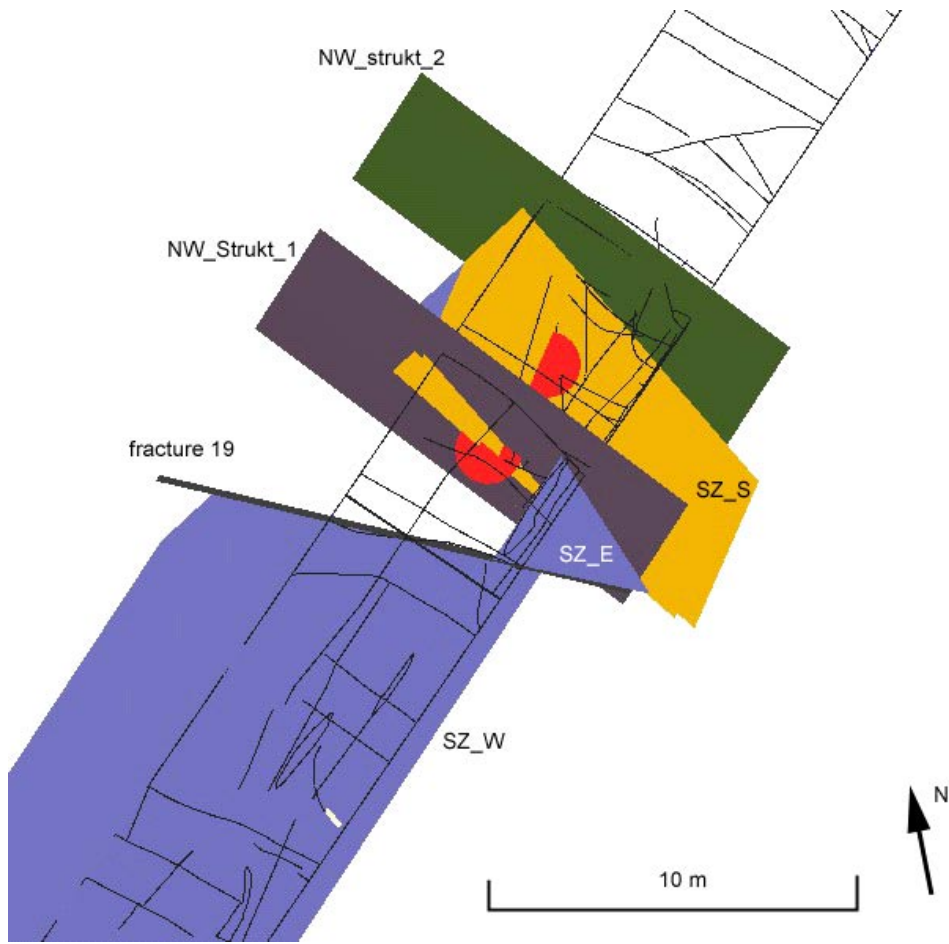


Figure 3-24. 3D visualisation of the main interpreted structures in the pillar experiment area. The red cylinders represent the planned large holes.

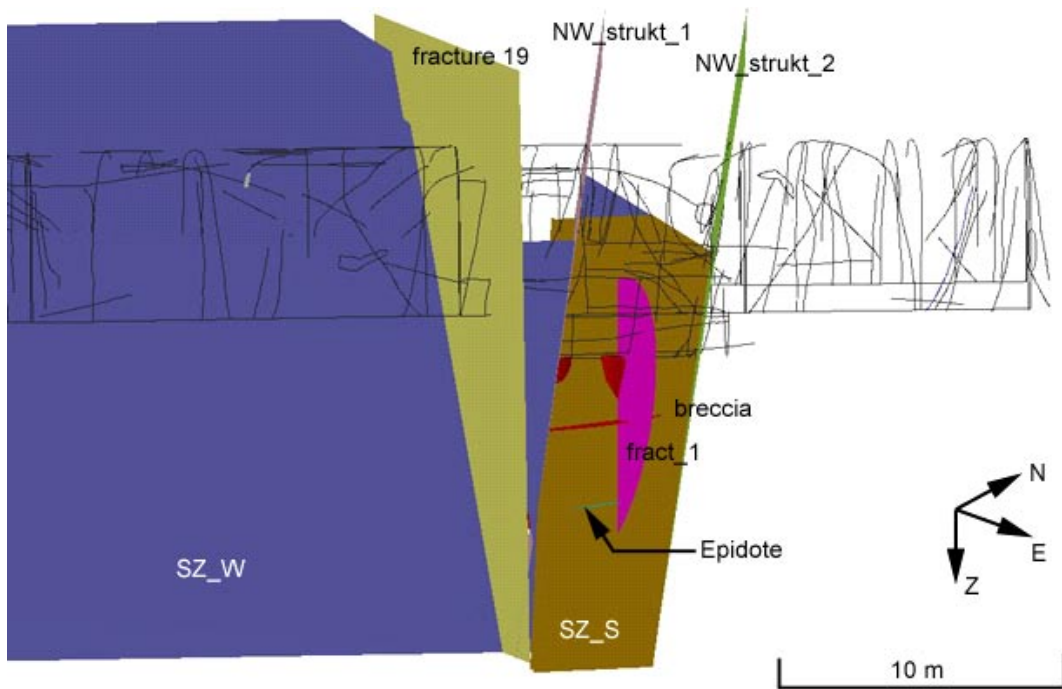


Figure 3-25. 3D visualisation of the fractures identified in the pillar and their relation to the main interpreted structures. The red cylinders represent the planned large holes.

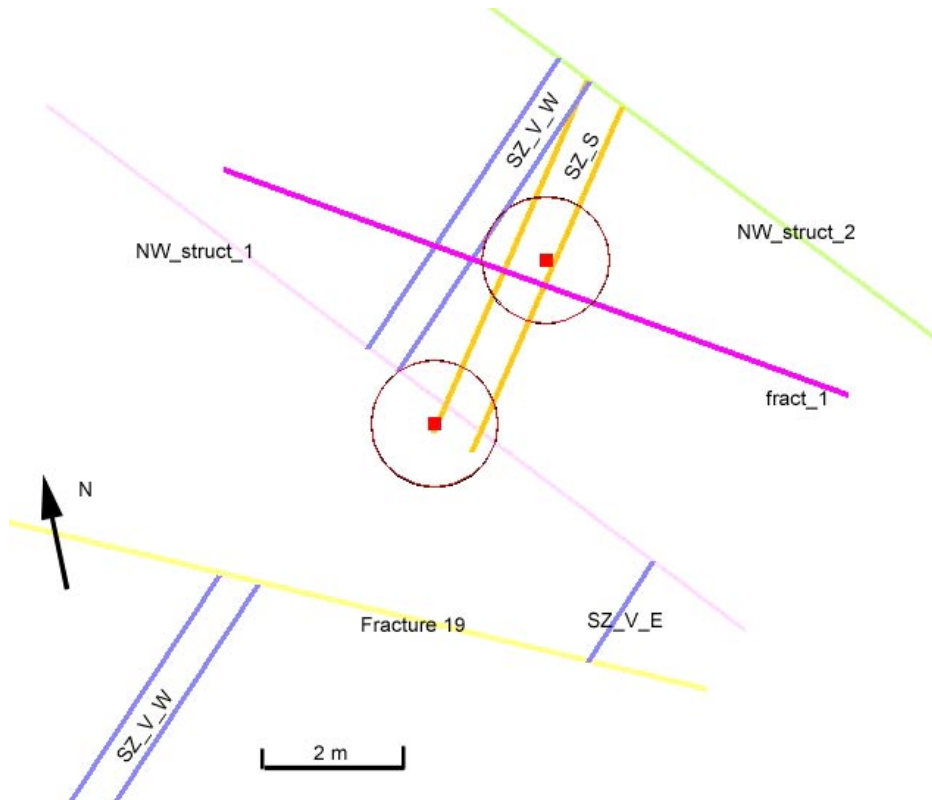


Figure 3-26. Intersections of the identified structures with the large holes (red cylinders) and the pillar (space in between) at 0.5 m below the tunnel floor.

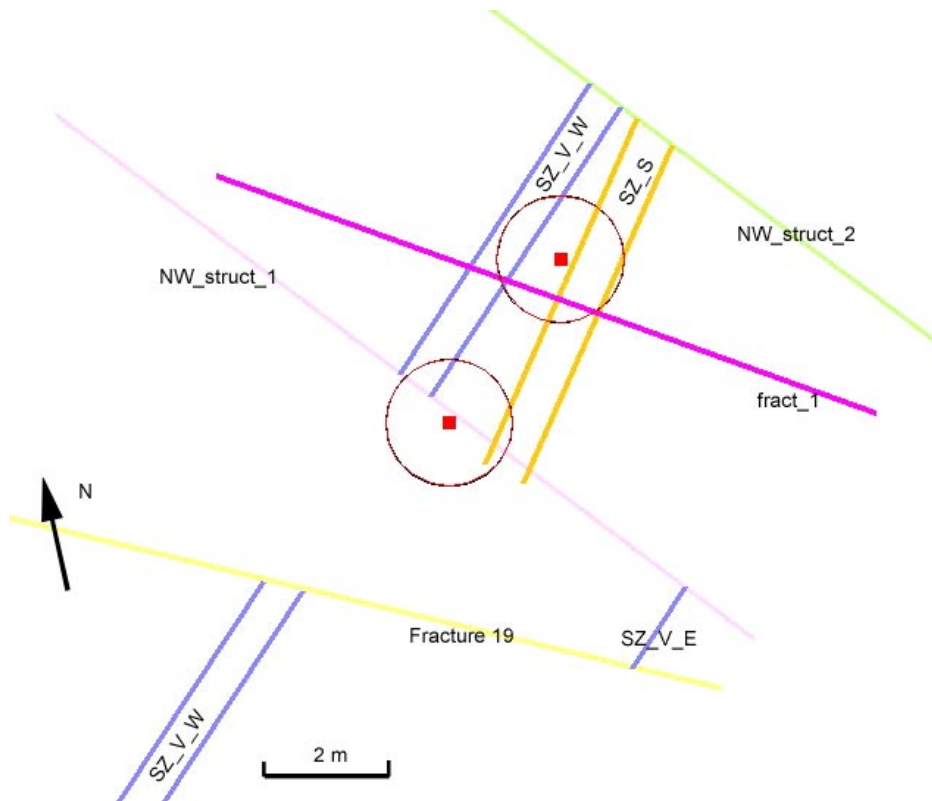


Figure 3-27. Intersections of the identified structures with the large holes (red cylinders) and the pillar (space in between) at 1.5 m below the tunnel floor.

3.4.2 Mapping observations from the deposition hole DQ0066G01

At the time of the reporting the first deposition hole has been drilled. In order to make a preliminary check of the predictions from the model the mapping of the hole is presented and shortly discussed. The mapping has been done by standing in the hole (1.8 m in diameter and 6.5 m deep) and unrolling structures on paper. The result is presented in Figure 3-28.

In order to facilitate the comprehension of the figure the sections interpreted as mylonite were coloured in blue. The red spots correspond to the spalling that occurred in the hole just after drilling.

An overview of the fractures mapped in the deposition hole reveal that subhorizontal fractures are more frequent than in the regular tunnel mapping, section 2. Two fractures belonging to the NW-SE subvertical fracture set identified in section 2 are mapped in the deposition hole. These fractures are associated to water leakage into the hole. The total measured inflow to the hole is approximately 30 l/min.

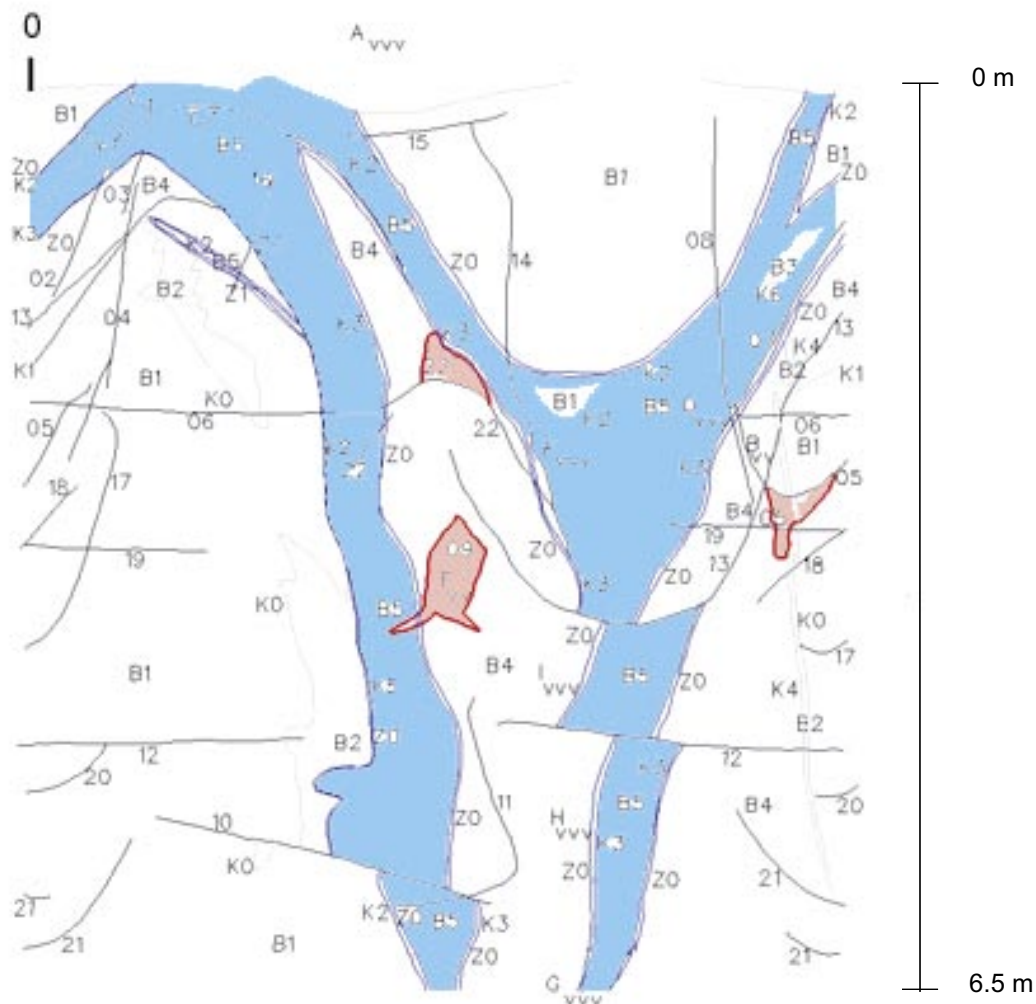


Figure 3-28. 2D mapping of the first deposition hole DQ0066G01 (inside image of the borehole wall, the 0 vertical line is located on the northern side of the hole along the tunnel axis). The blue area is a representation of the material inside the zone, the red spots localise spalling events during drilling. The different abbreviations refer to contacts between rock types, the numbers identify fractures, and Z0 correspond to the shear zone.

From the observation of the 2D mapping and Figure 3-29 it can be observed that the shear zone seems to be dipping more than what was predicted from the occurrence mapped on the floor. Complementary observations and analyses of the predictions of the model towards “reality” from the mapping of the deposition holes are to be done.

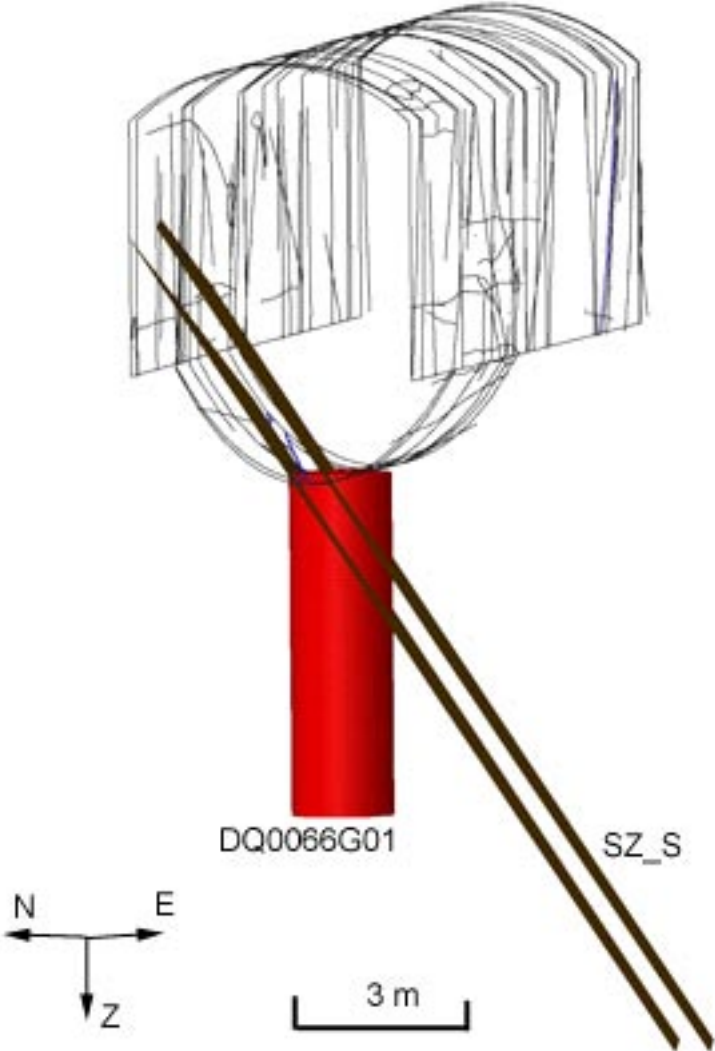


Figure 3-29. The modelled shear zone and its intersection with DQ0066G01.

4 Rock mass properties

4.1 General information on collected samples

In order to determine mechanical and thermal properties of the rock, samples were collected for testing in 5 boreholes at different depths, 1 subhorizontal borehole parallel to the TASQ tunnel; KA3376B01, and 4 subvertical pilot boreholes drilled in the target area for the pillar stability experiment: KQ0064G01, KQ0064G05, KQ0064G07 and KQ0065G01. The main tests that were conducted are:

- Mechanical properties:
 - on the intact rock: density, uniaxial compression tests, triaxial compression tests and tensile strength were made. Together with the strength parameters Young’s modulus, Poisson’s ratio, Crack Initiation Stress and Crack Damage Stress were determined from the results of these tests,
 - on fractures: fracture stiffness and fracture toughness (mode I and II),
 - Sonic and ultrasonic velocity measurements: back-calculation of deformation’s modulus for intact rock and rock mass.
- Thermal properties: thermal conductivity, thermal expansion and heat capacity.

Table 4-1 illustrates all tests conducted in the different boreholes in the frame of the Pillar stability experiment. The results of the tests are presented and discussed for intact rock in Section 4.2 and for fractures in Section 4.3.

Table 4-1. Summary of tests conducted on samples collected in different boreholes.

ID	Depth (m)	Uniaxial compression tests	Triaxial compression tests	Tensile tests	Density	Conductivity	Thermal expansion	Heat capacity	Fracture stiffness	Fracture toughness
			Confining stress (MPa)							
KA3376B01	31.70		x 2							
KA3376B01	31.7				x					
KA3376B01	31.90		x 7							
KA3376B01	31.9				x					
KA3376B01	32.24			x						
KA3376B01	32.27		x 2							
KA3376B01	32.27				x					
KA3376B01	33.29			x						
KA3376B01	33.32	x								
KA3376B01	60.85		x 7							
KA3376B01	60.85				x					
KA3376B01	61.55			x						
KA3376B01	61.58	x								
KA3376B01	61.72	x								
KA3376B01	62.05		x 7							
KA3376B01	62.05				x					
KA3376B01	64.30		x 2							
KA3376B01	64.3				x					

ID	Depth (m)	Uniaxial compression tests	Triaxial compression tests	Tensile tests	Density	Conductivity	Thermal expansion	Heat capacity	Fracture stiffness	Fracture toughness
			Confining stress (MPa)							
KA3376B01	73.77–74.06								x	x
KA3376B01	77.93–78.18								x	x
KA3376B01	78.18–78.44								x	x
KA3376B01	79.49–79.75								x	x
KQ0064G01	5.44		x 1							
KQ0064G01	6.23			x						
KQ0064G01	6.26	x								
KQ0064G01	6.60–6.85				x	x	x	x		
KQ0064G01	6.85–7.10				x	x	x	x		
KQ0064G05	5.77–6.01				x	x	x	x		
KQ0064G07	4.99	x								
KQ0064G07	5.13		x 1							
KQ0064G07	5.38	x								
KQ0064G07	5.53			x						
KQ0065G01	5.29	x								
KQ0065G01	5.43	x								
KQ0065G01	5.57			x						
KQ0065G01	6.37	x								
KQ0065G01	6.53		x 1							

4.2 Intact rock properties

4.2.1 Density measurements

Density measurements were conducted on 6 samples from the subhorizontal borehole KA3376B01, and 3 samples collected in subvertical boreholes KQ0064G01 and KQ0064G05. Wet and dry density measurements as well as porosity tests were conducted on these 3 samples. Results of density measurements on samples from KA3376B01 are presented in Appendix B. The laboratory test report for tests conducted on KQ0064G01 and KQ0064G05 is presented in Appendix D. The localization of the samples is illustrated in Figure 4-1.

The density and porosity values obtained for all samples are summarized in. The results show that the density values are quite homogeneous for samples collected in KQ0064G01 and KQ0065G01. The values obtained on samples collected in KA3376B01 show a larger discrepancy but they are also more dispersed in space than samples from the subvertical boreholes.

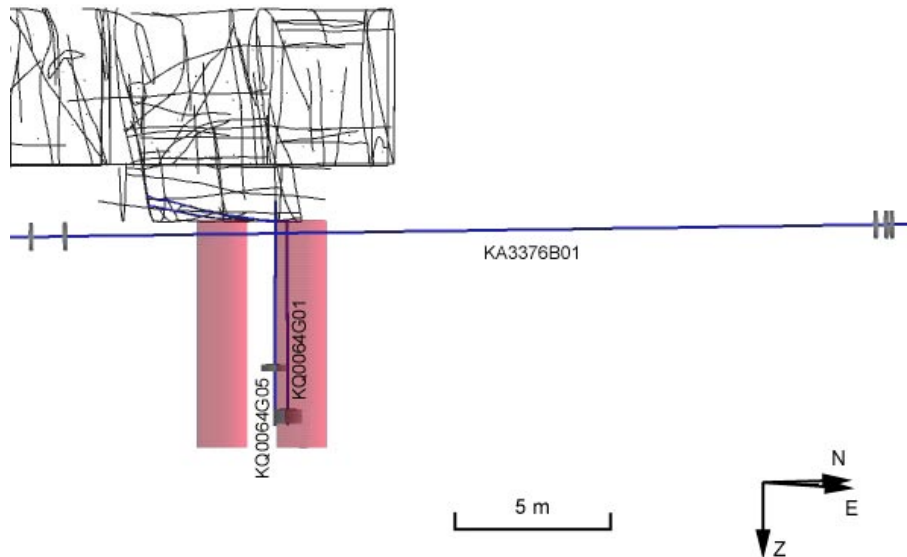


Figure 4-1. Localisation of the samples collected for density and porosity measurements. The two samples in KQ0064G01 are contiguous.

Table 4-2. Wet/dry density and porosity.

ID	Depth (m)	Density dry (kg/m ³)	Density wet (kg/m ³)	Density (kg/m ³)	Porosity (%)
KA3376B01	31.7			2,756	
KA3376B01	31.9			2,733	
KA3376B01	32.27			2,743	
KA3376B01	60.85			2,729	
KA3376B01	62.05			2,716	
KA3376B01	64.3			2,723	
KQ0064G01	6.60–6.85	2,740	2,750		0.35
KQ0064G01	6.60–6.85	2,740	2,750		0.4
KQ0064G01	6.85–7.10	2,750	2,760		0.36
KQ0064G01	6.85–7.10	2,750	2,760		0.4
KQ0064G05	5.77–6.01	2,750	2,750		0.15
Mean value		2,746	2,754	2,733.3	0.3
Std deviation		5.5	5.5	14.4	0.10

4.2.2 Mechanical properties

Eighteen samples were collected in one subhorizontal and 3 subvertical boreholes, see Table 4-1. The description of the tests and results are presented in details in Appendix B for borehole KA3376B01 and in Appendix C for boreholes KQ0064G01, KQ0064G07 and KQ0065G01.

The localization of the collected samples is illustrated in Figure 4-2 and Figure 4-3.

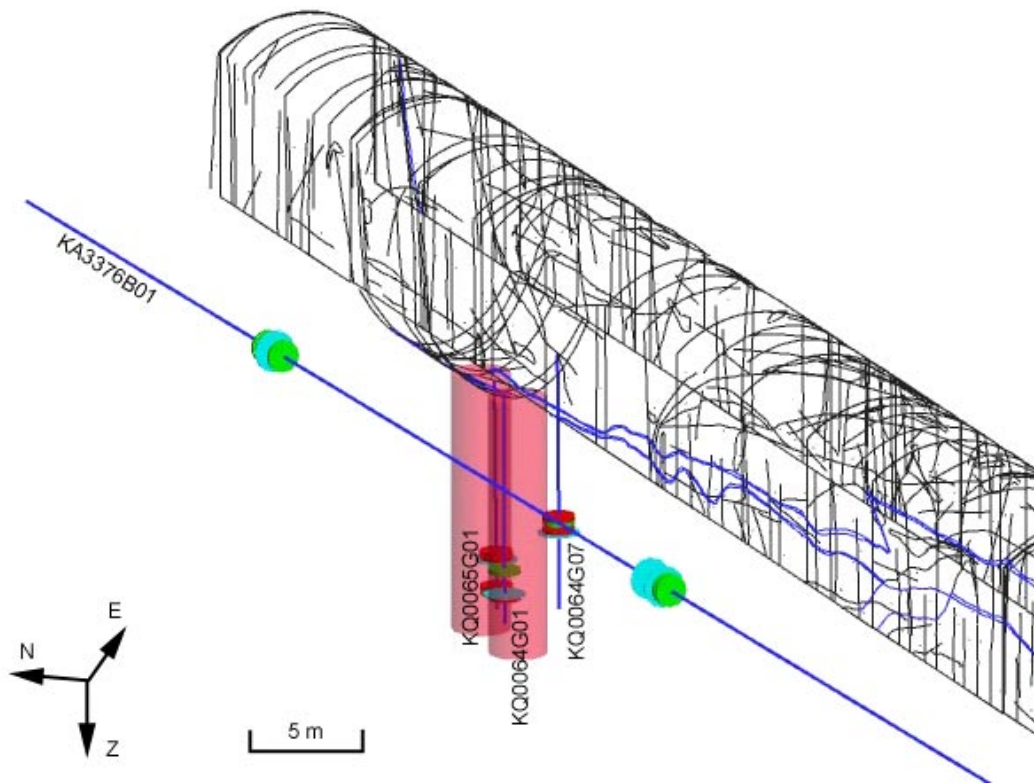


Figure 4-2. Localisation of the core samples collected for uniaxial compression tests (red discs), triaxial compression tests (green discs) and tensile tests (blue tests). The red cylinders represent the planned large holes. OBS: samples for the tensile tests have the same diameter as other samples, the diameter of the discs were increased for visualisation purposes.

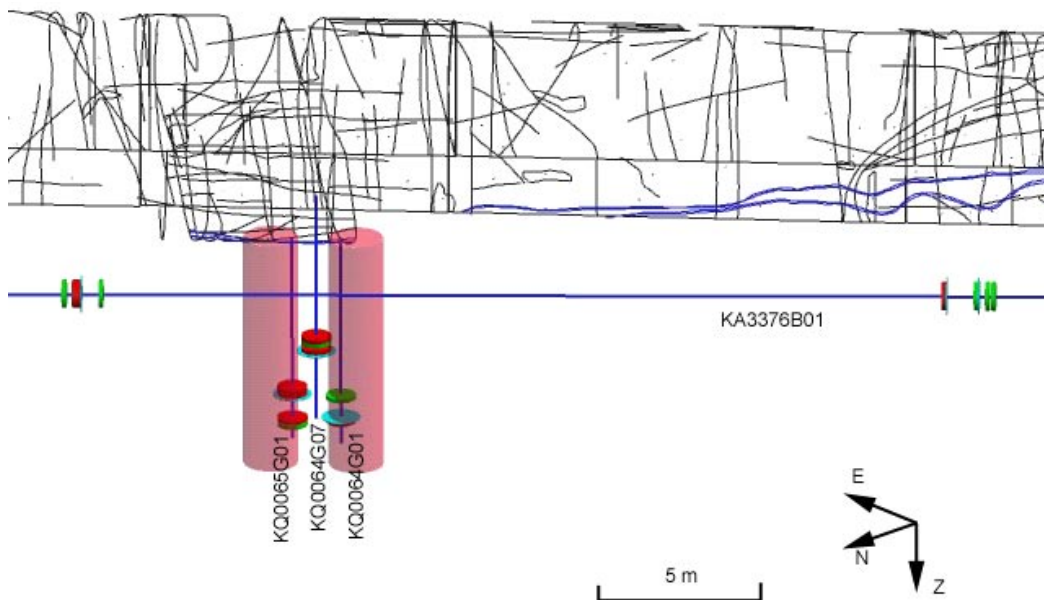


Figure 4-3. Localisation of the core samples collected for uniaxial compression tests (red discs), triaxial compression tests (green discs) and tensile tests (blue tests). The red cylinders represent the planned large holes. OBS: samples for the tensile tests have the same diameter as other samples, the diameter of the discs were increased for visualisation purposes.

Table 4-3 presents the mechanical properties obtained for each sample of intact rock collected in the different boreholes. All samples were identified as Äspö diorite. This table illustrates a large variation in mechanical parameters. The variation is particularly significant for the uniaxial compressive strength and the compressive strength. However variations in the compressive strength can not be evaluated statistically from this table as the different values reflect the confining stress during testing.

Figure 4-4 illustrates the frequency distribution of the Uniaxial Compressive Strength. The mean value for UCS is 188 MPa (all samples included) with a standard variation of 33.7 MPa (Figure 4-4a).

Table 4-3. Mechanical properties of the intact rock determined from laboratory testing.

ID	Depth (m)	UCS (MPa)	Compressive strength (MPa)		Young's modulus (GPa)	Poisson's ratio	Tensile strength (MPa)
				Confining stress (MPa)			
KA3376B01	31.70		175	2	70	0.22	
KA3376B01	31.90		265	7	74	0.24	
KA3376B01	32.24						15.9
KA3376B01	32.27		219	2	69	0.21	
KA3376B01	33.29						15.0
KA3376B01	33.32	195			67	0.27	
KA3376B01	60.85		252	7	75	0.24	
KA3376B01	61.55						15.4
KA3376B01	61.58	203			69	0.28	
KA3376B01	61.72	85			74	0.21	
KA3376B01	62.05		239	7	74	0.25	
KA3376B01	64.30		136	2	73	0.21	
KQ0064G01	5.44		243.5	1	79.1	0.26	
KQ0064G01	6.23						12.9
KQ0064G01	6.26	221.1			73.6	0.27	
KQ0064G07	4.99	189.5			74.1	0.28	
KQ0064G07	5.13		180.8	1	79.9	0.22	
KQ0064G07	5.38	131.7			72.8	0.27	
KQ0064G07	5.53						15.7
KQ0065G01	5.29	244.3			78.1	0.26	
KQ0065G01	5.43	236.7			76.8	0.28	
KQ0065G01	5.57						14.4
KQ0065G01	6.37	186.5			76.3	0.25	
KQ0065G01	6.53		255.9	1	77.3	0.23	
Mean value		210.9			73.8	0.25	14.9
1std deviation		23.3			3.6	0.02	1.1

Note: unstable samples during testing are marked in grey and have not been included for calculation of mean value and standard deviation in the table.

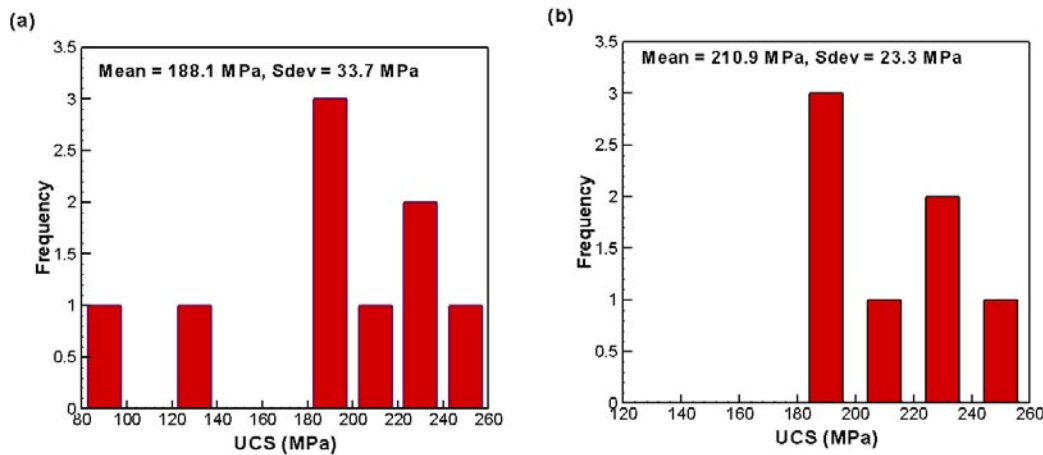


Figure 4-4. Frequency distribution of the uniaxial compressive strength, (a) all samples included, and (b) exclusive weak samples.

Some variations can be explained by weak samples. For example the sample from KA3376B01 at 61.72 m depth is a very weak specimen which exhibits sudden crack damage at 80 MPa (see Appendix B) that might be related to the presence of a thin closed fracture in the sample. The sample from KQ0064G07 at 5.38 m depth presents also an unstable behaviour. The elastic properties were calculated on the linear part of the curves between axial stress levels of 42 MPa and 52 MPa (see Appendix C). A thin inclined pegmatite vein is mapped in the sample. The sample at 5.13 m depth from KQ0064G07 used for triaxial test is also presenting distinct propagating cracks (see Appendix C). However their impact on the evaluated value is not trivial as different values of compressive strength are also related to different confining stresses applied during testing.

According to the structure of the samples and of the laboratory curves presence of thin veins or closed fractures might influence the results of the test and might constitute planes of weakness during the testing. Removing the samples clearly identified as weak in the laboratory tests report changes the frequency distribution of both parameters, but the influence of those samples is particularly obvious on the distribution of the UCS (Figure 4-4a and b). The mean value for the UCS when excluding the weak and unstable samples is 211 MPa and the standard deviation is 23.3 MPa (Table 4-3).

Values of deformation's modulus and Poisson's ratio are less sensitive to the structure of the samples as they are calculated on the section of the curve for elastic behaviour. Mean value and standard deviation exclusive weak samples are presented in Table 4-3.

Two different methods are available to evaluate the Crack Initiation Stress, CIS, and Crack Damage Stress, CDS:

- the volumetric stress/strain curves from the uniaxial and triaxial tests,
- the intensity of Acoustic Emission (AE) events recorded versus axial stress. Only samples used for uniaxial compressive tests have been used for AE measurements.

The values evaluated from both methods are presented in Table 4-4. There is a quite significant discrepancy in results between both methodologies and especially when evaluating the Crack Initiation Stress. The values determined for the Crack Damage Stress are quite similar.

Table 4-4. Values for CIS and CDS evaluated from the two different measurement methods stress/strain curve and AE-measurements.

ID	Depth (m)	CIS (MPa) (compressive tests)	CDS (MPa)	CIS (MPa) (AE measurements)	CDS (MPa)
KA3376B01	31.70	83.1	175.5		
KA3376B01	31.90	111.7	241		
KA3376B01	32.24				
KA3376B01	32.27	99.2	210.3		
KA3376B01	33.29				
KA3376B01	33.32	87.1	172		
KA3376B01	60.85	112.3	251.5		
KA3376B01	61.55				
KA3376B01	61.58	87	185.5		
KA3376B01	61.72	50.3	84.8		
KA3376B01	62.05	105.3	209.6		
KA3376B01	64.30	71.2	132.7		
KQ0064G01	5.44	97.6	229.5		
KQ0064G01	6.23				
KQ0064G01	6.26	89.2	189.2	135	210
KQ0064G07	4.99	88.7	189.5	160	190
KQ0064G07	5.13	93	–		
KQ0064G07	5.38	–	56	50	115
KQ0064G07	5.53				
KQ0065G01	5.29	111.7	213.4	130	215
KQ0065G01	5.43	100.5	215.4	100	220
KQ0065G01	5.57				
KQ0065G01	6.37	91.6	186.5	80	185
KQ0065G01	6.53	105.7	225.7		
Mean value		96.1	201.8	121	204
Std deviation		12.0	30.4	31.3	15.6

Note: unstable samples during testing are marked in grey and have not been included for calculation of mean value and standard deviation.

The interpretation of the mechanical tests from different boreholes and different tests show that the most significant factor for explaining the dispersion of parameters is geology and structure. Local variations in geology might affect strongly the quality of the samples. Detailed mapping of the cores illustrate that the Äspö diorite can be composed of large phenocrystals (or blasts) of feldspars that might affect the tests and their results (Figure 4-5). The Äspö diorite is also locally altered and different oxidisation grades are observed in sections of the cores (Figure 4-6 and Figure 4-7).



Figure 4-5. Picture of a “typical” example of the Äspö diorite.

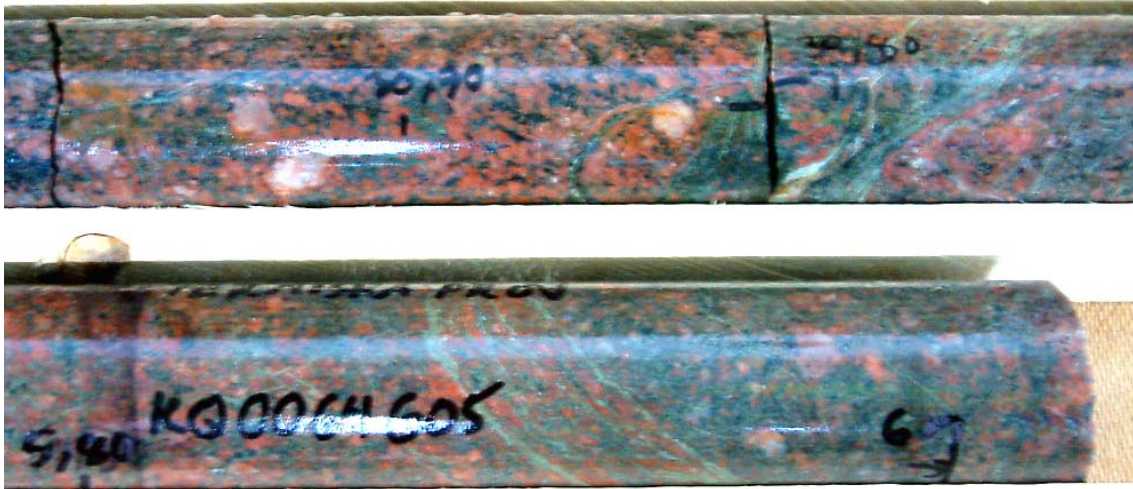


Figure 4-6. Picture of a slightly oxidised and altered section of Äspö diorite with sealed fractures.



Figure 4-7. Picture of a oxidised sample of Äspö diorite.

4.2.3 Thermal properties

Three samples were collected in 2 subvertical boreholes, see. The localization of the samples is illustrated in Figure 4-8. Samples collected in KQ0064G01 are contiguous.

Laboratory tests reports are presented in Appendix D for the measurement of thermal expansion, and in Appendix E for the measurement of heat capacity and heat conductivity.

Measurements of the coefficient of thermal expansion were made at 5 temperature intervals and three measurements were made on each sample at each temperature interval. Table 4-5 presents a summary of the obtained values.

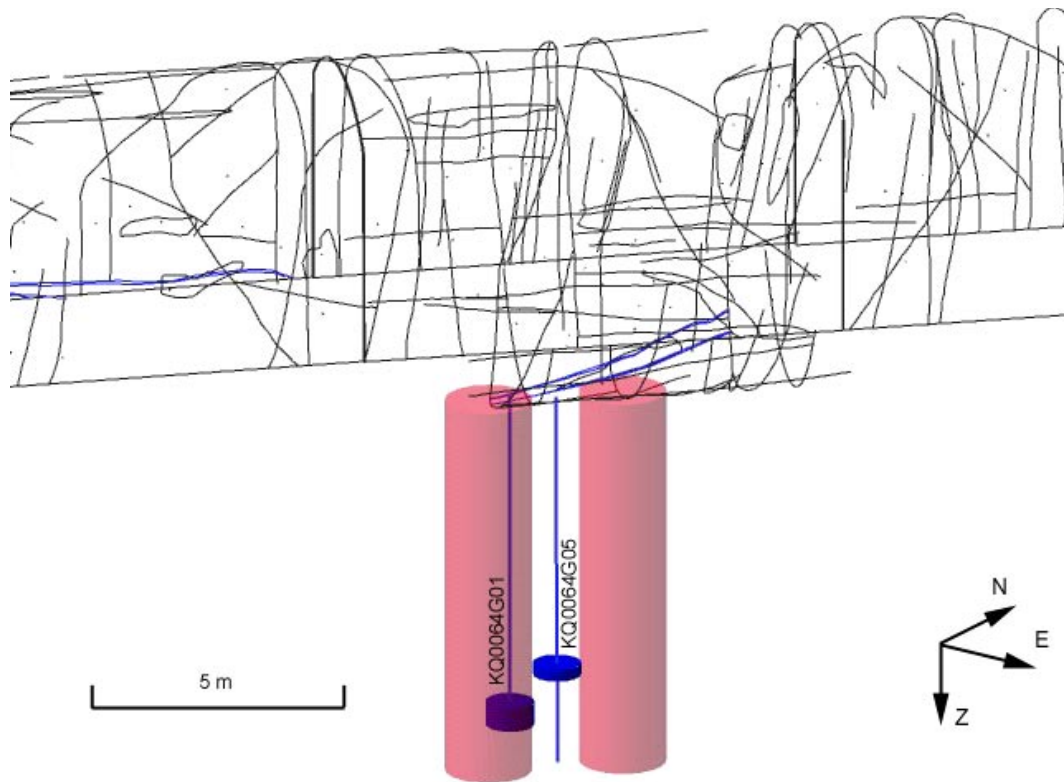


Figure 4-8. Localisation of the samples collected for testing of thermal properties. The red cylinders represent the planned large holes.

Table 4-5. Mean values obtained for the coefficient of thermal expansion at different temperature intervals.

ID	Depth (m)	20–40°C (mm/mm°C)	20–60°C (mm/mm°C)	20–80°C (mm/mm°C)	40–60°C (mm/mm°C)	60–80°C (mm/mm°C)	Rock type
KQ0064G01	6.60–6.85	7.1E–06	6.6E–06	6.9E–06	6.0E–06	7.5E–06	Diorite, grey
KQ0064G01	6.85–7.10	6.7E–06	6.6E–06	7.1E–06	6.6E–06	7.9E–06	Diorite, grey
KQ0064G05	5.77–6.01	8.1E–06	7.3E–06	7.1E–06	6.6E–06	6.7E–06	Diorite, red

The values are slightly different for the same temperature interval, even for two samples identified as equivalent as for geology (i.e. the two samples from KQ0064601). The influence of the grade of alteration of the diorite is difficult to assess from these 3 samples.

Thermal diffusivity, thermal conductivity and heat capacity were determined at 22, 40 and 60, and five measurements were made on each sample. Table 4-6 and present mean value and standard deviation of the thermal properties obtained for each tested sample.

The results on conductivity and diffusivity are rather homogeneous for both samples collected in KQ0064G01 at different temperatures. Values are slightly different for the samples collected in KQ0064G05 which is identified as oxidized diorite. The impact of temperature is greater on diffusivity than conductivity.

Table 4-6. Mean value of thermal conductivity, volume heat capacity and thermal diffusivity.

	ID	Depth (m)	Diffusivity (W/mK)	Diffusivity (mm ² /s)	Heat capacity (MJ/m ³ K)
22°	KQ0064G01	6.60–6.85	2.40	1.17	2.06
	KQ0064G01	6.85–7.10	2.54	1.12	2.28
	KQ0064G05	5.77–6.01	2.79	1.25	2.24
40°	KQ0064G01	6.60–6.85	2.42	1.12	2.17
	KQ0064G01	6.85–7.10	2.54	1.07	2.37
	KQ0064G05	5.77–6.01	2.79	1.25	2.32
60°	KQ0064G01	6.60–6.85	2.39	0.98	2.45
	KQ0064G01	6.85–7.10	2.48	0.99	2.50
	KQ0064G05	5.77–6.01	2.74	1.07	2.55

Table 4-7. Standard deviation of thermal conductivity, volume heat capacity and thermal diffusivity.

	ID	Depth (m)	Conductivity (W/mK)	Diffusivity (mm ² /s)	Heat capacity (MJ/m ³ K)
22°	KQ0064G01	6.60–6.85	0.008	0.009	0.011
	KQ0064G01	6.85–7.10	0.003	0.004	0.006
	KQ0064G05	5.77–6.01	0.005	0.02	0.032
40°	KQ0064G01	6.60–6.85	0.001	0.002	0.003
	KQ0064G01	6.85–7.10	0.001	0.001	0.003
	KQ0064G05	5.77–6.01	0.002	0.001	0.001
60°	KQ0064G01	6.60–6.85	0.010	0.040	0.110
	KQ0064G01	6.85–7.10	0.015	0.032	0.082
	KQ0064G05	5.77–6.01	0.018	0.030	0.075

4.3 Fracture properties

Fracture normal stiffness, and mode I and mode II fracture toughness were determined on 4 samples collected in the sub-horizontal borehole KA3376B01 (see Figure 4-9 and Table 4-1). The procedure was as first to determine the stiffness of the intact specimen. Each rock sample was then prepared for determination of mode I toughness. The fracture was propagated through the whole sample and the stiffness was estimated. The mode II fracture toughness was determined on the remaining halves of the sample.

The procedure used for the different tests implies that no natural fractures were testing.

The laboratory tests methodology is presented in Appendix F. Four tests for mode I fracture toughness and fracture stiffness were performed on each sample, but 12 tests were conducted at different confining stresses in order to determine mode II fracture toughness.

The results obtained for mode I fracture toughness are presented in Table 4-8. The corrected mode I fracture toughness is calculated based on a correction factor for non-linearity. The values are rather consistent between the four samples collected at different depth levels.



Figure 4-9. Localisation of samples collected for testing of fracture properties. The red cylinders represent the planned large holes.

Table 4-8. Corrected; K_{IC} , and uncorrected, K_{IC}^C , mode I fracture toughness.

ID	Depth (m)	K_{IC} (MPa m ^{1/2})	K_{IC}^C (MPa m ^{1/2})
KA3376B01	73.77–74.06	3.43	3.87
KA3376B01	77.93–78.18	2.81	3.79
KA3376B01	78.18–78.44	2.98	3.84
KA3376B01	79.49–79.75	3.30	3.8
Mean value		3.13	3.83

The values of mode II fracture toughness obtained at confining pressures 0, 5, 15, 30, 50 and 70 MPa for each sample are presented in Table 4-9. Two tests were conducted at the same confining pressure. The values of deformation's modulus and Poisson's ratio used for the determination of the mode II fracture toughness are $E = 68$ GPa and $\nu = 0.24$ (see Appendix F).

Table 4-9. Mode II fracture toughness, K_{IIc} , and applied confining pressure with increasing depth.

ID	Depth (m)	Confining pressure (MPa)	K_{IIc} (MPa m ^{1/2})
KA3376B01	73.82–73.87	0	4.6
KA3376B01	78.33–78.38	0	4.4
KA3376B01	73.77–73.82	5	7.5
KA3376B01	78.23–78.28	5	7.0
KA3376B01	78.13–78.18	15	10.1
KA3376B01	79.65–79.70	15	10.0
KA3376B01	78.07–78.12	30	12.6
KA3376B01	79.49–79.54	30	11.2
KA3376B01	73.98–74.03	50	12.5
KA3376B01	78.18–78.23	50	13.5
KA3376B01	77.93–77.98	70	12.7
KA3376B01	79.55–79.60	70	12.8

The results show that the values are rather homogeneous for the same confining pressure and that the mode II fracture toughness increases in relation to the confining stress applied. However the mode II fracture toughness is reported to become constant above a certain confining pressure level estimated at 35 MPa for the Äspödiorite (see Appendix F).

The fracture normal stiffness is evaluated on the ascending branch of the load. The results are summarised in Table 4-10.

Table 4-10. Intact rock stiffness, K_R , initial fracture stiffness (0–1.5 kN), K_{Ni} , and fracture stiffness (12–25 kN), K_{NH} .

ID	Depth (m)	K_R (kN/mm)	K_R (GPa/m)	K_{Ni} (kN/mm)	K_{Ni} (GPa/m)	K_{NH} (kN/mm)	K_R (GPa/m)
KA3376B01	73.77–74.06	2,440	2,451	310	311	2,800	2,813
KA3376B01	77.93–78.18	1,365	1,371	105	105	5,600	5,626
KA3376B01	78.18–78.44	1,820	1,829	130	131	45,000	45,212
KA3376B01	79.49–79.75	1,430	1,437	150	151	54,000	54,254
	Mean value		1,772		174.5		26,976.3

The table illustrates a large discrepancy on initial fracture stiffness and fracture stiffness. There is a factor 3 between extreme values for initial fracture stiffness and a factor 20 for fracture stiffness. With consideration to the high variability of estimated values the question of the liability of the tests and of the parameters determined must be raised. The values should be considered as indicative.

4.4 Sonic and ultrasonic velocity measurements

4.4.1 P-wave measurements in pilot hole cores

P-wave measurements were carried out on 24 core samples from the 3 subvertical boreholes KQ0048G01, KQ0064G01 and KQ0066G01, see Figure 4-10. The device used was specially designed for this project. A strong sine-wave pulse at the natural frequency of the transducers was used as the acoustic signal source. The measurement technique is presented in details in Appendix G.

In order to catch the eventual foliation of the cores the measurements were made around the core at 30° intervals starting parallel to the foliation and rotating clockwise when looking down the hole. Two consecutive measurements were made at each location (0, 30, 60, 90, 120 and 150) for each sample. When the foliation was not determined a random orientation was chosen for the origin of the measurements. The measured acoustic velocity and anisotropy ratio are presented in Table 4-11. These values were used to calculate the principal velocities V_X and V_Y , X being parallel to the foliation when identifiable. Results and figures are presented in Appendix G.

The P-wave velocity measurements are consistent in the three boreholes with maximum principal velocities in the order of 5,500–6,000 m/s and an anisotropy ratio in the range 1 to 1.04. No trend with depth could be identified but it can partly be imparted to the limited number of measurements conducted.

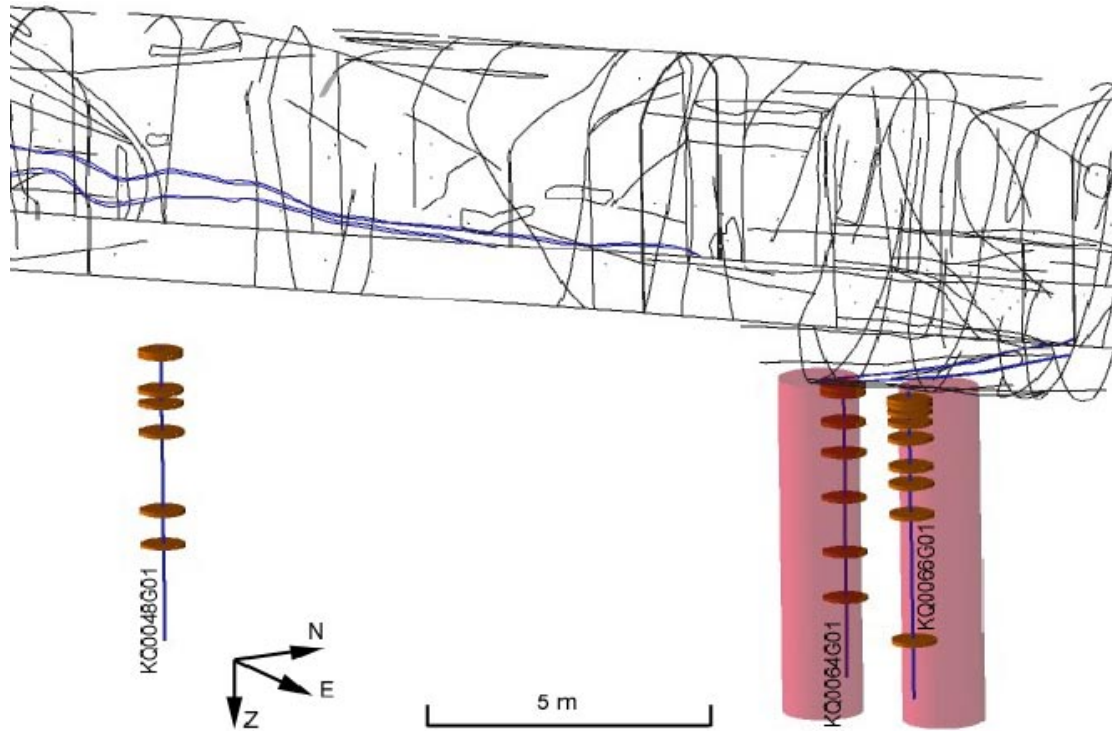


Figure 4-10. Localisation of samples for P-wave measurements. The red cylinders are the planned large holes.

Table 4-11. Measurements of acoustic velocity, transverse core in boreholes KQ0048G01, KQ0064G01 and KQ0066G01.

Depth m	Diameter mm	Velocity m/s						Anisotropy ratio
		Parallel to foliation			Perpendicular to foliation			
		0°	30°	60°	90°	120°	150°	
KQ0048G01								
0.06	50.82	5,558	5,619	5,651	5,657	5,582	5,528	1.02
0.15	50.82	5,934	5,969	5,920	5,873	6,040	5,948	1.03
0.98	50.81	5,624	5,563	5,449	5,313	5,426	5,503	1.06
1.32	50.83	5,658	5,571	5,683	5,735	5,741	5,690	1.03
2	50.77	5,894	6,013	5,977	6,020	5,922	5,942	1.02
3.9	50.77	5,915	5,806	5,908	5,887	5,867	5,887	1.02
4.7	50.81	6,046	6,046	6,046	6,025	5,996	6,046	1.01
KQ0064G01								
0.13	50.75	5,837	5,844	5,892	5,975	5,989	5,892	1.03
0.26	50.74	5,750	6,002	5,891	5,870	5,803	5,744	1.04
0.47	50.79	5,931	6,029	6,109	6,015	5,938	5,945	1.03
0.99	50.8	5,803	5,946	5,823	5,731	5,884	5,777	1.04
1.73	50.89	5,684	5,684	5,677	5,684	5,615	5,602	1.01
2.8	50.82	5,819	5,866	5,773	5,714	5,727	5,792	1.03
4.11	50.82	5,886	5,852	5,825	5,746	5,727	5,805	1.03
5.2	50.78	5,541	5,578	5,634	5,572	5,621	5,609	1.02
KQ0066G01								
0.15	50.86	5,307	5,324	5,484	5,397	5,188	5,290	1.06
0.27	50.86	5,680	5,777	5,817	5,770	5,699	5,502	1.06
0.45	50.87	5,954	6,010	5,996	5,947	6,060	6,068	1.02
0.7	50.77	5,683	5,670	5,658	5,702	5,787	5,728	1.02
1.08	50.78	5,529	5,742	5,748	5,697	5,684	5,634	1.04
1.77	50.74	6,045	6,023	6,009	6,023	6,038	6,023	1.01
2.17	50.85	5,910	5,890	5,724	5,842	5,959	6,001	1.05
2.92	50.85	5,910	5,987	5,994	5,945	5,910	5,945	1.01
5.93	50.85	5,802	5,763	5,862	5,966	5,945	5,910	1.04

The P-wave measurements conducted are a good way to appreciate the deformation's modulus of the intact rock. High amount of cores and measurements round the core at a same depth level allow estimating the variation of the deformation's modulus in the rock. The deformation's modulus is evaluated according to the following equation:

$$E = V_p^2 \cdot d \cdot \frac{(1+\nu) \cdot (1-2 \cdot \nu)}{(1-\nu)}$$

For the calculations the mean value of density ($d = 2,731 \text{ kg/m}^3$) and Poisson's ratio ($\nu = 0.245$) determined from laboratory tests (presented in Sections 4.2.1 and 4.2.2) are used.

The calculated values for deformation's modulus is $E = 75.6 \text{ GPa}$ with a standard variation of 6.5 GPa . The values are quite homogeneous in the different boreholes.

4.4.2 Borehole Velocity Profile Survey

The measurements were conducted in-situ by inserting the equipment in two pilot holes, KA0064G03 and KA0064G02 such that the measurement profile is perpendicular to the tunnel axis. The measurement technique and the results are presented in Appendix H. The volume of investigated rock is located in the immediate vicinity of the planned deposition hole DQ0063G01.

Figure 4-11 reveals an anomalously high velocity zone (peak velocity of $6,070 \text{ m}\cdot\text{s}^{-1}$) between 50 and 125 cm below the tunnel floor. This depth coincides with the mapped occurrence of the shear zone/mylonite in the deposition hole and the modelled shear zone in the pillar. Down the hole the profile shows a gradual decay to a P-wave velocity of approximately $5,950 \text{ m}\cdot\text{s}^{-1}$.

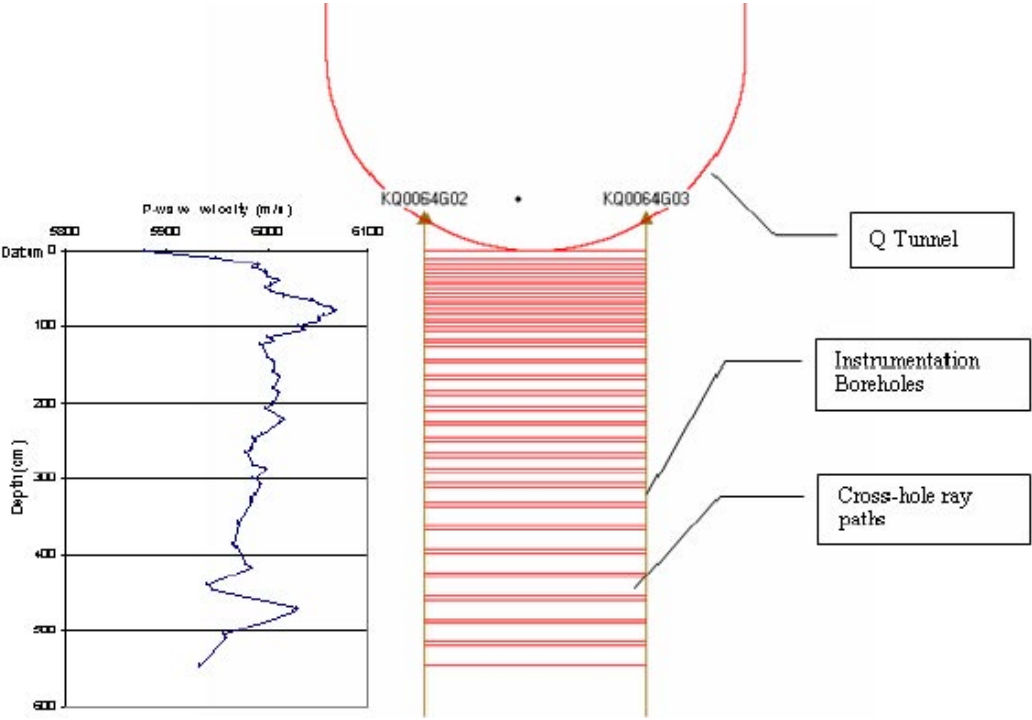


Figure 4-11. P-wave velocity profile with depth.

4.5 Discussions

Mechanical and thermal properties of the intact rock and mechanical properties of fractures were obtained by evaluation of laboratory tests and measurements. The values are summarized in Table 4-12 and Table 4-13.

The motivation of the parameters for intact rock is mostly presented in Section 4.2. Nevertheless some complementary comments can be made on the table:

- Values for the friction angle and cohesion of intact rock and rock mass are presented and discussed in /Staub et al. 2003/.
- The intact rock modulus values chosen are those calculated on P-wave velocities. The choice is motivated by the large amount of data which gave a good estimation of the discrepancy.
- Values for the CIS and CDS were taken from the AE measurement method.
- The chosen thermal properties are the mean value of all tested samples.

The evaluation of the parameters for fractures is presented in Section 4.3. Values of shear stiffness and residual angle are discussed and presented in /Staub et al. 2003/. The two values reflect different properties for subhorizontal and subvertical fracture sets.

Table 4-12. Mechanical and thermal properties of the intact rock (Äspö diorite), mean value.

Parameter	Mean value	Unit	Standard variation
Uniaxial compressive strength, low	130	MPa	
Uniaxial compressive strength, high	210	MPa	
Young's modulus, intact rock	76	GPa	6.5 GPa
Young's modulus, rock mass	55	GPa	
Poisson's ratio, intact rock	0.25	–	
Poisson's ratio, rock mass	0.26	–	
Friction angle, intact rock	49	Degrees	
Friction angle, rock mass	41	Degrees	
Cohesion, intact rock	31	MPa	
Cohesion, rock mass	16.4	MPa	
Tensile strength	14.3	MPa	
Thermal conductivity	2.60	W/m, K	
Volume heat capacity	2.10	MJ/m ³ , K	
Linear expansion	7.0E-06	l/K	
Density	2.731	g/cm ³	
Initial temperature of the rock mass	15	°C	
Crack initiation stress	121	MPa	
Crack damage stress	204	MPa	

Table 4-13. Mechanical properties of fractures, mean value.

Parameter	Mean value	Unit	Standard variation
Mode I toughness, K_{IC}	3.8	MPa/m ^{1/2}	0.1 MPa/m ^{1/2}
Mode II toughness, K_{IIC}	4.4 to 13.5	MPa/m ^{1/2}	
Initial normal fracture stiffness, K_{NI}	175	GPa/m	68
Normal fracture stiffness, K_{NH}	26,976	GPa/m	22,757
Shear stiffness	15.7/35.5	GPa/m	
Residual angle	31/30	Degrees	

5 Convergence measurements and back analyze

During the excavation of the TASQ tunnel convergence measurements was performed at chainage TASQ0049 with a Kern distometer. The measurements was made with the objective to verify the stress tensor in the rock volume that earlier was derived by use of several rock stress measurements by hydraulic fracturing and overcoring of the Borre probe in the vicinity of the experiment.

To get a good resolution of the measurements the blasting length of the pilot tunnel was reduced to two metres the first three blasts after the installation of the measurement pins. During the excavation of the bench, which was made after completion of the pilot drift, the blasting lengths were not reduced and the ordinary blast length of 4 metres was used. A cross section of the drift is presented in Figure 5-1.

To be able to verify the stress tensor with the convergence measurements the displacements were back calculated with Examine3D. During the back calculations the plunge and magnitudes of the stress tensor as well as Young's modulus of the rock mass was changed until a good fit between the modelled values and the measured ones were obtained.

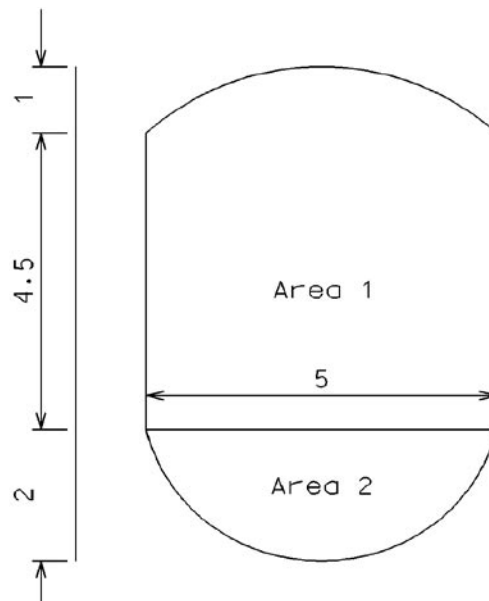


Figure 5-1. Dimensions of the excavated drift. Lengths in metres. Area 1 corresponds to the pilot drift which was entirely completed before the bench (Area 2) was excavated.

5.1 Measuring strategy

Totally seven pins for the convergence monitoring was installed into the rock, Figure 5-2. Twelve distances was measured between the seven pins. The distance between the pins no 1 and 2 was not measured during the pilot tunnelling due to problems with the coupling between that wire and the pins. The pins were made of reinforcement bars with a diameter of 25 mm and a length of approximately 700 mm. In each pin there was a screw tap attached at which the wire couplings could be connected, Figure 5-2.

The pins were grouted into boreholes. The top of the boreholes was drilled with a larger diameter to be able to totally countersink the taps into the rock wall and thus protect them during the excavations between the measurements figure .

The pins were installed approximately 0.3 to 0.5 metres behind the tunnel face and it was also at that chainage that the “zero” measurement was made.

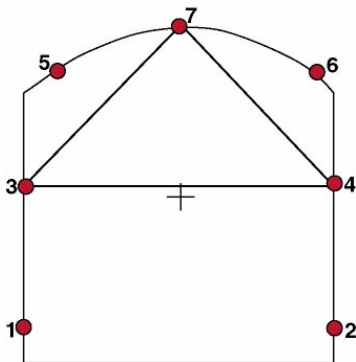


Figure 5-2. The approximate location of the seven pins in the pilot tunnel including example of three measured distances (left). Photograph of pin including screw tap and wire tap (right).



Figure 5-3. Photograph of Kern disotmeter attached at pin # 7 in the roof, note the countersink (left). The pins were installed approximately 0.3 to 0.5 m behind the face (right).

For each distance measured the spring in the Distometer was relaxed and then tensioned again to the designated load. This was repeated until a stable set of at least three measurements was noted. An example is presented in Table 5-1.

Table 5-1. Example of actual convergence measurement results between pins # 3 and 4. The values in bold were used to calculate the mean convergence for that measurement.

21.1	21.11	21.135
21.125	21.135	21.13

The uncertainty of the measurements are assessed to be 0.05 to 0.10 mm.

The convergence measurements during the excavation of the pilot drift and the bench were made with the face in the sections presented in Table 5-2.

Table 5-2. Sections where the face was located when the convergence measurements were performed.

Pilot drift, face location at measuring occasions (m)	Bench, face location at measuring occasions (m)
49	38
51	42.5
53	47
55	51.5
59	56

5.2 Measured results

In the Tables 5-3 to 5-7 the header is the point between which the measurements have been made. The column “last measurement” is the variation of the distance in millimetres with the measure made just before. The column “zero reading” is the difference of the distance in millimetres with the first reading (zero reading) made at chainage 49.

The location and numbering of the pins is presented in Figure 5-4.

The data is presented in graphical form in Figure 5-5. As can be seen in the figure the quality of the data is quite good. Pin # 7 was lost during the last measurements of the pilot drift and point # 2 was lost after the second blast in the bench.

The P stands for the Pilot drift blasting and the B stands for the Bench blasting. The pilot tunnel blasting was done entirely before the bench blasting started. The numbers behind the P or B is the section in metres, the pins being at 49 metres.

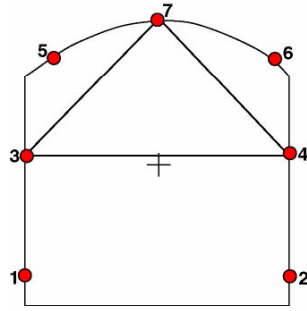


Figure 5-4. Location of the pins in the pilot drift section including their numbering. A measurement between pin no 3 and no 4 is labelled 3–4. The same location and numbering of the pins was used during the excavation of the bench.

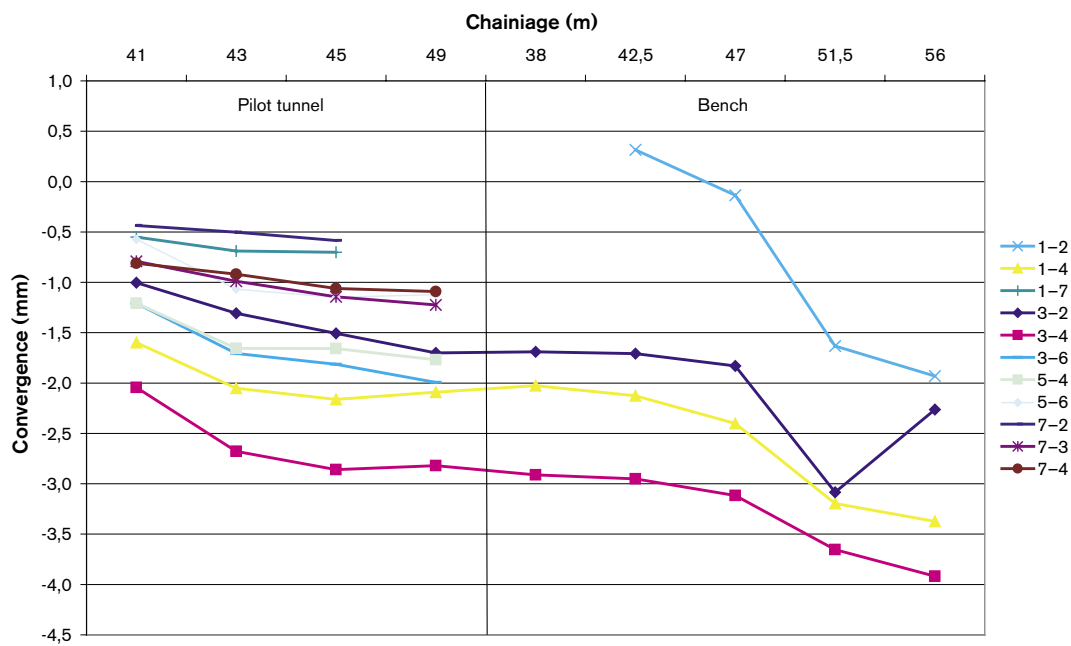


Figure 5-5. Graphical presentation of all the measured convergences. Convergence pins # 2 and 7 was lost at two separate occasions.

Table 5-3. Measured convergence in the horizontal sections 1–2, 3–4, and 5–6.

Section	1–2		3–4		5–6	
	Last measurement (mm)	Zero reading (mm)	Last measurement (mm)	Zero reading (mm)	Last measurement (mm)	Zero reading (mm)
P-49				0		0
P-51			-2.04	-2.04	-0.57	-0.57
P-53			-0.63	-2.68	-0.50	-1.07
P-55			-0.18	-2.86	-0.08	-1.15
P-59			0.04	-2.82	0.03	-1.12
B-38		0	-0.09	-2.91		
B-42,5	0.32	0.32	-0.04	-2.95		
B-47	-0.45	-0.14	-0.17	-3.12		
B-51,5	-1.50	-1.63	-0.54	-3.65		
B-56	-0.30	-1.93	-0.26	-3.92		

Table 5-4. Measured convergence in the sections 1–4 and 2–3.

Section	1–4		2–3	
	Last measurement (mm)	Zero reading (mm)	Last measurement (mm)	Zero reading (mm)
P-49		0		0
P-51	–1.60	–1.60	–1.00	–1.00
P-53	–0.45	–2.05	–0.30	–1.30
P-55	–0.11	–2.16	–0.20	–1.51
P-59	0.07	–2.09	–0.20	–1.70
B-38	0.06	–2.03	0.01	–1.69
B-42,5	–0.10	–2.13	–0.02	–1.71
B-47	–0.28	–2.40	–0.12	–1.83
B-51,5	–0.79	–3.20	–1.25	–3.08
B-56	–0.18	–3.37	0.82	–2.26

Table 5-5. Measured convergence in the sections 1–7 and 2–7.

Section	1–7		2–7	
	Last measurement (mm)	Zero reading (mm)	Last measurement (mm)	Zero reading (mm)
P-49		0		0
P-51	–0.55	–0.55	–0.44	–0.44
P-53	–0.14	–0.69	–0.07	–0.50
P-55	–0.01	–0.70	–0.08	–0.58

Table 5-6. Measured convergence in the sections 3–6 and 4–5.

Section	3–6		4–5	
	Last measurement (mm)	Zero reading (mm)	Last measurement (mm)	Zero reading (mm)
P-49		0		0
P-51	–1.21	–1.21	–1.21	–1.21
P-53	–0.50	–1.71	–0.45	–1.66
P-55	–0.11	–1.81	–0.00	–1.66
P-59	–0.18	–1.99	–0.11	–1.77

Table 5-7. Measured convergence in the sections 3–7 and 4–7.

Section	3–7		4–7	
	Last measurement (mm)	Zero reading (mm)	Last measurement (mm)	Zero reading (mm)
P-49		0		0
P-51	–0.79	–0.79	–0.81	–0.81
P-53	–0.20	–0.99	–0.11	–0.92
P-55	–0.16	–1.14	–0.14	–1.06
P-59	–0.08	–1.23	–0.03	–1.09

5.3 Numerical modelling

The numerical modelling with Examine3D was performed in the order listed below

1. Two models with the length of 30 metres were built, the first for the excavation of the pilot drift and the second for the excavation of the bench. The true measured section at 49 m was used for all the 30 metres of model. The shape of the tunnel face at 49 m was also included in the models. In the vicinity of the convergence pins the discretization was increased to an element size of approximately 0.5 m.
2. The excavation was simulated by inserting a number of field points along the drift. The first field points were located at the surveyed locations of the actual convergence pins in the tunnel. More points spaced 0.5 m were then distributed axially along the drift to approximately 5 m in front of the face (10 m for the bench modelling) and 10 m behind the face (Figure 5-6).
3. Realisations were made with different plunges and magnitudes of the primary and secondary stresses. Young's modulus of the rock mass was also varied.
4. The numerical results were plotted and compared to the measured ones and the best fit was identified. The stress tensor and Young's modulus used for that realisation is said to be the best estimation of the boundary conditions at section 49.

Listed in Table 5-8 and Table 5-9 are the input data for the different realisations made in Examine3D to find the best fit to the measured data.

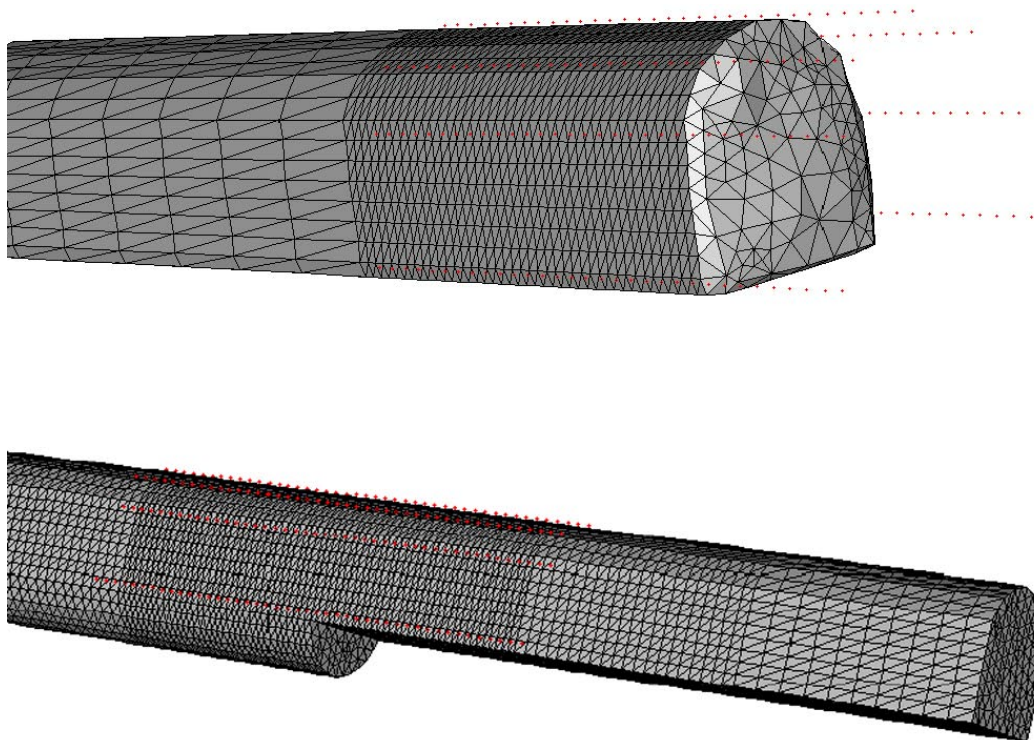


Figure 5-6. Model of pilot tunnel including the field points where displacement data were recorded (upper). Model of the bench excavation including the field point (lower).

Table 5-8. The different input variables used for the Examine3D realisations of the pilot drift. Plunge from horizontal.

S1 (MPa)	S2 (MPa)	Dip S1	Young (GPa)
23	10	0	35
23	10	0	40
23	10	5	40
23	10	7	40
23	10	0	45
25	10	0	40
25	10	7	40
25	10	0	45
25	10	5	45
25	10	7	45
25	10	10	45
25	10	0	50
25	10	5	50
25	10	5	55
27	10	0	45
27	10	0	50
27	10	5	50
27	10	0	55
27	10	5	55
27	10	10	55
30	10	0	50
30	10	0	55
30	12	0	55
30	15	0	55
30	17	0	55
30	15	30	55
30	10	0	60
30	10	5	60
35	10	5	60

Table 5-9. The different input variables used for the Examine3D realisations of the bench drift. Plunge from horizontal.

S1 (MPa)	S2 (MPa)	Dip S1 (Deg)	Young (GPa)
23	10	0	40
25	10	0	45
27	10	0	50
30	17	0	55
30	15	0	55
30	12	0	55
30	10	0	55

5.4 Evaluation of modelled data

To evaluate the modelled results and compare them to the measured displacements the following course of action was taken.

1. The modelled data was sorted so that the absolute displacements between the pins could be compared.
2. The measured displacements were added with the modelled displacement at a distance of 0.3 m from the face which is the approximate distance from the face that the pins were installed. This was made to compensate for the displacements that took place before the pins were installed.
3. The vertical difference between the compensated measured displacements (blue triangles in the figure below) and the modelled displacements was added. A “total difference” for the different distances between the pins for each realisation could then be compared. When the difference is small the triangles are close to the modelled displacements and the fit to the measurements is good.

Most of the numerical realisations where performed before detailed laboratory testing were performed on core specimens. The specimens were taken from the location of the pillar in section 65. The results from these tests gave a Poisson’s ratio of 0.26 but in the numerical model the assessed value of 0.24 was used. A sensitivity analysis has been made where only Poisson’s ratio was changed from 0.24 to 0.26. The difference in total convergence was approximately 0.002 mm. Since the difference is so small no new realisations were made and the final results are given for a ratio of 0.26.

In Figure 5-7 the result from realisation P2 in Table 5-10 is presented as an example.

In Table 5-10 the total errors for the convergence distances studied for the pilot drift are presented. For some of the different realisations the measured point with the added displacements gets a lower value than the numerical model at the same point. In the table has though only positive values been used when calculating the error sums.

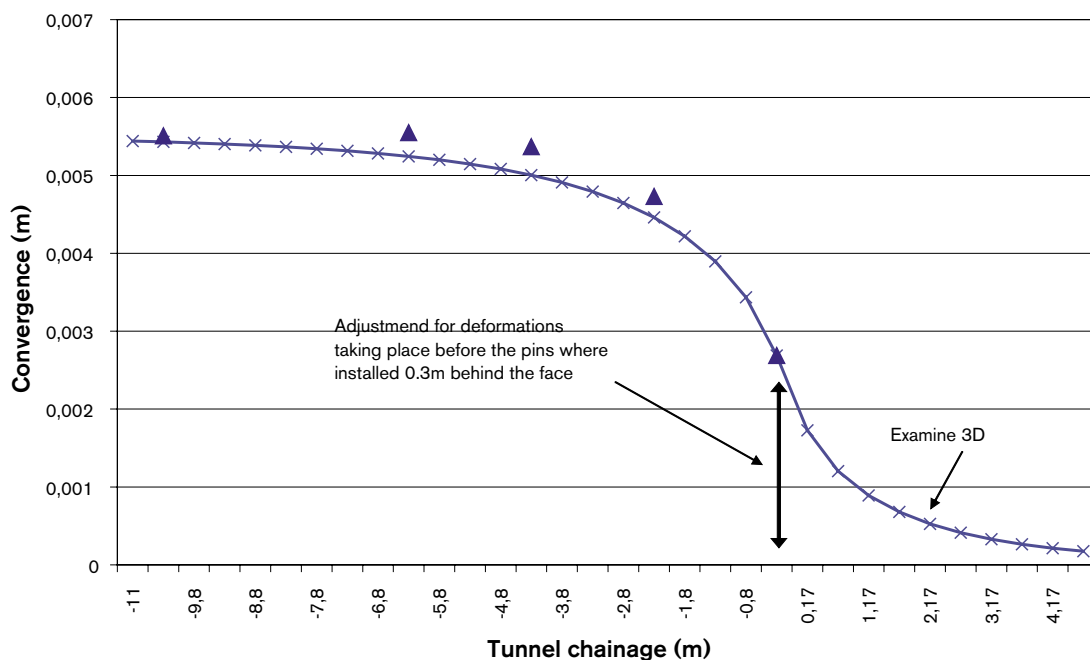


Figure 5-7. Results from realisation #2 between pins 3 and 4. The “total difference” is the sum of the vertical distances between the blue triangles and the modelled curve.

Table 5-10. Total errors for the compared distances from the pilot drift. Table sorted by increasing error sum, only absolute values used.

Realisation #	S1 (MPa)	S2 (MPa)	Dip S1	Young (GPa)	3-4 (mm)	5-6 (mm)	3-7 (mm)	Sum (mm)
P1	23	10	0	40	0.643	1.130	0.436	2.209
P2	30	10	0	55	1.015	0.910	0.321	2.246
P3	30	12	0	55	1.173	0.819	0.265	2.257
P4	25	10	0	45	0.858	0.970	0.430	2.258
P5	30	15	0	55	1.411	0.680	0.188	2.279
P6	27	10	0	50	1.118	0.850	0.360	2.328
P7	23	10	0	45	1.629	0.570	0.154	2.353
P8	27	10	5	50	1.069	0.860	0.440	2.369
P9	30	17	0	55	1.570	0.589	0.217	2.376
P10	23	10	5	40	0.622	1.150	0.613	2.385
P11	25	10	5	45	0.807	0.990	0.610	2.407
P12	25	10	0	50	1.812	0.480	0.141	2.433
P13	27	10	0	55	1.961	0.420	0.057	2.438
P14	30	10	0	60	1.797	0.510	0.147	2.454
P15	27	10	0	45	0.466	1.380	0.629	2.475
P16	30	10	0	50	0.468	1.390	0.654	2.512
P17	25	10	5	50	1.767	0.497	0.250	2.514
P18	23	10	7	40	0.638	1.110	0.780	2.528
P19	27	10	5	55	1.917	0.420	0.220	2.557
P20	30	10	5	60	1.754	0.520	0.300	2.574
P21	25	10	10	45	0.955	0.860	0.760	2.575
P22	25	10	7	45	1.548	0.980	0.052	2.580
P23	35	10	5	60	0.570	1.270	0.870	2.710
P24	25	10	0	40	0.410	1.580	0.760	2.750
P25	25	10	7	40	0.417	1.590	1.020	3.027
P26	30	15	30	55	2.823	0.101	0.382	3.306
P27	23	10	0	35	0.877	1.850	0.927	3.654
P28	25	10	5	55	2.533	1.197	0.327	4.057
P29	27	10	10	55	19.000	8.970	5.347	33.317

The results in Table 5-10 gives a possible range for the magnitude of the major principal stress from 23 to 30 MPa with corresponding values for Young's modulus from 40 to 55 GPa. The magnitude for the second principal stress seems to range between 10 to 15 MPa. The table gives a quite clear indication that the major principal stress is horizontal. When comparing the error sums for the realisations made on the pilot drift the differences are small. An important part of the interpretation is therefore the results from the modelling of the bench. The four realisations with the least error sum in Table 5-10 have also been run with the bench geometry of the drift and the results are presented in Table 5-11.

For the bench excavation the differences between the error sums for the realisations are greater than for the pilot drift since two and not three distances are compared in this case but the sums are about the same. The figures from the pilot and the bench can not be directly compared since a slight different approach needs to be taken when adjusting the values for the bench. Instead one has to look at the internal order in the two tables. If taking both Table 5-10 and Table 5-11 into consideration the best fit choice is a horizontal major principal stress magnitude of 30 MPa combined with a Young's modulus of 55 GPa. There the magnitude of the second principal stress should be chosen to 15 MPa. The conclusion is

based on that the tensor with this magnitude is better ranked in the pilot drift comparisons and that the difference is small to the best ranked tensor in the bench comparison. The recommended stress tensor is presented in Table 5-12.

In the following Figures 5-8 to 5-12 the measured data is compared with the best fit stress tensor presented in Table 5-12 and a Young’s modulus of 55 GPa (realisations P5 and B2). Tunnel chainage in the figures means the distance from the face. Negative values are behind the face and positive in front of it.

Table 5-11. Total errors for the compared distances from the bench. Table sorted by increasing error sum, only absolute values used.

Realisation #	S1 (MPa)	S2 (MPa)	Dip S1	Young (GPa)	3-4 (mm)	1-4 (mm)	Sum (mm)
B1	30	17	0	55	0.884	1.986	2.870
B2	30	15	0	55	1.134	1.78	2.914
B3	30	12	0	55	0.410	2.729	3.139
B4	27	10	0	50	0.437	3.006	3.443
B5	30	10	0	55	0.458	3.03	3.488
B6	25	10	0	45	0.522	3.290	3.812
B7	23	10	0	40	1.010	3.860	4.870

Table 5-12. The best fit stress tensor derived by numerical modelling using a Young’s modulus of 55 GPa.

	Magnitude (MPa)	Trend/Plunge (degrees)
Sigma 1	30	310/00
Sigma 2	15	090/90
Sigma 3	10	208/00

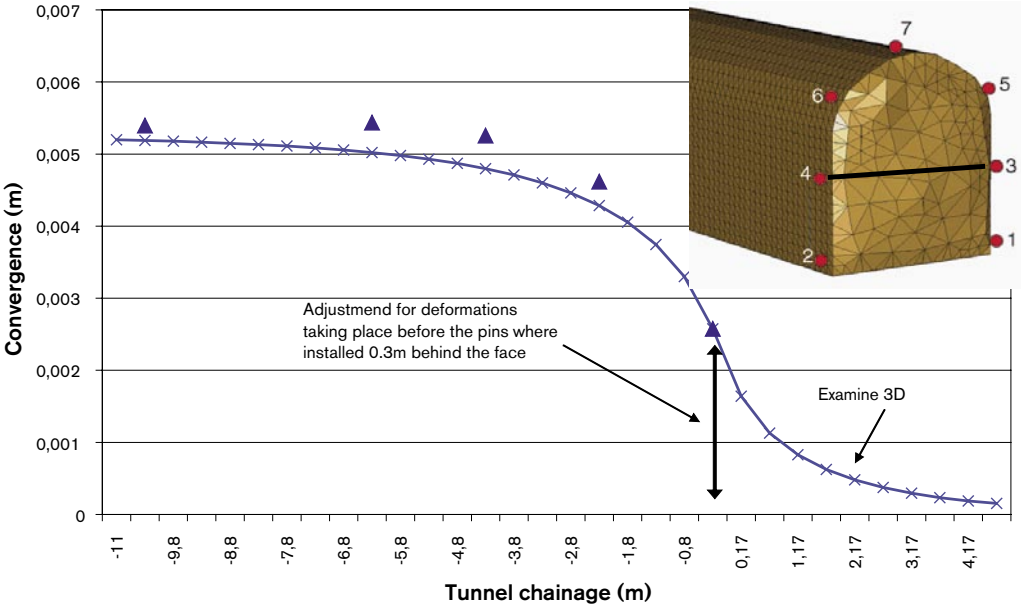


Figure 5-8. Comparison of modelled and measured displacements between pins no 3 and 4 for the stress tensor in Table 5-12. Tunnel chainage is the distance from the face, negative chainages are behind the face.

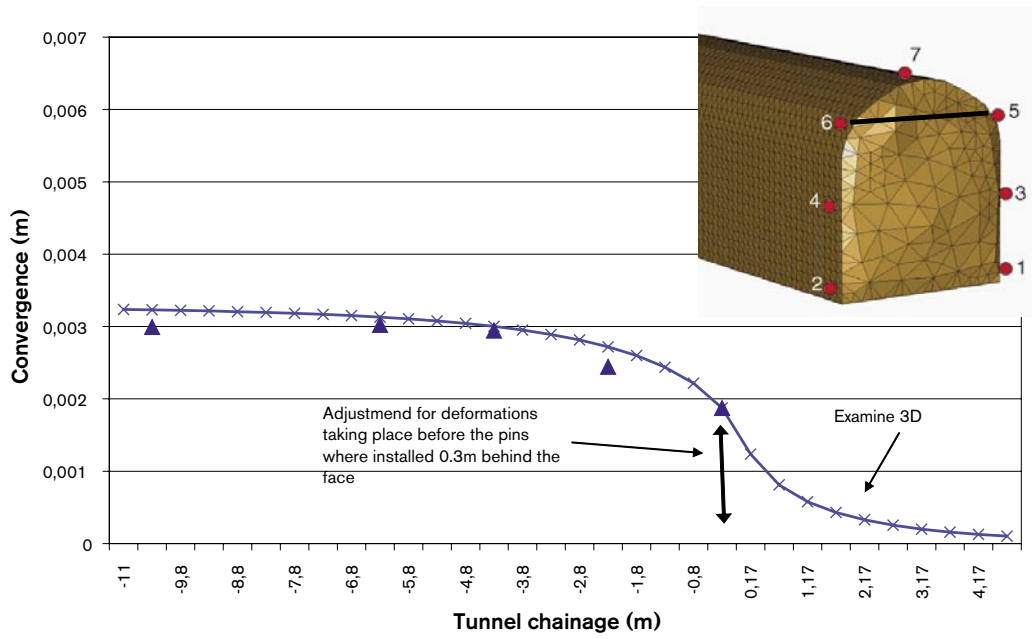


Figure 5-9. Comparison of modelled and measured displacements between pins no 5 and 6 for the stress tensor in Table 5-12.

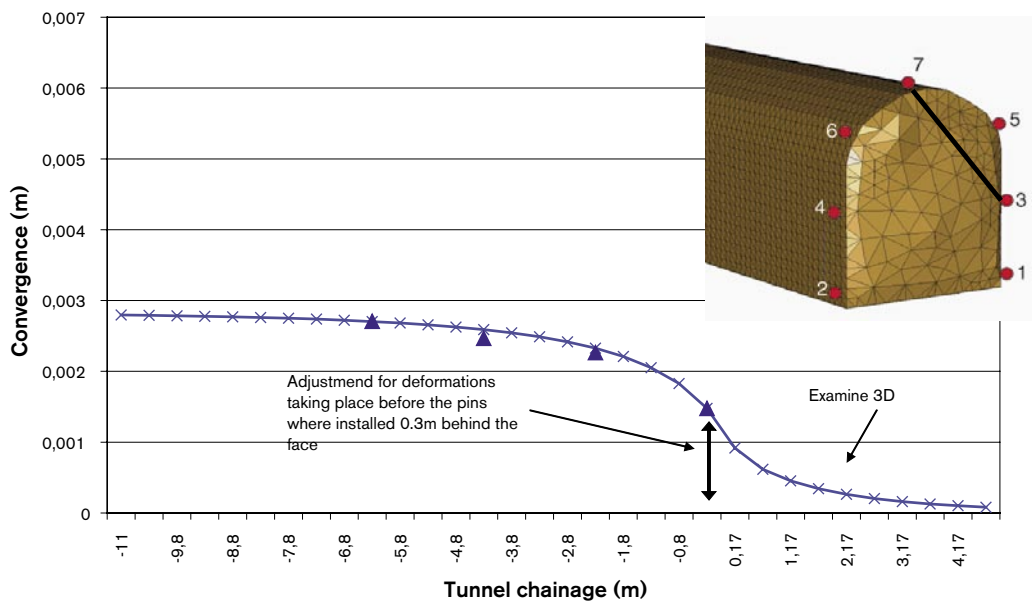


Figure 5-10. Comparison of modelled and measured displacements between pins no 3 and 7 for the stress tensor in Table 5-12.

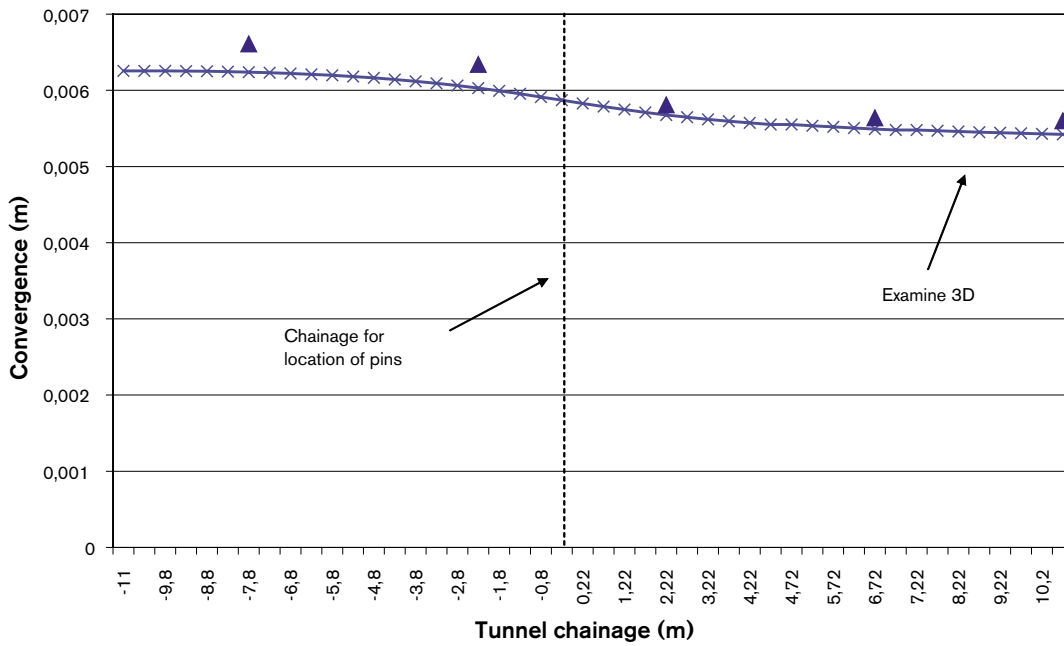


Figure 5-11. Comparison of modelled and measured displacements during bench excavation between pins no 3 and 4 for the stress tensor in Table 5-12

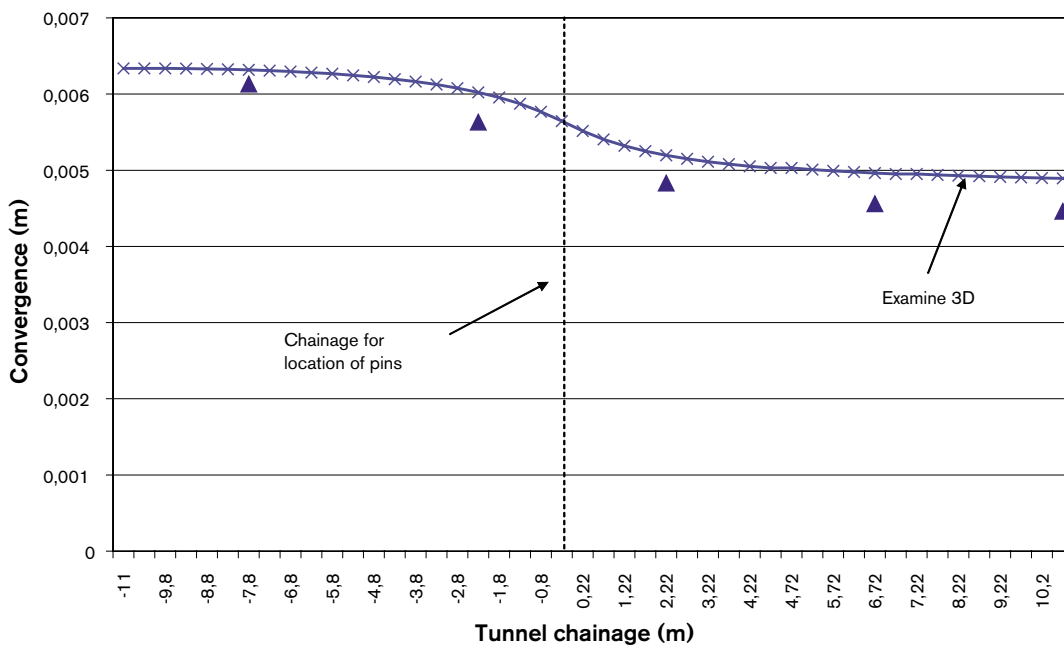


Figure 5-12. Comparison of modelled and measured displacements during bench excavation between pins no 1 and 4 for the stress tensor in Table 5-12

The input data in Table 5-12 has been used for a 2D finite element model in the Phase² code. The agreement between the Examine3D model is quite good, Figure 5-13.

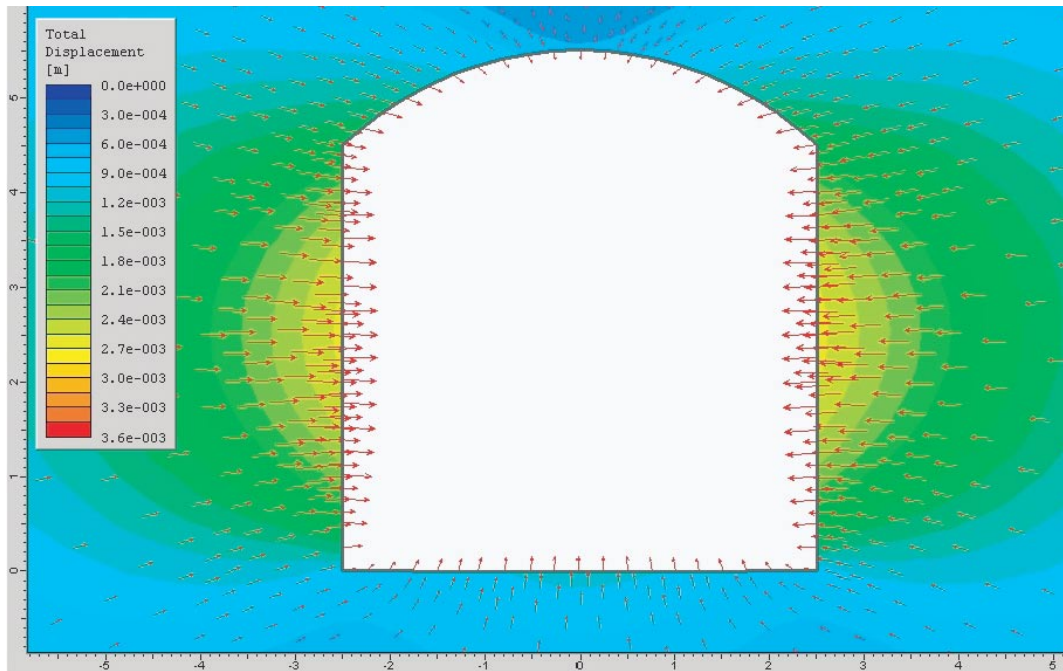


Figure 5-13. Result from a 2D-realisation with the Phase² code. The displacements agrees well with the results from the Examine3D model presented in Figure 5-8 to Figure 5-10. The same input data has been used in both models.

5.5 Influence of tunnel face geometry

In for example /Chang, 1994/ it is summarized that the amount of deformations that takes place in the tunnel face before the pins are installed and the first displacement measurements done are 25 to 30% of the total. This is though only valid if the rock mass is considered to be totally elastic and the stress field isotropic. This is not the case for the APSE site but it is a check that can be made to see that the results are roughly right.

The geometry of the Examine3D models that have been run included the actual shape of the face as surveyed during the excavation. As can be seen in the upper part of Figure 5-6 the face is buckling a bit into the rock mass in front of it. This makes the face less stiff and hence the deformations at the face will be larger than if a flat face is modelled. Two displacement curves are presented in Figure 5-14, the best fit stress tensor and Young's modulus according to Table 5-12 has been used in both cases. The curve for the flat face gives displacements close to 30% of the total displacements which fits well with /Chang, 1994/.

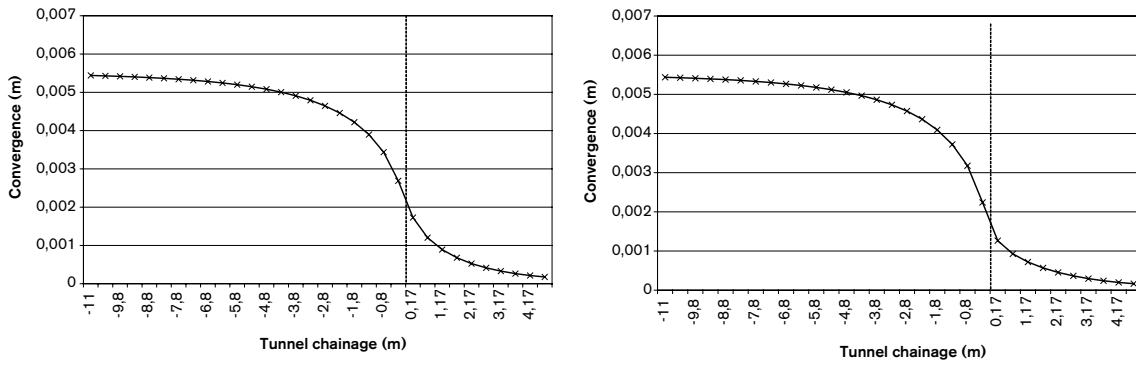


Figure 5-14. Comparison of modelling results using (left) the actual shape of the face and (right) a flat face. The vertical lines represent the chainage of the front.

5.6 Geology at chainage TASQ0049

Figure 5-15 and Figure 5-16 are excerpts from the geological mapping and the fracture visualisation of the TASQ drift. As can be seen in the figures there are quite few fractures at chainage 49 where the pins were installed, especially perpendicular to the measured section. It can therefore be assessed that Young's modulus of the rock in the convergence section should be quite high which coincides well with the findings from the modelling.

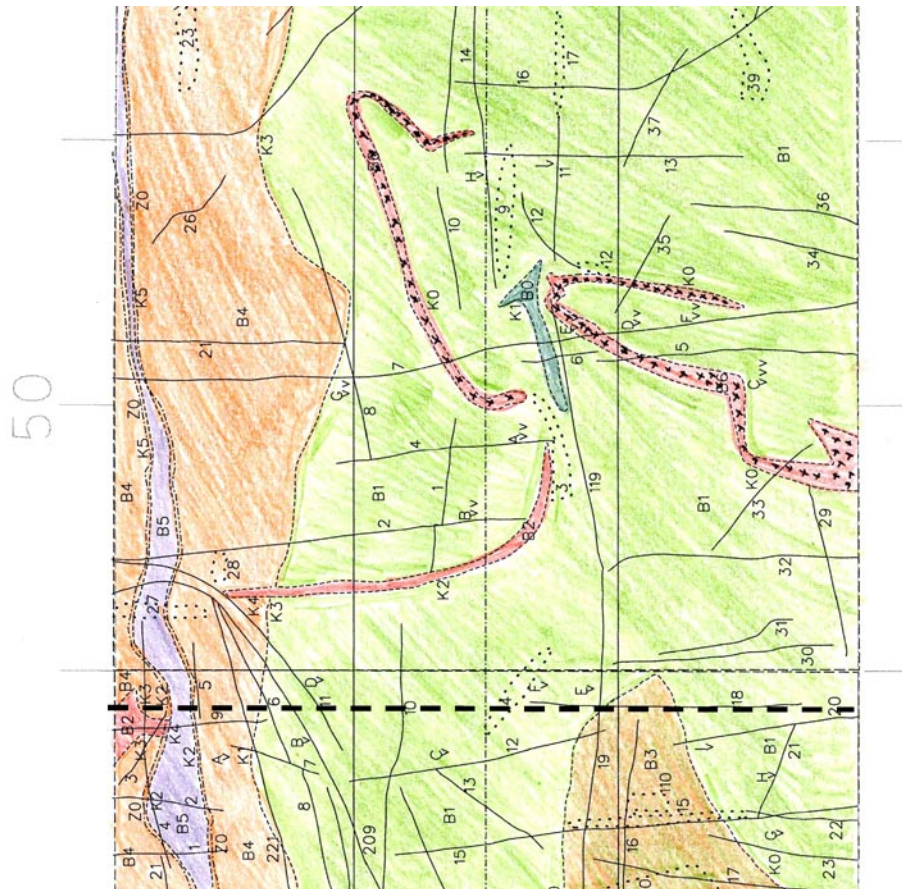


Figure 5-15. Excerpt of the geological mapping in the vicinity of the section for the convergence measurements, dashed-line.

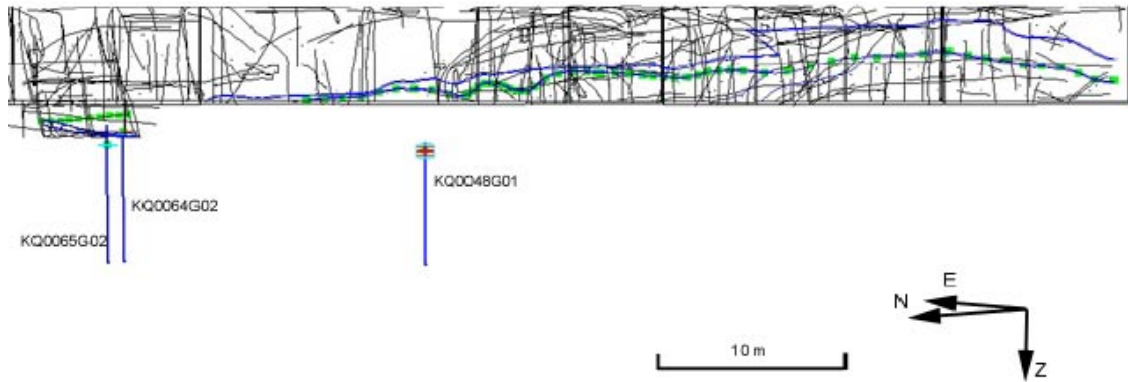


Figure 5-16. Excerpt from the fracture visualisation of the TASQ drift. The dashed line indicates the convergence measurement section and as can be seen it was by coincidence the least fractured part of the drift.

5.7 Discussion

The back calculations of the convergence measurements made gives the properties of the stress field according to Table 5-13 in the experiment volume together with a Young's modulus of 55 GPa and a Poisson's ratio of 0.26.

This stress tensor's magnitudes are identical to the most probable values for the in-situ stress in the experiment volume presented by /Staub et al. 2003/. There is though a clear difference in the plunge. Staub presents a Sigma 1 plunge of 30 degrees. The previously recommended tensor has been used in a realisation presented in Table 5-10 (realisation P26) and as can be seen there it gives a poor fit. The weight of the overburden is approximately 12 MPa at this depth. The resulting magnitude of 15 MPa for the second principal stress is hence higher than the weight of the overburden.

The modulus of the rock mass derived from the modelling is quite high compared to other assessments that have been made /Staub et al. 2002; Röshoff and Lanaro, 2002/. A reason for this is probably the low fracture density in the immediate vicinity of the section where the convergence measurements were performed. Especially the fact that there only are a few fractures oriented perpendicular to the convergence section should imply a high modulus of the rock mass. A cross borehole P-wave velocity survey has been performed by Pettitt et al. (Appendix H) between two boreholes across the pillar. The boreholes are two of the four that are used for the acoustic emission monitoring system. The boreholes are spaced approximately 2.8 m apart and the surveyed velocities between them were

Table 5-13. Resulting stress tensor from the back calculations of the convergence measurements.

	Magnitude (MPa)	Trend/Plunge (degrees)
Sigma 1	30	310/00
Sigma 2	15	090/90
Sigma 3	10	208/00

quite high resulting in a dynamic Young's modulus of 80 GPa using Poisson's ratio 0,26 in Equation 1 in /Eissa and Kazi, 1988/. Eissa and Kazi also presented a relationship between the static and dynamic Young's modulus as Equation 2, the relationship is assessed to have a confidence of 90%.

$$\text{Equation 1.} \quad E_{dy} = V_p^2 \frac{(1 + \mu)(1 - 2\mu)\gamma}{(1 - \mu)}$$

$$\text{Equation 2.} \quad E_{st} = 1.26 E_{dy} - 29.5$$

where

V_p = velocity of compressional wave,

V_s = velocity of shear wave,

γ = density,

μ = Poisson's ratio.

Using $E_{dy} = 80$ GPa and $\gamma = 2.731$ g/cm³ in Equation 2 gives a static modulus E_{st} of 67 GPa which can be regarded as quite high, but the value derived from the modelling of 55 GPa lies well within the confidence interval for the relationship in Equation 2.

Q-logging of TASQ reported in /Barton, 2004/ also includes estimations of the rock mass Young's modulus based on Q-values. At the convergence section the estimations gives a very high modulus, more than 80 GPa. Which seems unreasonable since the value is higher than what is derived from the compressive tests made on core-pieces. It is likely that the estimations made by Barton over-estimates the modulus of the rock mass when the Q-value is high depending on sparse fracturing.

It is reasonable to assess that the static module is most likely closer to 55 than 67 GPa depending on the fact that there are only a few fractures that the P-wave travels through and that the fractures are most likely healed or clamped together by the stresses. This will give a low reduction of the velocities but a static loading will probably initiate displacements in the fractures and hence reduce the modulus for the rock mass.

6 Conclusions

A comprehensive site characterization has been performed in the rock volume that hosts the Äspö Pillar Stability Experiment. The major findings from the characterization are summarized in the sections below. The most important result of the characterization is that the selected site for the experiment is suitable and that the experiment can be performed as planned. The detailed characterisation of the experiment volume constitutes a solid basis for the numerical modelling.

6.1 Geological structures

The rock type in the TASQ drift is the typical Äspö diorite and the fracture sets found in the tunnel coincide well with the geological data set from the Äspö Hard Rock Laboratory. A unique occurrence of a heavily oxidized, brittle-ductile shear-zone in the drift makes it different to the other experiment locations at Äspö. The shear zone is present in the pillar volume but it is much less pronounced than in the other parts of TASQ. Moreover the zone is mainly sealed and is therefore not assessed to threaten the outcome of the experiment.

The visualisation of the other structures in the rock volume surrounding the experiment volume does not indicate that a successful outcome of the experiment is threatened. There are a few both open and sealed discontinuities present in the pillar volume. They are however not assessed to be able to interact and create block movements in the pillar volume.

The location selected for the experiment is both fully suitable and assessed to be the best location that can be found in the drift.

6.2 In-situ stress

Extensive rock stress measurements were earlier performed in close proximity to the experiment site /Janson and Stigsson, 2002/. These sets of data have been complemented with convergence measurements that were performed during the excavation of TASQ. The measurements were back calculated to find the best fit stress field and Young's modulus for the data set obtained from the measurements. The modelling resulted in a stress field where the second principal stress is vertical and approximately 25% higher than the weight of the overburden. Young's modulus was found to be higher in the measured section than what's earlier has been assumed for the rock mass. The reason is probably the small amount of fracturing in that part of the tunnel.

6.3 Rock properties

A quite extensive laboratory test programme has been performed on core samples taken from the immediate vicinity of the pillar volume. The strength of the samples is quite similar to the strength determined on rock samples from different parts of the Äspö Hard

Rock Laboratory during the years. The oxidized part of the rock associated with the shear zone has a lower compressive strength than the fresh diorite. The ratio is approximately 0.5–0.6.

The thermal properties of the rock in the experiment volume are what could be expected for this kind of rock and only small adjustments were made in these parameters for the final modelling when the general Äspö data was changed to site specific.

6.4 Other Äspö Pillar Stability Experiment reports

A number of working reports have been produced during the modelling and design phase of the experiment. The important results from the preliminary modelling and the design have been compiled in the references below which together with this report give the best description of the experiment as per April 2004.

1. Andersson J C, 2003. Äspö Pillar Stability Experiment, Summary of preparatory work and predictive modelling. SKB R-03-02, Svensk Kärnbränslehantering AB.
2. Fredriksson A, Staub I, Outters N, 2004. Äspö Pillar Stability Experiment, Final 2D coupled thermo-mechanical modelling. SKB R-04-02, Svensk Kärnbränslehantering AB.
3. Rinne M, Lee H-S, Shen B, 2004. Äspö Pillar Stability Experiment, Modelling of fracture stability by FRACOD. SKB R-04-04, Svensk Kärnbränslehantering AB.
4. Wanne T, Johansson E, Potyondy D, 2004. Äspö Pillar Stability Experiment, Final coupled 3D thermo-mechanical modelling. Preliminary particle-mechanical modelling. SKB R-04-03, Svensk Kärnbränslehantering AB.

7 References

- Andersson J C, 2003.** Äspö Hard Rock Laboratory, Äspö Pillar Stability Experiment, Feasibility Study. SKB IPR-03-01, Svensk Kärnbränslehantering AB.
- Barton N, 2004.** Äspö Pillar Stability Experiment, Q-logging of the TASQ tunnel for rock quality assessment and for development of preliminary model parameters. SKB IPR-04-07, Svensk Kärnbränslehantering AB.
- Berglund J, Curtis Ph, Eliasson T, Ohlsson T, Starzec P, Tullborg E-L, 2003.** Update of the geological model 2002. SKB IPR-03-34, Svensk Kärnbränslehantering AB.
- Chang Y, 1994.** Tunnel Support with Shotcrete in Weak Rock – A Rock Mechanics Study. Doctoral Thesis, Division of Soil and Rock Mechanics, Royal Institute of Technology, Stockholm, Sweden 1994.
- Eissa E A, Kazi A, 1988.** Relation Between Static and Dynamic Young's Moduli of Rocks. Int. J. Rock Mech. Min. Sci & Geomech. Abstr. Vol. 25, No 6, pp 479–482.
- Emmelin A, Eriksson M, Fransson Å, 2004.** Characterisation, design and execution of two grouting fans at 450 m level, Äspö HRL. SKB R-04-58, Svensk Kärnbränslehantering AB.
- Fredriksson A, Staub I, Janson T, 2003.** Äspö Pillar Stability Experiment. Design of heaters and preliminary results from coupled 2D thermo-mechanical modelling. SKB IPR-03-03, Svensk Kärnbränslehantering AB.
- Hansen L M, Hermanson J, 2002.** Äspö Hard Rock Laboratory. Local model of geological structures close to the F-tunnel. SKB IPR-02-48, Svensk Kärnbränslehantering AB.
- Janson T, Stigsson M, 2002.** Test with different stress measurement methods in two orthogonal bore holes in Äspö HRL. SKB R-02-26, Svensk Kärnbränslehantering AB.
- Magnor B, 2004.** Geological mapping of tunnel TASQ. SKB IPR-04-03, Svensk Kärnbränslehantering AB.
- Rhén I, Gustafson G, Stanfors R, Wikberg P, 1997.** Äspö HRL – Geoscientific evaluation 1997/5. Models based on site characterization 1986–1995. SKB TR-97-06, Svensk Kärnbränslehantering AB.
- Röshoff K, Lanaro F, 2002.** Strategy for a Rock Mechanics Site Descriptive Model Development and testing of the empirical approach. SKB R-02-01, Svensk Kärnbränslehantering AB.
- Staub I, Fredriksson A, Outters N, 2002.** Strategy for a Rock Mechanics Site Descriptive Model, Development and testing of the theoretical approach. SKB R-02-02, Svensk Kärnbränslehantering AB.
- Staub I, Janson T, Fredriksson A, 2003.** Äspö Pillar Stability Experiment. Geology and properties of the rock mass around the experiment volume. SKB, IPR-03-02, Svensk Kärnbränslehantering AB.

Wikman H, Kornfält K-A, 1995. Updating of a lithological model of the bedrock of the Äspö area. SKB PR 25-95-04, Svensk Kärnbränslehantering AB.

Tunnel mapping

Geological map of the TASQ.

Contacts: K_{ID-NUMBER} and dashed lines.

Fractures: ID-NUMBER and continuous lines.









Blanks: ID-NUMBER (included in fractures) and dotted lines.

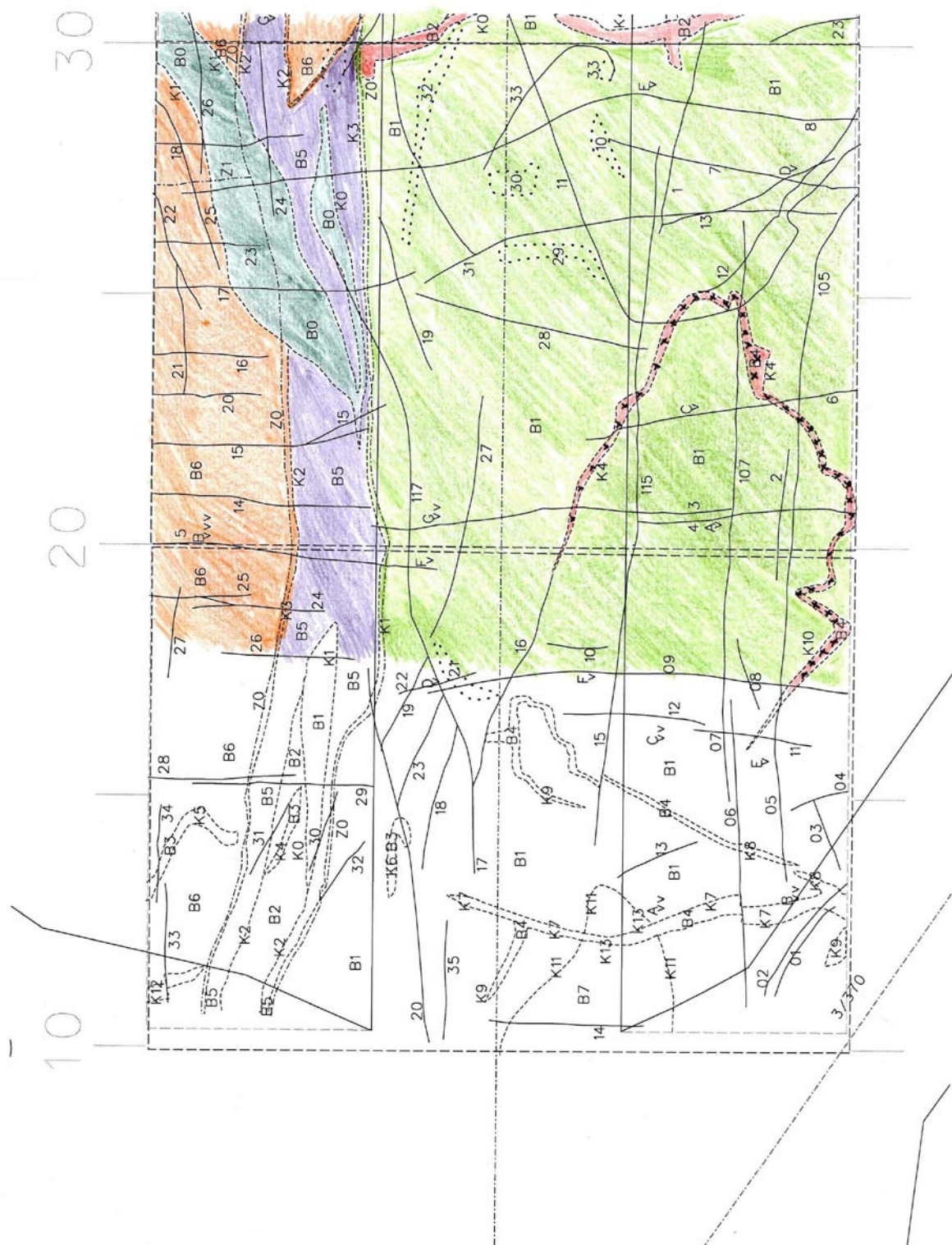
Fracture zones: Z_{ID-NUMBER} and dash dotted lines.

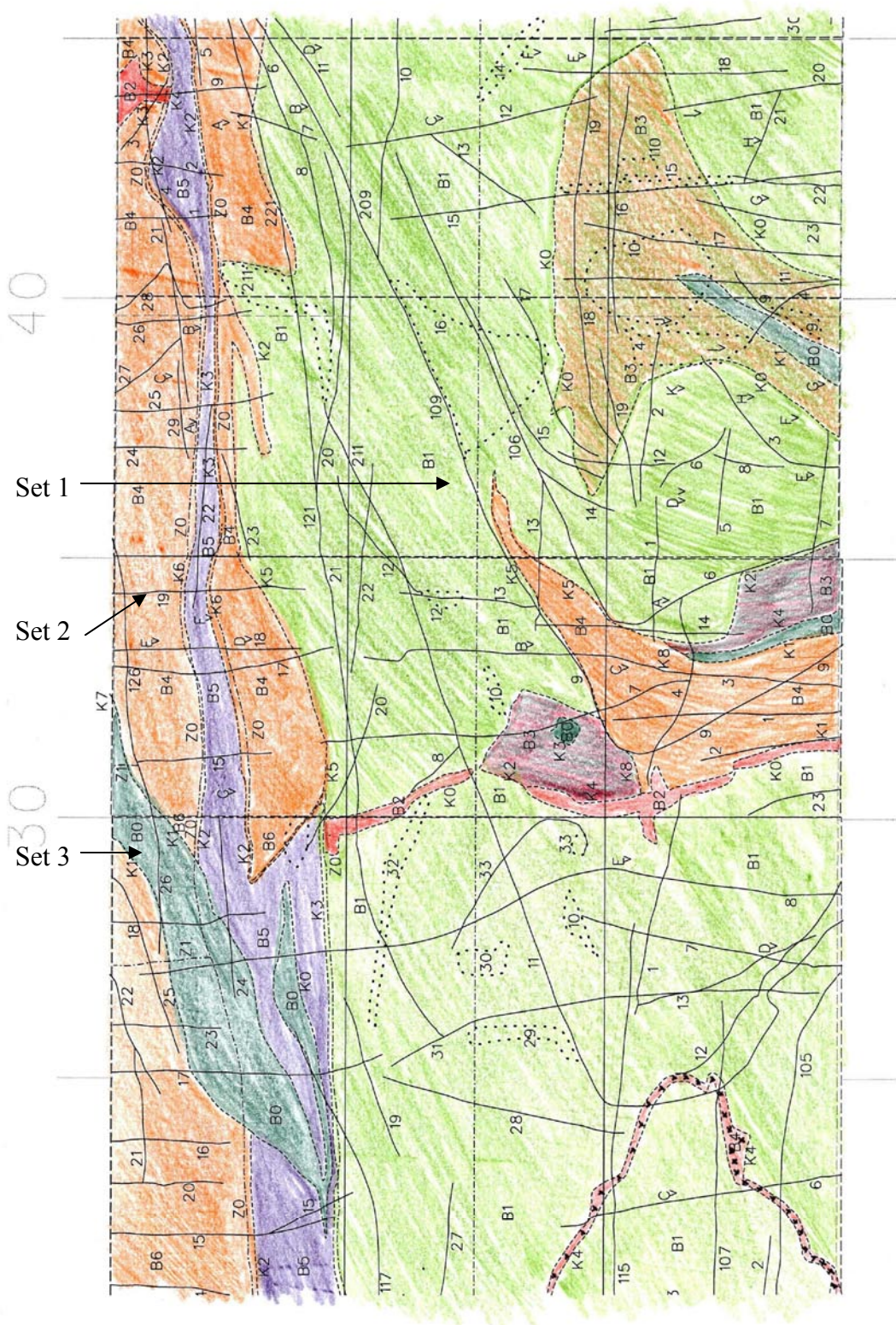
Water: Capital letter and v-vvv (v = moisture, vv = drops seepage, vvv = flowing).

Not that each mapping cell has its own set of numbers.

Mapping cells: 10–20 m, 20–30 m, 30–35 m, 35–40 m, 40–45 m, 45–60 m, 60–70 m, 70–80 m, 80 m front.

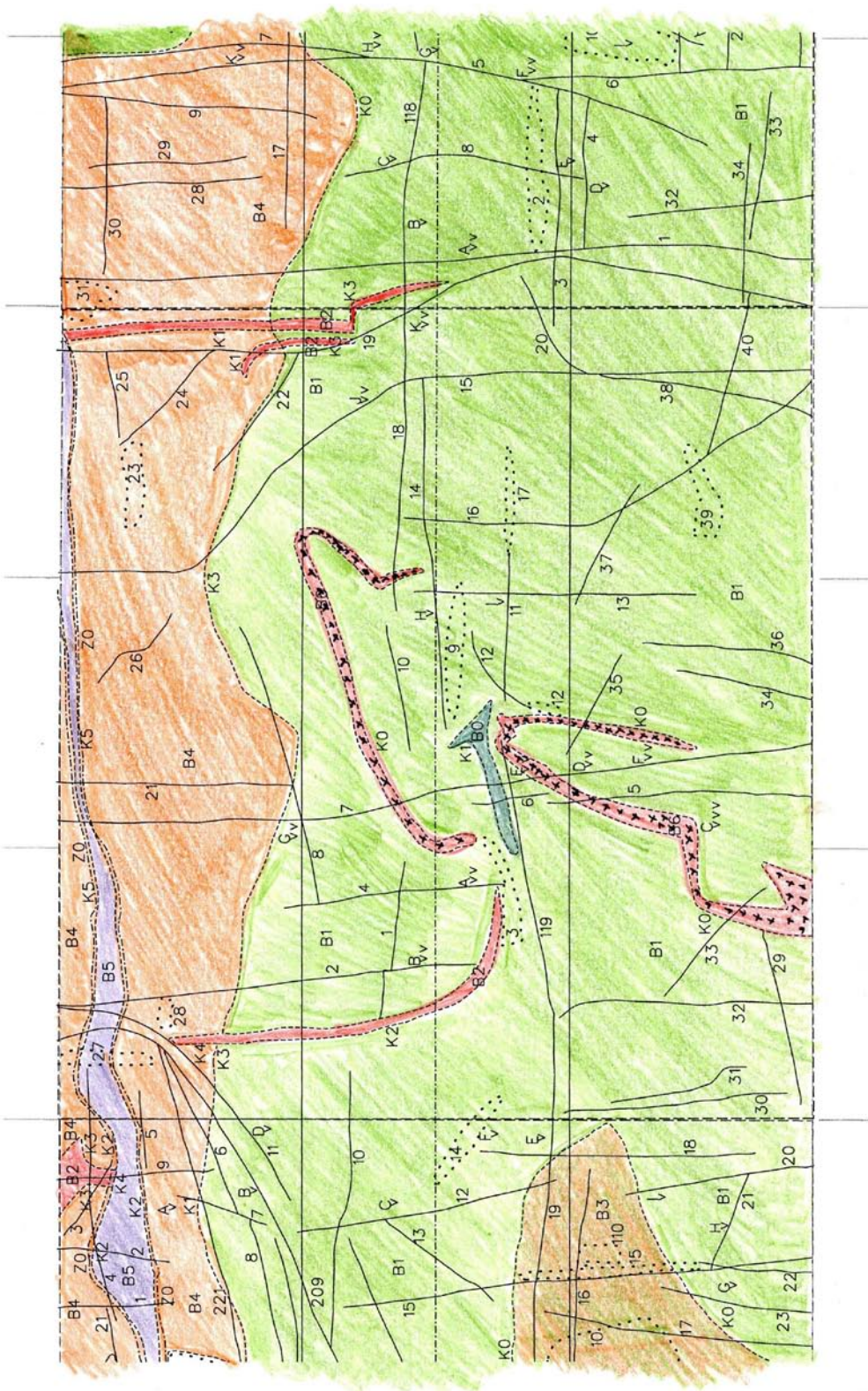
	ÄSPÖ DIORITE, UNALTERED
	ÄSPÖ DIORITE, OXIDIZED
	ÄSPÖ DIORITE, GRANITIC AND CRYSTALLOBLASTIC
	ÄSPÖ DIORITE WITH MORE MAFIC COMPOSITION
	GREENSTONE
	MYLONITE
	FINE- GRAINED GRANITE
	PEGMATITE





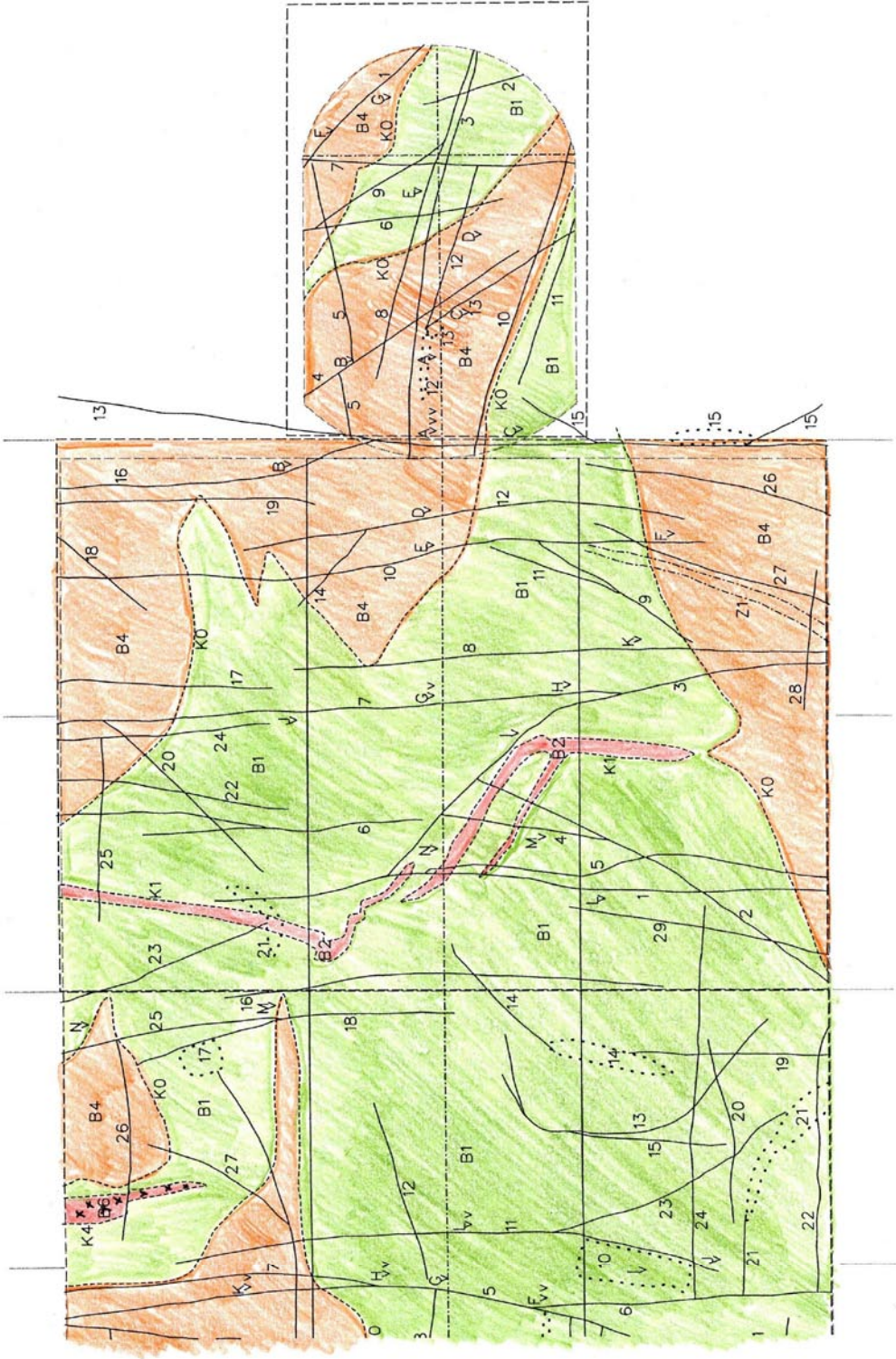
60

50



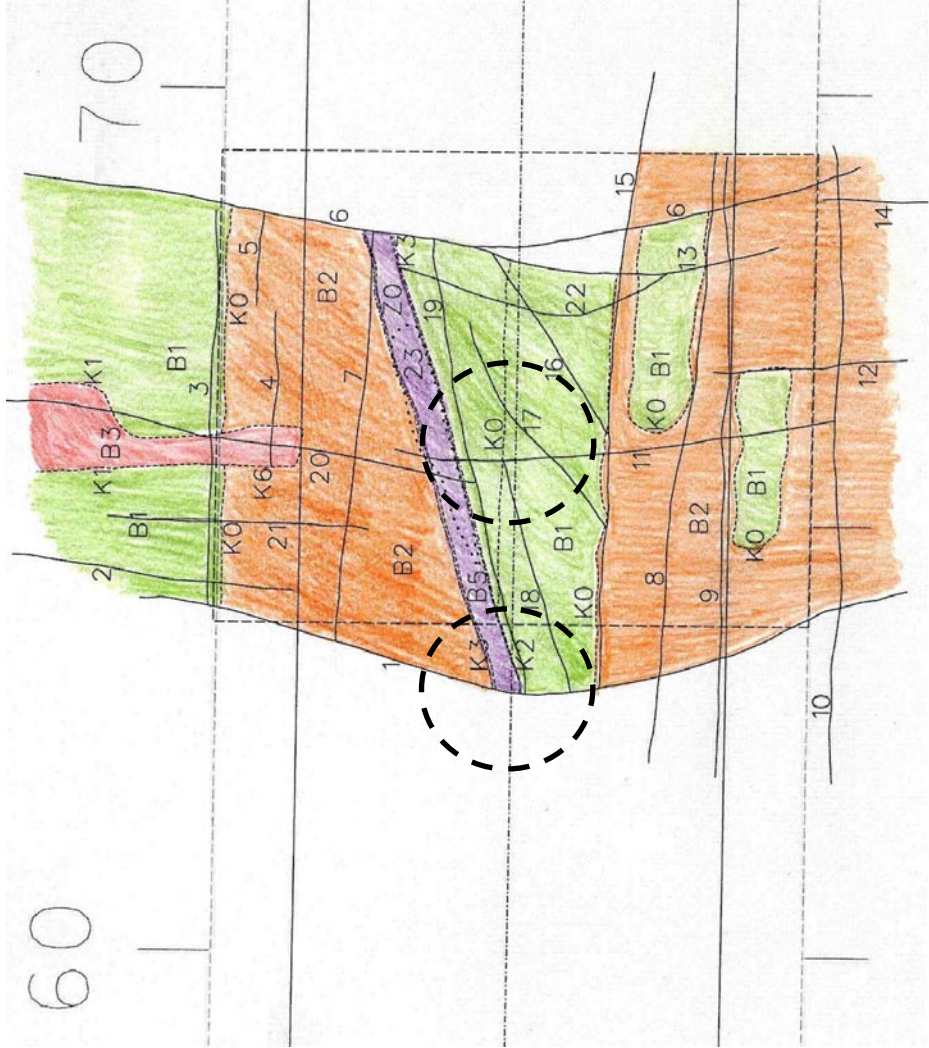
80

70



Floor mapping

Dashed circles indicate approximate locations of the deposition holes.



Mechanical testing on samples from KA3376B01

**Core sample KA3376B01
from Äspö HRL, Sweden**

Pekka Särkää, Pekka Eloranta
Helsinki University of Technology

June 2003

Sample Core sample KA3376B01 from Äspö HRL, Sweden containing the following sections:
 31.68 - 31.89
 31.89 - 32.08
 32.08 - 32.63
 33.14 - 33.52
 60.83 - 61.05
 61.45 - 62.24
 64.28 - 64.54

Commissioned analysis of the sample

Three (3) uniaxial compression tests with acoustic emission monitoring, three (3) triaxial compression tests with confining stress of 2 MPa, three (3) triaxial compression tests with confining stress of 7 MPa and three (3) indirect Brazil tensile tests.

Method of analysis and results

Test specimens were prepared and tested according to the suggested methods of International Society of Rock Mechanics, ISRM (Brown 1981). The specimens were stored and tested in room conditions. Tests were carried out with a MTS 815 rock mechanics test system according to procedures developed by Hakala & Heikkilä 1997.

Elastic parameters i.e. Young's modulus and Poisson's ratio were calculated as secant values between axial stress levels at -0.01% of radial strain and 50% of peak strength.

The results of the uniaxial compression tests are presented in Table 1 and in Appendices 1-3. Acoustic emission (AE) of these uniaxial compression test specimens was measured with a Mistras 2001 AE-equipment. Interpretation of the AE data is presented in Appendix 10.

The results of the triaxial compression tests are presented in Table 2 and in Appendices 4-9.

The results of the indirect Brazil tensile tests are presented in Table 3.

Table 1. Uniaxial compression tests (see Appendices 1-3).

Sample depth	Length (mm)	Diameter (mm)	Density (kg/m ³)	UCS (MPa)	Young's modulus (GPa)	Poisson's ratio
33.32	142.4	50.9	2742	195	67	0.27
61.58	142.5	50.9	2730	203	69	0.28
61.72	142.4	50.9	2724	85	74	0.21

Table 2. Triaxial compression tests (see Appendices 4-9).

Sample depth	Length (mm)	Diameter (mm)	Density (kg/m ³)	Confining stress (MPa)	Compressive strength (MPa)	Young's modulus (GPa)	Poisson's ratio
31.70	142.1	50.9	2756	2	175	70	0.22
31.90	142.1	50.9	2733	7	265	74	0.24
32.27	143.7	50.9	2743	2	219	69	0.21
60.85	142.1	50.9	2729	7	252	75	0.24
62.05	143.7	50.9	2716	7	239	74	0.25
64.30	142.5	50.9	2723	2	136	73	0.21

Table 3. Indirect Brazil tensile tests.

Sample depth	Length (mm)	Diameter (mm)	Force (kN)	Tensile strength (MPa)
32.24	26.5	50.9	33.7	15.9
33.29	26.6	50.9	31.9	15.0
61.55	25.8	50.9	31.7	15.4

Visual inspection of the tested specimens suggests that the specimen 61.72 failed through a weakness plane (closed or healed fracture). In the specimens 60.85 and 62.05 healed fractures may have contributed to failure to some extent. Other specimens seem to be failed through intact rock.

The results are valid only for the tested specimens. Crack initiation and crack damage stress levels in Appendices 1-3 were interpreted from the volumetric strain data and therefore may not agree with the levels interpreted from acoustic emission data in Appendix 10.

Acknowledgments

Matti Hakala (Gridpoint Finland Oy) interpreted the acoustic emission data.

References

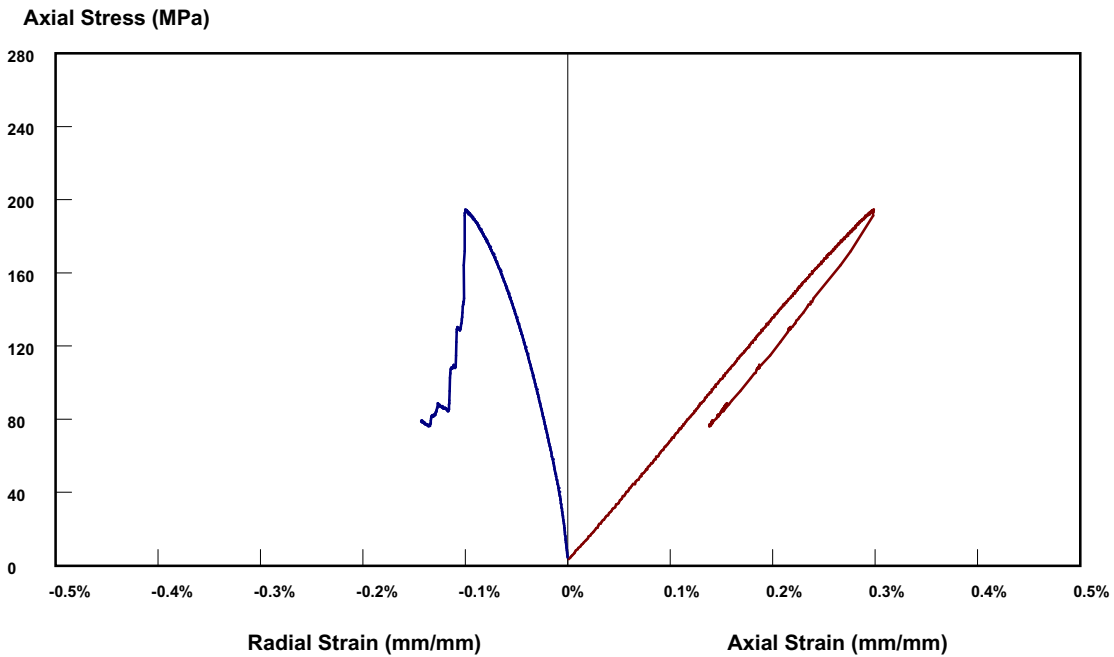
Brown, E.T. (Ed.) (1981) Rock characterization, testing and monitoring. ISRM suggested methods. 211 p. Oxford: Pergamon Press. ISBN 0-08-027309-2.

Hakala, M. & Heikkilä, E. (1996) Summary report – Development of laboratory test and the stress –strain behaviour of Olkiluoto mica gneiss. Posiva Report Posiva-97-04. 150 p. Helsinki: Posiva. ISBN 951-652-029-4

Appendices

- 1-9 Stress-strain curves
- 10 AE interpretation

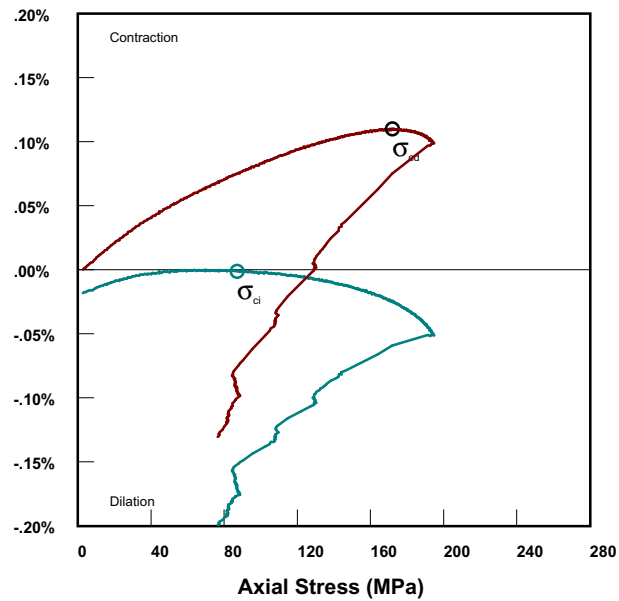
Uniaxial Test of KA3376B01 - 33.32



Failure Pattern



Volumetric Strain (mm³/mm³)



Test Data

Client:	SKB	Test Date:	2003-06-10
Order Number:		Loading Control:	Radial Strain Rate
Test:	Uniaxial	Equivalent Loading Rate:	0.75 MPa/s
Equipment:	MTS 815	Confining Stress:	0 MPa

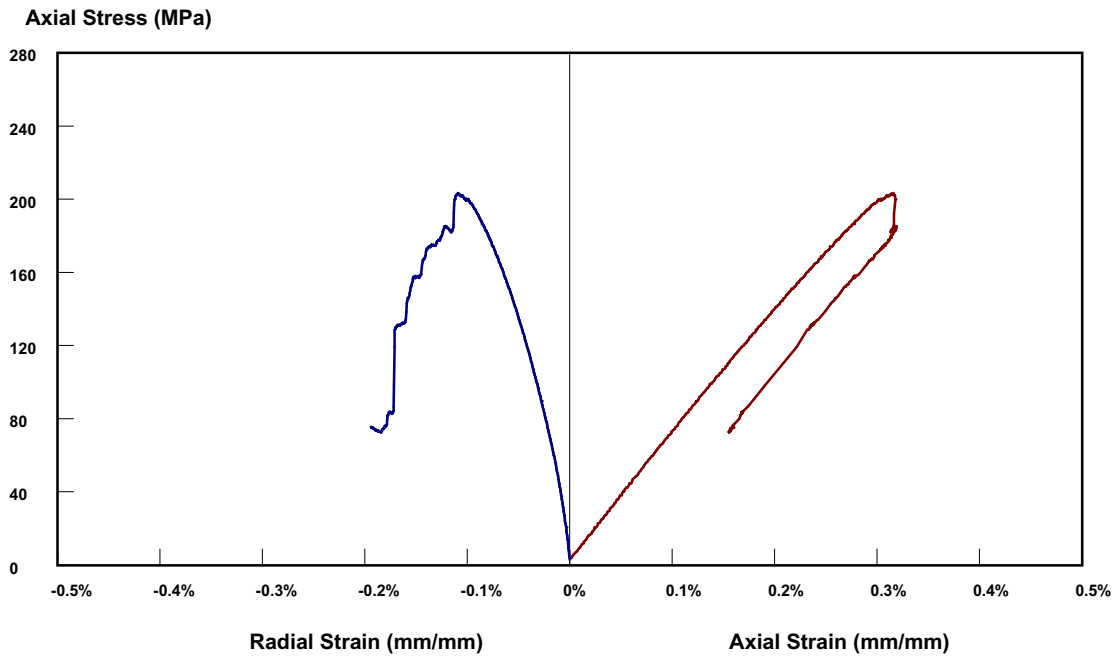
Specimen Data

Site:	Äspö	Diameter:	50.9 mm
Rock Type:	Diorite	Length/Diameter:	2.80
Hole:	KA3376B01	Density:	2742 kg/m ³
Depth:	33.32	Porosity:	
		Test Saturation:	

Test Results

Young's Modulus:	67.4 GPa	Peak Strength:	195.1 MPa
Poisson's Ratio:	0.27	Crack Damage Stress:	172.0 MPa
		Crack Initiation Stress:	87.1 MPa

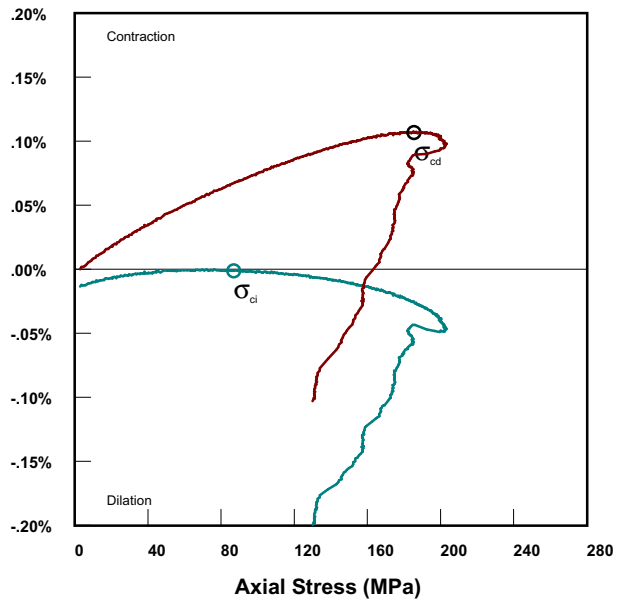
Uniaxial Test of KA3376B01 - 61.58



Failure Pattern



Volumetric Strain (mm³/mm³)



Test Data

Client:	SKB	Test Date:	2003-06-10
Order Number:		Loading Control:	Radial Strain Rate
Test:	Uniaxial	Equivalent Loading Rate:	0.75 MPa/s
Equipment:	MTS 815	Confining Stress:	0 MPa

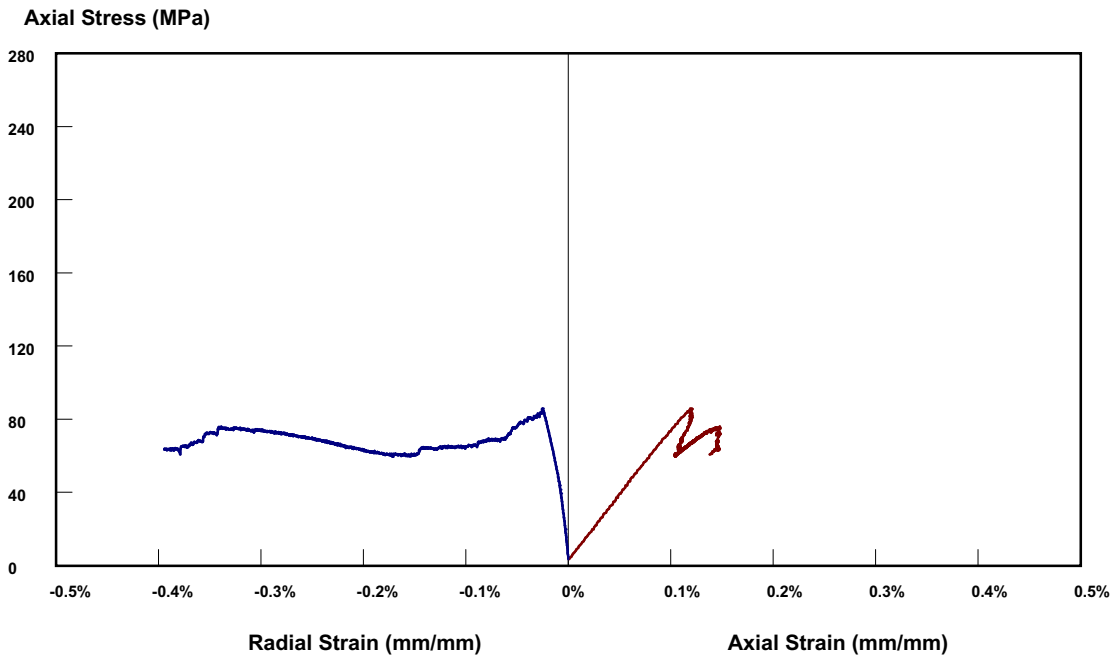
Specimen Data

Site:	Äspö	Diameter:	50.91 mm
Rock Type:	Diorite	Length/Diameter:	2.80
Hole:	KA3376B01	Density:	2730 kg/m ³
Depth:	61.58	Porosity:	
		Test Saturation:	

Test Results

Young's Modulus:	68.8 GPa	Peak Strength:	202.6 MPa
Poisson's Ratio:	0.28	Crack Damage Stress:	185.5 MPa
		Crack Initiation Stress:	87.0 MPa

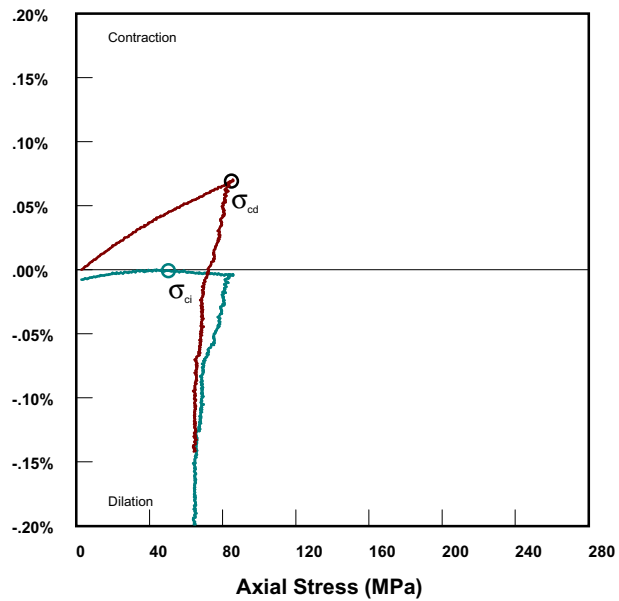
Uniaxial Test of KA3376B01 - 61.72



Failure Pattern



Volumetric Strain (mm³/mm³)



Test Data

Client:	SKB	Test Date:	2003-06-10
Order Number:		Loading Control:	Radial Strain Rate
Test:	Uniaxial	Equivalent Loading Rate:	0.75 MPa/s
Equipment:	MTS 815	Confining Stress:	0 MPa

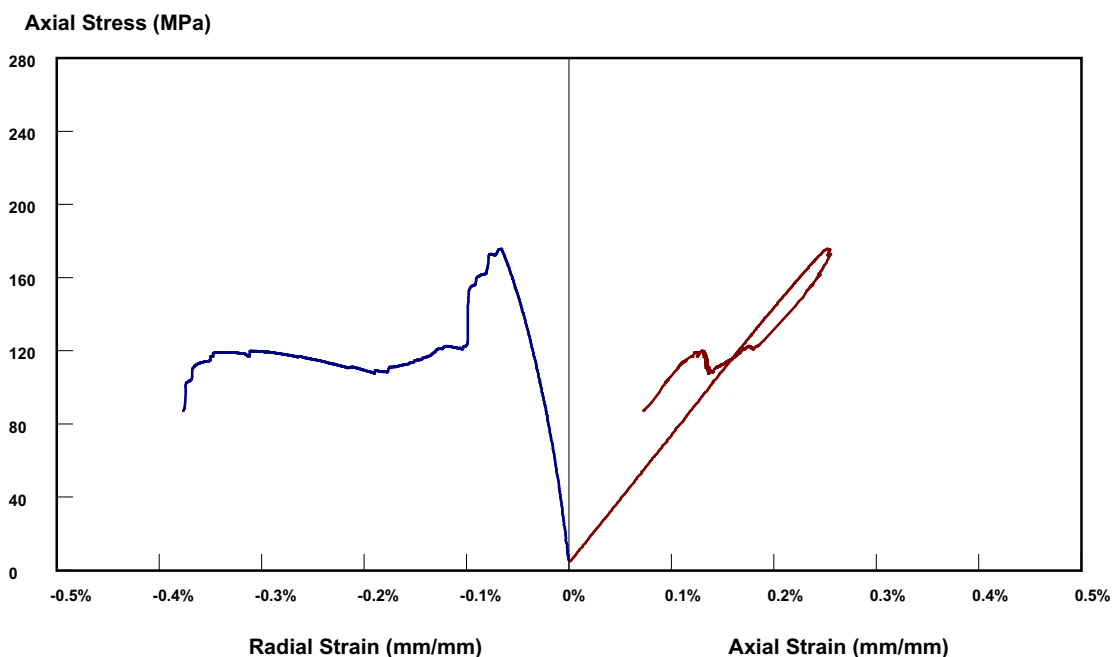
Specimen Data

Site:	Äspö	Diameter:	50.92 mm
Rock Type:	Diorite	Length/Diameter:	2.80
Hole:	KA3376B01	Density:	2724 kg/m ³
Depth:	61.72	Porosity:	
		Test Saturation:	

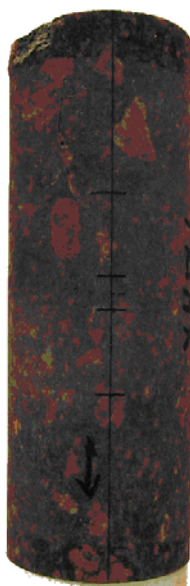
Test Results

Young's Modulus:	74.0 GPa	Peak Strength:	84.8 MPa
Poisson's Ratio:	0.21	Crack Damage Stress:	84.8 MPa
		Crack Initiation Stress:	50.3 MPa

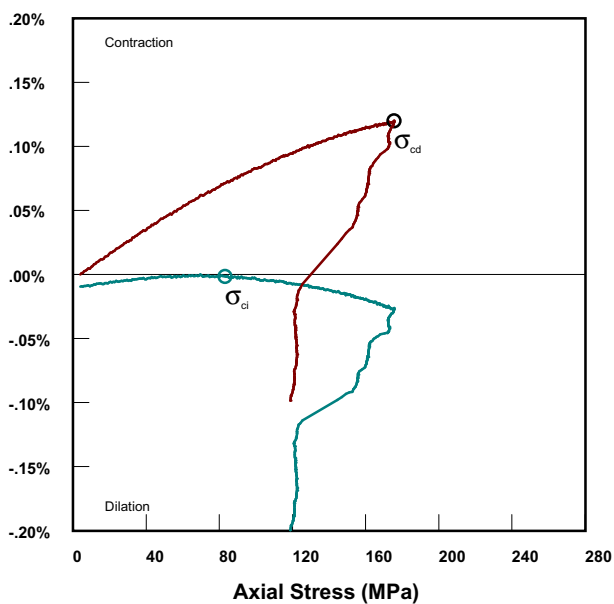
Triaxial Test of KA3376B01 - 31.70



Failure Pattern



Volumetric Strain (mm³/mm³)



Test Data

Client:	SKB	Test Date:	2003-06-17
Order Number:		Loading Control:	Radial Strain Rate
Test:	Triaxial	Equivalent Loading Rate:	0.75 MPa/s
Equipment:	MTS 815	Confining Stress:	2 MPa

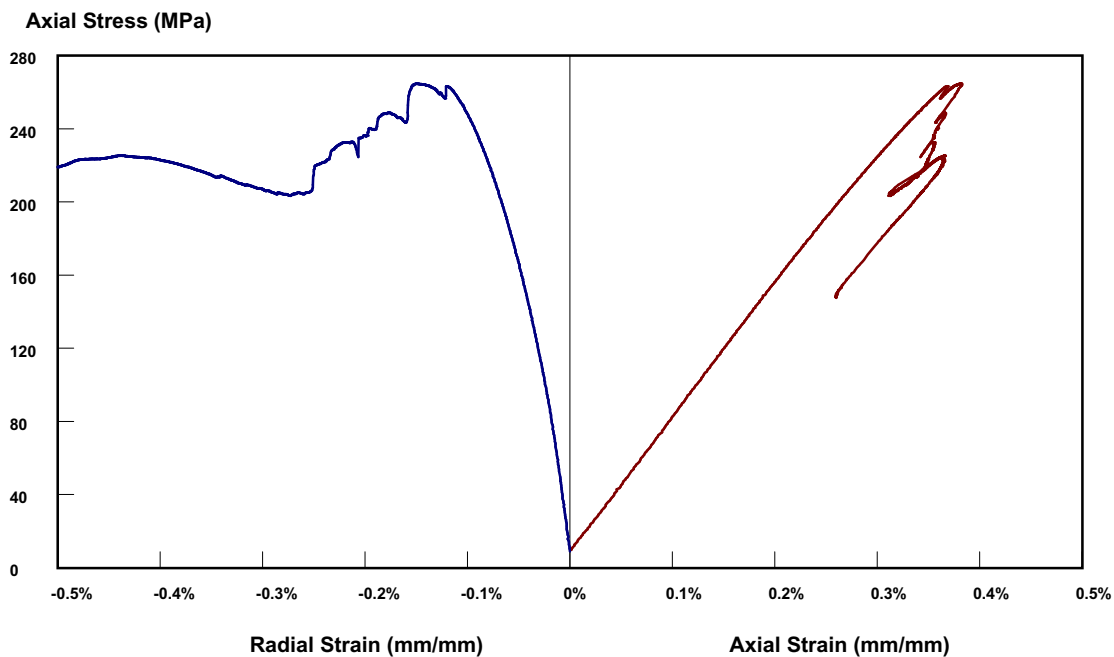
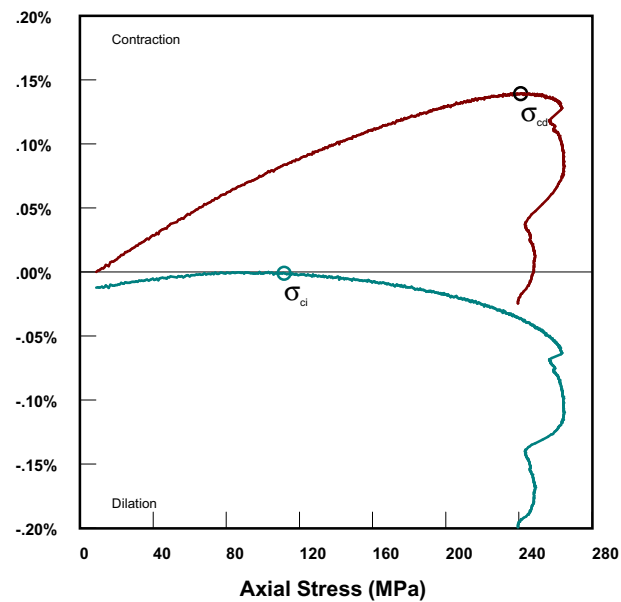
Specimen Data

Site:	Äspö	Diameter:	50.89 mm
Rock Type:	Diorite	Length/Diameter:	2.79
Hole:	KA3376B01	Density:	2756 kg/m ³
Depth:	31.70	Porosity:	
		Test Saturation:	

Test Results

Young's Modulus:	70.3 GPa	Peak Strength:	175.5 MPa
Poisson's Ratio:	0.22	Crack Damage Stress:	175.5 MPa
		Crack Initiation Stress:	83.1 MPa

Triaxial Test of KA3376B01 - 31.90

**Failure Pattern****Volumetric Strain (mm³/mm³)****Test Data**

Client:	SKB	Test Date:	2003-06-18
Order Number:		Loading Control:	Radial Strain Rate
Test:	Triaxial	Equivalent Loading Rate:	0.75 MPa/s
Equipment:	MTS 815	Confining Stress:	7 MPa

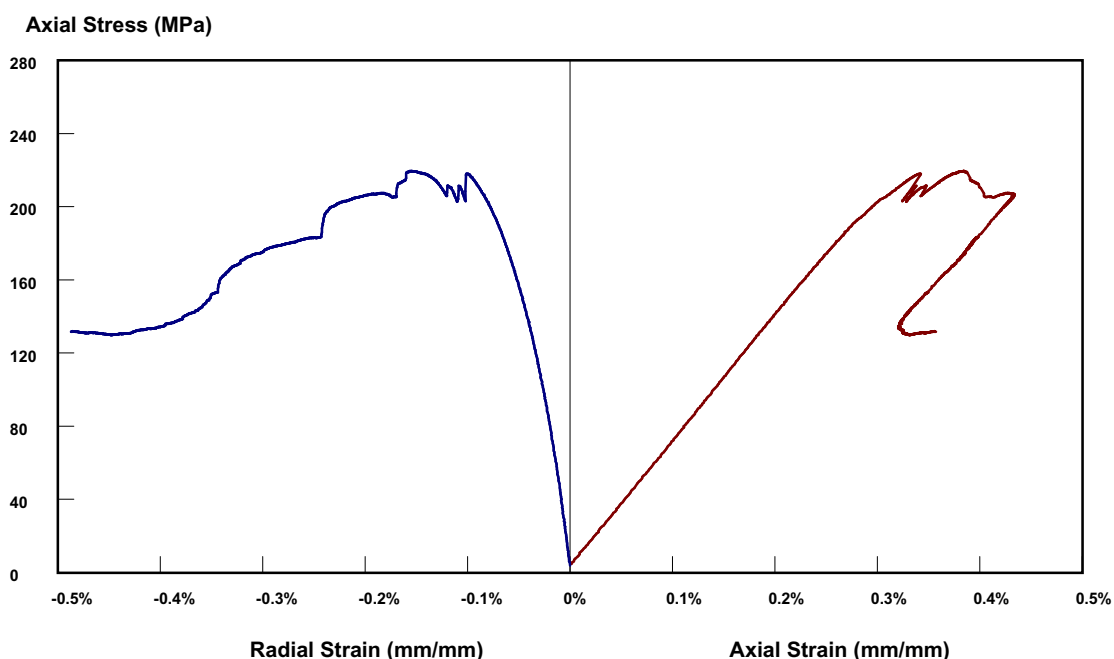
Specimen Data

Site:	Äspö	Diameter:	50.89 mm
Rock Type:	Diorite	Length/Diameter:	2.79
Hole:	KA3376B01	Density:	2733 kg/m ³
Depth:	31.90	Porosity:	
		Test Saturation:	

Test Results

Young's Modulus:	74.3 GPa	Peak Strength:	264.6 MPa
Poisson's Ratio:	0.24	Crack Damage Stress:	241.0 MPa
		Crack Initiation Stress:	111.7 MPa

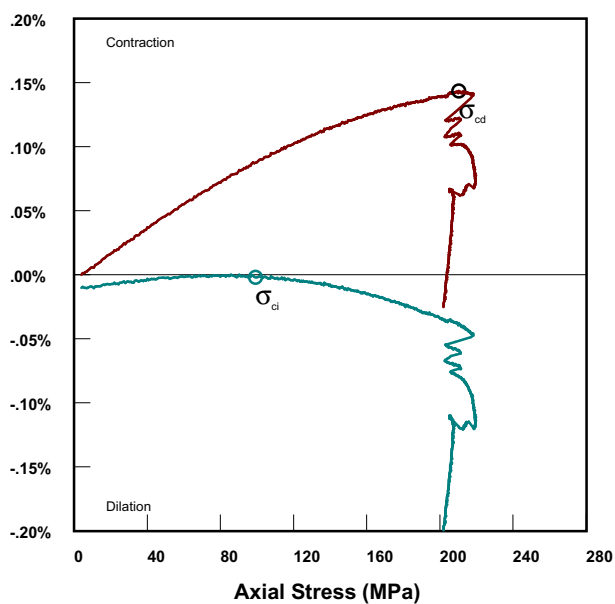
Triaxial Test of KA3376B01 - 32.27



Failure Pattern



Volumetric Strain (mm³/mm³)



Test Data

Client:	SKB	Test Date:	2003-06-17
Order Number:		Loading Control:	Radial Strain Rate
Test:	Triaxial	Equivalent Loading Rate:	0.75 MPa/s
Equipment:	MTS 815	Confining Stress:	2 MPa

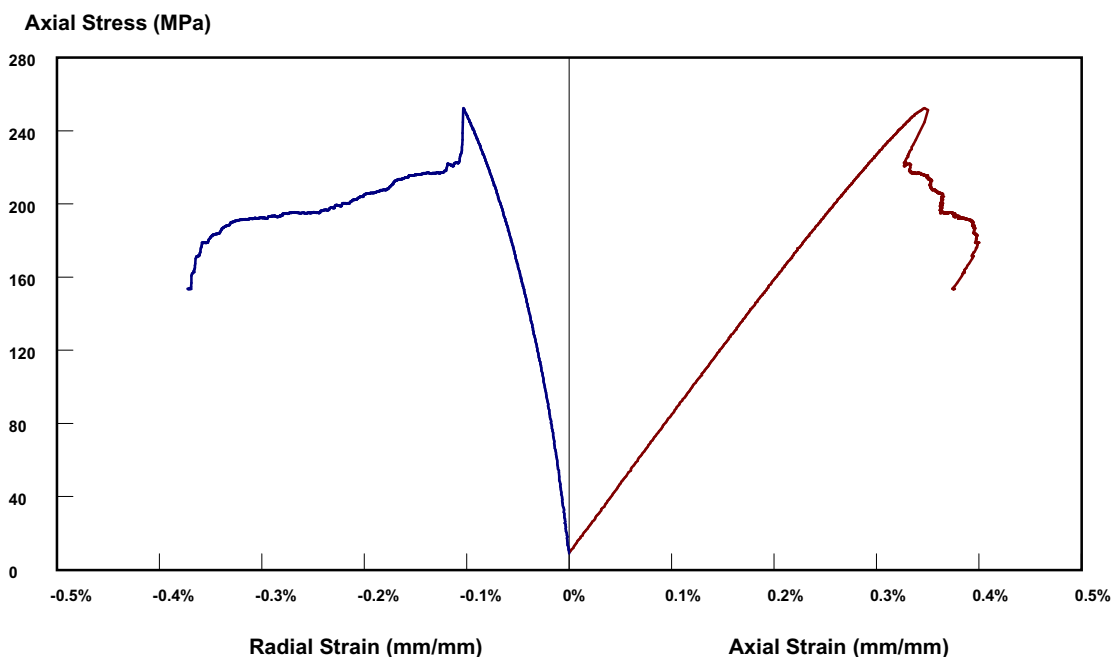
Specimen Data

Site:	Äspö	Diameter:	50.88 mm
Rock Type:	Diorite	Length/Diameter:	2.83
Hole:	KA3376B01	Density:	2743 kg/m ³
Depth:	32.27	Porosity:	
		Test Saturation:	

Test Results

Young's Modulus:	69.0 GPa	Peak Strength:	219.4 MPa
Poisson's Ratio:	0.21	Crack Damage Stress:	210.3 MPa
		Crack Initiation Stress:	99.2 MPa

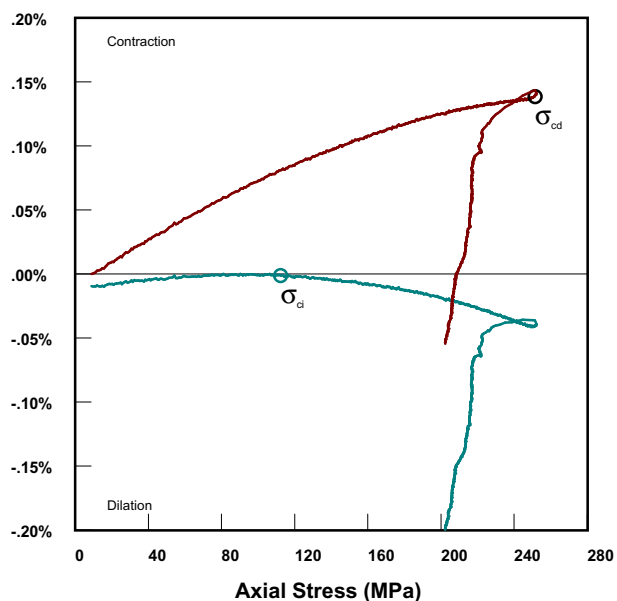
Triaxial Test of KA3376B01 - 60.85



Failure Pattern



Volumetric Strain (mm³/mm³)



Test Data

Client:	SKB	Test Date:	2003-06-18
Order Number:		Loading Control:	Radial Strain Rate
Test:	Triaxial	Equivalent Loading Rate:	0.75 MPa/s
Equipment:	MTS 815	Confining Stress:	7 MPa

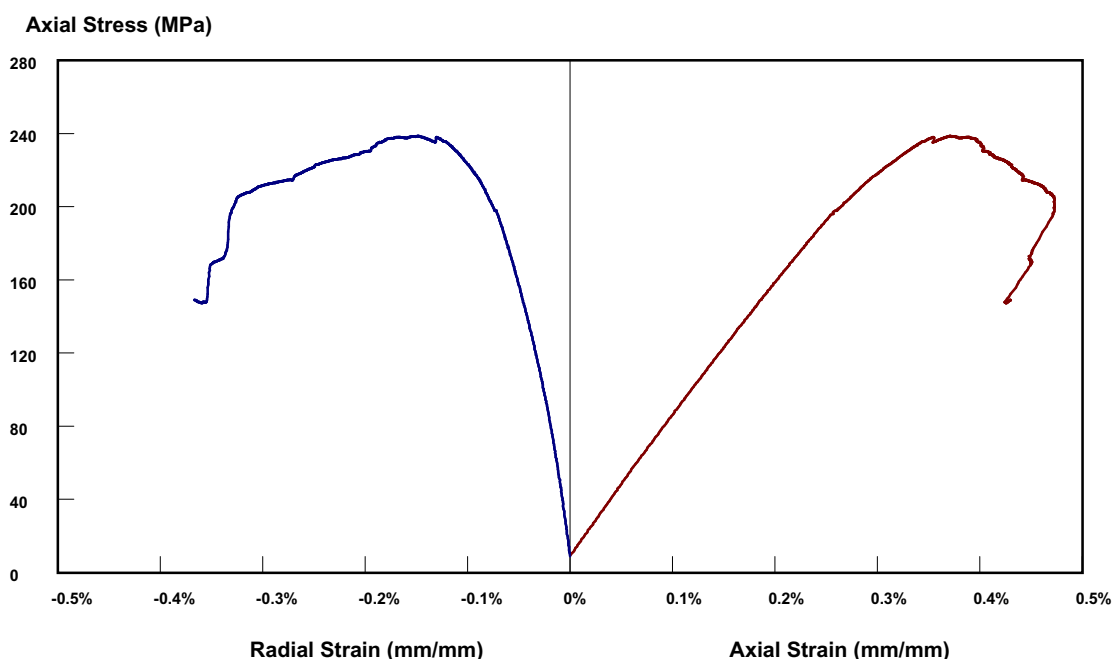
Specimen Data

Site:	Äspö	Diameter:	50.88 mm
Rock Type:	Diorite	Length/Diameter:	2.79
Hole:	KA3376B01	Density:	2729 kg/m ³
Depth:	60.85	Porosity:	
		Test Saturation:	

Test Results

Young's Modulus:	74.7 GPa	Peak Strength:	251.5 MPa
Poisson's Ratio:	0.24	Crack Damage Stress:	251.5 MPa
		Crack Initiation Stress:	112.3 MPa

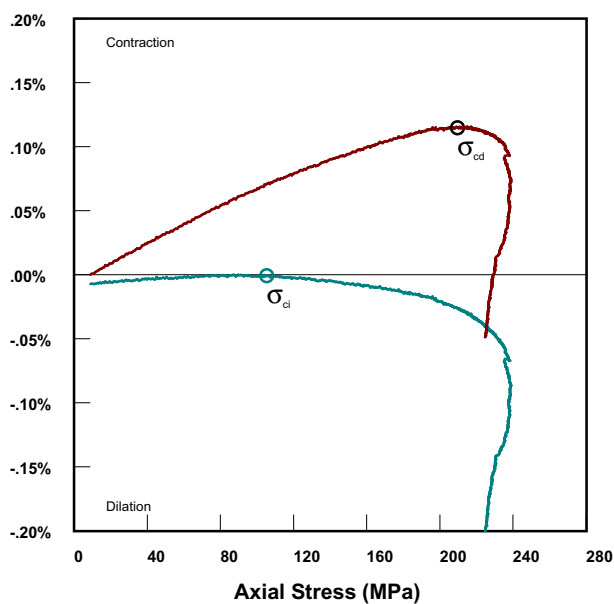
Triaxial Test of KA3376B01 - 62.05



Failure Pattern



Volumetric Strain (mm³/mm³)



Test Data

Client:	SKB	Test Date:	2003-06-19
Order Number:		Loading Control:	Radial Strain Rate
Test:	Triaxial	Equivalent Loading Rate:	0.75 MPa/s
Equipment:	MTS 815	Confining Stress:	7 MPa

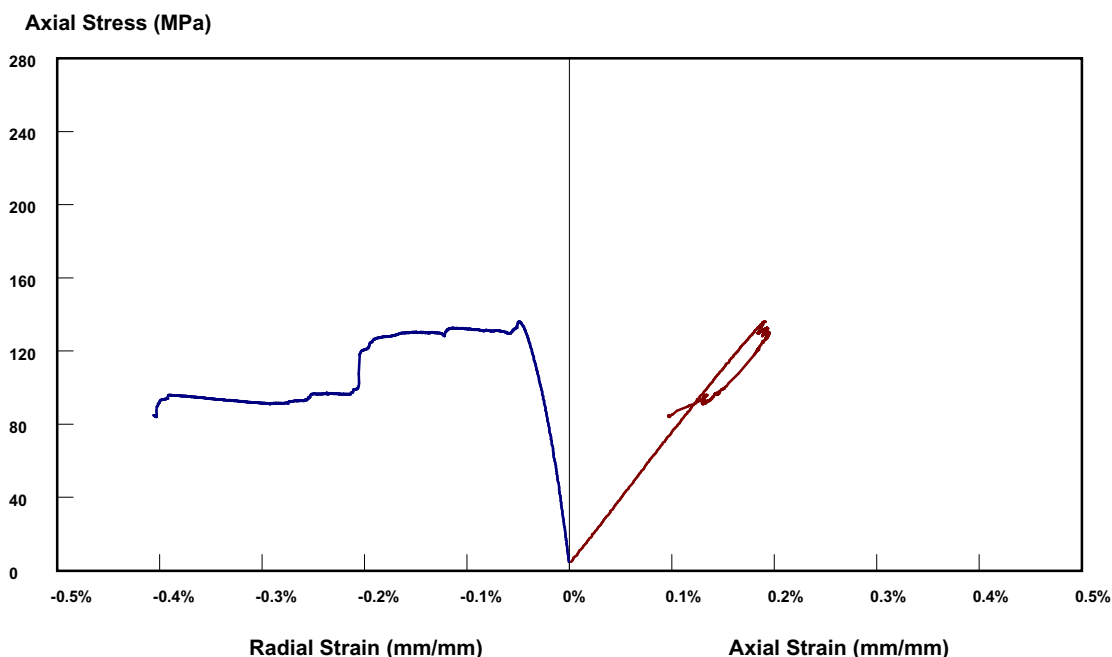
Specimen Data

Site:	Äspö	Diameter:	50.93 mm
Rock Type:	Diorite	Length/Diameter:	2.82
Hole:	KA3376B01	Density:	2716 kg/m ³
Depth:	62.05	Porosity:	
		Test Saturation:	

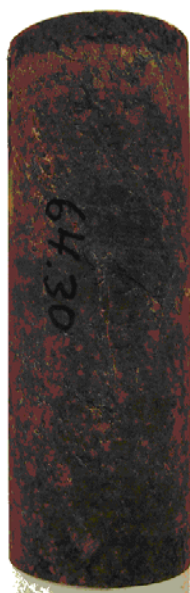
Test Results

Young's Modulus:	74.4 GPa	Peak Strength:	238.6 MPa
Poisson's Ratio:	0.25	Crack Damage Stress:	209.6 MPa
		Crack Initiation Stress:	105.3 MPa

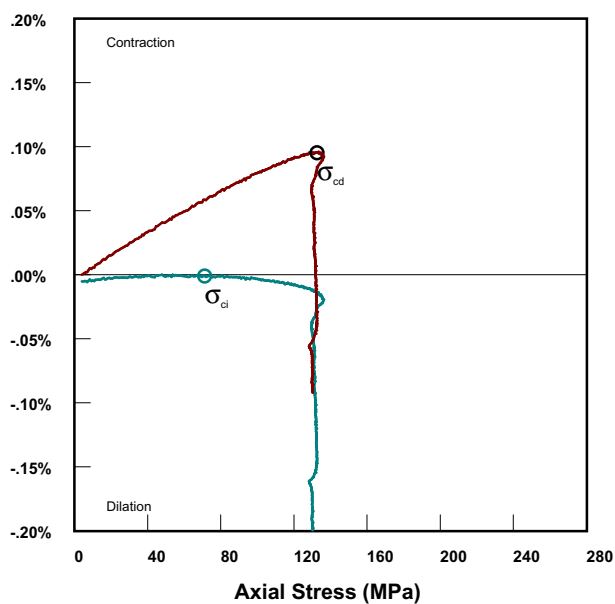
Triaxial Test of KA3376B01 - 64.30



Failure Pattern



Volumetric Strain (mm³/mm³)



Test Data

Client:	SKB	Test Date:	2003-06-18
Order Number:		Loading Control:	Radial Strain Rate
Test:	Triaxial	Equivalent Loading Rate:	0.75 MPa/s
Equipment:	MTS 815	Confining Stress:	2 MPa

Specimen Data

Site:	Äspö	Diameter:	50.87 mm
Rock Type:	Diorite	Length/Diameter:	2.80
Hole:	KA3376B01	Density:	2723 kg/m ³
Depth:	64.30	Porosity:	
		Test Saturation:	

Test Results

Young's Modulus:	72.8 GPa	Peak Strength:	136.0 MPa
Poisson's Ratio:	0.21	Crack Damage Stress:	132.7 MPa
		Crack Initiation Stress:	71.2 MPa

AE-MEASUREMENT INTERPRETATION FOR SKB SPECIMENS

Background

The results are presented as cumulative number of acoustic emission (AE) events versus axial stress. The events are classified based on event energy. The energy bands are defined so that the number of events in each band is approximately 30%, 30%, 30%, 5% and 5% i.e. the total number of events below energy limits are 30%, 60%, 90%, 95% and 100%. The cumulative number of AE events in energy bands are presented in linear scale while sum of all bands is presented in logarithmic scale. Two figures are presented first (a) scaled to show all events and second (b) to show only first big events.

Based on previous tests with Finnish granitic and gneissic rocks following pre-failure AE phases are commonly observed:

- a) moderate amount of small or medium energy events in the beginning of loading, probably caused mainly by settling of specimen ends and closing/shearing of open micro fractures.
- b) if settling ramp is done, as in these tests, quiet unloading and reloading
- c) quiet elastic loading
- d) onset of small or medium energy events *i.e. crack initiation*
- e) stable crack growth i.e. cumulative number of events is increasing 'linearly' with loading
- f) onset of high energy events = beginning of destruction
- g) onset of unstable crack growth i.e. amount of events starts to increase exponentially with loading *i.e. crack damage*
- h) exponential increase of events with any energy at *peak strength*

Specimen KA3376B01 – 61.58

There is not any clear elastic part either the crack initiation but the damaging is continuous (Figure 1a). The destruction starts round 100 MPa but the clear onset of crack damage is round 180 MPa (Figure 1b).

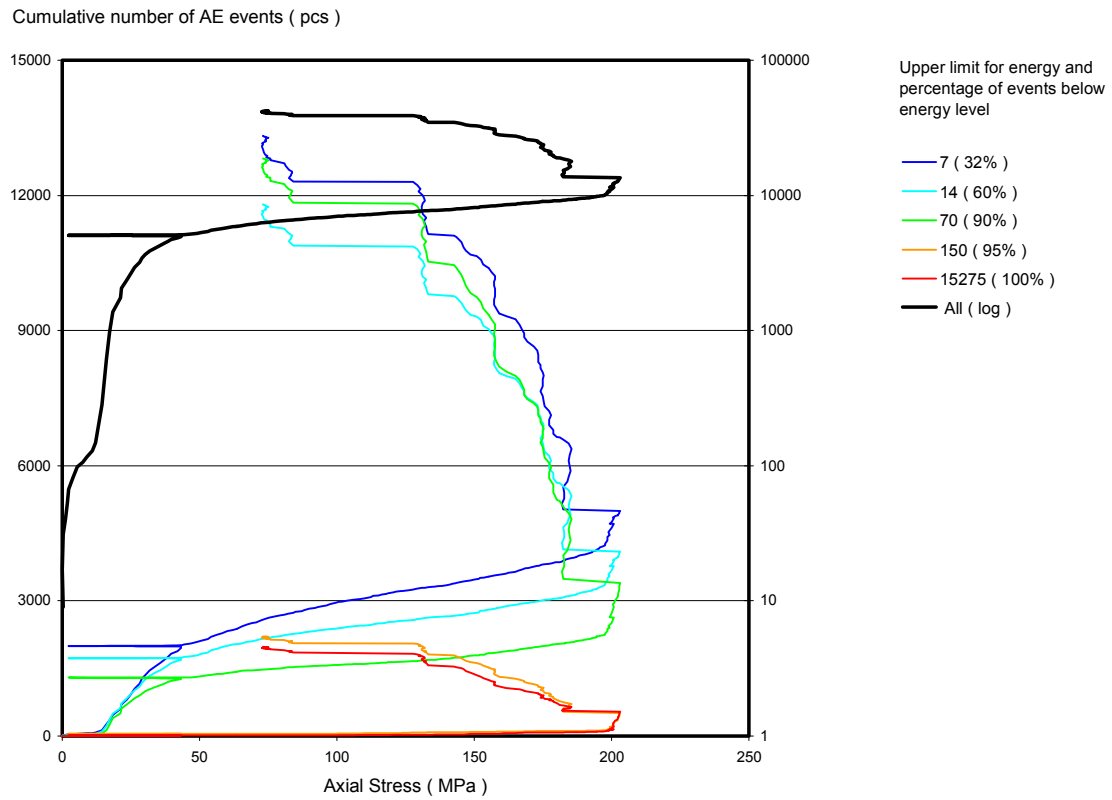


Figure 1a Cumulative number of acoustic emission events in energy bands as a function of axial stress for specimen KA3376B01 – 61.58.

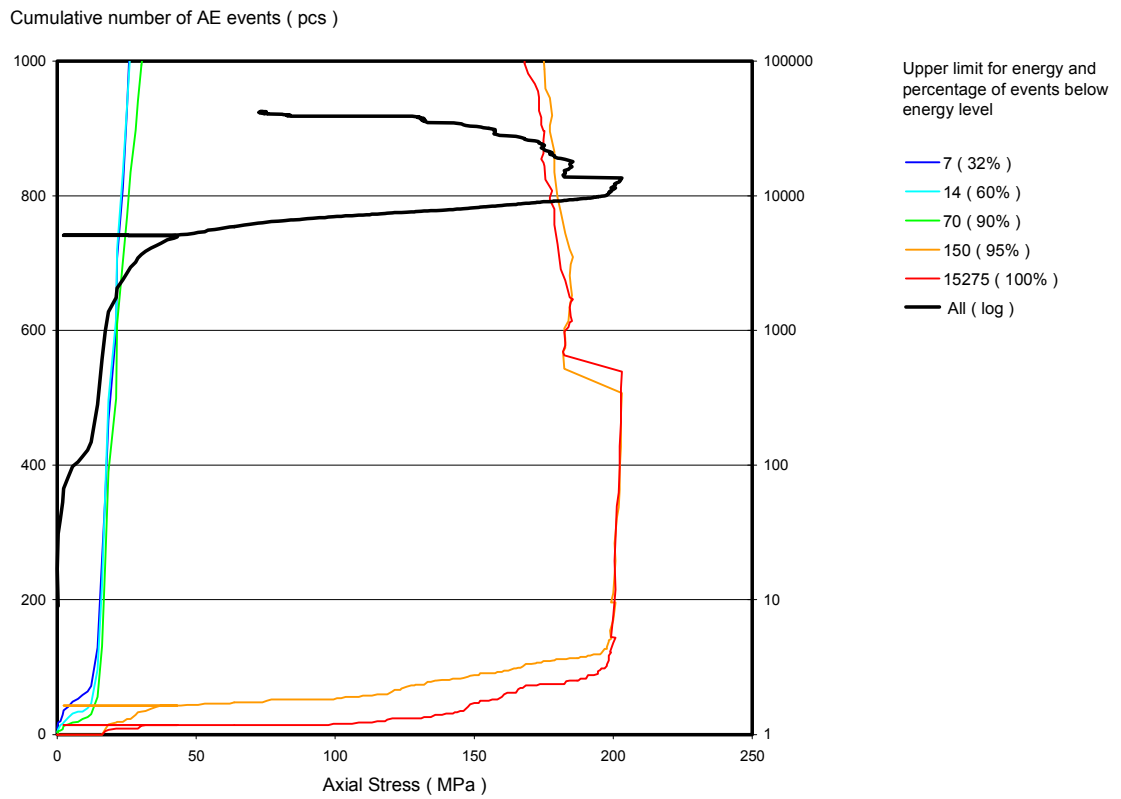


Figure 1b Cumulative number of acoustic emission events in energy bands as a function of axial stress for specimen KA3376B01 – 61.58, scale to show high-energy events.

Specimen KA3376B01 - 61.72

Specimen shows clear elastic part from 12 MPa to 70 MPa where the cracking initiates and turns immediately to sudden crack damage at 80 MPa (Figures 2a and 2b). This specimen had a closed fracture.

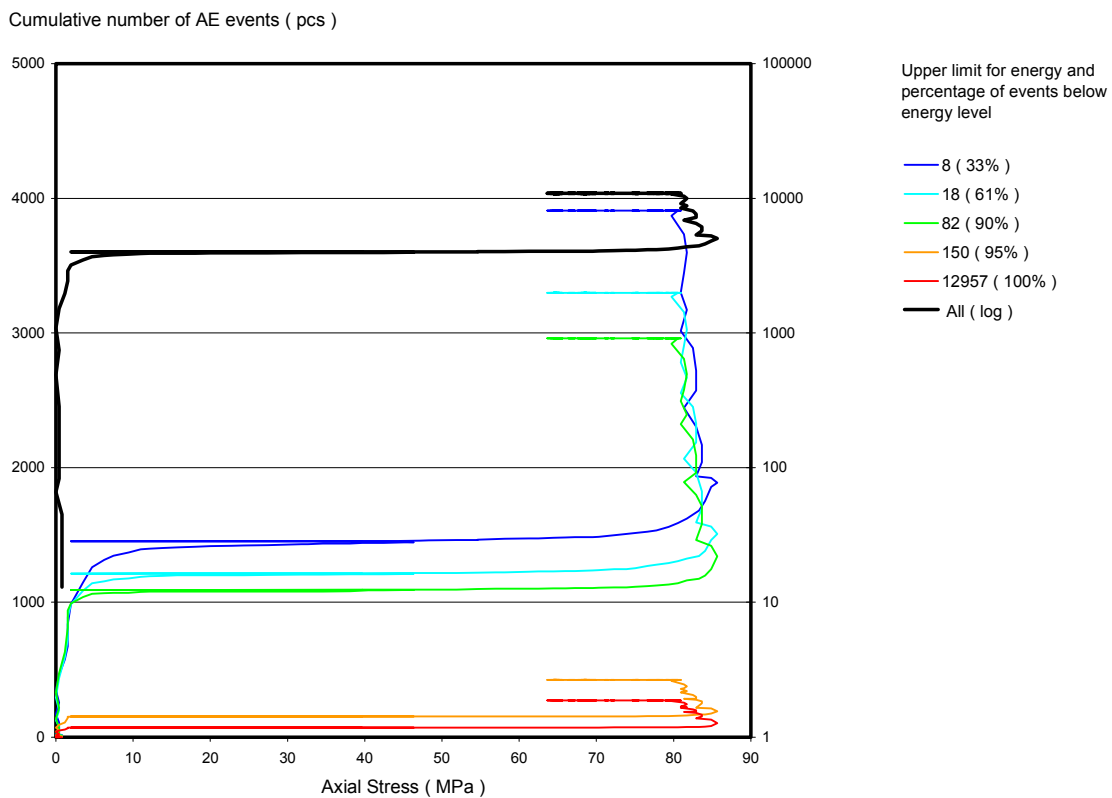


Figure 2a Cumulative number of acoustic emission events in energy bands as a function of axial stress for specimen KA3376B01 – 61.72.

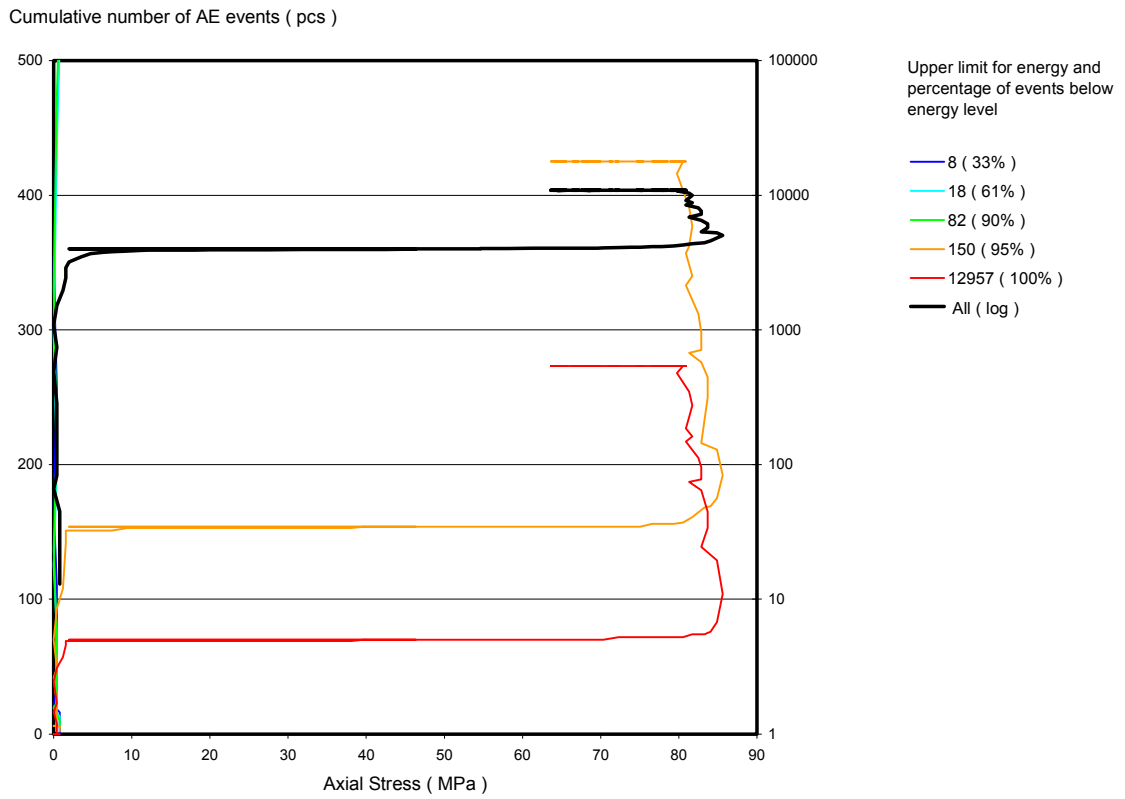


Figure 2b Cumulative number of acoustic emission events in energy bands as a function of axial stress for specimen KA3376B01 – 61.72, scale to show high-energy events.

Specimen KA3376B01 - 33.32

All damaging phases are somewhat overlapping. Elastic phase starts round 30 MPa but small energy damaging continues. Crack initiation stress is about 130 MPa but first high-energy events take place at the same time. Crack damage is round 180 MPa.

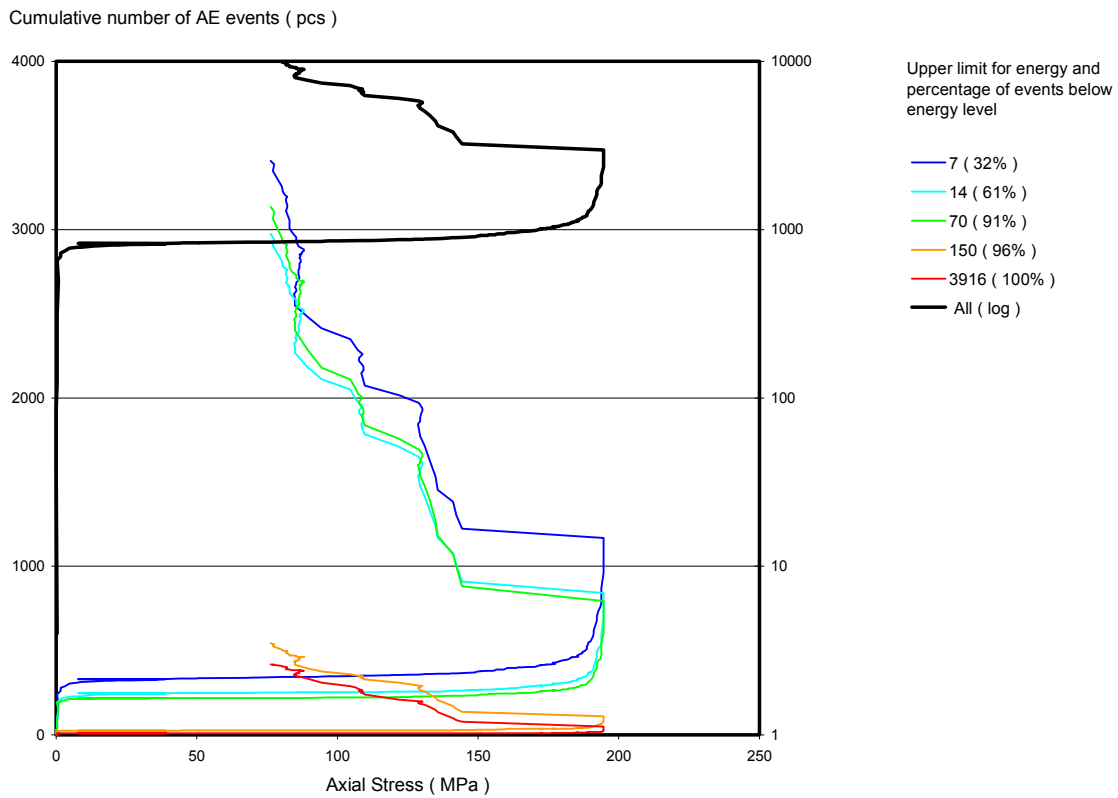


Figure 3a Cumulative number of acoustic emission events in energy bands as a function of axial stress for specimen KA3376B01 – 33.32.

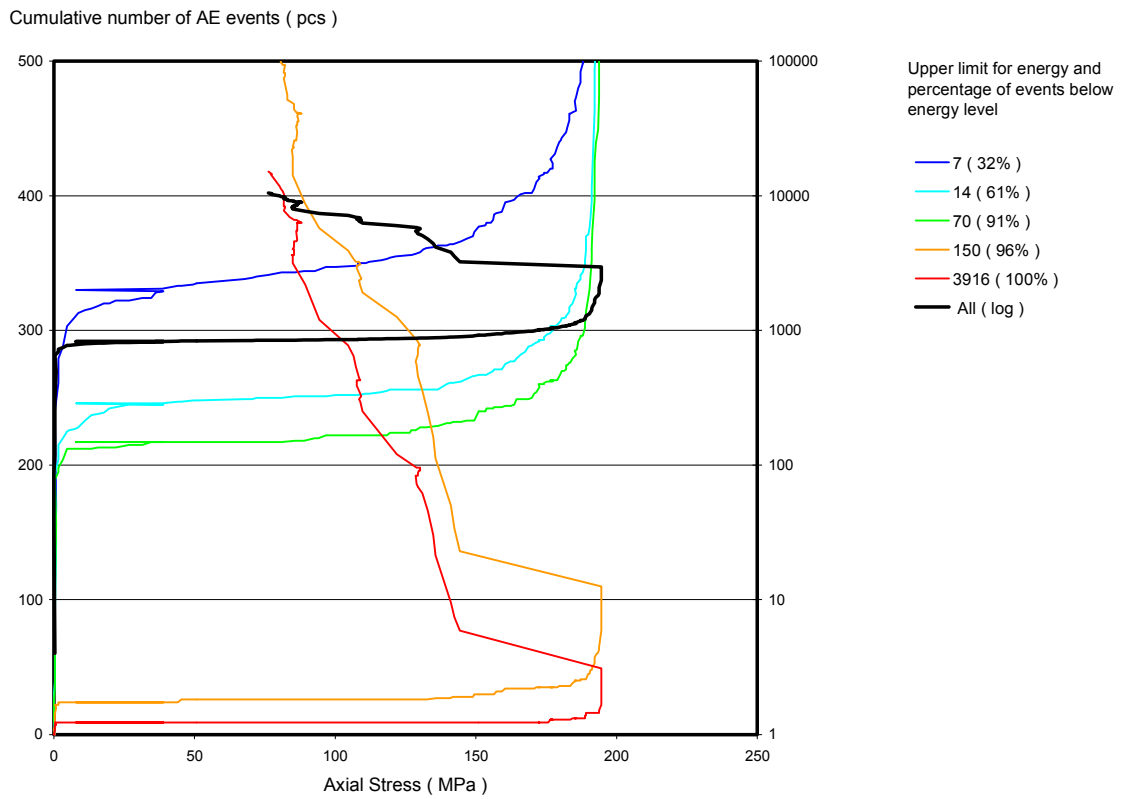


Figure 3b Cumulative number of acoustic emission events in energy bands as a function of axial stress for specimen KA3376B01 – 33.32, scale to show high-energy events.

**Mechanical testing on samples from KQ0064G01, KQ0064G07
and KQ0065G01**

**Core samples from Äspö HRL,
Sweden**

**KQ0064G01, KQ0064G07 and
KQ0065G01**

Harri Kuula, Pekka Eloranta
Helsinki University of Technology

October 2003

Sample Core samples from Äspö HRL, Sweden containing the following sections:
 KQ0064G01 5.43-5.60
 KQ0064G01 6.14-6.43
 KQ0065G01 7.36-7.50
 KQ0065G01 7.50-7.72
 KQ0065G01 5.25-5.95
 KQ0064G07 4.80-5.77

Commissioned analysis of the sample

Six (6) uniaxial compression tests with acoustic emission monitoring, three (3) triaxial compression tests with confining stress of 1 MPa and three (3) indirect Brazil tensile tests.

Method of analysis and results

Test specimens were prepared and tested according to the suggested methods of International Society of Rock Mechanics, ISRM (Brown 1981). The specimens were stored and tested in room conditions. Tests were carried out with a MTS 815 rock mechanics test system according to procedures developed by Hakala & Heikkilä 1997.

Elastic parameters i.e. Young's modulus and Poisson's ratio were calculated as secant values between axial stress levels at -0.01% of radial strain and 50% of peak strength. The density of the specimens was calculated from the physical dimensions and the weight of the dry specimens.

The results of the uniaxial compression tests are presented in Table 1 and in Appendices 1-3. Acoustic emission (AE) of these uniaxial compression test specimens was measured with a Mistras 2001 AE-equipment. Interpretation of the AE data is presented in Appendix 10.

The results of the triaxial compression tests are presented in Table 2 and in Appendices 4-9.

The results of the indirect Brazil tensile tests are presented in Table 3.

Table 1. Uniaxial compression tests (see Appendices 1-6).

Core sample code	Depth (m)	Length (mm)	Diameter (mm)	Density (kg/m ³)	Uniaxial compressive strength (MPa)	Young's modulus (GPa)	Poisson's ratio
KQ0064G01	6.26	138.5	50.9	2741	221.1	73.6	0.27
KQ0065G01	7.37	133.1	50.9	2747	186.5	76.3	0.25
KQ0065G01	5.29	139.2	50.8	2751	244.3	78.1	0.26
KQ0065G01	5.43	139.8	50.9	2740	236.7	76.8	0.28
KQ0064G07	4.99	139.8	50.9	2715	189.5	74.1	0.28
KQ0064G07	5.38	139.8	50.9	2717	131.7	72.8	0.27

Table 2. Triaxial compression tests (confining stress 1 MPa) (see Appendices 7-9).

Core sample code	Depth (m)	Length (mm)	Diameter (mm)	Density (kg/m ³)	Compressive strength (MPa)	Young's modulus (GPa)	Poisson's ratio
KQ0064G01	5.44	138.8	50.7	2716	243.5	79.1	0.26
KQ0065G01	7.53	139.2	50.8	2732	255.9	77.3	0.23
KQ0064G07	5.13	139.8	50.8	2725	180.8	79.9	0.22

Table 3. Indirect Brazil tensile tests.

Core sample code	Depth (m)	Length (mm)	Diameter (mm)	Force (kN)	Tensile strength (MPa)
KQ0064G01	6.23	27.2	50.9	28.1	12.9
KQ0065G01	5.57	26.7	50.8	30.7	14.4
KQ0064G07	5.53	26.9	50.9	33.7	15.7

The uniaxial test specimen 5.38 failed through a weakness plane (fracture) causing unstable behaviour during the test as can be seen on the stress-strain curves in Appendix 6. Elastic parameters were therefore calculated on the linear part of the curves between axial stress levels of 42 MPa and 52 MPa.

The results are valid only for the tested specimens. Crack initiation and crack damage stress levels in Appendices 1-9 were interpreted from the volumetric strain data and therefore may not agree with the levels interpreted from acoustic emission data in Appendix 10.

References

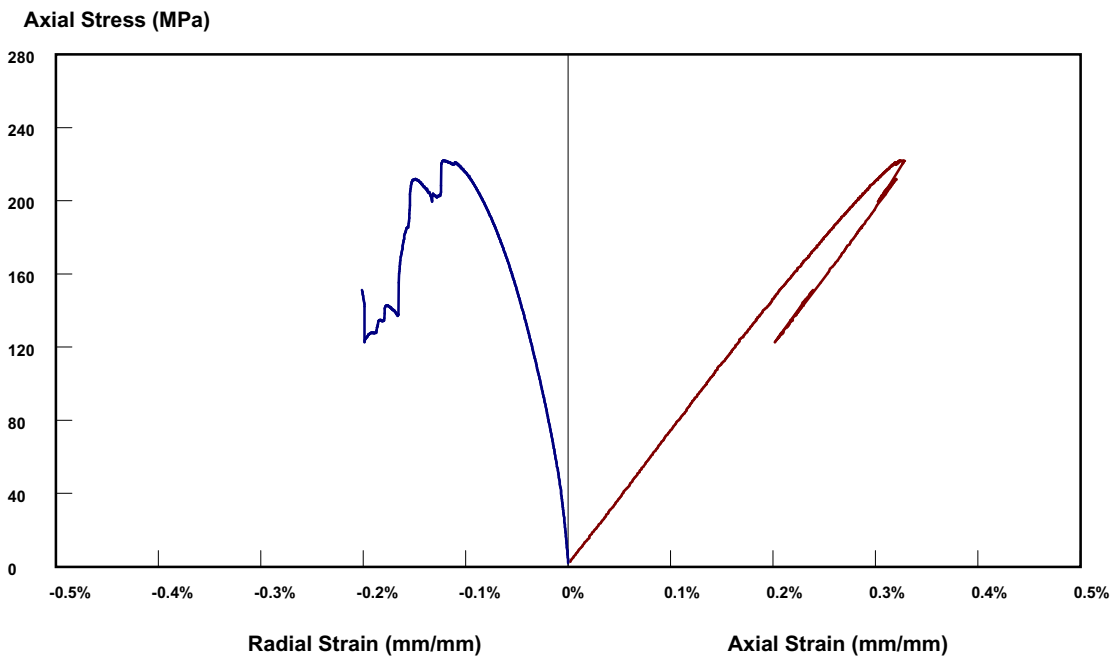
Brown, E.T. (Ed.) (1981) Rock characterization, testing and monitoring. ISRM suggested methods. 211 p. Oxford: Pergamon Press. ISBN 0-08-027309-2.

Hakala, M. & Heikkilä, E. (1996) Summary report – Development of laboratory test and the stress –strain behaviour of Olkiluoto mica gneiss. Posiva Report Posiva-97-04. 150 p. Helsinki: Posiva. ISBN 951-652-029-4

Appendices

- 1-9 Stress-strain curves
- 10 AE interpretation

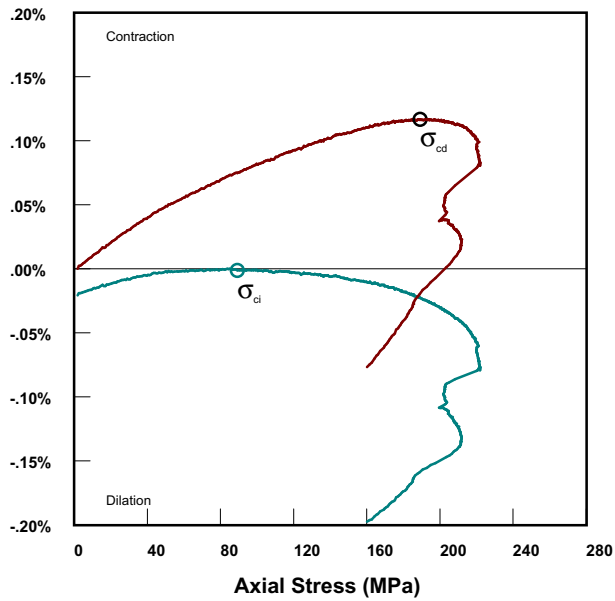
Uniaxial Test of KQ0064G01 - 6.26



Failure Pattern



Volumetric Strain (mm³/mm³)



Test Data

Client:	SKB	Test Date:	2003-09-18
Order Number:	9376	Loading Control:	Radial Strain Rate
Test:	Uniaxial	Equivalent Loading Rate:	0.75 MPa/s
Equipment:	MTS 815	Confining Stress:	0 MPa

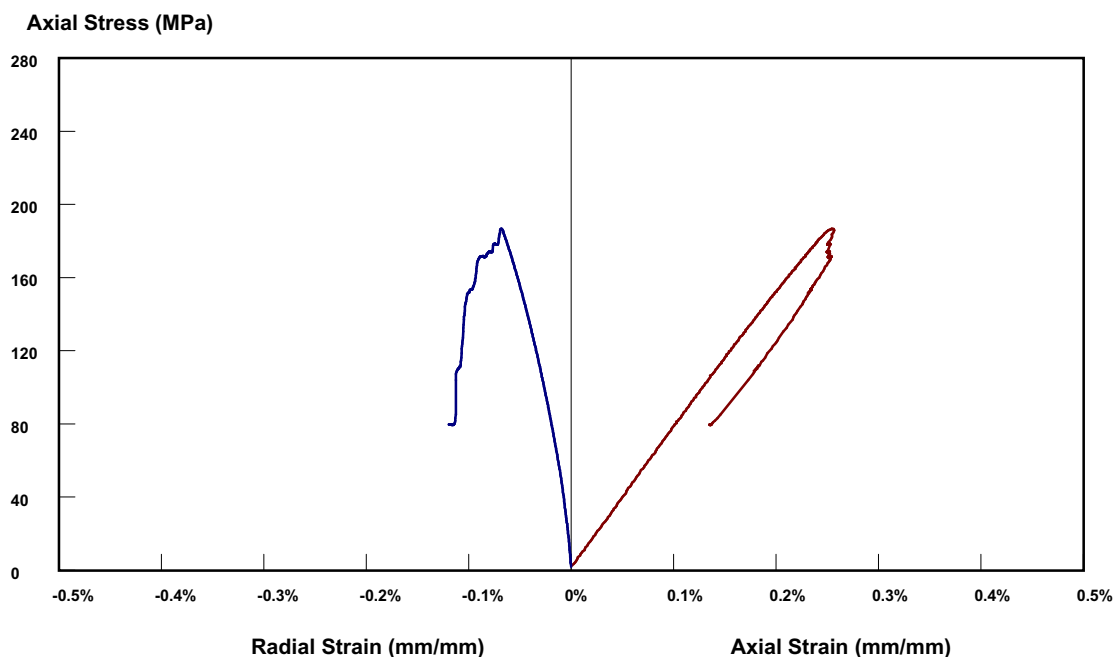
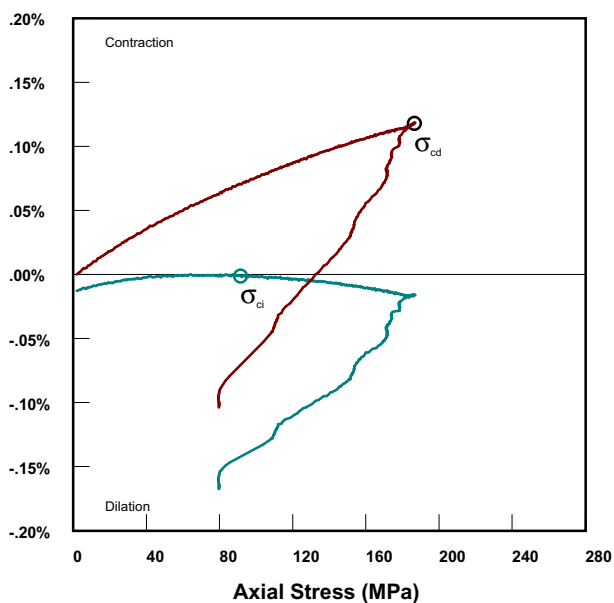
Specimen Data

Site:	Äspö	Diameter:	50.85 mm
Rock Type:		Length/Diameter:	2.72
Hole:	KQ0064G01	Density:	2741 kg/m ³
Depth:	6.26	Porosity:	
		Test Saturation:	

Test Results

Young's Modulus:	73.6 GPa	Peak Strength:	222.1 MPa
Poisson's Ratio:	0.27	Crack Damage Stress:	189.2 MPa
		Crack Initiation Stress:	89.2 MPa

Uniaxial Test of KQ0065G01 - 7.37

**Failure Pattern****Volumetric Strain (mm³/mm³)****Test Data**

Client:	SKB	Test Date:	2003-09-19
Order Number:	9376	Loading Control:	Radial Strain Rate
Test:	Uniaxial	Equivalent Loading Rate:	0.75 MPa/s
Equipment:	MTS 815	Confining Stress:	0 MPa

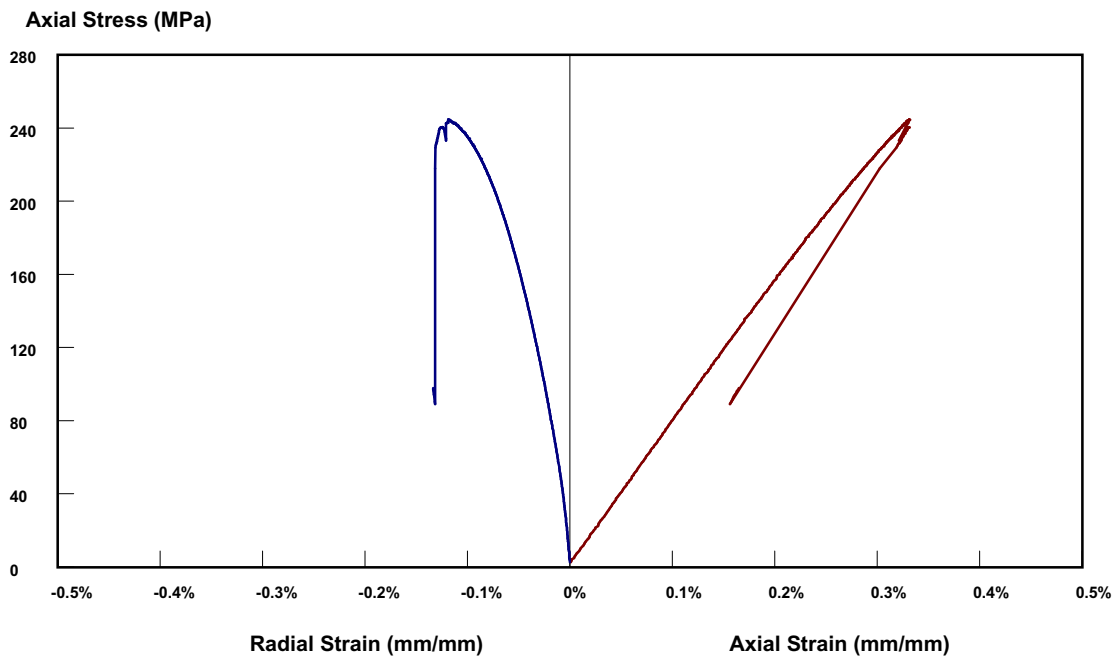
Specimen Data

Site:	Äspö	Diameter:	50.85 mm
Rock Type:		Length/Diameter:	2.62
Hole:	KQ0065G01	Density:	2747 kg/m ³
Depth:	7.37	Porosity:	
		Test Saturation:	

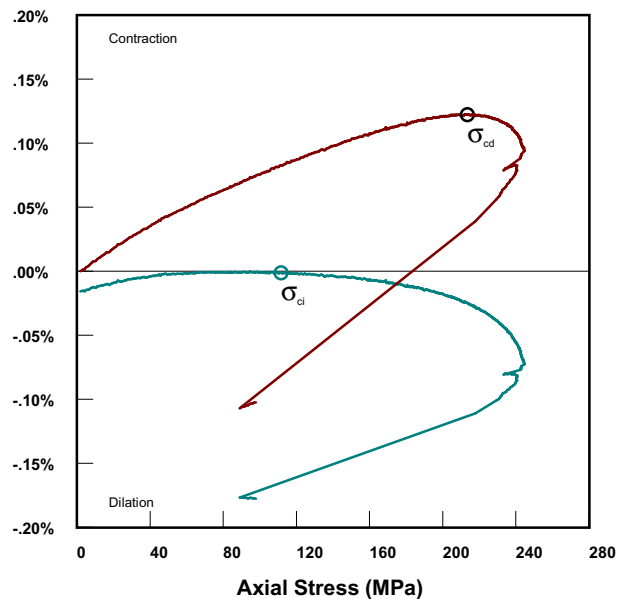
Test Results

Young's Modulus:	76.3 GPa	Peak Strength:	186.5 MPa
Poisson's Ratio:	0.25	Crack Damage Stress:	186.5 MPa
		Crack Initiation Stress:	91.6 MPa

Uniaxial Test of KQ0065G01 - 5.29



Failure Pattern

Volumetric Strain (mm^3/mm^3)**Test Data**

Client:	SKB	Test Date:	2003-09-19
Order Number:	9376	Loading Control:	Radial Strain Rate
Test:	Uniaxial	Equivalent Loading Rate:	0.75 MPa/s
Equipment:	MTS 815	Confining Stress:	0 MPa

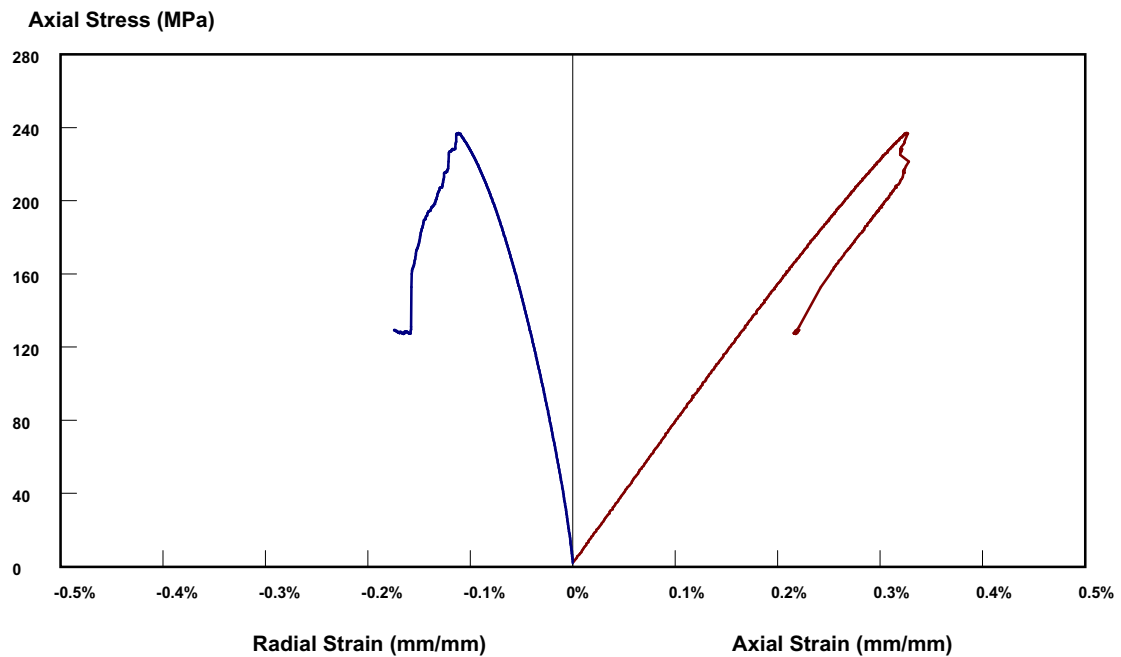
Specimen Data

Site:	Äspö	Diameter:	50.84 mm
Rock Type:		Length/Diameter:	2.74
Hole:	KQ0065G01	Density:	2751 kg/m ³
Depth:	5.29	Porosity:	
		Test Saturation:	

Test Results

Young's Modulus:	78.1 GPa	Peak Strength:	244.3 MPa
Poisson's Ratio:	0.26	Crack Damage Stress:	213.4 MPa
		Crack Initiation Stress:	111.7 MPa

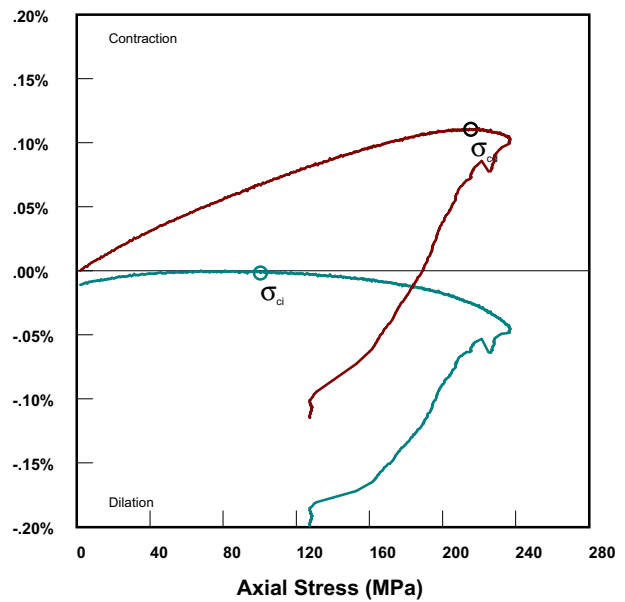
Uniaxial Test of KQ0065G01 - 5.43



Failure Pattern



Volumetric Strain (mm³/mm³)



Test Data

Client:	SKB	Test Date:	2003-09-19
Order Number:	9376	Loading Control:	Radial Strain Rate
Test:	Uniaxial	Equivalent Loading Rate:	0.75 MPa/s
Equipment:	MTS 815	Confining Stress:	0 MPa

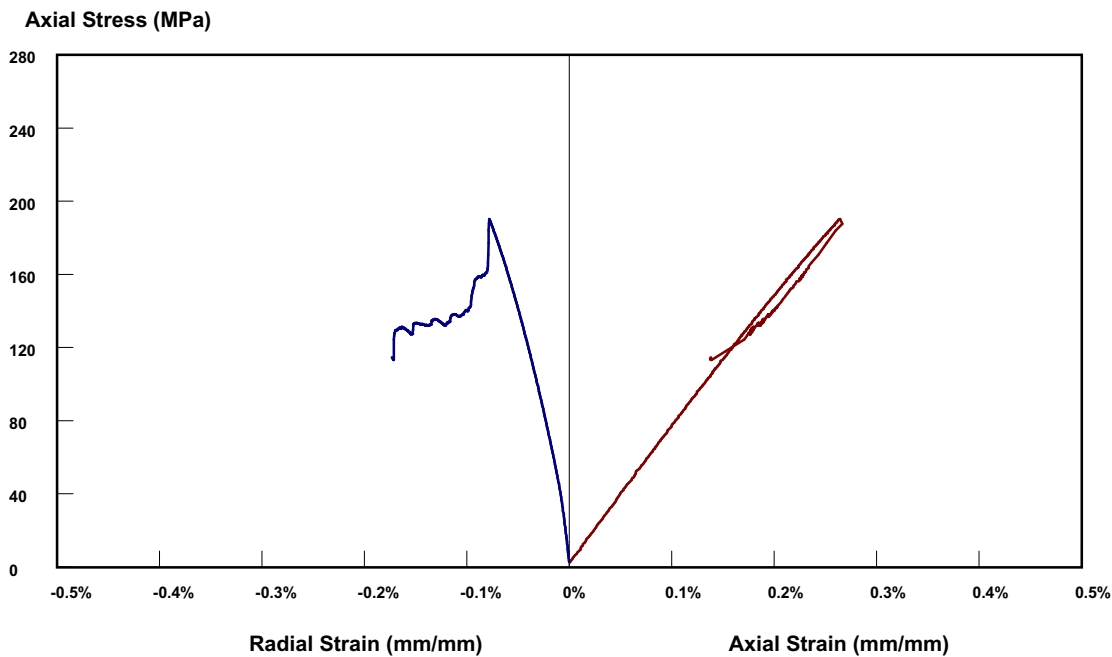
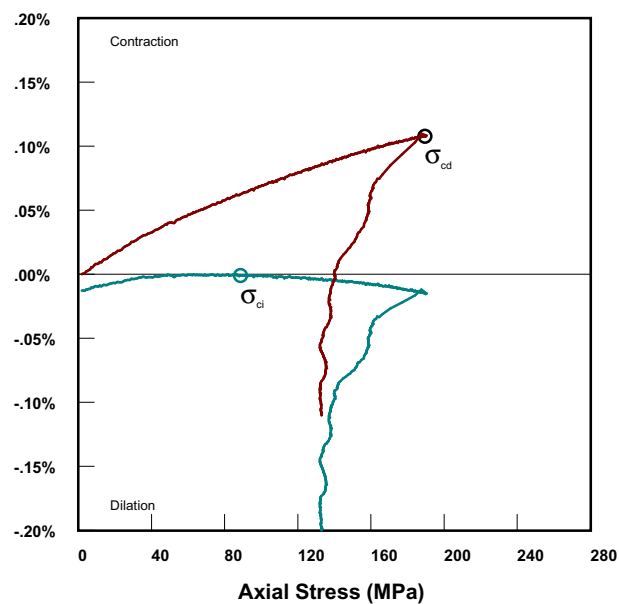
Specimen Data

Site:	Äspö	Diameter:	50.85 mm
Rock Type:		Length/Diameter:	2.75
Hole:	KQ0065G01	Density:	2740 kg/m ³
Depth:	5.43	Porosity:	
		Test Saturation:	

Test Results

Young's Modulus:	76.8 GPa	Peak Strength:	236.7 MPa
Poisson's Ratio:	0.28	Crack Damage Stress:	215.4 MPa
		Crack Initiation Stress:	100.5 MPa

Uniaxial Test of KQ0064G07 - 4.99

**Failure Pattern****Volumetric Strain (mm³/mm³)****Test Data**

Client:	SKB	Test Date:	2003-09-19
Order Number:	9376	Loading Control:	Radial Strain Rate
Test:	Uniaxial	Equivalent Loading Rate:	0.75 MPa/s
Equipment:	MTS 815	Confining Stress:	0 MPa

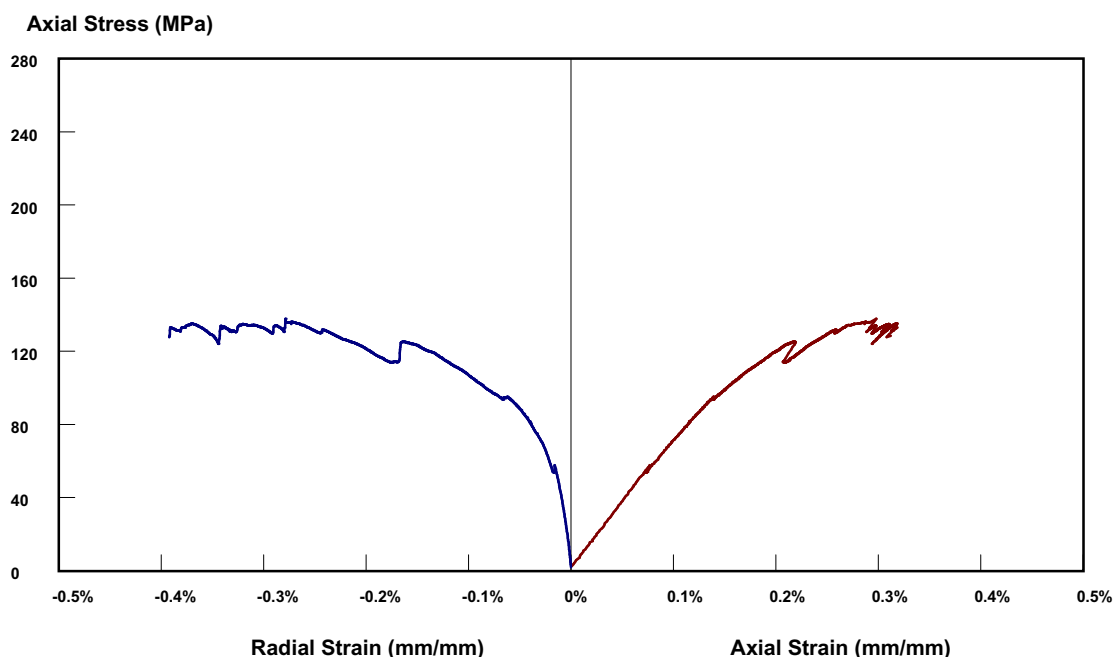
Specimen Data

Site:	Äspö	Diameter:	50.85 mm
Rock Type:		Length/Diameter:	2.75
Hole:	KQ0064G07	Density:	2715 kg/m ³
Depth:	4.99	Porosity:	
		Test Saturation:	

Test Results

Young's Modulus:	74.1 GPa	Peak Strength:	189.5 MPa
Poisson's Ratio:	0.28	Crack Damage Stress:	189.5 MPa
		Crack Initiation Stress:	88.7 MPa

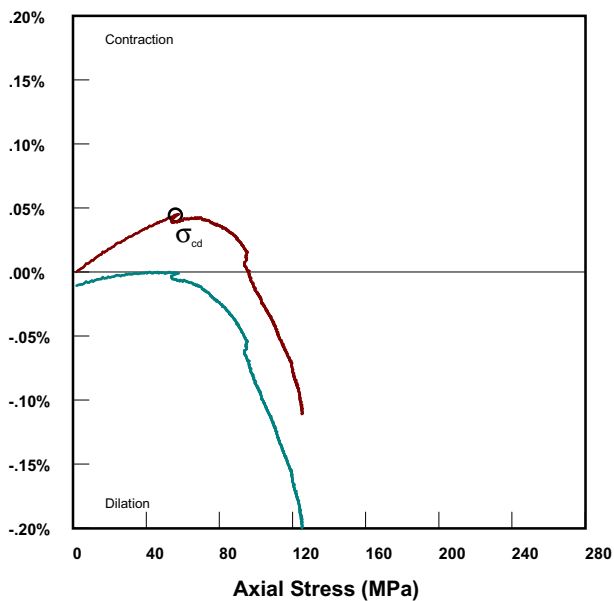
Uniaxial Test of KQ0064G07 - 5.38



Failure Pattern



Volumetric Strain (mm³/mm³)



Test Data

Client:	SKB	Test Date:	2003-09-19
Order Number:	9376	Loading Control:	Radial Strain Rate
Test:	Uniaxial	Equivalent Loading Rate:	0.75 MPa/s
Equipment:	MTS 815	Confining Stress:	0 MPa

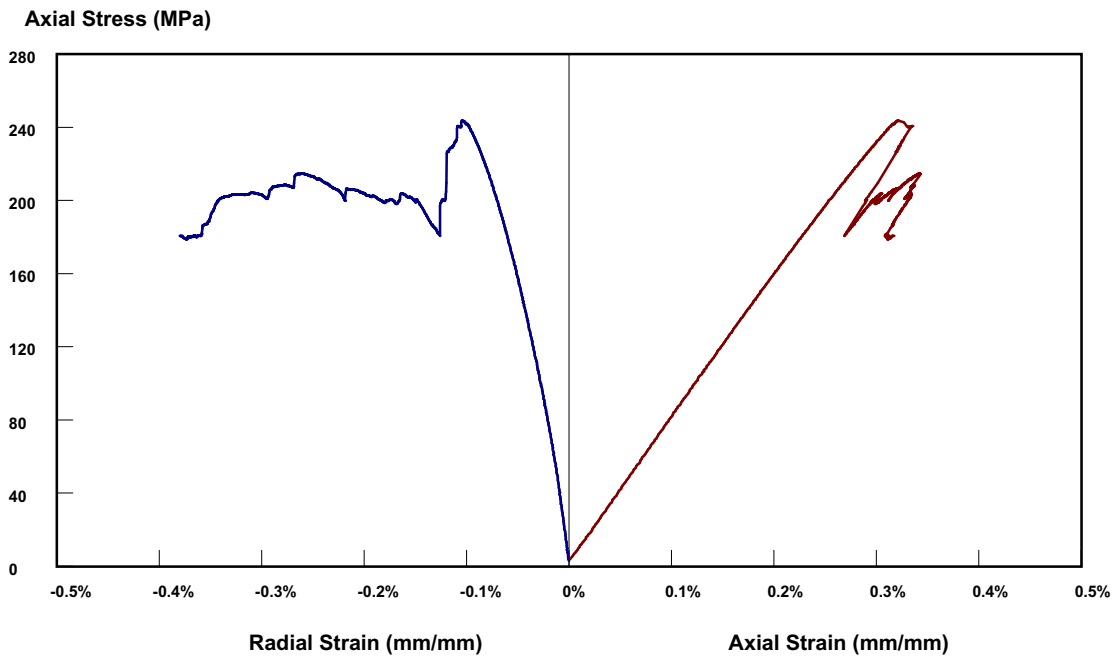
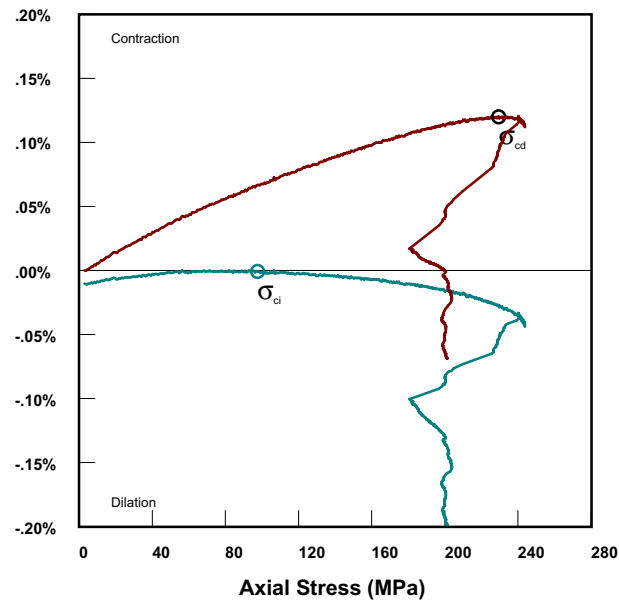
Specimen Data

Site:	Äspö	Diameter:	50.86 mm
Rock Type:		Length/Diameter:	2.75
Hole:	KQ0064G07	Density:	2717 kg/m ³
Depth:	5.38	Porosity:	
		Test Saturation:	

Test Results

Young's Modulus:	72.8 GPa	Peak Strength:	131.7 MPa
Poisson's Ratio:	0.27	Crack Damage Stress:	56.0 MPa
		Crack Initiation Stress:	

Triaxial Test of KQ0064G01 - 5.44

**Failure Pattern****Volumetric Strain (mm³/mm³)****Test Data**

Client:	SKB	Test Date:	2003-09-25
Order Number:	9376	Loading Control:	Radial Strain Rate
Test:	Triaxial	Equivalent Loading Rate:	0.75 MPa/s
Equipment:	MTS 815	Confining Stress:	1 MPa

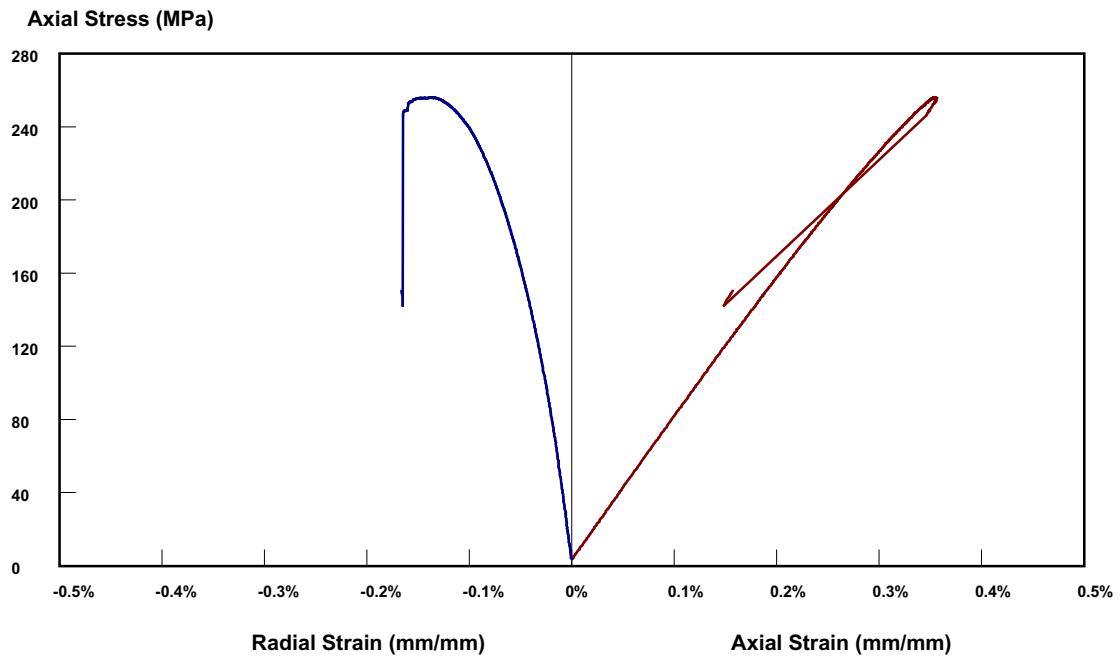
Specimen Data

Site:	Äspö	Diameter:	50.7 mm
Rock Type:		Length/Diameter:	2.74
Hole:	KQ0064G01	Density:	2716 kg/m ³
Depth:	5.44	Porosity:	
		Test Saturation:	

Test Results

Young's Modulus:	79.1 GPa	Peak Strength:	243.5 MPa
Poisson's Ratio:	0.26	Crack Damage Stress:	229.5 MPa
		Crack Initiation Stress:	97.6 MPa

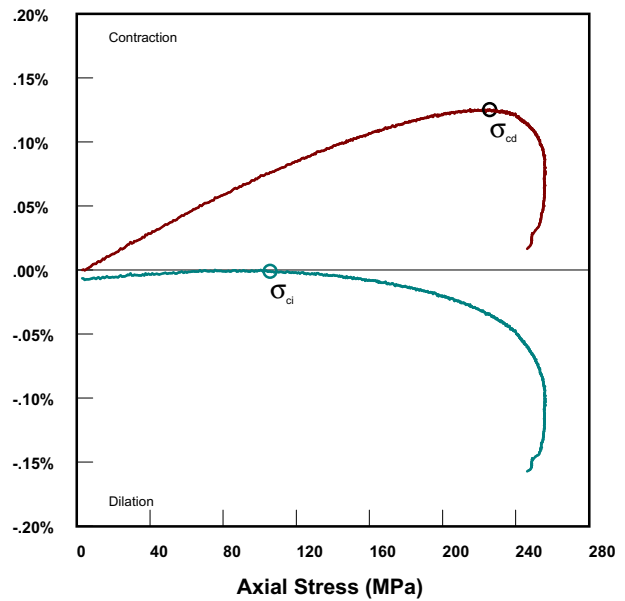
Triaxial Test of KQ0065G01 - 7.53



Failure Pattern



Volumetric Strain (mm³/mm³)



Test Data

Client:	SKB	Test Date:	2003-09-25
Order Number:	9376	Loading Control:	Radial Strain Rate
Test:	Triaxial	Equivalent Loading Rate:	0.75 MPa/s
Equipment:	MTS 815	Confining Stress:	1 MPa

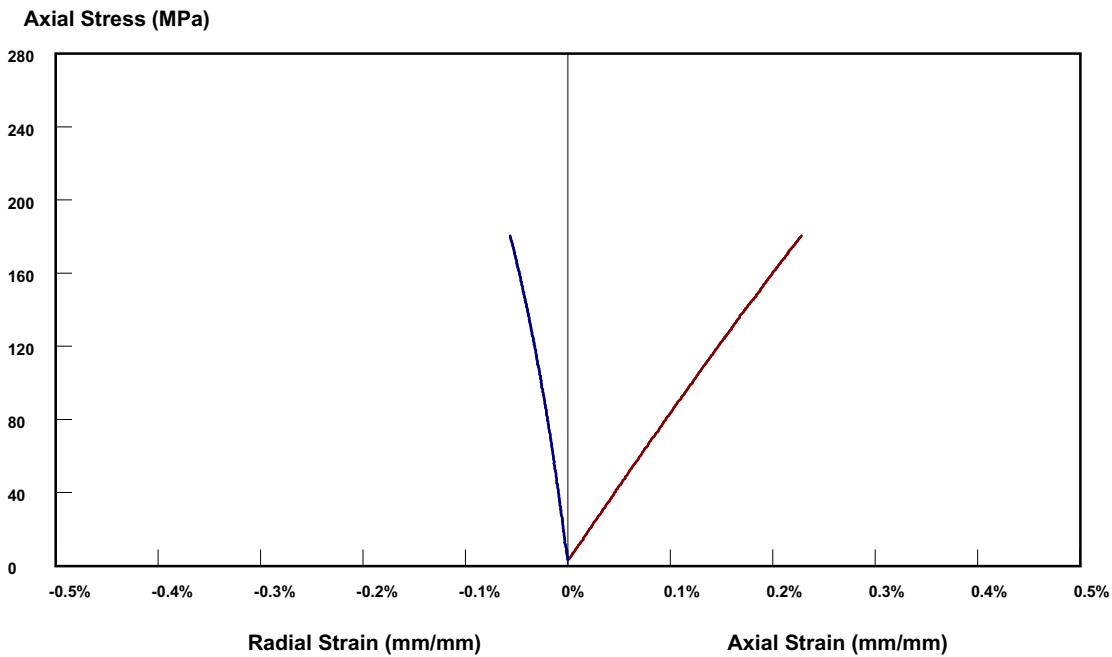
Specimen Data

Site:	Äspö	Diameter:	50.83 mm
Rock Type:		Length/Diameter:	2.74
Hole:	KQ0065G01	Density:	2732 kg/m ³
Depth:	7.53	Porosity:	
		Test Saturation:	

Test Results

Young's Modulus:	77.3 GPa	Peak Strength:	255.9 MPa
Poisson's Ratio:	0.23	Crack Damage Stress:	225.7 MPa
		Crack Initiation Stress:	105.7 MPa

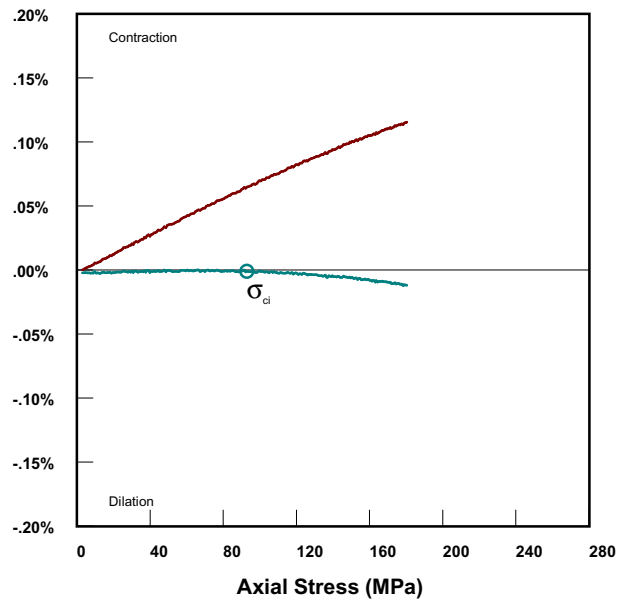
Triaxial Test of KQ0064G07 - 5.13



Failure Pattern



Volumetric Strain (mm³/mm³)



Test Data

Client:	SKB	Test Date:	2003-09-25
Order Number:	9376	Loading Control:	Radial Strain Rate
Test:	Triaxial	Equivalent Loading Rate:	0.75 MPa/s
Equipment:	MTS 815	Confining Stress:	1 MPa

Specimen Data

Site:	Äspö	Diameter:	50.84 mm
Rock Type:		Length/Diameter:	2.75
Hole:	KQ0064G07	Density:	2725 kg/m ³
Depth:	5.13	Porosity:	
		Test Saturation:	

Test Results

Young's Modulus:	79.9 GPa	Peak Strength:	180.8 MPa
Poisson's Ratio:	0.22	Crack Damage Stress:	00.0 MPa
		Crack Initiation Stress:	93.0 MPa

AE-MEASUREMENT INTERPRETATION FOR SKB SPECIMENS

Background

The results are presented as cumulative number of acoustic emission (AE) events versus axial stress. The events are classified based on event energy. The energy bands are defined so that the number of events in each band is approximately 30%, 30%, 30%, 5% and 5% i.e. the total number of events below energy limits are 30%, 60%, 90%, 95% and 100%. The cumulative number of AE events in energy bands are presented in linear scale while sum of all bands is presented in logarithmic scale. Two figures are presented: the first (a) scaled to show all events and the second (b) to show only the first big events.

Based on previous tests with Finnish granitic and gneissic rocks the following pre-failure AE phases are commonly observed:

- a) moderate amount of small or medium energy events in the beginning of loading, probably caused mainly by settling of specimen ends and closing/shearing of open micro fractures.
- b) if settling ramp is done, as in these tests, quiet unloading and reloading
- c) quiet elastic loading
- d) onset of small or medium energy events *i.e. crack initiation*
- e) stable crack growth i.e. cumulative number of events is increasing 'linearly' with loading
- f) onset of high energy events = beginning of destruction
- g) onset of unstable crack growth i.e. amount of events starts to increase exponentially with loading *i.e. crack damage*
- h) exponential increase of events with any energy at *peak strength*

Specimen KQ0064G01 - 6.26

Elastic phase starts around 20 MPa but small energy damaging continues. Crack initiation stress is about 135. Crack damage stress is around 210 MPa.

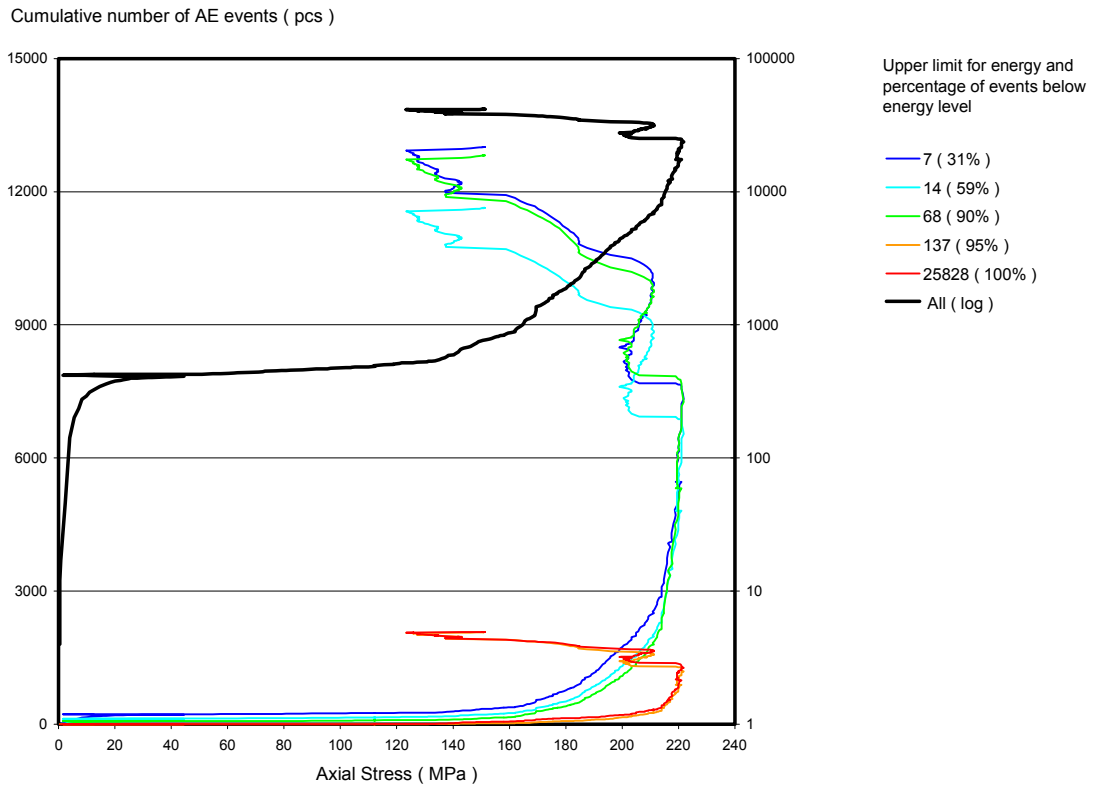


Figure 1a. Cumulative number of acoustic emission events in energy bands as a function of axial stress for specimen KQ0064G01 - 6.26.

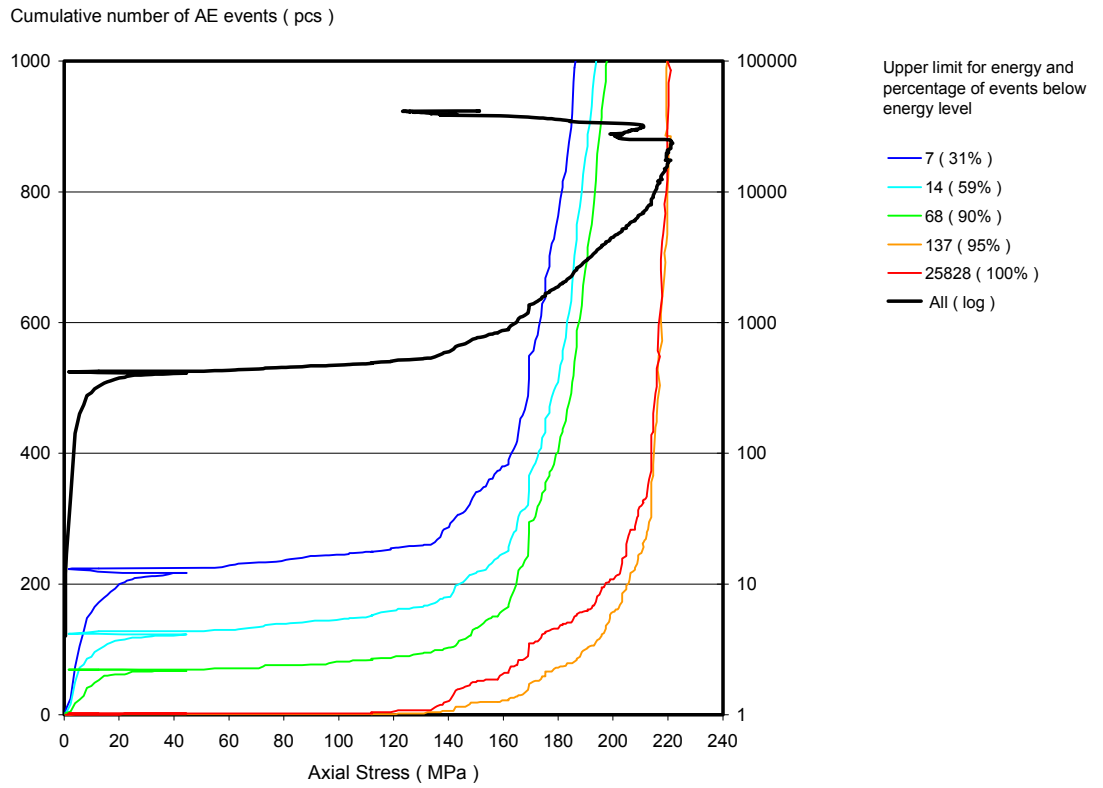


Figure 1b. Cumulative number of acoustic emission events in energy bands as a function of axial stress for specimen KQ00064G01 – 6.26, scale to show high-energy events.

Specimen KQ0065G01 – 7.37

Cracking initiates around 80 MPa and turns immediately to sudden crack damage at about 185 MPa.

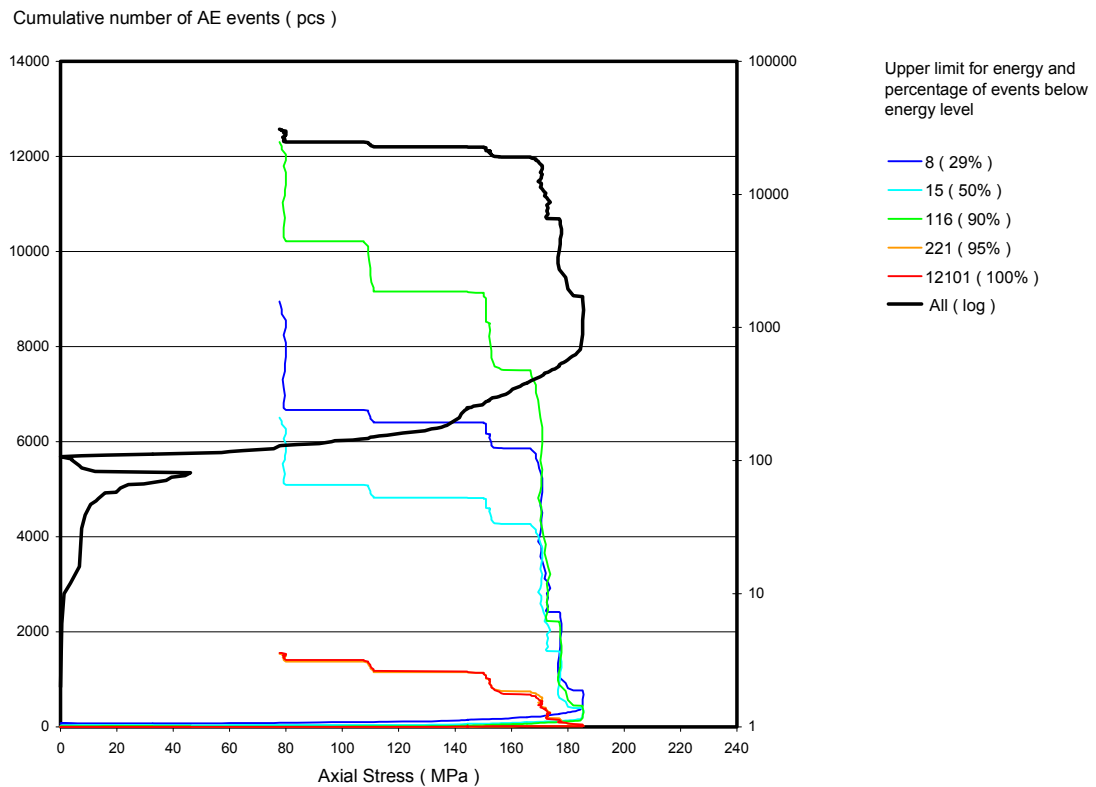


Figure 2a. Cumulative number of acoustic emission events in energy bands as a function of axial stress for specimen KQ0065G01 – 7.37.

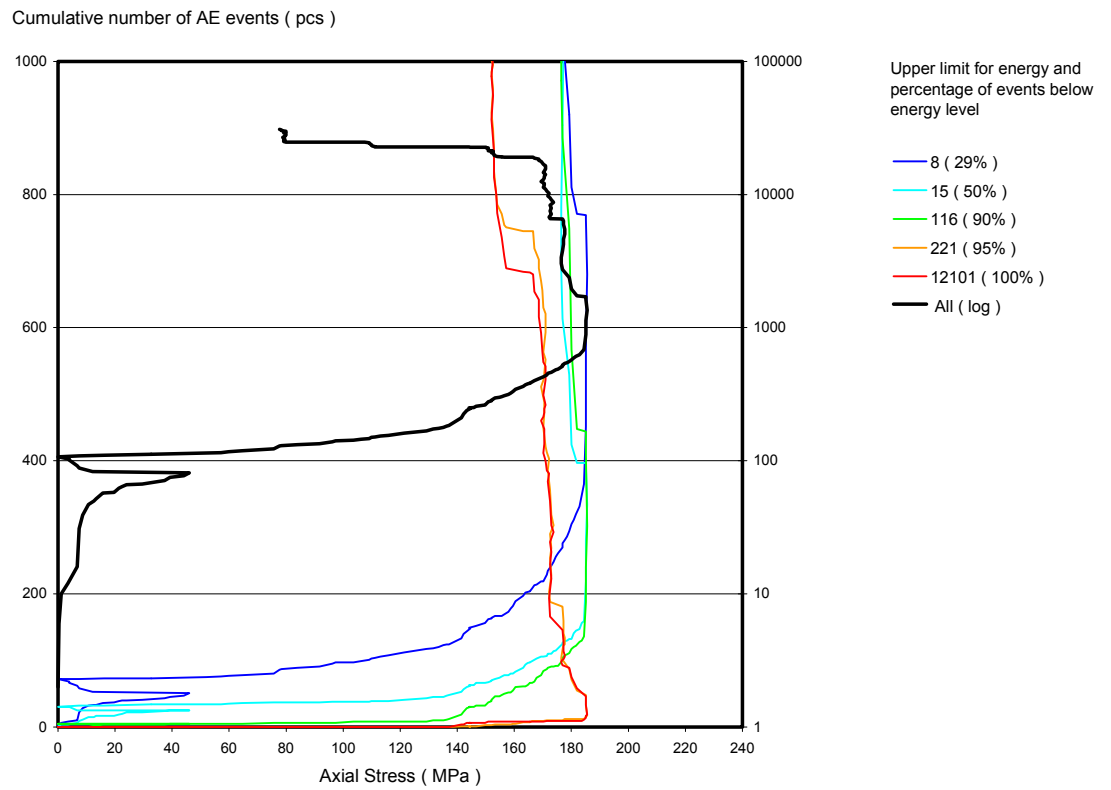


Figure 2b. Cumulative number of acoustic emission events in energy bands as a function of axial stress for specimen KQ0065G01 – 7.37, scale to show high-energy events.

Specimen KQ0065G01 – 5.29

Elastic phase starts around 20 MPa but small energy damaging continues. Crack initiation stress is about 130 MPa. Crack damage stress is around 215 MPa.

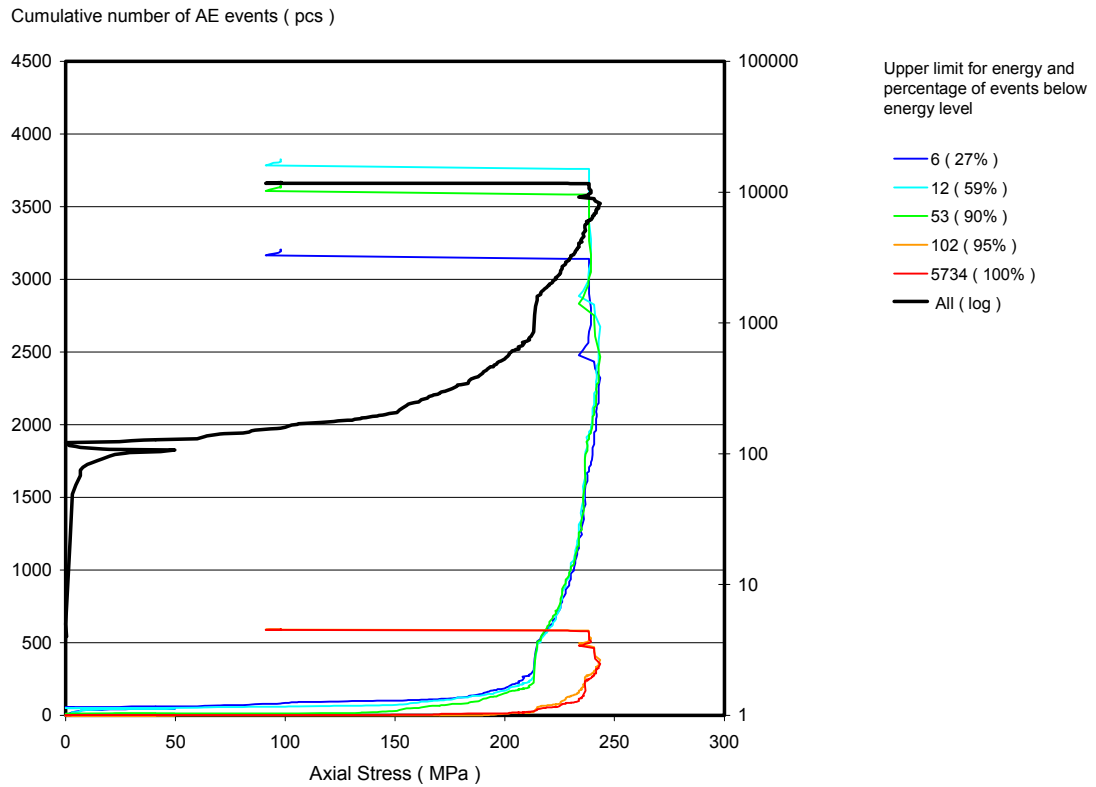


Figure 3a. Cumulative number of acoustic emission events in energy bands as a function of axial stress for specimen KQ0065G01 – 5.29.

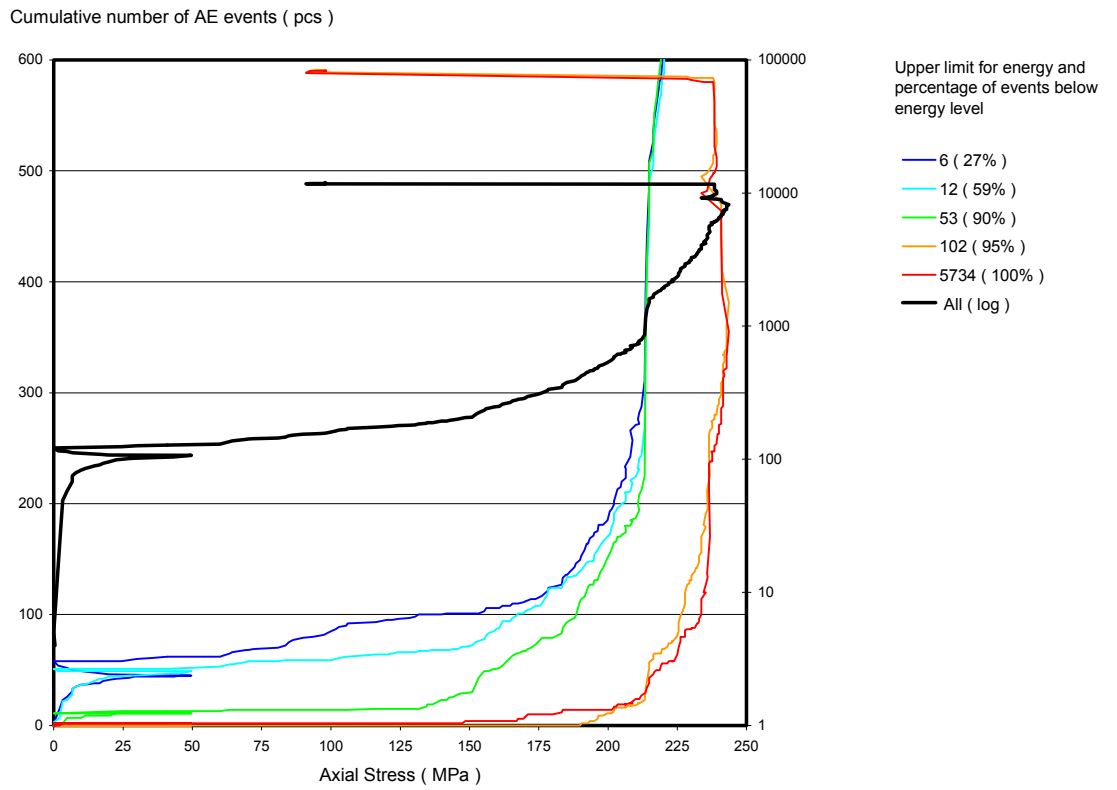


Figure 3b. Cumulative number of acoustic emission events in energy bands as a function of axial stress for specimen KQ0065G01 – 5.29, scale to show high-energy events.

Specimen KQ0065G01 – 5.43

Clear elastic phase starts around 10 MPa. Crack initiation stress is about 100 MPa. Crack damage stress is not obvious, but somewhere around 220 MPa.

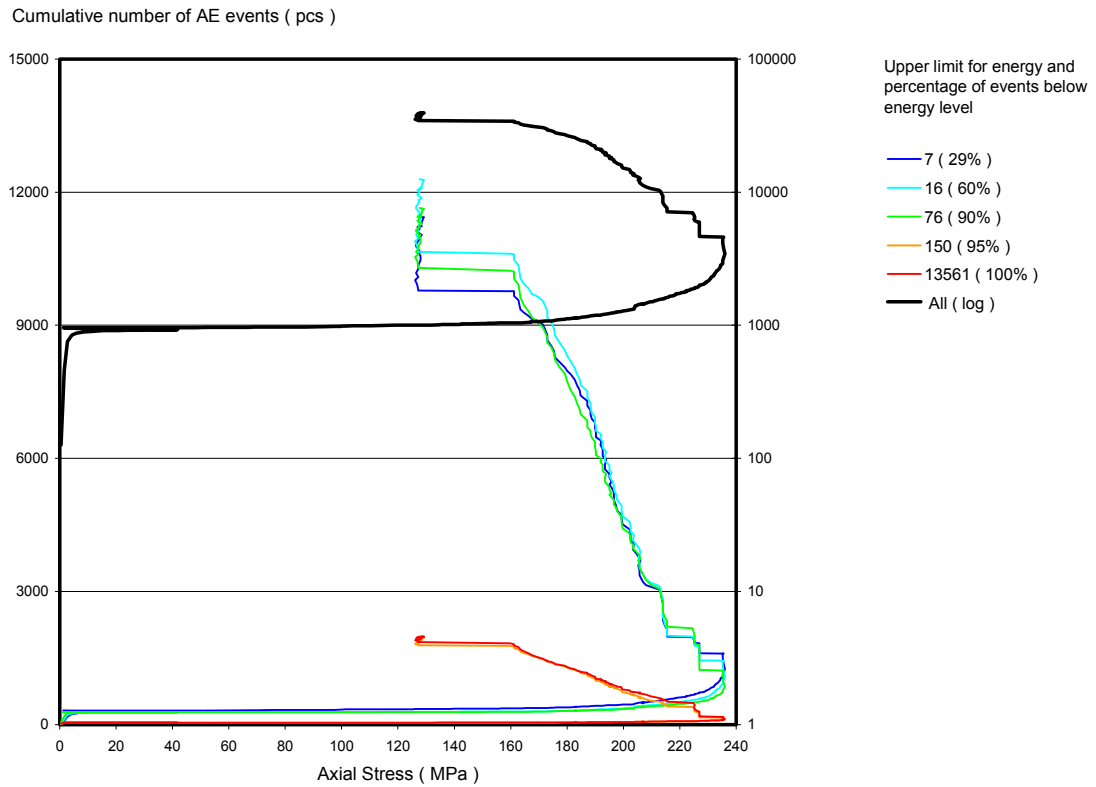


Figure 4a. Cumulative number of acoustic emission events in energy bands as a function of axial stress for specimen KQ0065G01 – 5.43.

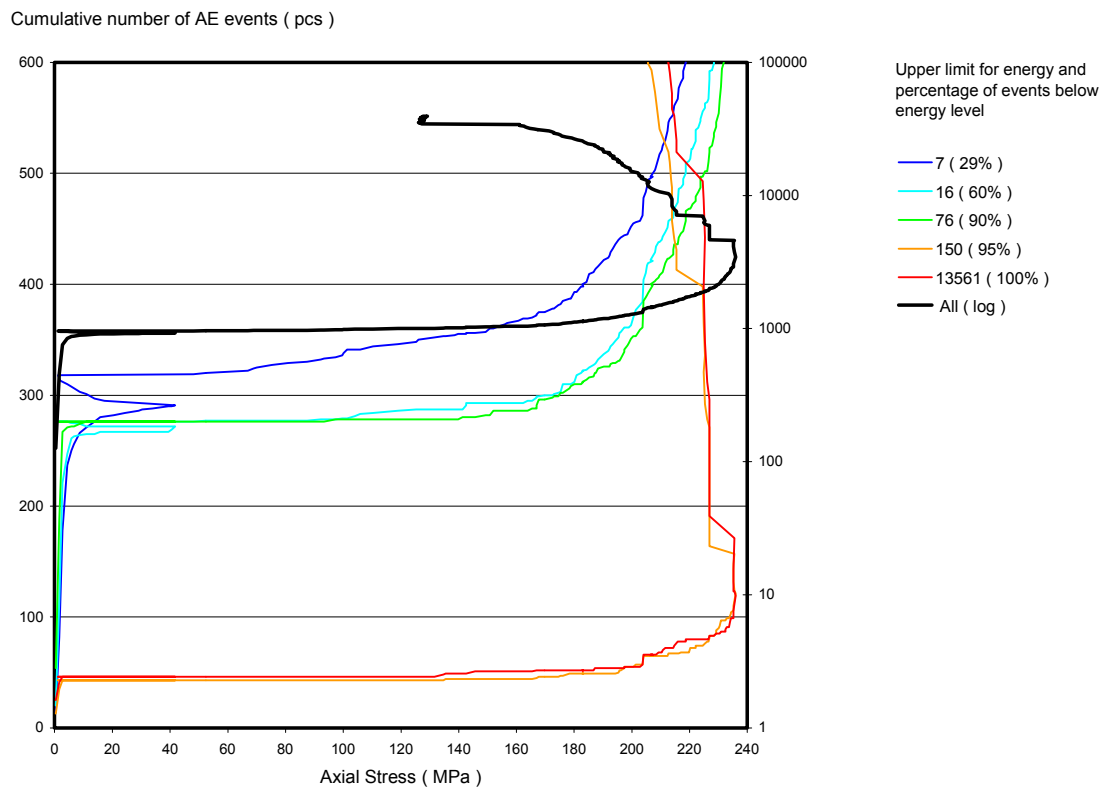


Figure 4b. Cumulative number of acoustic emission events in energy bands as a function of axial stress for specimen KQ0065G01 – 5.43, scale to show high-energy events.

Specimen KQ0064G07 – 4.99

Acoustic emission data for this specimen is limited to one channel due to a bad contact in the microphone at the other channel. Elastic phase starts around 10 MPa. Crack initiation stress is about 160 MPa. Sudden crack damage coincides with peak strength around 190 MPa.

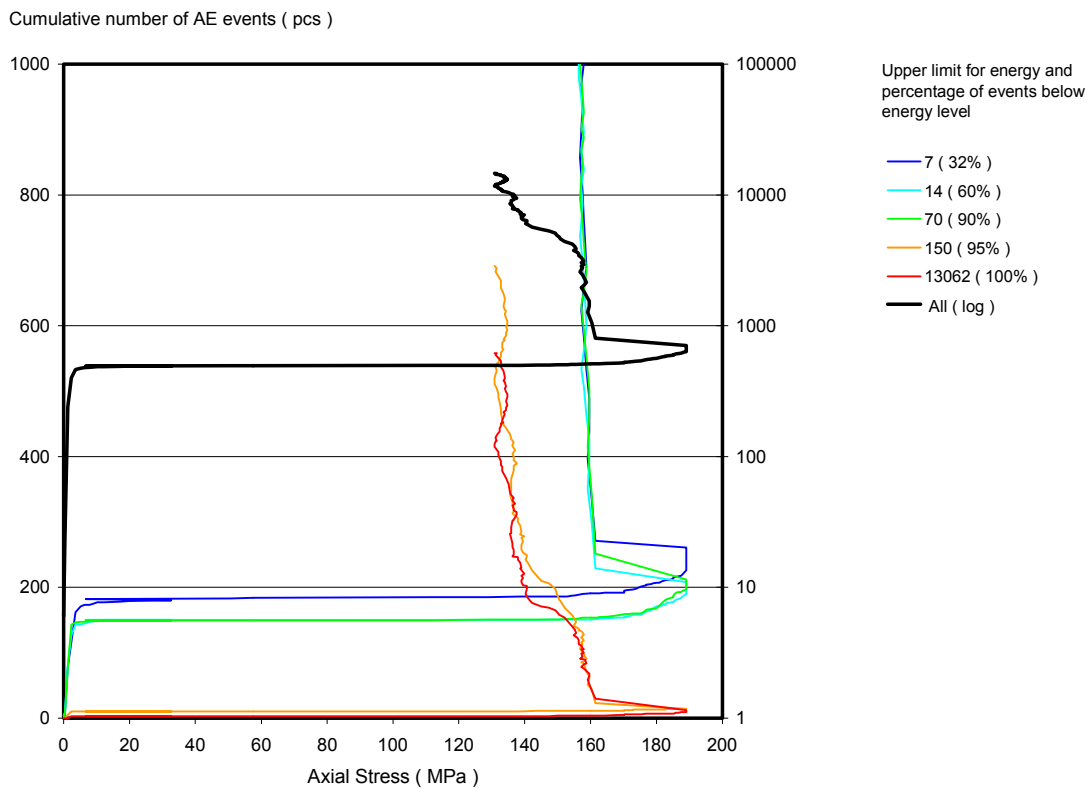


Figure 5a. Cumulative number of acoustic emission events in energy bands as a function of axial stress for specimen KQ0064G07 – 4.99.

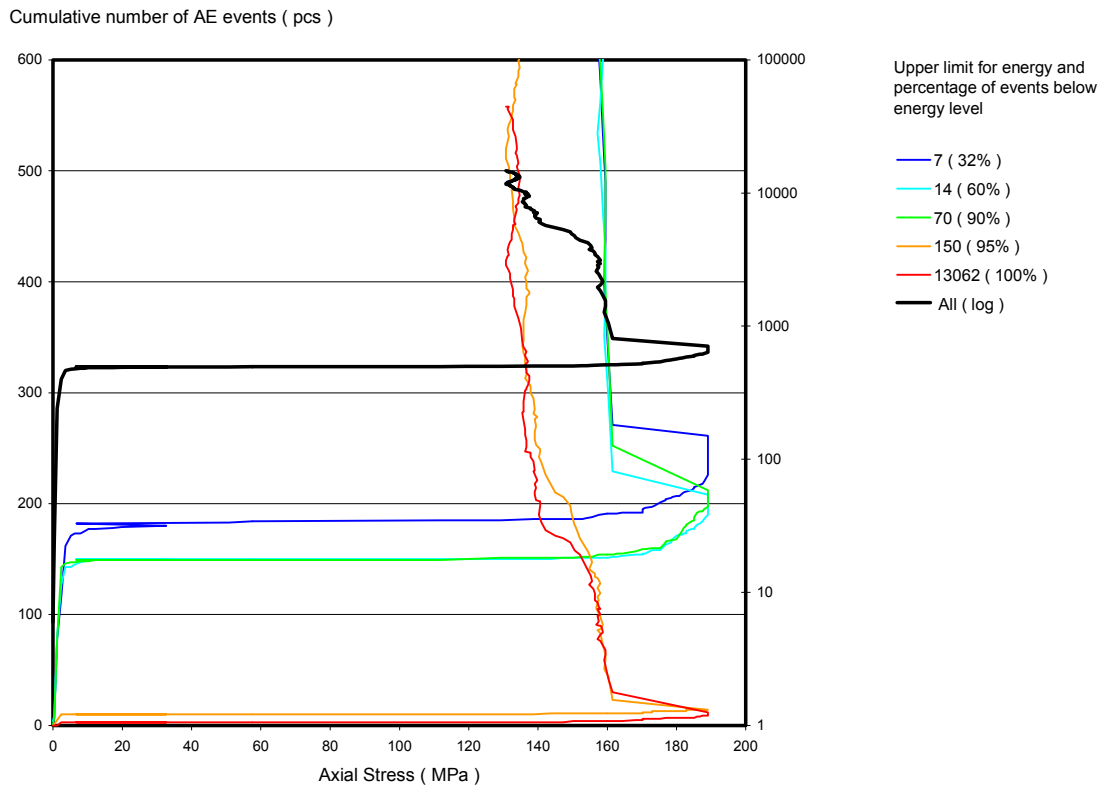


Figure 5b. Cumulative number of acoustic emission events in energy bands as a function of axial stress for specimen KQ0064G07 – 4.99, scale to show high-energy events.

Specimen KQ0064G07 – 5.38

A pre-existing fracture resulted in an unstable behaviour of the specimen. Elastic phase starts around 10 MPa. Crack initiation stress is about 50 MPa coinciding with the first high-energy events (evidently the pre-existing fracture is failing). Crack damage is around 115 MPa.

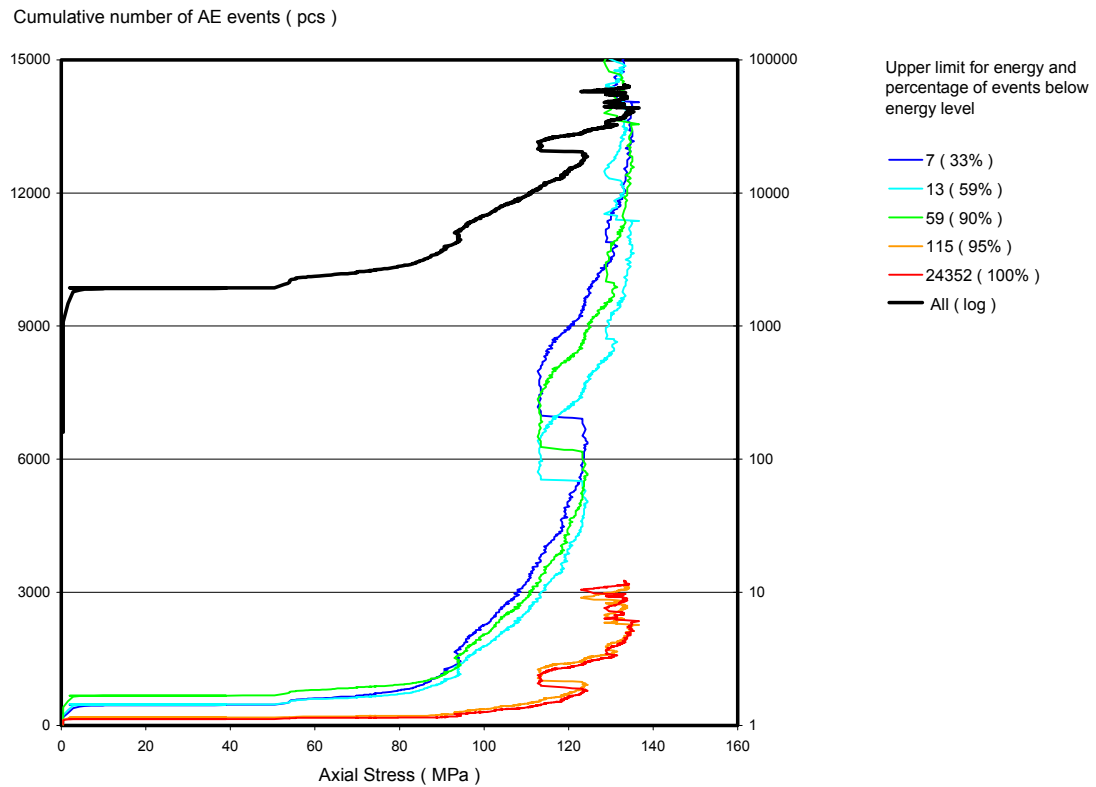


Figure 6a. Cumulative number of acoustic emission events in energy bands as a function of axial stress for specimen KQ0064G07 –5.38.

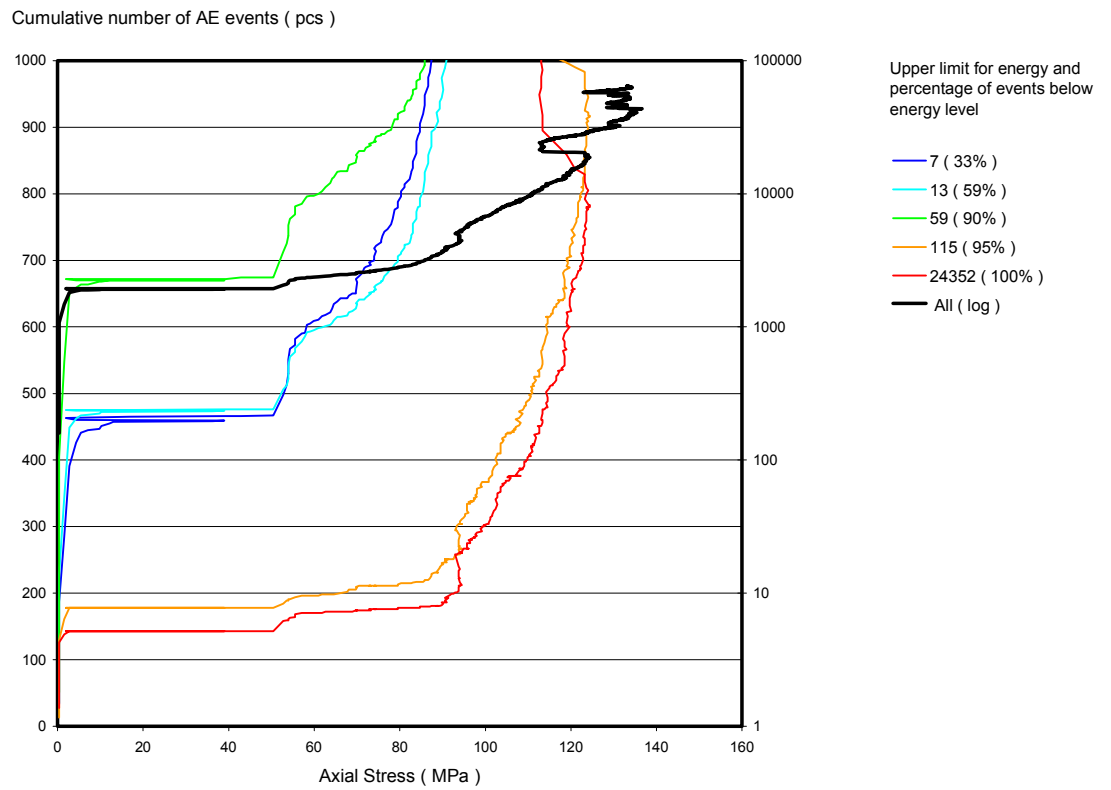


Figure 6b. Cumulative number of acoustic emission events in energy bands as a function of axial stress for specimen KQ0064G07 – 5.38, scale to show high-energy events.

Laboratory tests report for measurement of coefficient of thermal expansion, density and porosity

Äspö Hard Rock Laboratory (HRL)

KQ0064G01 and KQ0064G05

Coefficient of thermal expansion of rock – using an extensometer

Determination of density and porosity

Urban Åkesson

Swedish National Testing and Research Institute, SP

October 2003

Keywords: Rock, Coefficient of thermal expansion, Density, Porosity.

Abstract

The coefficient of thermal expansion, density and porosity has been determined on three specimens; two sampled from drill hole KQ0064G01 and one from KQ0064G05. The rock type in KQ0064G01 is an isotropic medium-grained grey diorite with phenocrysts consisting of K-feldspar. The rock type in KQ0064G05 is an isotropic medium-grained red diorite. The coefficient of thermal expansion has been determined between the temperature intervals 20–40, 40–60, and 60–80°C. The results indicated that the thermal expansion was almost linear and the coefficient of thermal expansion in the temperature interval 20–80°C was calculated to be 7×10^{-6} mm/mm°C for all specimens. The wet density and porosity range between 2,750–2,760 kg/m³ and 0.2–0.4% respectively.

Contents

1	Introduction	128
2	General information	129
2.1	Description of the samples	129
2.2	Equipment	129
2.3	Execution	129
3	Results	130
3.1	Description and presentation of the specimen	130
3.2	Results for the entire test series	133
	References	133
	Appendix 1	134
	Appendix 2	139

1 Introduction

The purpose is to determine the linear coefficient of thermal expansion for rock cores in water-saturated condition between +20–80°C. and the specimen's density and porosity.

The cores are sampled from two boreholes in the Äspö area, called KQ0064G01 and KQ0064G05. It was sampled 28 August 2003 by Christer Andersson, Swedish Nuclear Fuel and Waste Management Co (SKB) and delivered to The Swedish National Testing and Research Institute (SP). The rock cores arrived to SP 2 September 2003. The testing were performed during September and October 2003 (see Appendix 1).

Determination of the coefficient of thermal expansion was made in accordance with SKB's method description SKB MD 191.002 version 2.0. The wet density and porosity was determined in accordance with the SKB MD 160.002 version 2.0. The department of Building Technology and Mechanics (BM) at SP performed the test.

2 General information

2.1 Description of the samples

From the Äspö Hard Rock Laboratory (HRL), Oskarshamn, Sweden were two cores sampled from borehole KQ0064G01 and KQ0064G05. The bore holes starts at a depth of 450 m. Three specimens, with a length of 250 mm were sampled from the two rock cores. SP made this sampling. Table D-1 show the rock type and identification marks of the specimens.

Table D-1. Rock type and identification marks (The rock type identification was made by SP).

Rock type	Identification (rock core secup-seclow)
Diorite, grey	KQ0064G01 6.60–6.85
Diorite, grey	KQ0064G01 6.85–7.10
Diorite, red (with chlorite veins)	KQ0064G05 5.77–6.01

2.2 Equipment

Following equipment have been used for the analyses:

- Extensometer (DEMEC inv no 102266) for measurements of the thermal expansion.
- Reference bar in invar steel for calibrate the extensometer.
- Heating chamber (inv no 102284) with an accuracy of $\pm 0.7^{\circ}\text{C}$ at 80°C for heating up the specimens.
- A covered plastic box filled with water for keeping the specimens water saturated.

2.3 Execution

The execution procedure followed the prescription in SKB MD 191.002 version 2.0 and SKB MD 160.002 version 2.0. and the following steps were performed:

Moment	Activity
1	The specimens were cut according to the marks on the rock cores.
2	Two measuring points with a distance of 200 mm were glued on the specimens.
3	The specimens were photographed in JPEG-format.
4	The dry weight was measured.
5	The specimens were water saturated for 72 h.
6	The dry density was determined (see Appendix 4).
7	The wet density was determined (see Appendix 4).
8	The coefficient of thermal expansion was determined. The coefficient of thermal expansion was determined between 20–40, 40–60, 60–80, 20–60 and 20–80°C. On each temperature level was three measurements done with 24 h intervals in order to know that the expansion was completed for each temperature level (see Appendix 2). The uncertainty in the measurement is $\pm 3.97 \times 10^{-6}$ mm/mm (strain) which for these samples equals an uncertainty of the coefficient of thermal expansion of $\pm 0.2 \times 10^{-6}$ mm/mm°C for a temperature difference of 20 degrees C. Calibration of the instrument was done before the measurements on every new temperature (see Appendix 3).

3 Results

3.1 Description and presentation of the specimen

The temperature of water for water saturation was 21.6°C and the density of the water was 998 kg/m³.

KQ0064G01 6.60–6.85

Specimen KQ0064G01 6.60–6.85 had a dry density of 2,740 kg/m³ and a wet density of 2,750 kg/m³. The porosity was calculated to be 0.4%.

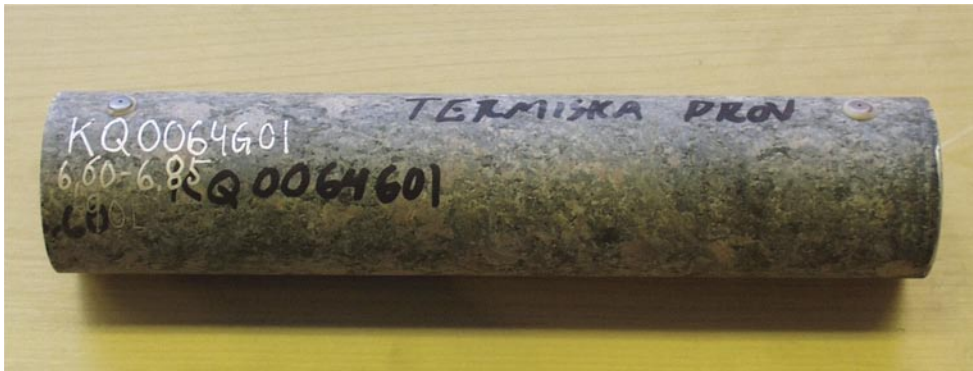


Figure D-1. Specimen KQ0064G01 6.60–6.85.

Table D-2. Coefficient of thermal expansion of specimen KQ0064G01 6.60–6.85.

Temperature	20–40°C (mm/mm°C)	20–60°C (mm/mm°C)	20–80°C (mm/mm°C)	40–60°C (mm/mm°C)	60–80°C (mm/mm°C)
Measure 1	6.2E–06	6.2E–06	6.6E–06	6.2E–06	7.3E–06
2	7.1E–06	6.6E–06	6.9E–06	6.0E–06	7.5E–06
3	7.3E–06	6.6E–06	6.9E–06	5.8E–06	7.5E–06
Median	7.1E–06	6.6E–06	6.9E–06	6.0E–06	7.5E–06

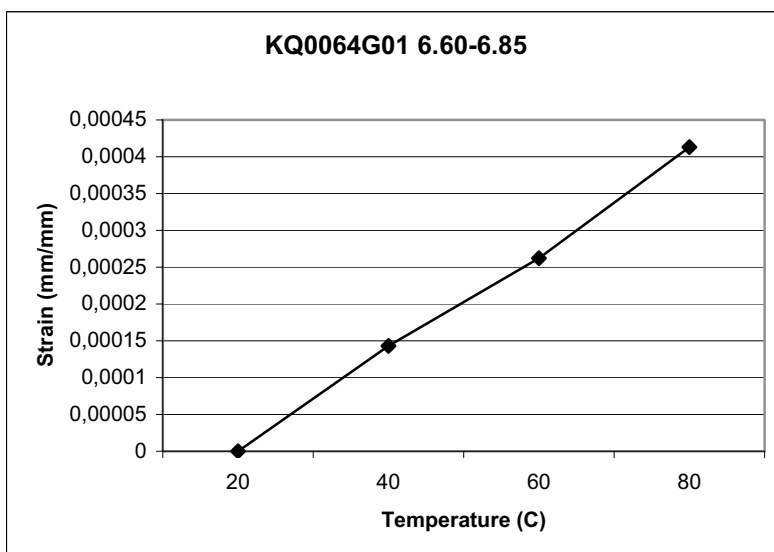


Figure D-2. Thermal expansion for specimen KQ0064G01 6.60–6.85 (median values plotted).

KQ0064G01 6.85–7.10

Specimen KQ0064G01 6.85–7.10 had a dry density of 2,750 kg/m³ and a wet density of 2,760 kg/m³. The porosity was calculated to be 0.4%.

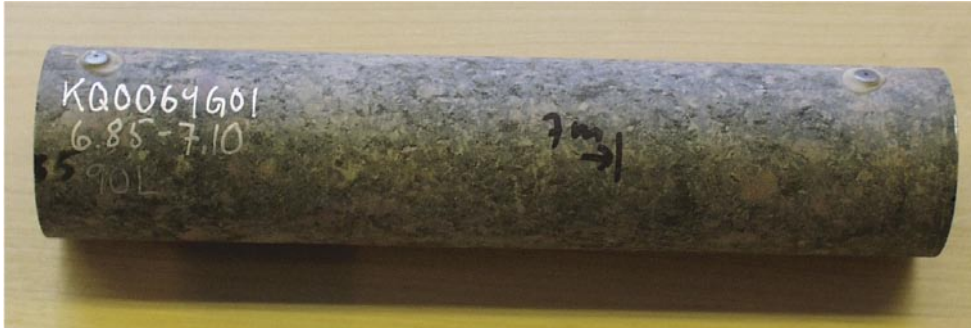


Figure D-3. Specimen KQ0064G01 6.85–7.10.

Table D-3. Coefficient of thermal expansion of specimen KQ0064G01 6.85–7.10.

Temperature	20–40°C (mm/mm°C)	20–60°C (mm/mm°C)	20–80°C (mm/mm°C)	40–60°C (mm/mm°C)	60–80°C (mm/mm°C)
Measure 1	6.2E–06	6.3E–06	7.1E–06	6.4E–06	8.7E–06
2	6.7E–06	6.8E–06	7.1E–06	6.9E–06	7.5E–06
3	6.7E–06	6.6E–06	7.1E–06	6.6E–06	7.9E–06
Median	6.7E–06	6.6E–06	7.1E–06	6.6E–06	7.9E–06

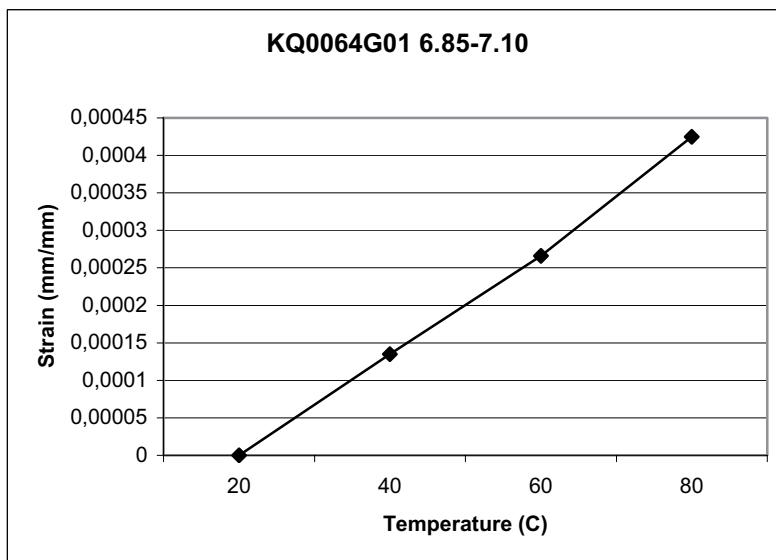


Figure D-4. Thermal expansion for specimen KQ0064G01 6.85–7.10 (median values plotted).

KQ0064G05 5.77-6.01

Specimen KQ0064G05 5.77-6.01 had a dry density of 2,750 kg/m³ and a wet density of 2,750 kg/m³. The porosity was calculated to be 0.2%.



Figure D-5. Specimen KQ0064G05 5.77-6.01.

Table D-4. Coefficient of thermal expansion of specimen KQ0064G05 5.77-6.01.

Temperature	20-40°C (mm/mm°C)	20-60°C (mm/mm°C)	20-80°C (mm/mm°C)	40-60°C (mm/mm°C)	60-80°C (mm/mm°C)
Measure 1	7.1E-06	6.5E-06	7.4E-06	5.8E-06	9.3E-06
2	8.1E-06	7.3E-06	7.1E-06	6.6E-06	6.7E-06
3	8.3E-06	7.3E-06	6.9E-06	6.4E-06	6.0E-06
Median	8.1E-06	7.3E-06	7.1E-06	6.6E-06	6.7E-06

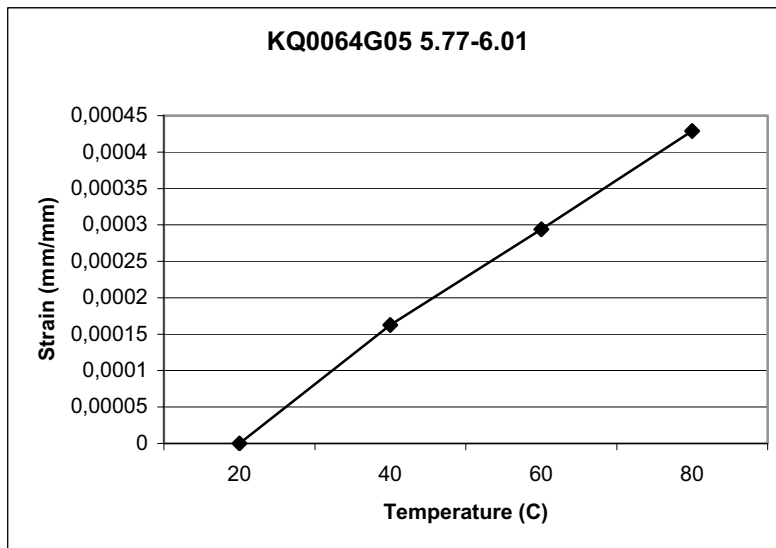


Figure D-6. Thermal expansion for specimen KQ0064G05 5.77-6.01 (median values plotted).

3.2 Results for the entire test series

Table D-5. Summary of the results of the porosity dry and wet densities for the investigated specimens, measured in water temperature 21.6°C.

Specimen	Porosity (%)	Dry density (kg/m ³)	Wet density (kg/m ³)
KQ0064G01 6.60–6.85	0.35	2,740	2,750
KQ0064G01 6.85–7.10	0.36	2,750	2,760
KQ0064G05 5.77–6.01	0.15	2,750	2,750

Table D-6. Summary of the coefficient of thermal expansion for the investigated specimens (median values).

Temperature	20–40°C (mm/mm°C)	20–60°C (mm/mm°C)	20–80°C (mm/mm°C)	40–60°C (mm/mm°C)	60–80°C (mm/mm°C)	Rock type
KQ0064G01 6.60–6.85	7.1E–06	6.6E–06	6.9E–06	6.0E–06	7.5E–06	Diorite, grey
KQ0064G01 6.85–7.10	6.7E–06	6.6E–06	7.1E–06	6.6E–06	7.9E–06	Diorite, grey
KQ0064G05 5.77–6.01	8.1E–06	7.3E–06	7.1E–06	6.6E–06	6.7E–06	Diorite, red

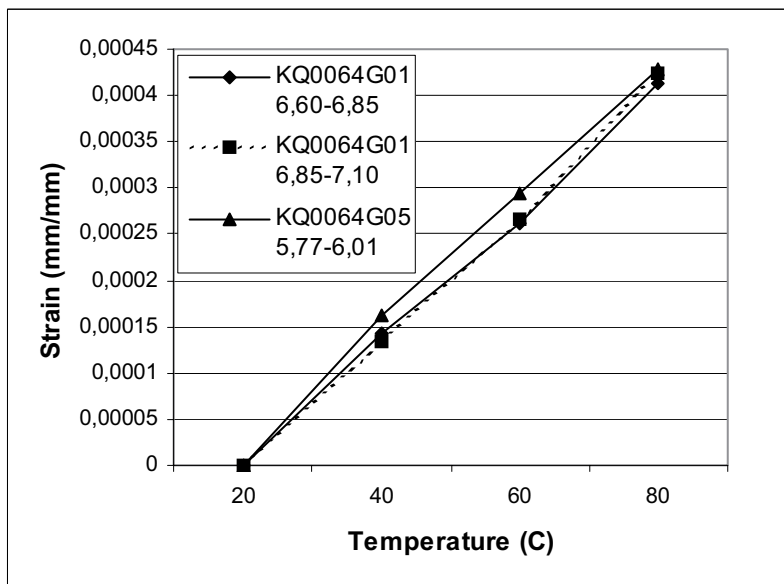


Figure D-7. Thermal expansion for the investigated specimens (median values plotted).

References

SKB MD 191.002 Version 2.0. Method description for coefficient of thermal expansion of rock – using an extensometer.

SKB MD 160.002 Version 2.0. Method description for determining the density and porosity of intact rock.

SP-QD 13.1. Verksamhetsmanual projekt SKB.

Appendix 1

Beräkning av längdutvidgningskoefficient

Längdutvidgningskoefficient

Uppdragsnummer: P303123

Provningsmetod: NT BUILD 479

100% fuktighet temperaturintervall +20, 40, 60, 80C

1 skaldel motsvarar 3,97 mikrostrain = $3,97 \times 10^{-6}$ strain

Borrhåll/nivå:

Delta l = längdförändringen i mm = strain * l

Prov id	Skalvärde start 20C 2003-09-15	Skalvärde vid mätning 60C 2003-09-25	Differens skaldelar	Strain (mm/mm)	Delta l	l	Längdutvidgningskoeff mm/mm per grader C	Längdutr mm/mm
KQ0064G01	6,60–6,85	111	99	0,00039303	0,078606	200,0	0,00000655	0,000393
KQ0064G01	6,85–7,10	18	107	0,00042479	0,084958	200,0	0,00000708	0,000425
KQ0064G05	5,77–6,01	100	112	0,00044464	0,088928	200,0	0,00000741	0,000445

Längdutvidgningskoefficient

Uppdragsnummer: P303123

Provningsmetod: NT BUILD 479

100% fuktighet temperaturintervall +20, 40, 60, 80C

1 skaldel motsvarar 3,97 mikrostrain = $3,97 \times 10^{-6}$ strain

Borrhåll/nivå:

Delta l = längdförändringen i mm = strain * l

Prov id	Skalvärde start 20C 2003-09-15	Skalvärde vid mätning 60C 2003-09-26	Differens skaldelar	Strain (mm/mm)	Delta l	l	Längdutvidgningskoeff mm/mm per grader C	Längdutr mm/mm
KQ0064G01	6,60–6,85	116	104	0,00041288	0,082576	200,0	0,00000688	0,000413
KQ0064G01	6,85–7,10	18	107	0,00042479	0,084958	200,0	0,00000708	0,000425
KQ0064G05	5,77–6,01	100	108	0,00042876	0,085752	200,0	0,00000715	0,000429

Längdutvidgningskoefficient

Uppdragsnummer: P303123

Provningmetod: NT BUILD 479

100% fuktighet temperaturintervall +20, 40, 60, 80C

1 skaldel motsvarar 3,97 mikrostrain = $3,97 \times 10^{-6}$ strain

Borrhål/nivå:

Delta l = längdförändringen i mm = strain x l

Prov id	Skalvärde start 20C 2003-09-15	Skalvärde vid mätning 60C 2003-09-29	Differens skaldelar	Strain (mm/mm)	Delta l	l	Längdutvidgningskoeff mm/mm per grader C	Längdutr mm/mm
KQ0064G01 6,60-6,85	12	116	104	0,00041288	0,082576	200,0	0,00000688	0,000413
KQ0064G01 6,85-7,10	-89	18	107	0,00042479	0,084958	200,0	0,00000708	0,000425
KQ0064G05 5,77-6,01	100	204	104	0,00041288	0,082576	200,0	0,00000688	0,000413

Sammanställning längdutvidgningskoefficient

Uppdragsnummer: p303123

Längdutvidgningskoefficient (mm/mm°C)

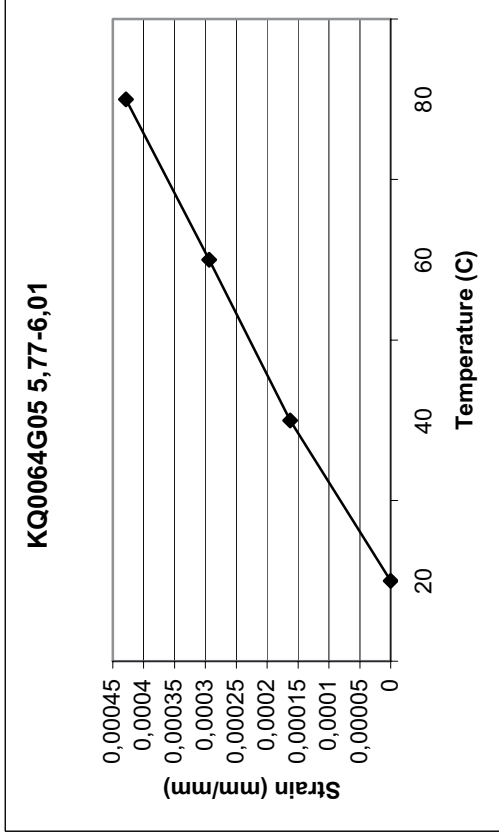
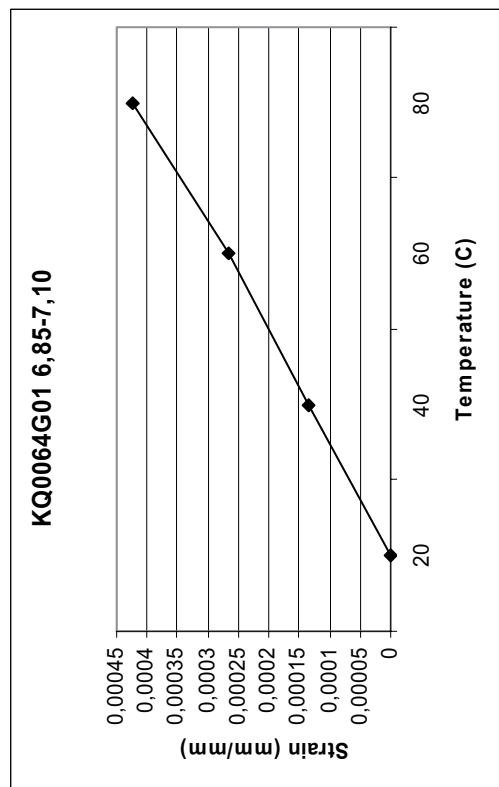
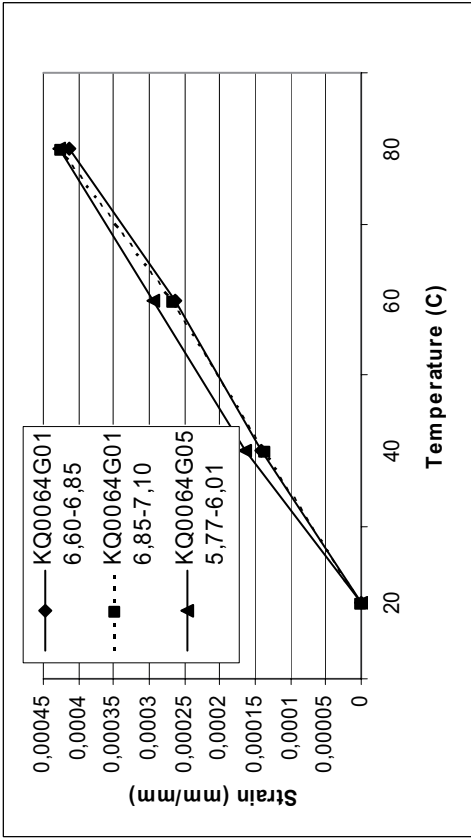
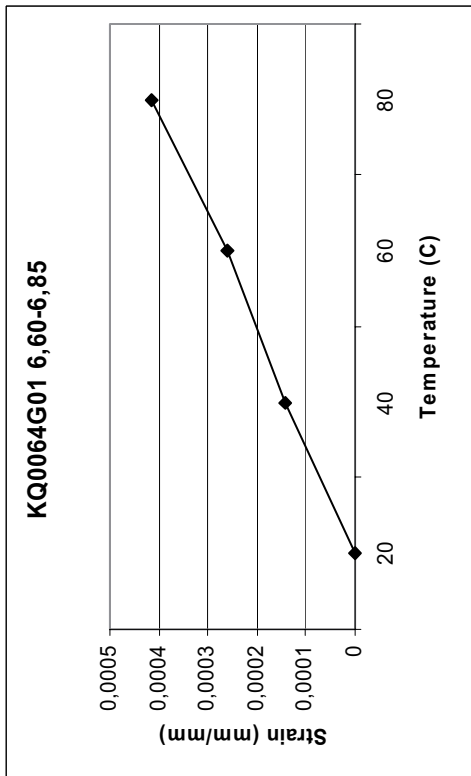
Temperatur	20–40°C (mm/mm°C)	20–60°C (mm/mm°C)	20–80°C (mm/mm°C)	40–60°C (mm/mm°C)	60–80°C (mm/mm°C)
KQ0064G01 6,60–6,85	6,2E–06	6,2E–06	6,6E–06	6,2E–06	7,3E–06
	7,1E–06	6,6E–06	6,9E–06	6,0E–06	7,5E–06
	7,3E–06	6,6E–06	6,9E–06	5,8E–06	7,5E–06
mean	6,9E–06	6,4E–06	6,8E–06	6,0E–06	7,5E–06
median	7,1E–06	6,6E–06	6,9E–06	6,0E–06	7,5E–06

Temperatur	20–40°C (mm/mm°C)	20–60°C (mm/mm°C)	20–80°C (mm/mm°C)	40–60°C (mm/mm°C)	60–80°C (mm/mm°C)
KQ0064G01 6,85–7,10	6,2E–06	6,3E–06	7,1E–06	6,4E–06	8,7E–06
	6,7E–06	6,8E–06	7,1E–06	6,9E–06	7,5E–06
	6,7E–06	6,6E–06	7,1E–06	6,6E–06	7,9E–06
mean	6,6E–06	6,6E–06	7,1E–06	6,6E–06	8,1E–06
median	6,7E–06	6,6E–06	7,1E–06	6,6E–06	7,9E–06

Temperatur	20–40°C (mm/mm°C)	20–60°C (mm/mm°C)	20–80°C (mm/mm°C)	40–60°C (mm/mm°C)	60–80°C (mm/mm°C)
KQ0064G05 5,77–6,01	7,1E–06	6,5E–06	7,4E–06	5,8E–06	9,3E–06
	8,1E–06	7,3E–06	7,1E–06	6,6E–06	6,7E–06
	8,3E–06	7,3E–06	6,9E–06	6,4E–06	6,0E–06
mean	7,9E–06	7,0E–06	7,1E–06	6,2E–06	7,3E–06
median	8,1E–06	7,3E–06	7,1E–06	6,6E–06	6,7E–06

Temperatur	20–40°C (mm/mm°C)	20–60°C (mm/mm°C)	20–80°C (mm/mm°C)	40–60°C (mm/mm°C)	60–80°C (mm/mm°C)
KQ0064G01 6,60–6,85	7,1E–06	6,6E–06	6,9E–06	6,0E–06	7,5E–06
KQ0064G01 6,85–7,10	6,7E–06	6,6E–06	7,1E–06	6,6E–06	7,9E–06
KQ0064G05 5,77–6,01	8,1E–06	7,3E–06	7,1E–06	6,6E–06	6,7E–06

Längdutvidgning (mm/mm)					
	20	40	60	80	
	0	0,00012307	0,0002461	0,000393	
		0,00014292	0,000262	0,00041288	
		0,00014689	0,000262	0,00041288	
		0,00013763	0,0002567	0,00040626	medel
KQ0064G01 6,60–6,85	0	0,00014292	0,000262	0,00041288	median
	0	0,00012307	0,0002501	0,00042479	
		0,00013498	0,0002739	0,00042479	
		0,00013498	0,000266	4,25E-04	
		0,00013101	0,0002633	0,00042479	medel
KQ0064G01 6,85–7,10	0	0,00013498	0,000266	0,00042479	median
	0	0,00014292	0,0002581	0,00044464	
		0,00016277	0,0002938	0,00042876	
		0,00016674	0,0002938	0,00041288	
		0,00015748	0,0002819	0,00042876	medel
KQ0064G05 5,77–6,01	0	0,00016277	0,0002938	0,00042876	median



Appendix 2

Beräkning densitet

Densitet och porositet, SKB

Uppdrags nr: P303123
Metod: prEN 13775
Provad av: mhs
Datum: 2003-09-15

Provmärkning:	Vikt i vatten, Msub (g)	Yttor vikt, Msat (g)	Torr vikt, Ms (g)	Bulk volym, V (cm ³)	Por volym, Vv (cm ³)	Porositet, n (%)	Torr densitet, pd (g/cm ³)	Våt densitet (g/cm ³)
1 KQ0064G05 5,77–6,01	836,97	1 314,31	1 313,59	478,34	0,72	0,15	2,746	2,748
2 KQ0064G01 6,60–6,85	850,85	1 336,2	1 334,51	486,37	1,69	0,35	2,744	2,747
3 KQ0064G01 6,85–7,10	839,97	1 317,13	1 315,4	478,16	1,73	0,36	2,751	2,755
Medel	842,597	1 322,547	1 321,167	480,960	1,383	0,287	2,747	2,750
std avvikelse	7,303	11,908	11,591	4,687	0,573	0,118	0,004	0,004

Vattnets temperature (°C): 21,6

Våg, inv.nr: 102084

Vattnets densitet (°C): 0,9979

Termometer, inv.nr: 102080
torkad i 105 grader C före provning

**Laboratory tests report for measurement of heat conductivity
and heat capacity**

Äspö Hard Rock Laboratory (HRL)

KQ0064G01 and KQ0064G05

**The thermal properties heat
conductivity and heat capacity
determined using the TPS method**

Bijan Adl-Zarrabi

SP Swedish National Testing and Research Institute

November 2003

Keywords: Thermal properties, Thermal conductivity, Thermal diffusivity, Heat capacity, Transient Plane Source.

Abstract

Thermal properties, density and porosity on three specimens were measured at elevated temperature. Two were sampled from drill hole KQ0064G01 and one from KQ0064G05. The rock type in KQ0064G01 is an isotropic medium-grained grey diorite with phenocrysts consisting of K-feldspar. The rock type in KQ0064G05 is an isotropic medium-grained red diorite. Measurements were performed according to SKB's method descriptions SKB MD 191.001 (Determination of thermal properties, thermal conductivity and specific heat, by using TPS-method: SKB internal controlling document) and SKB MD 160.002 (Determination of density and porosity of the intact rocks: SKB internal controlling document).

Density of the samples was about 2,750 kg/m³ and the porosity of samples was in the range of 0.2-0.4%.

Thermal conductivity of KQ0064G05 was determined to 2.79 W/mK at 22°C and 2.74 W/mK at 60°C. The mean thermal conductivity of two specimens sampled from KQ0064G01 was determined to 2.47 W/mK at 22°C and 2.44 W/mK at 60°C respectively.

Thermal diffusivity of KQ0064G05 was determined to 1.25 mm²/s at 22°C and 1.07 mm²/s at 60°C. The mean thermal diffusivity of two specimens sampled from KQ0064G01 was determined to 1.15 mm²/s at 22°C and 0.99 mm²/s at 60°C respectively.

Generally, the influence of temperature was greater on the thermal diffusivity than on the conductivity.

Contents

1	Introduction	143
2	General information	143
2.1	Description of the samples	143
2.2	Equipment	143
2.3	Test Procedure	144
3	Results	144
3.1	Description and presentation of the specimen	144
3.2	Results for the entire test series	148
	References	149
	Appendix A	149

1 Introduction

The objective of this investigation was to measure thermal properties, density and porosity of KQ0064G05 and KQ0064G01 (in Äspö area, Oskarshamn) at different temperature levels by using the TPS-method.

The Swedish Nuclear Fuel and Waste Management Co (SKB) delivered the samples, (KQ0064G05 and KQ0064G01), to Swedish National Testing and Research Institute (SP). The rock cores arrived to SP on September 2, 2003. The testing was performed during September and October 2003.

Determination of thermal properties was made in accordance with SKB's method description SKB MD 191.001 (SKB's internal controlling document) at the department of Fire Technology at SP. Density was determined in accordance with SKB MD 160.002 (SKB's internal controlling document) at department of Building Technology at SP.

2 General information

2.1 Description of the samples

Two cores were sampled from borehole KQ0064G01 and KQ0064G05 by Äspö Hard Rock Laboratory (HRL), Oskarshamn, Sweden. The boreholes start at a depth of 450 m. Three specimens, with a length of 250 mm were sampled from the two rock cores at SP. These samples were used for determination of thermal expansion. Table E-1 show the rock type and identification marks of the specimens. For more information about the rock type refer to /1/.

Table E-1. Rock type and identification marks (The rock type identification was made by SP).

Rock type	Identification (rock core secup-seclow)	Identification of samples
Diorite, red (with chlorite veins)	KQ0064G05 (5.77–6.01)	A
Diorite, grey	KQ0064G01 (6.60–6.85)	B
Diorite, grey	KQ0064G01 (6.85–7.10)	C

Two specimens, 50×50×25 mm were cut from each of the 250 mm long specimens and prepared for determination of thermal properties. In this report, the specimens are called A (KQ0064G05 5,77–6,01), B (KQ0064G01 6,60–6,85) and C (KQ0064G01 6,85–7,10).

2.2 Equipment

Technical devices are prescribed in SKB MD 191.001 and SKB MD 160.002. The devices used were;

- TPS-apparatus: Bridge version.
- Software: Hot Disk version 5.4.

- Radius of Kapton sensor for thermal measurements was 6.394 mm and Output of power was 0.75 W.
- Water temperature is controlled by using immersion heater, Grant type TD. The accuracy of the thermostat is 0.004°C.

2.3 Test Procedure

The measurement procedure followed the prescription in SKB MD 191.001 and SKB MD 160.002. Thermal properties, density and porosity measurements were performed during September 2003.

The following steps were performed:

1. Samples (length of 250 mm) were dried and weighed. Dry weight was measured after the samples had been dried to constant mass according to ISMR (1974) at 105°C. The drying procedure took seven days.
2. Samples were water saturated. Volume, wet density and dry density were determined.
3. Coefficient of thermal expansion is determined.
4. Samples were cut and polished.
5. Samples (length of 25 mm) were sent from SP Building Technology to SP Fire Technology.
6. Thermal properties were determined at 22, 40 and 60°C. Five measurements on each temperature level were done.

In order to remain water saturation and obtain desired temperature, the samples and the sensor were kept in a plastic bag during the measurement at 22°C. At 40 and 60°C the sensor were kept in a plastic bag plastic and the bag was under water.

7. Samples were sent from SP Fire Technology to SP Building Technology.
8. The specimens were photographed in JPEG-format.

2.3.1 Deviations

According to SKB's procedures drying of samples should be performed after measuring the thermal properties. Drying of samples was done as the first step of measuring procedures in order to gain time that was essential in this project.

3 Results

3.1 Description and presentation of the specimen

The rock type in KQ0064G01 is an isotropic medium-grained grey diorite with phenocrysts consisting of K-feldspar. The rock type in KQ0064G05 is an isotropic medium-grained red diorite.

Sample A (KQ0064G05 5,77–6,01)

Table E-2. Porosity, wet and dry density of specimen A.

Sample	Density, wet (kg/m ³)	Density, dry (kg/m ³)	Porosity (%)
A	2,750	2,750	0.2



Figure E-1. Sample A (KQ0064G05 5,77–6,01).

Table E-3. Thermal properties of sample A, at different temperatures.

Measurement number	Conductivity (W/mK)	Diffusivity (mm ² /s)	Heat capacity (MJ/m ³ K)
22°C			
1	2.78	1.21	2.29
2	2.79	1.24	2.25
3	2.79	1.25	2.22
4	2.80	1.26	2.22
5	2.80	1.25	2.22
40°C			
1	2.79	1.20	2.32
2	2.79	1.21	2.32
3	2.79	1.21	2.32
4	2.79	1.21	2.32
5	2.79	1.21	2.32
60°C			
1	2.77	1.10	2.50
2	2.75	1.03	2.66
3	2.73	1.08	2.52
4	2.73	1.05	2.59
5	2.72	1.10	2.49

Sample B (KQ0064G01 6,60–6,85)

Table E-4. Porosity, wet and dry density of specimen A, B and C.

Sample	Density, wet (kg/m ³)	Density, dry (kg/m ³)	Porosity (%)
B	2,750	2,740	0.4



Figure E-2. Sample B (KQ0064G01 6,60–6,85).

Table E-5. Thermal properties of sample B at different temperatures.

Measurement number	Conductivity (W/mK)	Diffusivity (mm ² /s)	Heat capacity (MJ/m ³ K)
22°C			
1	2.39	1.15	2.08
2	2.41	1.17	2.06
3	2.41	1.17	2.07
4	2.41	1.17	2.06
5	2.41	1.18	2.05
40°C			
1	2.43	1.12	2.17
2	2.43	1.12	2.16
3	2.43	1.12	2.17
4	2.43	1.12	2.17
5	2.43	1.12	2.17
60°C			
1	2.39	0.92	2.61
2	2.40	1.00	2.39
3	2.39	1.00	2.39
4	2.38	0.95	2.50
5	2.37	1.00	2.36

Sample C (KQ0064G01 6,85–7,10).

Table E-6. Porosity, wet and dry density of specimen A, B and C.

Sample	Density, wet (kg/m ³)	Density, dry (kg/m ³)	Porosity (%)
C	2,760	2,750	0.4



Figure E-3. Sample C (KQ0064G01 6,85–7,10).

Table E-7. Thermal properties of sample C at different temperatures.

Measurement number	Conductivity (W/mK)	Diffusivity (mm ² /s)	Heat capacity (MJ/m ³ K)
22°C			
1	2.54	1.11	2.29
2	2.54	1.11	2.28
3	2.55	1.12	2.28
4	2.55	1.12	2.28
5	2.55	1.12	2.27
40°C			
1	2.53	1.07	2.37
2	2.54	1.07	2.37
3	2.54	1.07	2.36
4	2.54	1.07	2.37
5	2.54	1.07	2.37
60°C			
1	2.47	1.02	2.43
2	2.47	0.94	2.62
3	2.49	1.00	2.50
4	2.46	1.02	2.41
5	2.50	1.00	2.51

Total time of the measurement, the ratio of total time and characteristic time and the number of analyzed points at different temperatures are presented in Appendix A.

3.2 Results for the entire test series

Table E-8–E-10 shows the mean value of five repeated measurements of the thermal properties. Standard deviation at different temperature levels is shown in Table E-11–E-13.

Table E-8. Mean value of thermal properties of samples A–C at 22°C.

Sample identification	Conductivity (W/mK)	Diffusivity (mm ² /s)	Heat capacity (MJ/m ³ K)
A	2.79	1.25	2.24
B	2.40	1.17	2.06
C	2.54	1.12	2.28

Table E-9. Mean value of thermal properties of samples A–C at 40°C.

Sample identification	Conductivity (W/mK)	Diffusivity (mm ² /s)	Heat capacity (MJ/m ³ K)
A	2.79	1.20	2.32
B	2.42	1.12	2.17
C	2.54	1.07	2.37

Table E-10. Mean value of thermal properties of samples A–C at 60°C.

Sample identification	Conductivity (W/mK)	Diffusivity (mm ² /s)	Heat capacity (MJ/m ³ K)
A	2.74	1.07	2.55
B	2.39	0.98	2.45
C	2.48	0.99	2.50

Table E-11. Standard deviation of measured values at 22°C.

Sample identification	Conductivity (W/mK)	Diffusivity (mm ² /s)	Heat capacity (MJ/m ³ K)
A	0.005	0.02	0.032
B	0.008	0.009	0.011
C	0.003	0.004	0.006

Table E-12. Standard deviation of measured values at 40°C.

Sample identification	Conductivity (W/mK)	Diffusivity (mm ² /s)	Heat capacity (MJ/m ³ K)
A	0.002	0.001	0.001
B	0.001	0.002	0.003
C	0.001	0.001	0.003

Table E-13. Standard deviation of measured values at 60°C.

Sample identification	Conductivity (W/mK)	Diffusivity (mm ² /s)	Heat capacity (MJ/m ³ K)
A	0.018	0.030	0.075
B	0.010	0.040	0.110
C	0.015	0.032	0.082

Generally, the influence of temperature was greater on the thermal diffusivity than on the conductivity.

Thermal conductivity decreases with increasing temperature. Variation of thermal conductivity between 20°C and 40°C is almost constant.

References

1. **Urban Åkesson, 2003.** Äspö Hard Rock Laboratory (HRL), KQ0064G01 and KQ0064G05, Coefficient of thermal expansion of rock – using an extensometer, Determination of density and porosity, SP Swedish National Testing and Research Institute.

Appendix A

Table A-1. Total time of the measurement, the ratio of total time and characteristic time and the number of analyzed points at 22°C.

Measurement number	Total time(s)	Total/Char. Time	Points
Sample A			
1	20	0.59	31-200
2	20	0.60	31-200
3	20	0.61	31-200
4	20	0.61	31-200
5	20	0.61	31-200
Sample B			
1	20	0.47	51-169
2	20	0.56	40-200
3	20	0.44	52-154
4	20	0.57	35-200
5	20	0.57	31-200
Sample C			
1	20	0.54	31-200
2	20	0.54	30-200
3	20	0.54	30-200
4	20	0.54	29-200
5	20	0.54	31-200

Table A-2. Total time of the measurement, the ratio of total time and characteristic time and the number of analyzed points at 40°C.

Measurement number	Total time(s)	Total/Char. Time	Points
Sample A at 40°C			
1	20	0.55	36-190
2	20	0.55	37-189
3	20	0.57	36-195
4	20	0.52	40-178
5	20	0.50	32-171
Sample B at 40°C			
1	20	0.45	64-165
2	20	0.43	50-158
3	20	0.45	57-166
4	20	0.44	56-162
5	20	0.45	57-167
Sample C at 40°C			
1	20	0.52	33-200
2	20	0.52	30-200
3	20	0.52	30-200
4	20	0.52	30-200
5	20	0.52	30-200

Table A-3. Total time of the measurement, the ratio of total time and characteristic time and the number of analyzed points at 60°C.

Measurement number	Total time(s)	Total/Char. Time	Points
Sample A at 60°C			
1	20	0.54	93-200
2	20	0.50	93-200
3	20	0.49	113-186
4	20	0.40	44-155
5	20	0.47	75-179
Sample B at 60°C			
1	20	0.34	82-155
2	20	0.39	70-162
3	20	0.49	85-200
4	20	0.46	118-200
5	20	0.46	77-190
Sample C at 60°C			
1	20	0.44	76-178
2	20	0.45	112-198
3	20	0.48	87-200
4	20	0.49	86-200
5	20	0.45	84-187

More details are available in attached excel files, digital format.

**Laboratory test report for determination of fracture stiffness,
and mode I and mode II fracture toughness**

Äspö Hard Rock Laboratory

**Determination of Mode I and Mode II
fracture toughness and fracture normal
stiffness of Äspödiorite**

Tobias Backers, GFZ Potsdam

September 2003

Summary

Fracture normal stiffness, Mode II fracture toughness under influence of confining pressure and Mode I fracture toughness, have been determined on Äspödiorite samples from SKB borehole KA3376B01. Four tests each for determination of Mode I fracture toughness and fracture stiffness were carried out. The Mode II fracture toughness was determined on a series of twelve samples with confining pressures of 0, 5, 15, 30, 50 and 70 MPa and two tests per confining pressure level. In summary 4 K_{IC} , 4 K_N and 12 K_{IIC} tests were performed.

The mean value of Mode I fracture toughness at room temperature and confining pressure of 0.1 MPa is 3.8 ± 0.1 MPa m^{1/2}. The Mode II fracture toughness increases from 4.4 to 13.5 MPa m^{1/2} with increase of confining pressure. K_{IIC} becomes almost constant above a confining pressure of about 35 MPa. The initial fracture normal stiffness, K_{NI} , varies between 105 GPa/m and 311 GPa/m; the average is 175 ± 68 GPa/m. The average fracture normal stiffness, K_{NH} , at loading between ~ 12 and 25 MPa is $26,976 \pm 22,757$ GPa/m, the values are from 2,813 GPa/m to 54,254 GPa/m. The high variability of the fracture normal stiffness values suggests carrying out a more detailed study on this parameter.

Contents

1	Introduction	153
1.1	Samples	153
1.2	Sample preparation	153
1.3	Testing equipment	154
2	Testing methods	154
2.1	Mode I fracture toughness testing	155
2.2	Fracture normal stiffness testing	156
2.3	Mode II fracture toughness testing	156
3	Results and discussion	157
3.1	Mode I fracture toughness, K_{IC}	157
3.2	Fracture normal stiffness, K_N	158
3.3	Mode II fracture toughness, K_{IIC}	159
4	Conclusions	161
5	References	161
Appendix A Catalogue of cores and samples		162
Appendix B Results		163
Appendix C Diagrams		164

1 Introduction

A test series on Äspödiorite from borehole KA3376B01 was carried out. The testing series includes the determination of Mode I fracture toughness, fracture normal stiffness, and Mode II fracture toughness under the influence of confining pressure.

This report contains a description of the delivered samples, sample preparation and testing procedures. Mechanical data are reported and comprehensive tables summarise the results.

1.1 Samples

The core samples (~ 51 mm diameter) were delivered in one sample-box and were wrapped in protective foil. The boxes as well as the samples showed no sign of transport damage. The samples were catalogued (Table F-1). The quality of cores is good, some sections of the cores are not straight but curved. The persistence of individual core-pieces is up to 0.6 m. A sufficient amount of the core-bits are suitable for specimen preparation. Selected samples were taken from core no 3, 6 and 8 (Table F-1).

Table F-1. List of delivered cores with location depth including indication of which section specimens were taken. For additional details about specimen locations, refer to Appendix A.

Core no	Depth		Specimen
	bottom (m)	top (m)	
1	73.56	71.96	
2	74.30	73.77	
3	74.86	74.42	D3, D3-1, D3-2, D3-3
4	75.53	75.22	
5	77.65	76.88	
6	78.46	77.82	D2, D2-1, D2-3, D2-4, D4, D4-1, D4-2, D4-3
7	79.02	78.68	
8	79.78	79.22	D1, D1-1, D1-2, D1-3
9	80.21	79.78	

1.2 Sample preparation

Sample preparation was carried out according to /Backers et al. 2002a/ (K_{IC}), /Donath, 2002/ (K_N) and /Ouchterlony, 1988/ (K_{IC}).

Samples of sufficient length for Mode I fracture toughness determination were selected from high quality sections. Typical specimen dimensions are given in Table F-2. The samples were cut to a length > 200 mm. The end surfaces were manufactured perpendicular to the core axis within an accuracy of at least 3° and ground to a surface roughness of 100 µm. In the middle of each core a chevron shaped notch was cut perpendicular to the core axis, and two knives that span centred about five millimetres over the notch tip were glued to the core mantle (Figure F-1). These knives serve to hold a clip-gage for measurement of the clip-gage opening displacement, cod , during testing. Prepared samples are ready for Mode I fracture toughness, K_{IC} , and fracture normal stiffness, K_N , testing, respectively.

Table F-2. Dimensions of the Chevron Bend (CB-) sample for K_{IC} determination. The parameters are according to the ISRM Suggested Method /Ouchterlony, 1988/. For indication of the geometrical parameters see Figure F-1.

Geometrical parameter	Value	This study
Specimen diameter	D	~ 51 mm
Specimen length, L	> 3.5 D	200–250 mm
Support span, S	(3.33 ± 0.02) D	169.5 mm
Chevron angle, θ	90.0° ± 1.0°	90°
Chevron tip position, a_0	(0.15 ± 0.01) D	7.50 ± 0.06 mm
Notch width, t	0.03 D	1.5 mm

The remaining specimen halves after K_{IC} and K_N testing were used for sample preparation for the Mode II fracture toughness, K_{IIc}, determination. Table F-3 gives typical specimen dimensions. The samples were cut to a length of 50 mm. The end surfaces were ground and polished perpendicular to the specimen axis to a surface roughness of 100 μ m. Notches were drilled centred into the end surfaces (Figure F-3).

The position of each specimen within the original cores is given in Appendix A.

Table F-3. Dimension of the PTS-specimen used. See Figure F-3 for geometrical parameters.

Geometrical parameter	Value	This study
Specimen height	W	50 mm
Specimen diameter	D	~ 51 mm
Notch Diameter	ID	25 mm
Upper notch depth	a	5 mm
Lower notch depth	b	30 mm
Notch tip width	t	1.5 mm
Intact portion	IP	15 mm

1.3 Testing equipment

Tests are carried out on a stiff, servo-controlled MTS (Material Test Systems Corporation, Minneapolis, MI, USA) loading machine. The maximum force capacity is 4,600 kN and the confining pressure system can provide confining pressures, P, up to 200 MPa. For application of low confining pressures (P < 20 MPa) a Hoek-Cell (Rocktest Inc) is used.

2 Testing methods

The tests were carried out in the following sequence. First the stiffness of the intact CB-specimen was tested, then the Mode I fracture toughness was determined. The fracture was propagated through the whole sample and afterwards the stiffness of the fractured sample was estimated. Finally, after additional sample preparation, the Mode II fracture toughness test was carried out and the Mode II fracture toughness was determined.

2.1 Mode I fracture toughness testing

Fracture toughness tests were carried out according to the ISRM Suggested Method /Ouchterlony, 1988/, chevron bend (CB-) method, level II testing. The specimen was subjected to a point load and supported by two rollers resulting in three-point bending (Figure F-1). The load was increased, controlled by constant opening rate of the notch (cod-rate). During testing the load was released in at least 4 cycles, this to be able to perform a ‘plasticity’ correction which accounts for the degree of plasticity exhibited by the specimen between two points on the loading curve where the fracture is growing /Barker, 1979/.

For details of the evaluation refer to /Ouchterlony, 1988, 1989/ and /Barker, 1979/. The uncorrected Mode I fracture toughness, K_{IC} is calculated by

$$K = A_{\min} \cdot F_{\max} / D^{1.5}$$

where

$$A_{\min} = [1.835 + 7.15 \cdot a_0 / D + 9.85(a_0 / D)^2] \cdot S / D$$

The correction for non-linearity¹ is done according to /Barker, 1979/ and the corrected fracture toughness is calculated by

$$K_{IC}^c = \sqrt{\frac{1+p}{1-p} \frac{F_c}{F_{\max}}} \cdot K_{IC}, \text{ including additional corrections.}$$

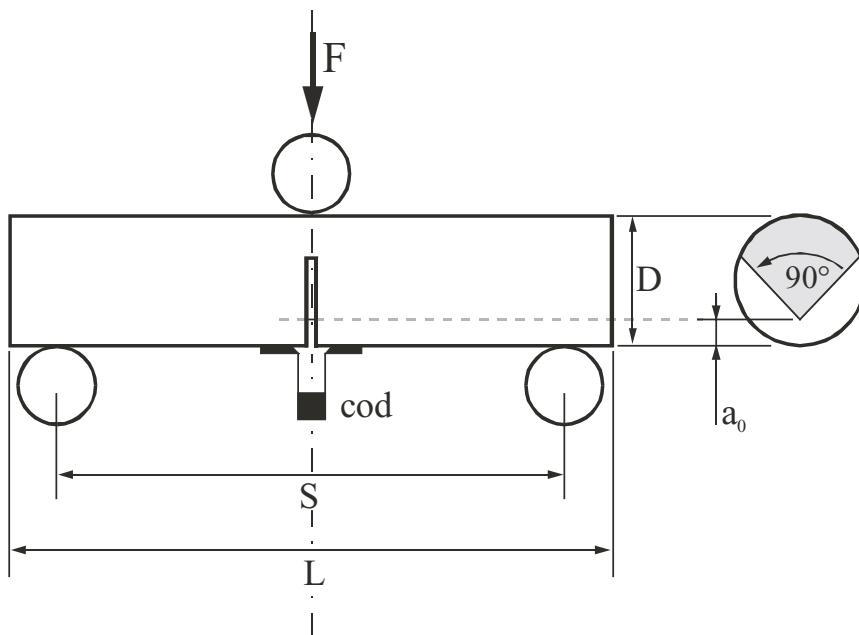


Figure F-1. Chevron-Bend (CB-) specimen. Dimensions and loading configuration. D : diameter, L : specimen length, S : support span, cod : clip-gage opening displacement and a_0 : chevron notch tip position. /Ouchterlony, 1988/.

¹ Non-linearity correction factor, p . It describes the change in slope of two neighbouring unloading/reloading cycles spanning the peak load in the force vs displacement plot.

2.2 Fracture normal stiffness testing

The method makes use of the fracture inserted into the CB-specimen during Mode I testing. The fracture is propagated until the crack driving force is 50 N. Hence, a small rock bridge remains (~ 2 mm) that holds the newly formed fracture faces in position. This guarantees that the fracture faces are matched. The specimen is loaded perpendicular to the fracture. A cyclic load is applied in axial displacement control and the fracture closure is measured using a clip gage (cod) (Figure F-2). Four loading cycles are carried out with increasing maximum force (10 and three times 25 kN). The displacement is measured to an accuracy of 0.5 μm . The maximum force that can be applied with a sufficient accuracy is 25 kN².

The normal stiffness, K_N , is determined on the last loading cycle. The three first cycles provide closure of the fracture. The displacements of the last cycle of unfractured³ and fractured specimen are subtracted from each other for the same load, yielding the fracture stiffness plot. For details of testing procedure and evaluation refer to /Donath, 2002/.

2.3 Mode II fracture toughness testing

The Punch Through Shear (PTS-) Test is used to determine the Mode II fracture toughness and to study the influence of confining pressure on this material property /Backers et al. 2002a,b/. The sample assembly is given in Figure F-3. To measure K_{IIC} at elevated pressure the assembly is covered by a rubber sleeve to prevent intrusion of confining pressure medium. The inner cylinder of the sample is punched down at a constant displacement rate of 0.2 mm/min, generating a high shear stress between the upper and lower notch.

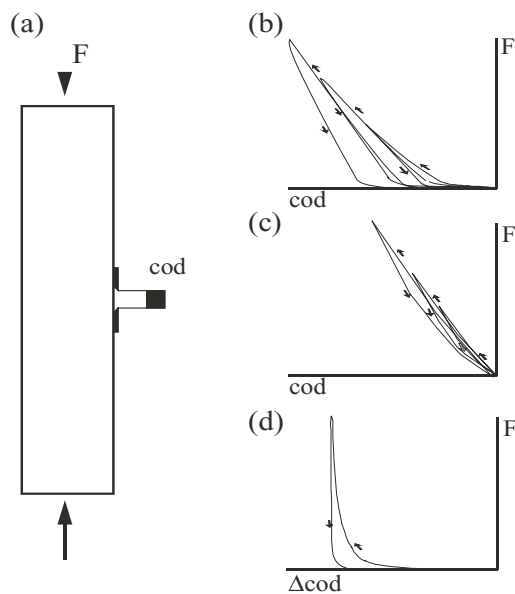


Figure F-2. (a) Loading set-up for fracture normal stiffness testing. (b)–(d) force vs cod plots of (b) fractured rock, (c) unfractured rock and (d) displacements of unfractured rock are subtracted from displacements of fractured rock.

² Other available load cells do not have a sufficient accuracy to estimate the initial fracture stiffness.

³ In principle the above-described procedure is also used to determine the stiffness of the unfractured sample.

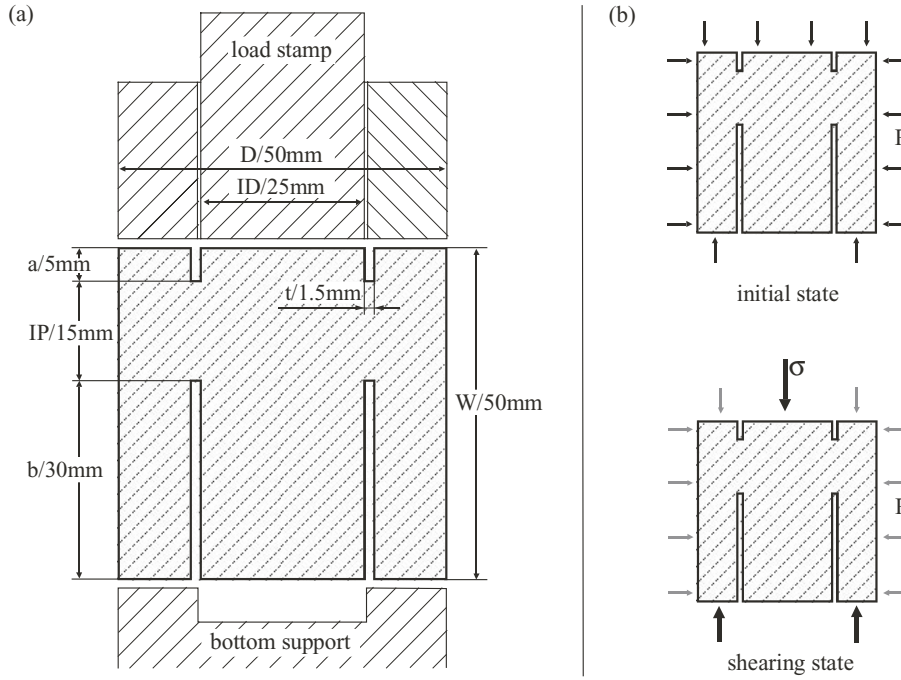


Figure F-3. Sample geometry, principle loading, set-up and dimension for the PTS-Test. (a) Sample geometry and dimension. W : sample height, D : sample diameter, ID : inner notch diameter, a : upper notch depth, b : lower notch depth, IP : intact rock portion and t : notch width. (b) Loading. s : axial stress, and P : confining pressure. Top: initial stress state due to confining pressure. Bottom: loading regime during application of shear stress. /Backers et al. 2002a/.

The principle adopted to calculate K_{IIC} is to exploit the shear displacement evolving in the shear plane between the notches at peak stress conditions, using a finite element method /Phase², 1999/ to perform a back analysis of the applied stresses, which yields the maximum displacement gradient. K_{IIC} is calculated from the maximum displacement gradient, ζ , the initial crack length, $c = t$, the Young's Modulus, E , and the Poisson's Ratio, ν :

$$K_{IIC} = \zeta \cdot \frac{E}{2(1+\nu)} \sqrt{\pi c}.$$

3 Results and discussion

Four tests for determination of Mode I fracture toughness and fracture stiffness were carried out. The Mode II fracture toughness was determined on a series of twelve samples with confining pressures of 0, 5, 15, 30, 50 and 70 MPa and two tests per confining pressure level. In summary 4 K_{IC} , 4 K_{II} and 12 K_{IIC} tests that could be evaluated successfully were performed. The results and sample dimensions of each experiment are summarised in Appendix B. Force vs displacement plots of all tests can be found in Appendix C. Tests were run at room temperature and confining pressures of 0.1 MPa unless otherwise stated.

3.1 Mode I fracture toughness, K_{IC}

Table F-4 gives the K_{IC} and K_{IC}^C values determined for each sample. The variability is within the expected geological and experimental scatter. The average Mode I fracture toughness is $3.8 \pm 0.1 \text{ MPa m}^{1/2}$.

Table F-4. Mode I fracture toughness. For each sample the depth, peak load, uncorrected and corrected fracture toughness and 'plasticity' correction factor, p , is given.

Sample	Depth (m)	Max. force (kN)	K_{Ic} (MPa m ^{1/2})	p	K_{Ic}^c (MPa m ^{1/2})
D1	79.49–79.75	3.65	3.30	0.18	3.80
D2	77.93–78.18	3.10	2.81	0.32	3.79
D3	73.77–74.06	3.78	3.43	0.12	3.87
D4	78.18–78.44	3.30	2.98	0.25	3.84
Average			3.13±0.24		3.83±0.03

3.2 Fracture normal stiffness, K_N

The stiffness is evaluated on the ascending branch of the load vs cod plot within the force interval 0–25 kN (Figure F-4). Table F-5 summarises the intact rock stiffness, K_R , initial fracture normal stiffness, K_{NI} , and the fracture normal stiffness between 12 and 25 kN, K_{NH} , where the slope is almost linear. The cross-sectional area of the loaded fractures is approximately $A^4 = 995 \text{ mm}^2$.

Table F-5. Intact rock stiffness, K_R , initial fracture stiffness (0–1.5 kN), K_{NI} , and fracture stiffness (12–25 kN), K_{NH} , for the ascending branch.

Sample	Depth (m)	K_R (kN/mm)	(GPa/m)	K_{NI} (kN/mm)	(GPa/m)	K_{NH} (kN/mm)	(GPa/m)
D1	79.49–79.75	1,430	1,437	150	151	54,000	54,254
D2	77.93–78.18	1,365	1,371	105	105	5,600	5,626
D3	73.77–74.06	2,440	2,451	310	311	2,800	2,813
D4	78.18–78.44	1,820	1,829	130	131	45,000	45,212
Average		1,764±366	1,772±368	174±68	175±68	26,850±22,650	26,976±22,757

The force vs cod plot of the intact samples is very linear for the tested loads. K_R variation of all samples is about twenty per cent. The value of specimen D3 is higher than the stiffness of the other specimen.

The values of the initial fracture stiffness, K_{NI} , for all samples show an even larger error than K_R . The error is about 39%. The highest value was obtained for sample D3.

The variability of K_{NH} is very high. K_{NH} of samples D2 and D3 show significant offset to samples D1 and D4.

⁴ The area of the fracture face was calculated using the ligament projection method as given by /Ouchterlony, 1988/. $1 \text{ kN/mm} = 1.0047 \text{ GPa/m}$

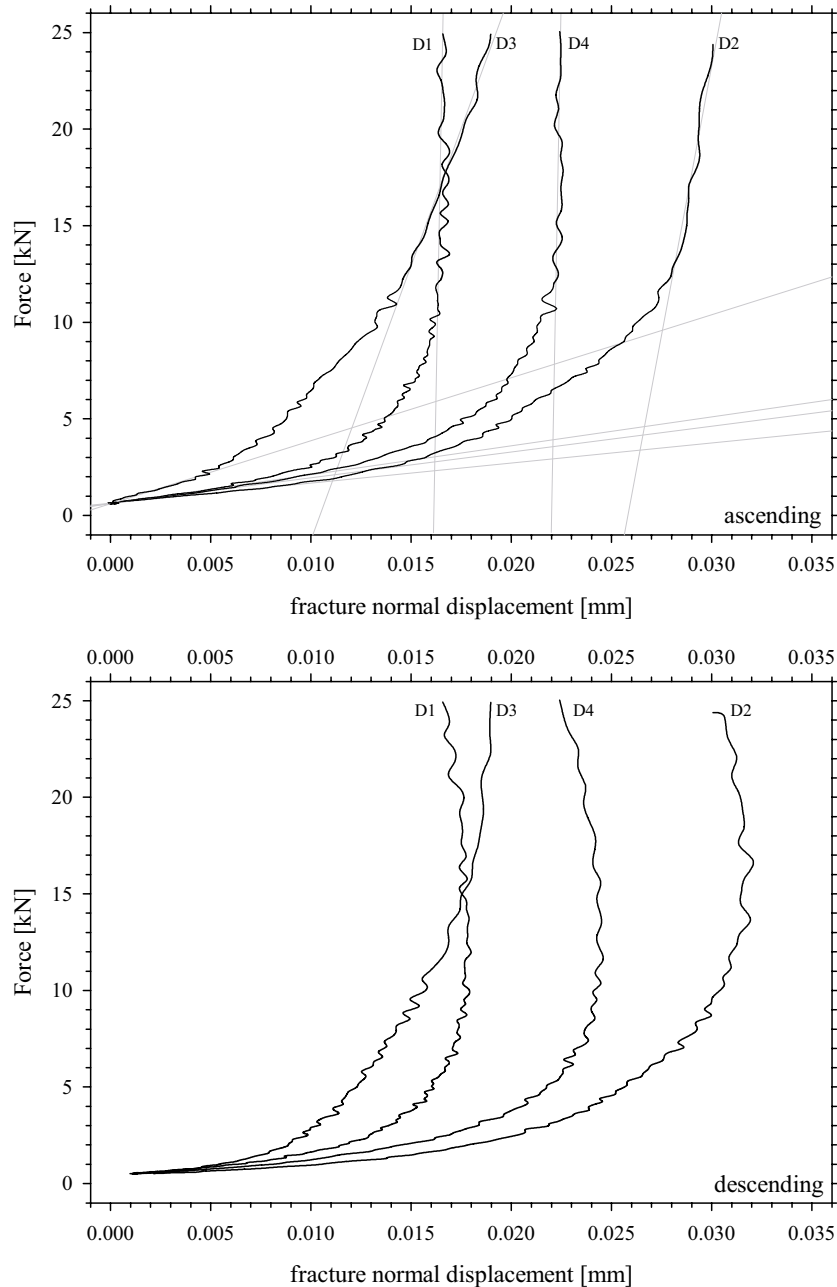


Figure F-4. Force vs normal displacement plots for determination of fracture normal stiffness. Top. Ascending branches. Linear regressions are indicated in grey. Bottom. Descending branches.

3.3 Mode II fracture toughness, K_{IIc}

For evaluation of the Mode II fracture toughness the Young's modulus and Poisson's ratio are required. These were provided by FRACOM Ltd, Farfarsbacken 14, 02400 Kyrkslätt, Finland, in an email dated 01.04.2003; hence $E \approx 68$ GPa and $\nu \approx 0.24$.

Table F-6 provides the determined Mode II fracture toughness for each sample.

Table F-6. Mode II fracture toughness. For each sample the depth, applied confining pressure, peak load and fracture toughness is given.

Sample	Depth (m)	Confining pressure (MPa)	Max force (kN)	K _{IIC} (MPa m ^{1/2})
D1-1	79.49–79.54	30	142	11.2
D1-2	79.55–79.60	70	171	12.8
D1-3	79.65–79.70	15	123	10.0
D2-1	77.93–77.98	70	170	12.7
D2-3	78.07–78.12	30	159	12.6
D2-4	78.13–78.18	15	124	10.1
D3-1	74.03–73.98	50	163	12.5
D3-2	73.77–73.82	5	91	7.5
D3-3	73.82–73.87	0	56	4.6
D4-1	78.18–78.23	50	175	13.5
D4-2	78.23–78.28	5	86	7.0
D4-3	78.33–78.38	0	53	4.4

Figure F-5 shows the influence of confining pressure on K_{IIC}. The Mode II fracture toughness values increase with increasing confining pressure and show an asymptotic rise to a maximum value. A curve fit yields:

$$K_{IIC}^{(P)} = K_{IIC}^{(0)} + K_{IIC}^{(\infty)} [1 - e^{-xP}],$$

where $x = 0.07$, $K_{IIC}^{(0)} = 4.57 \text{ MPa m}^{1/2}$ and $K_{IIC}^{(\infty)} = 8.40 \text{ MPa m}^{1/2}$.

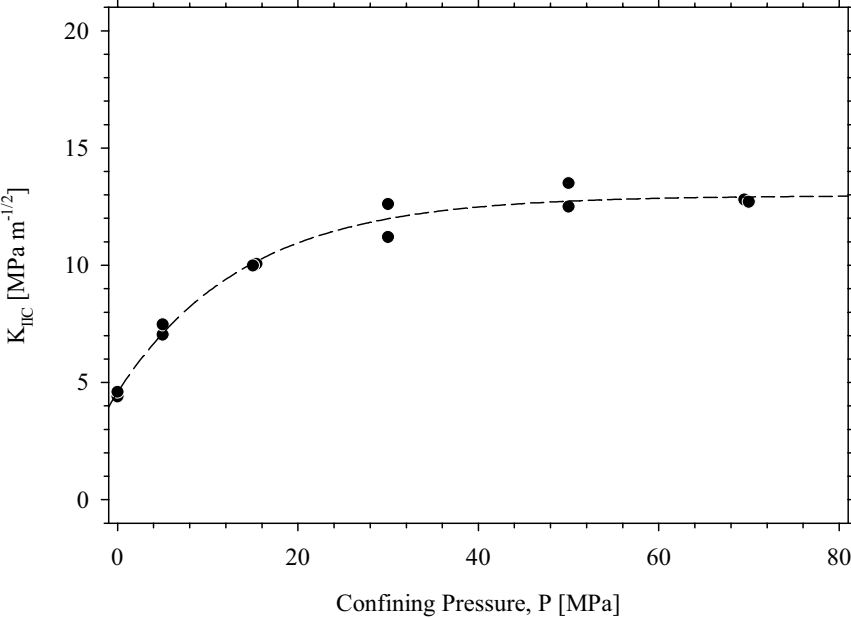


Figure F-5. Influence of confining pressure on Mode II fracture toughness, K_{IIC}. K_{IIC} increases with increasing confining pressure. Curve fit is indicated (dashed).

K_{IIC} at zero confining pressure is therefore 4.6 MPa m^{1/2}, the upper asymptote at high confining pressures is 13.0 MPa m^{1/2}. The fracture toughness has been reported to become constant above a certain confining pressure level, usually 20–40 MPa /Backers et al. 2002a/. For the Äspö-diorite the confining pressure level for constant K_{IIC} is about 35 MPa.

4 Conclusions

The Mode I fracture toughness and Mode II fracture toughnesses show moderate variability and therefore give good estimates of the fracture toughnesses.

The fracture normal stiffness shows much scatter in the results. Therefore the results presented here can only be seen as a first estimate. A detailed study of the fracture normal stiffness is suggested.

5 References

Backers T, Stephansson O, Rybacki E, 2002a. Rock Fracture Toughness Testing in Mode II – Punch-Through Shear Test. *Int. J. Rock Mech. & Min. Sci.*, 39: 755–769.

Backers T, Rybacki E, Alber M, Stephansson O, 2002b. Fractography of rock from the new Punch-Through Shear Test. In: Dyskin, A.V., Hu, X. & Sahouryeh, E. (eds.) *Structural Integrity and Fracture – The International Conference on Structural Integrity and Fracture*, Perth, Australia: 303–308.

Barker L M, 1979. Theory for determining K_{IC} from small, non-LEFM specimens, supported by experiments on aluminium. *Int. J. Fract.*, 15: 515–536.

Donath B, 2002. Stiffness of rock fractures – an experimental investigation. Diploma thesis. Technical University of Berlin.

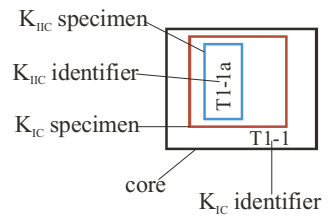
Ouchterlony F, 1988. Suggested methods for determining the fracture toughness of rock. *Int. J. Rock Mech. Min. Sci. & Geomech. Abstr.*, 25: 71–96.

Ouchterlony F, 1989. On the background to the formulae and accuracy of rock fracture toughness measurements using ISRM standard core specimens. *Int. J. Rock Mech. Min. Sci. & Geomech. Abstr.*, 26: 13–23.

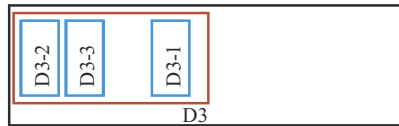
Phase², 1999. Finite element program version 4.053. Rocscience Inc. 31 Balsam Ave. Toronto ON M4E 3B5. Canada.

Appendix A

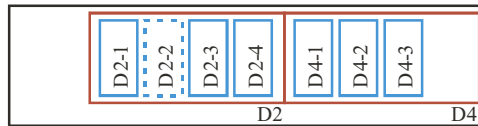
Catalogue of cores and samples



Core 3



Core 6



Core 8



Appendix B

Results

Table B-1. Dimension of Mode I fracture toughness samples and results from testing.

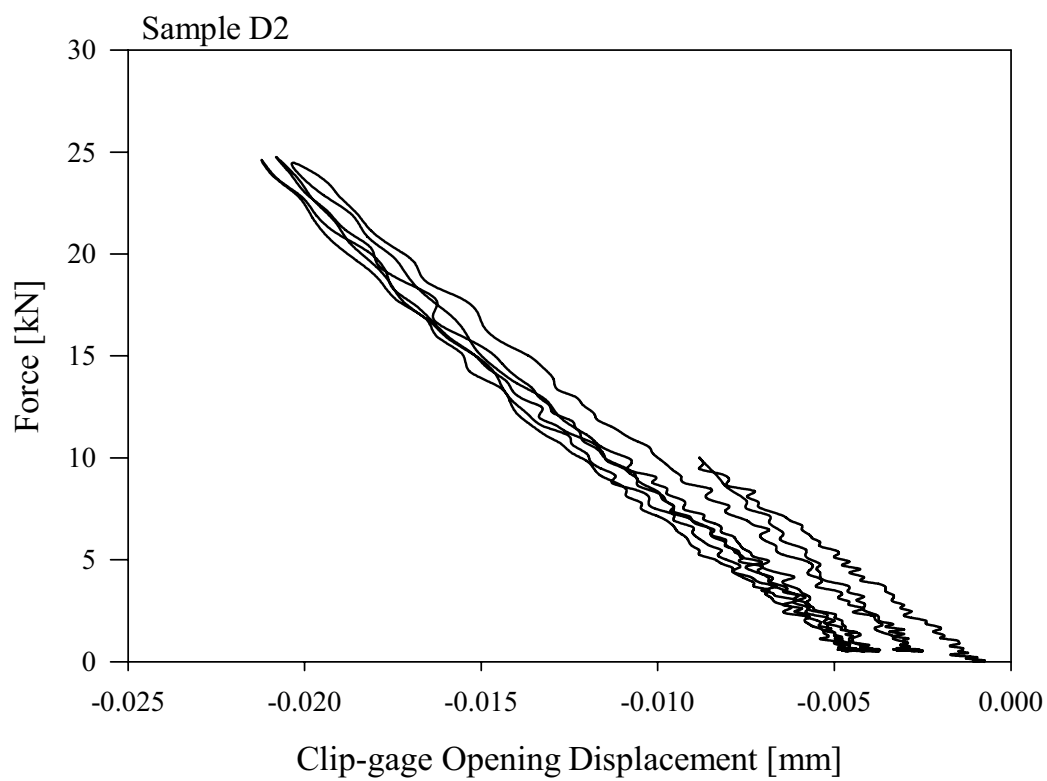
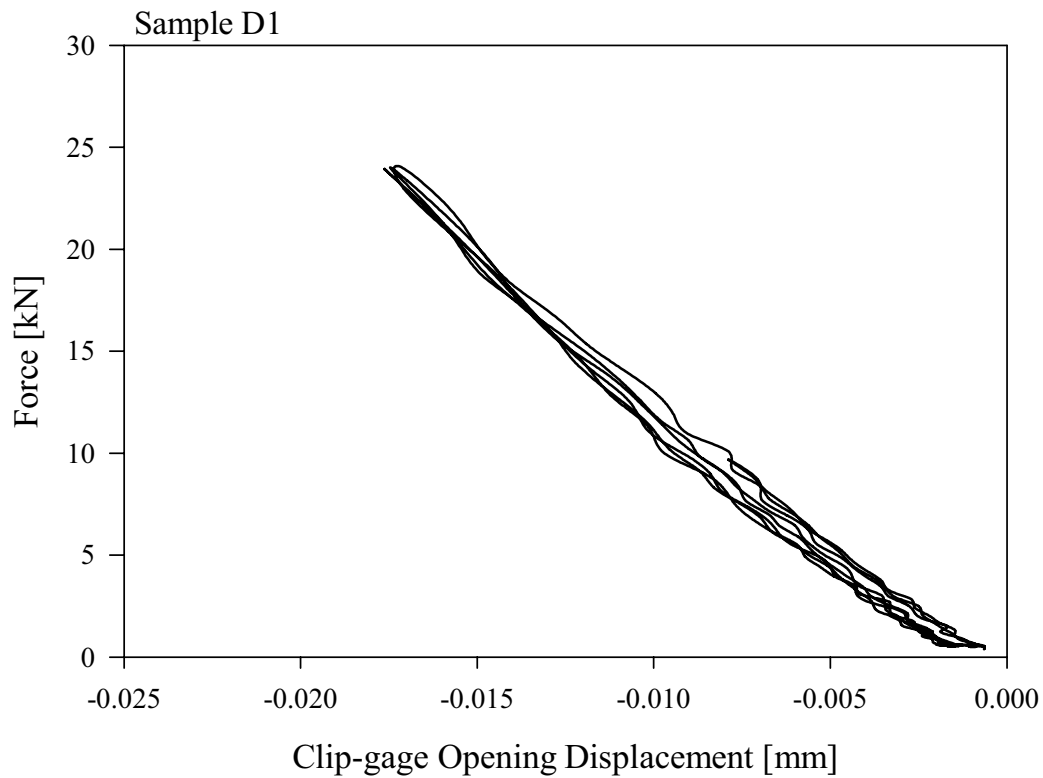
No	Depth		Diameter (mm)	Length (mm)	Support span (mm)	Chevron tip position (mm)	F_{max} (kN)	K_{IC} (MN/m ^{3/2})	p ()	K_{IC}^C (MN/m ^{3/2})
D1	79.49	79.75	50.98	260	169.5	7.50	3.65	3.30	0.18	3.80
D2	77.93	78.18	50.91	250	169.5	7.50	3.10	2.81	0.32	3.79
D3	73.77	74.06	50.90	290	169.5	7.50	3.78	3.43	0.12	3.87
D4	78.18	78.44	51.02	260	169.5	7.50	3.30	2.98	0.25	3.84

Table B-2. Dimension of Mode II fracture toughness samples and results from testing.

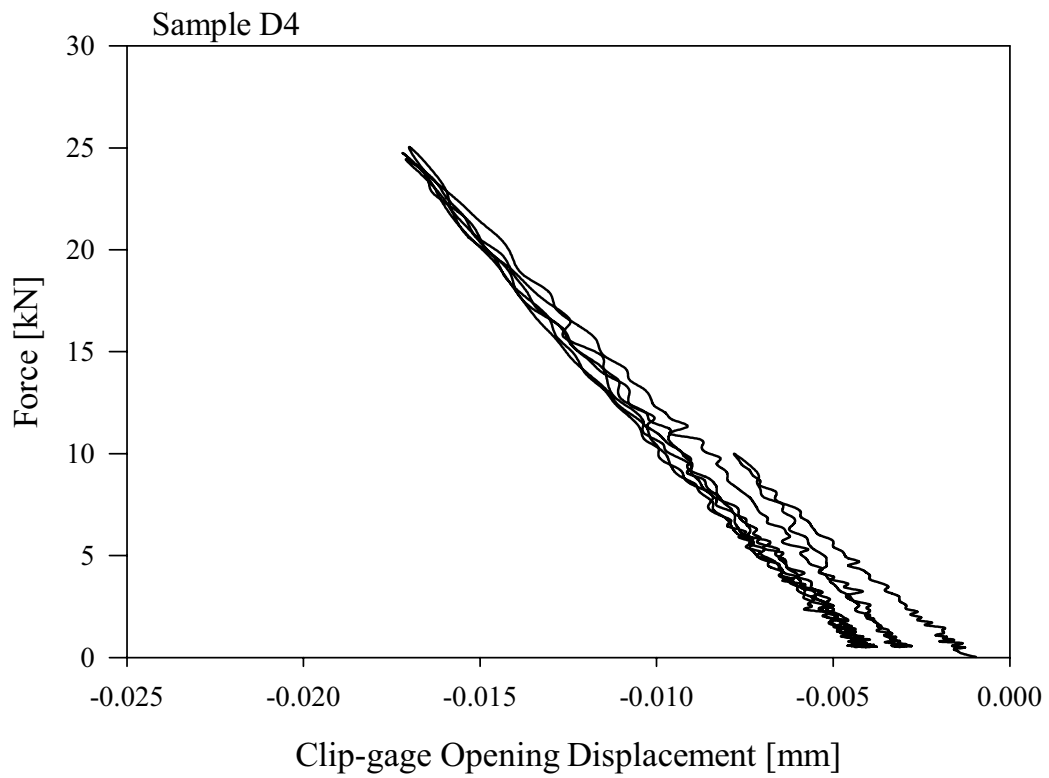
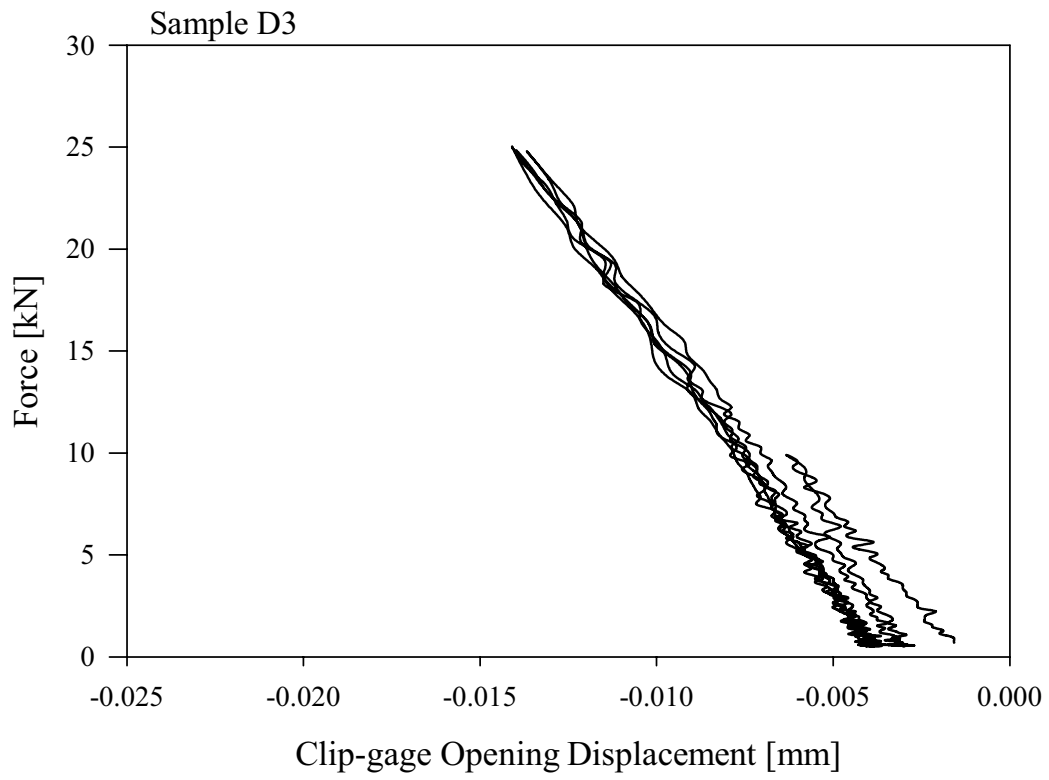
No	Dimensions			a (mm)	b (mm)	IP (mm)	Test variables		Test results		
	D (mm)	W (mm)	ID (mm)				P (MPa)	Rate (mm/min)	F_{max} (kN)	$\sigma_{max.}$ (MPa)	K_{IC} (MN/m ^{3/2})
D1-1	50.98	50.03	25	5.66	30.33	14.04	30	0.2	142	290	11.2
D1-2	50.93	50.10	25	5.25	30.61	14.24	70	0.2	171	348	12.8
D1-3	57.01	50.07	25	5.17	30.66	14.24	15	0.2	123	250	10.0
D2-1	50.91	49.94	25	5.32	30.21	14.41	70	0.2	170	346	12.7
D2-2	50.94	50.00	25	5.37	30.66	13.97	–	0.2	–	–	–
D2-3	50.94	50.06	25	5.69	30.66	13.71	30	0.2	159	324	12.6
D2-4	50.94	50.01	25	5.55	30.19	14.27	15	0.2	124	252	10.1
D3-1	50.90	50.14	25	5.07	30.63	14.44	50	0.2	163	332	12.5
D3-2	50.91	50.05	25	5.31	30.18	14.56	5	0.2	91	186	7.5
D3-3	50.97	48.57	25	5.48	30.19	12.90	0	0.2	56	115	4.6
D4-1	50.89	50.12	25	5.52	30.77	13.83	50	0.2	175	357	13.5
D4-2	50.95	50.13	25	5.30	30.69	14.14	5	0.2	86	175	7.0
D4-3	51.11	50.03	25	5.38	30.64	14.01	0	0.2	54	109	4.4

Appendix C

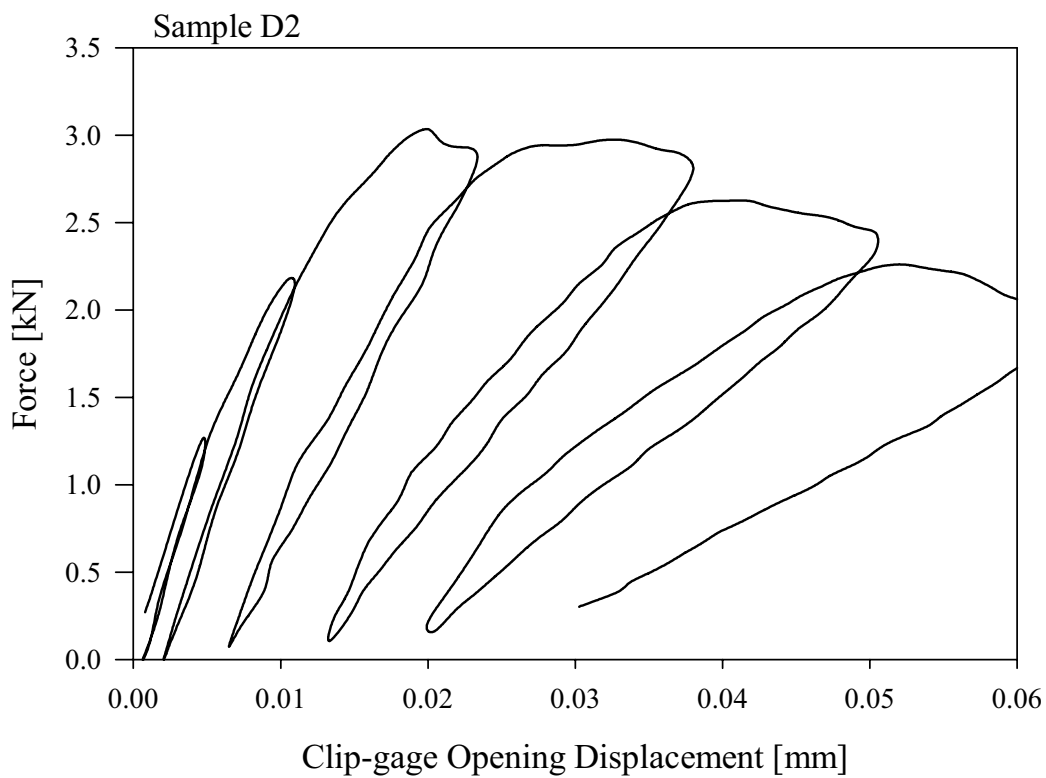
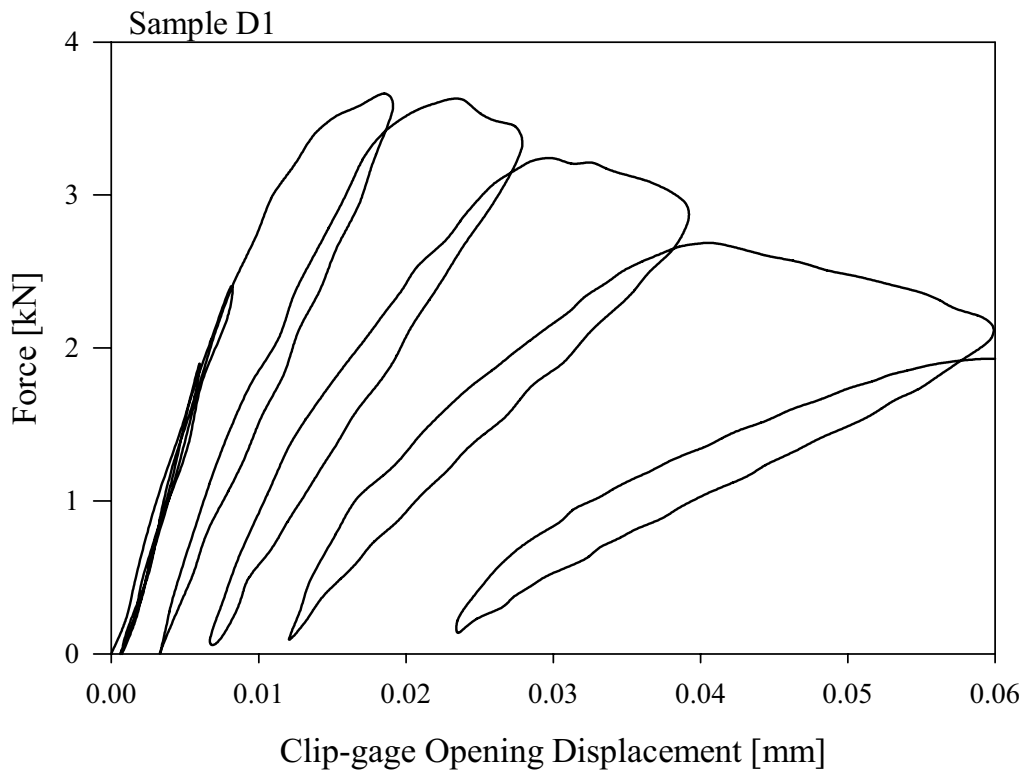
Diagrams



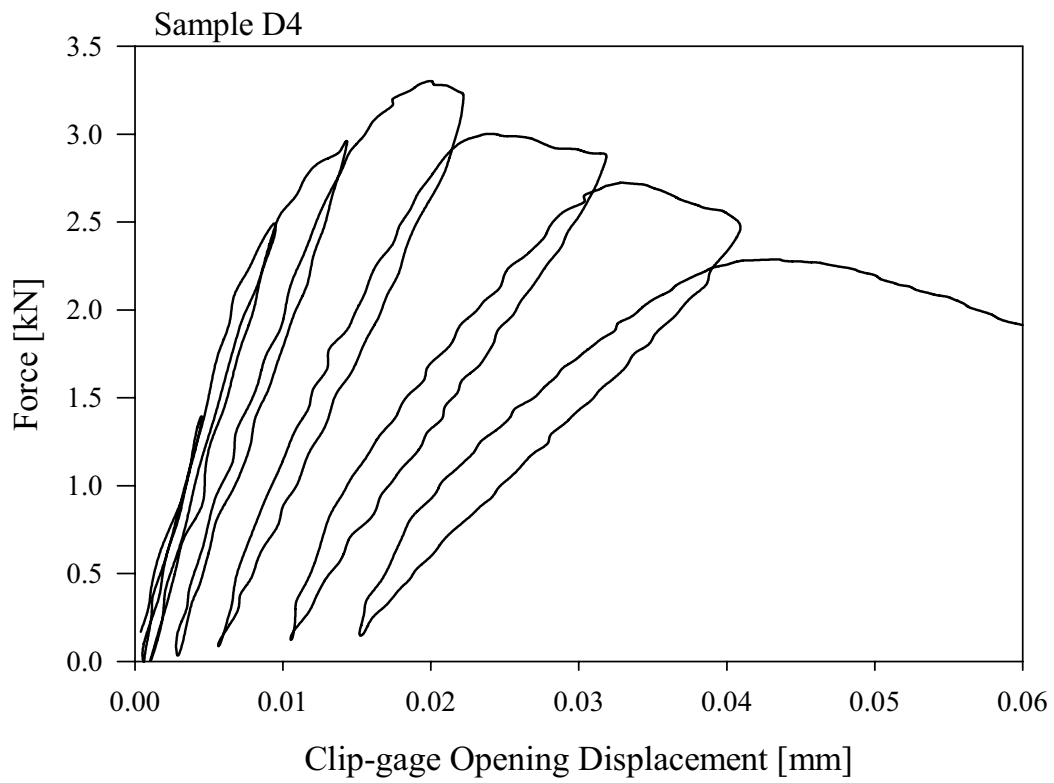
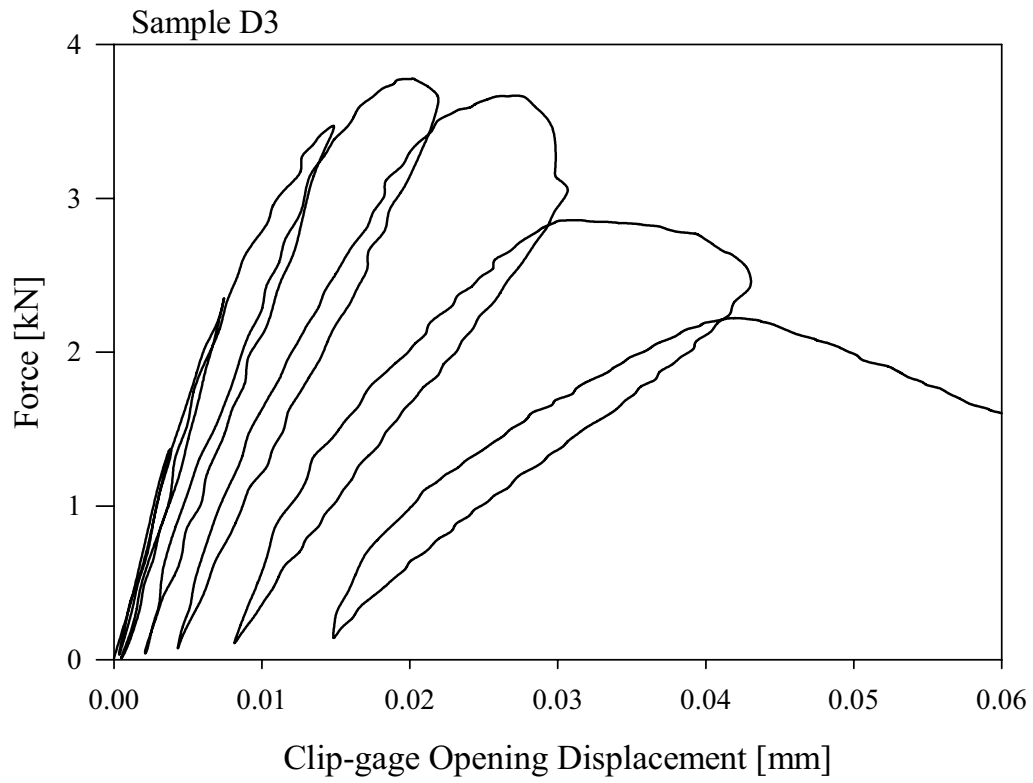
Rock Stiffness. Force vs Clip-gage Opening Displacement plots of K_R testing. The stiffness is determined on the last loading/unloading cycle (1/2).



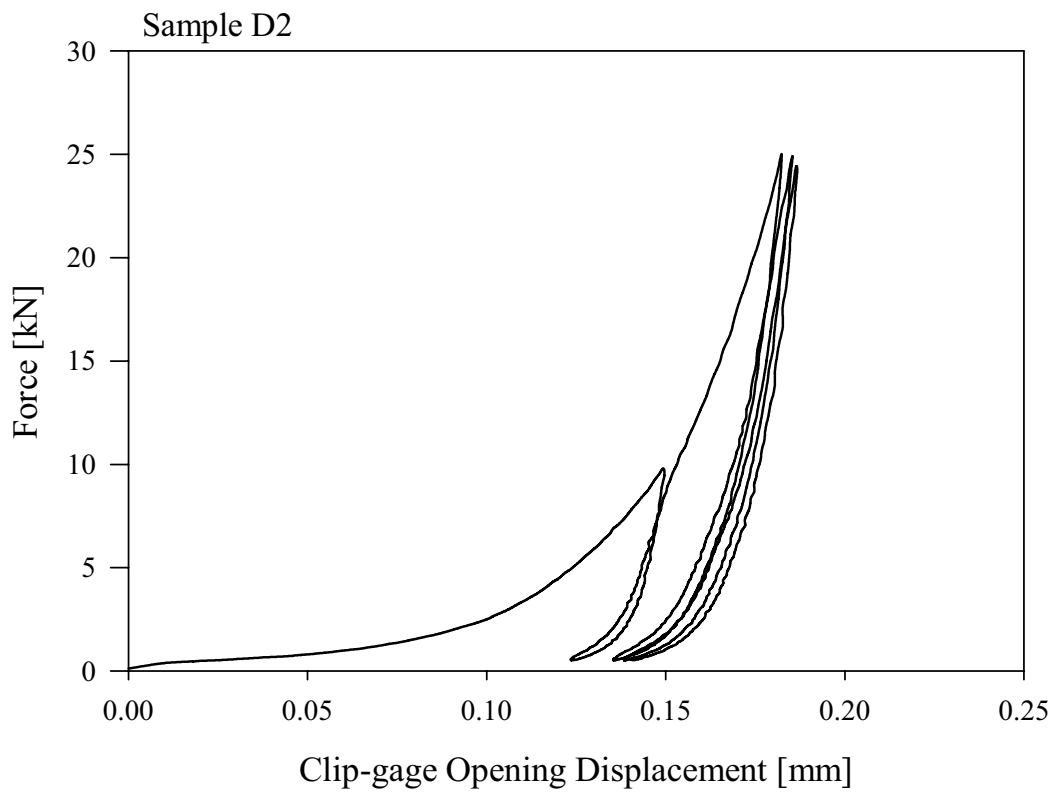
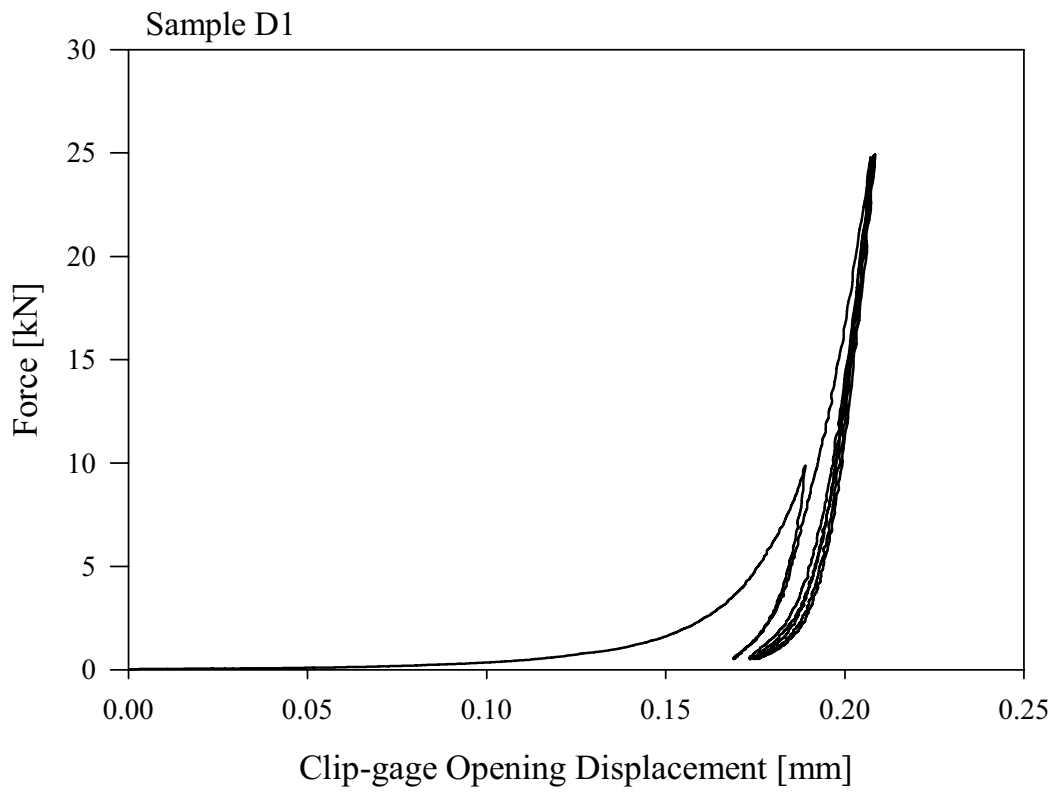
Rock Stiffness. Continued (2/2).



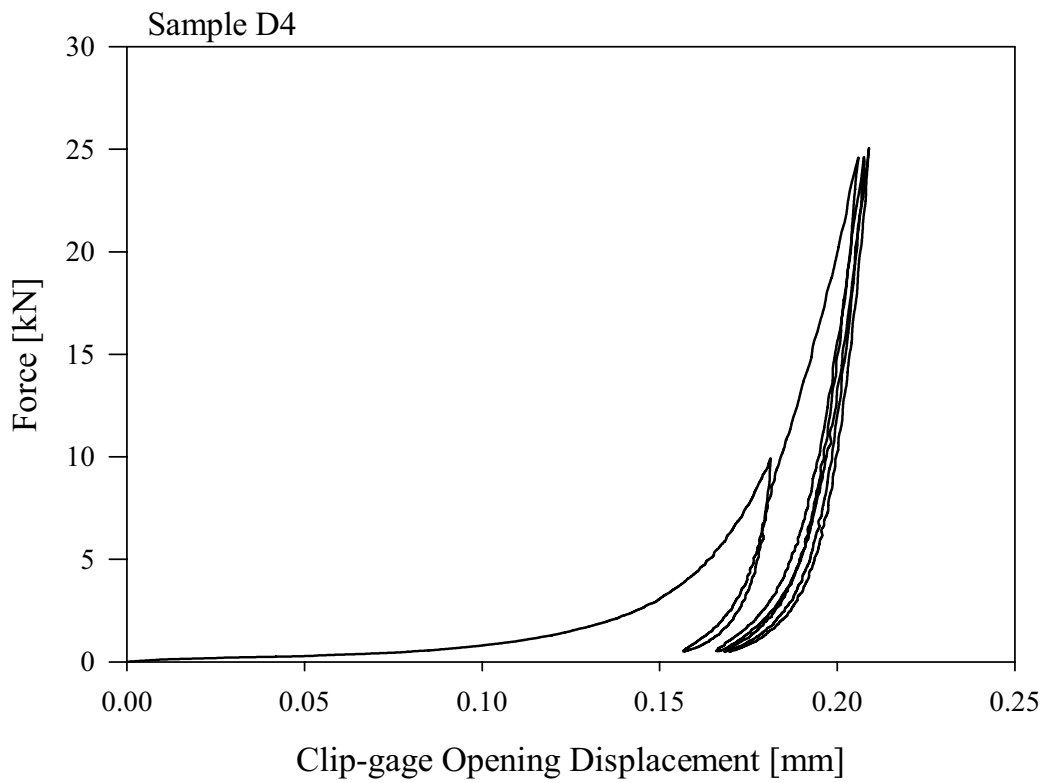
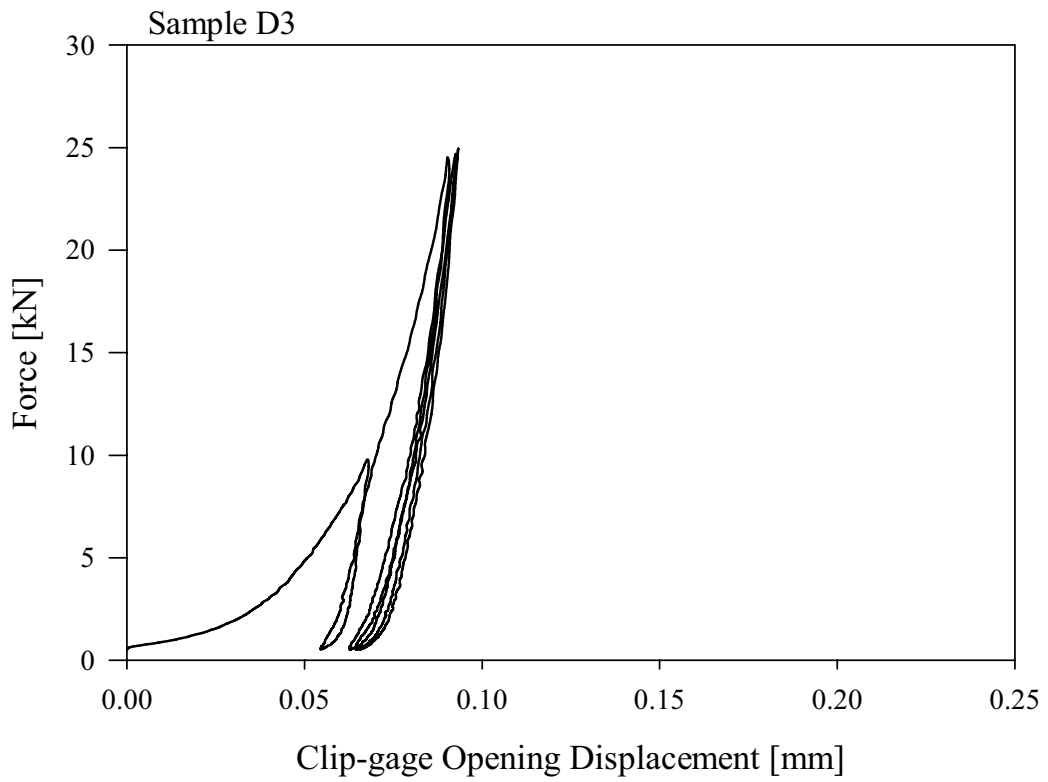
Mode I fracture toughness. Force vs Clip-gage Opening Displacement plots. Only the peak load region is shown as of interest for determination of K_{IC} (1/2).



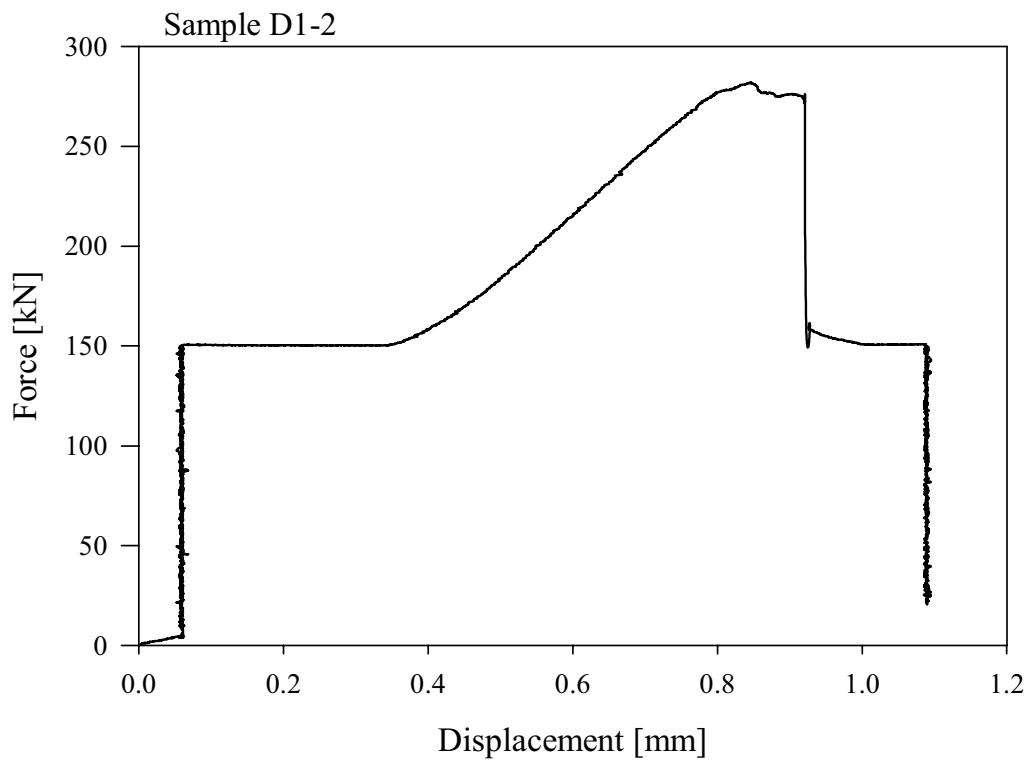
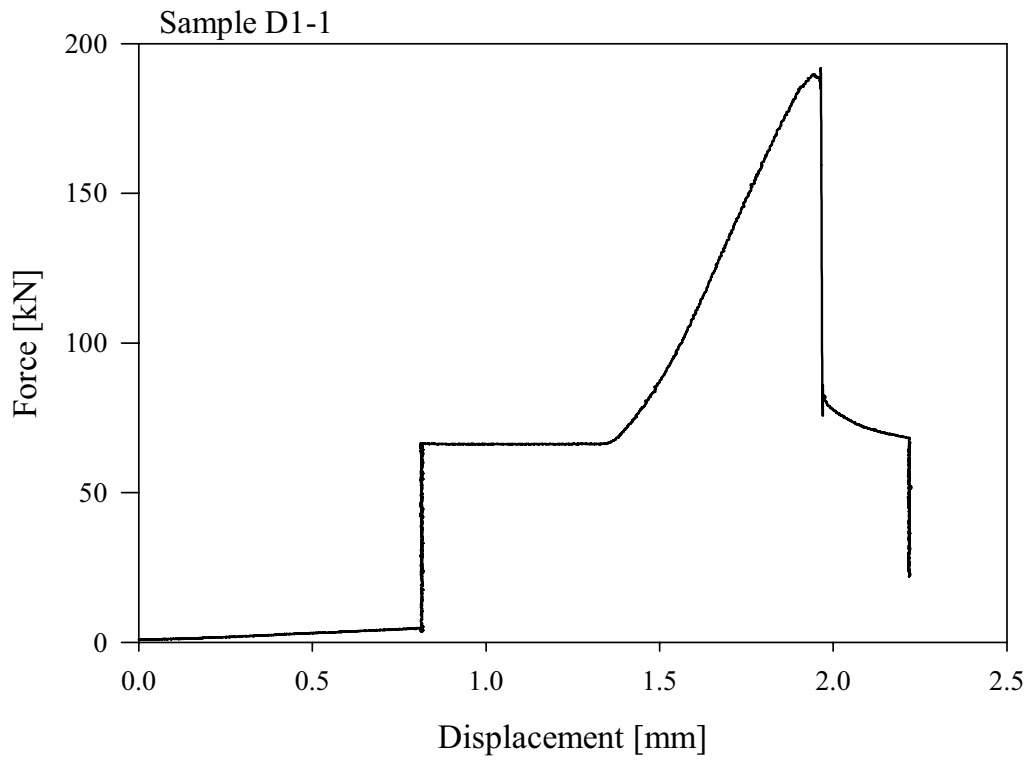
Mode I fracture toughness. Continued (2/2).



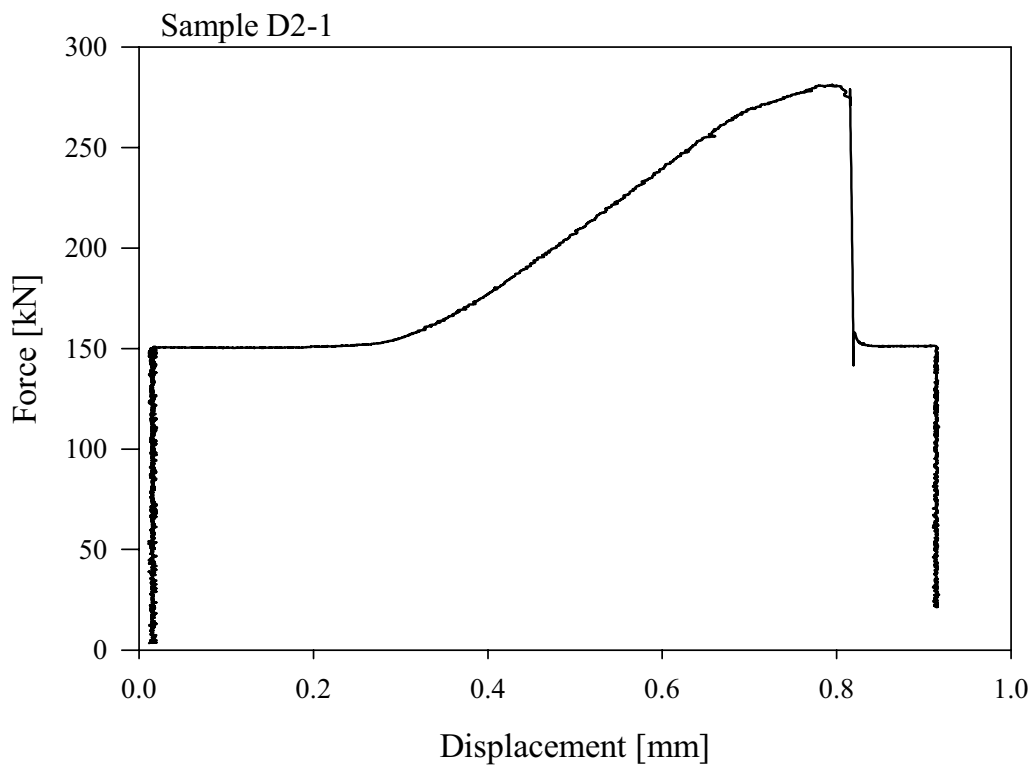
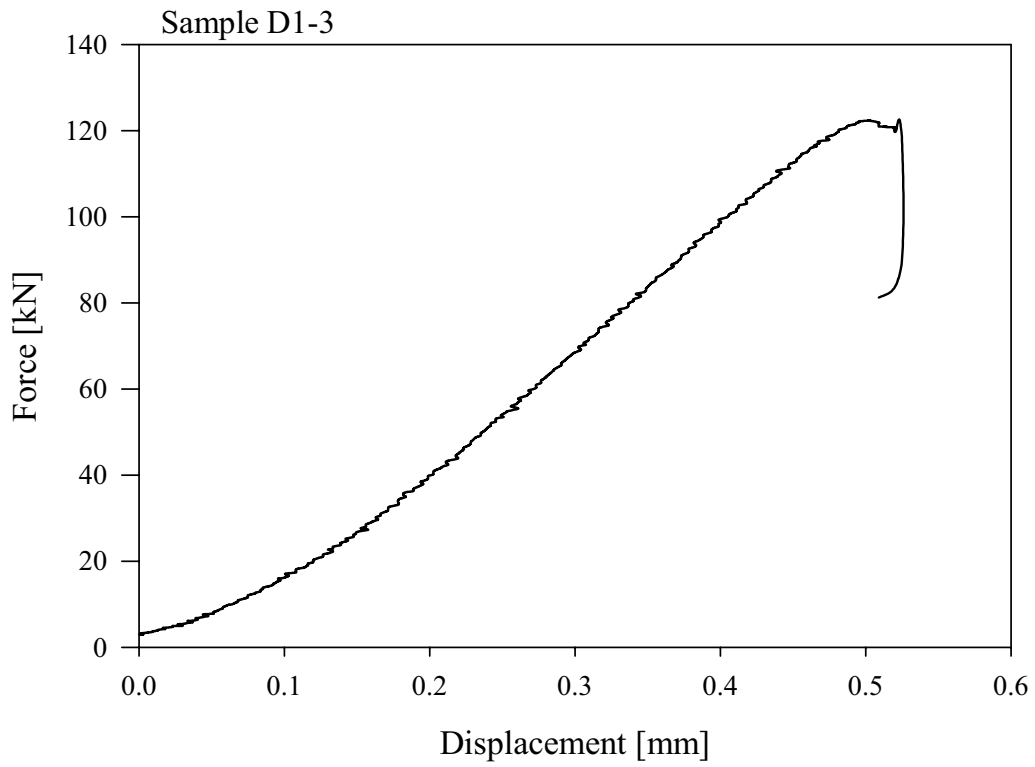
Fracture Normal Stiffness. Force vs Clip-gage Opening Displacement plots of K_N testing (1-2).



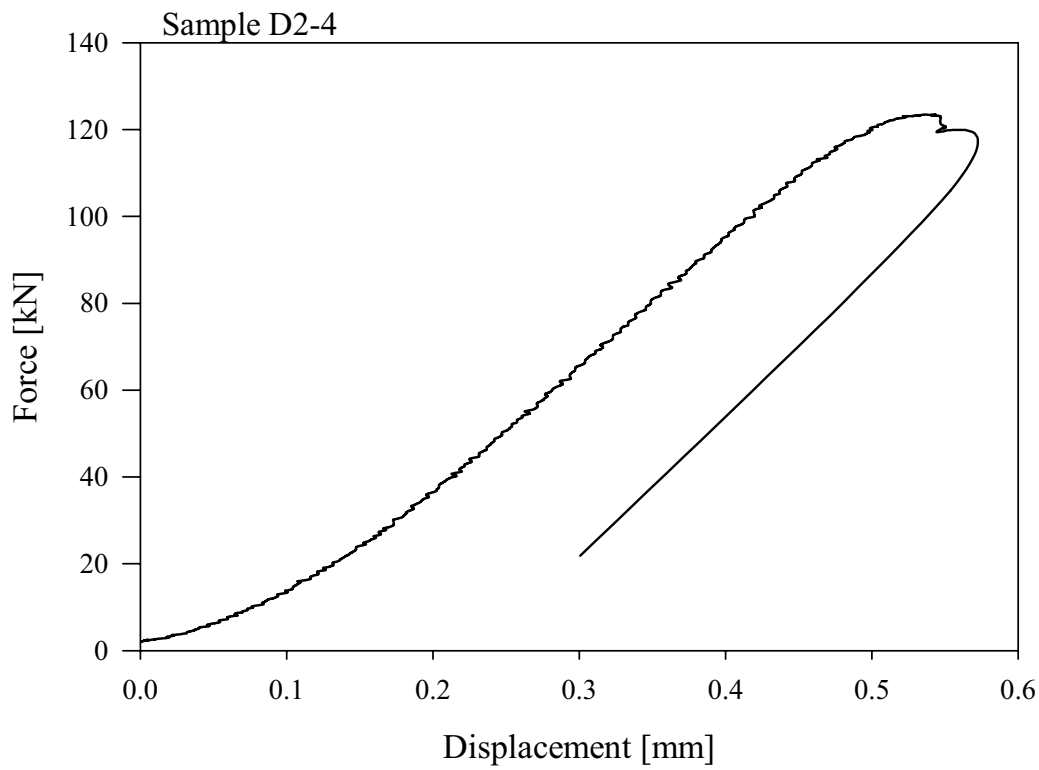
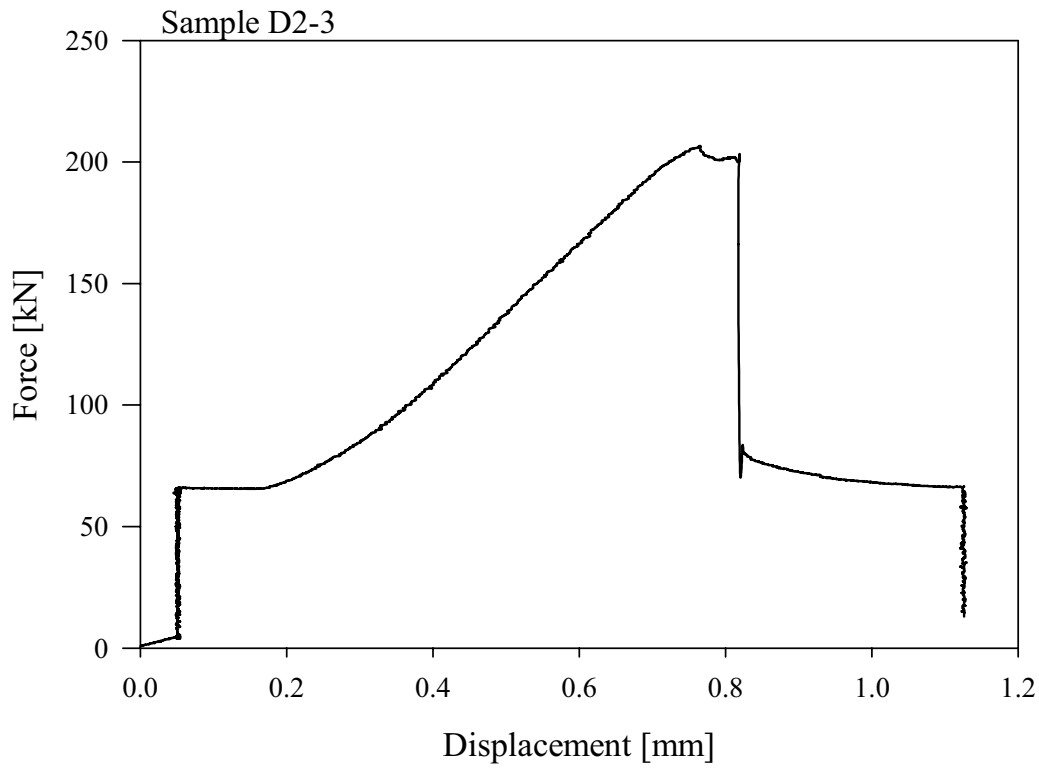
Fracture Normal Stiffness. Continued (2-2).



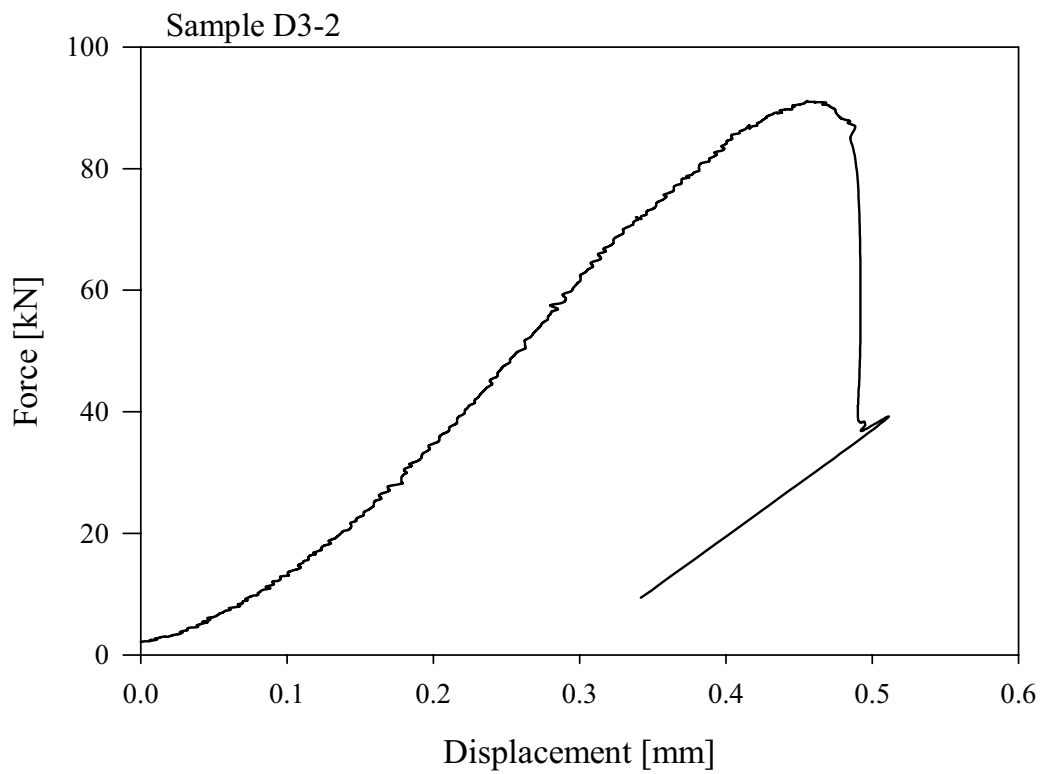
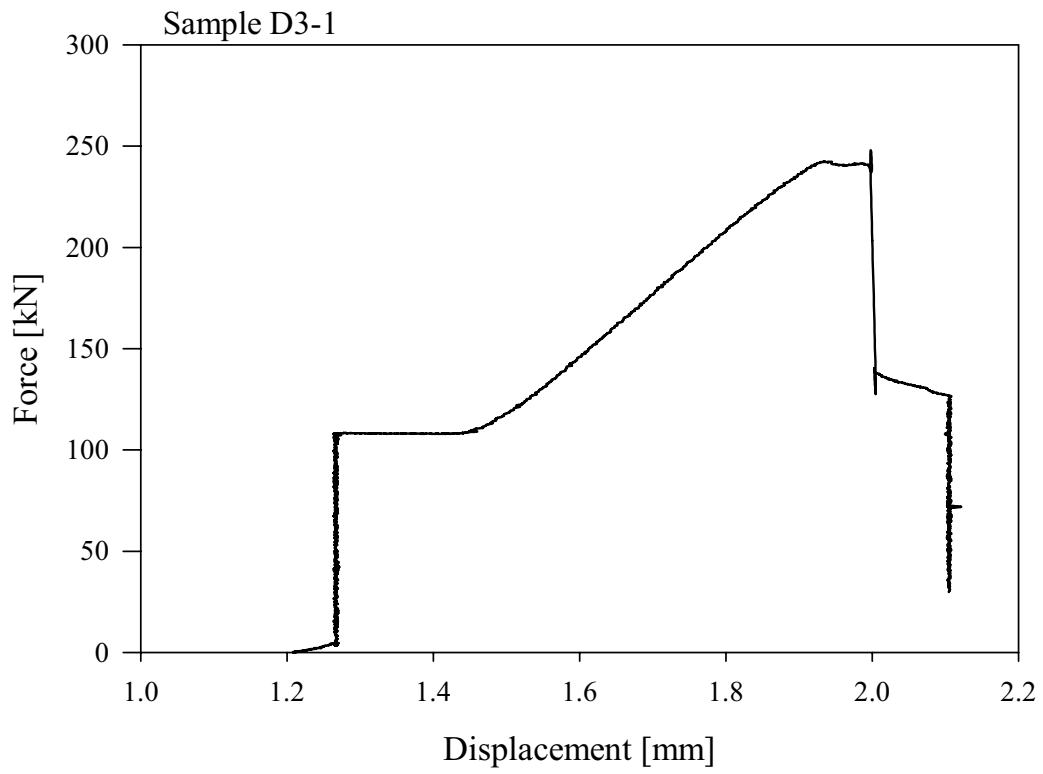
Mode II fracture toughness. Force vs Displacement plots. The sections of increasing force without increase of displacement refer to application of confining pressure in the pressure vessel. Force data is not corrected for confining pressure (1/6).



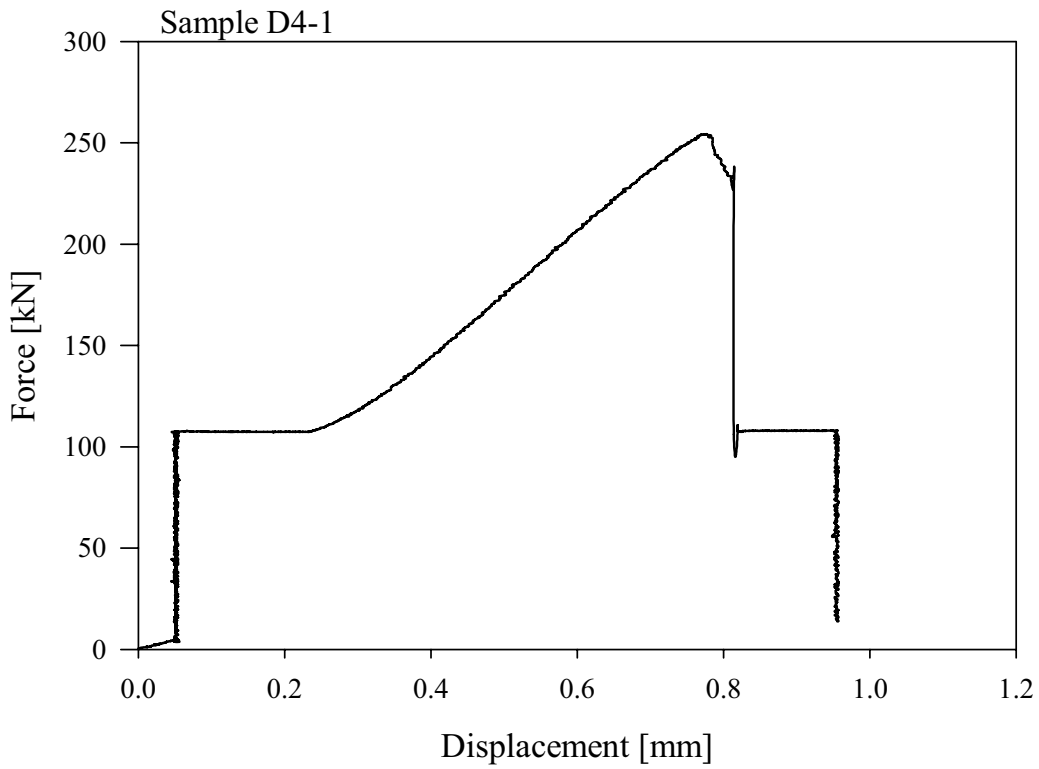
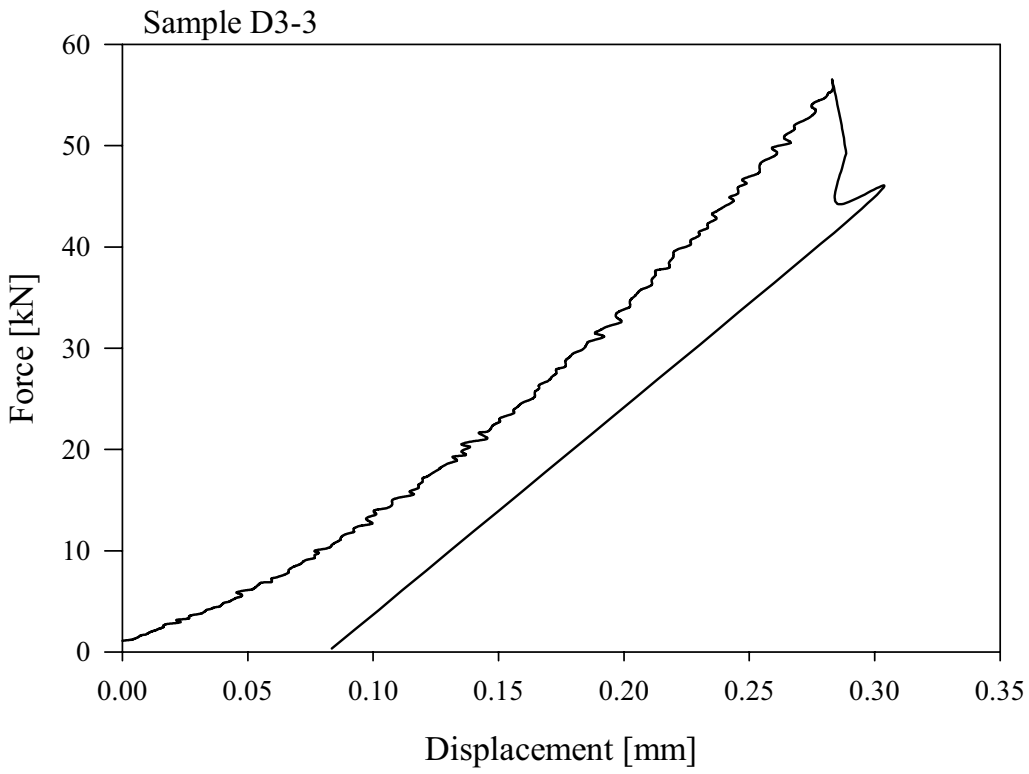
Mode II fracture toughness. Continued (2/6).



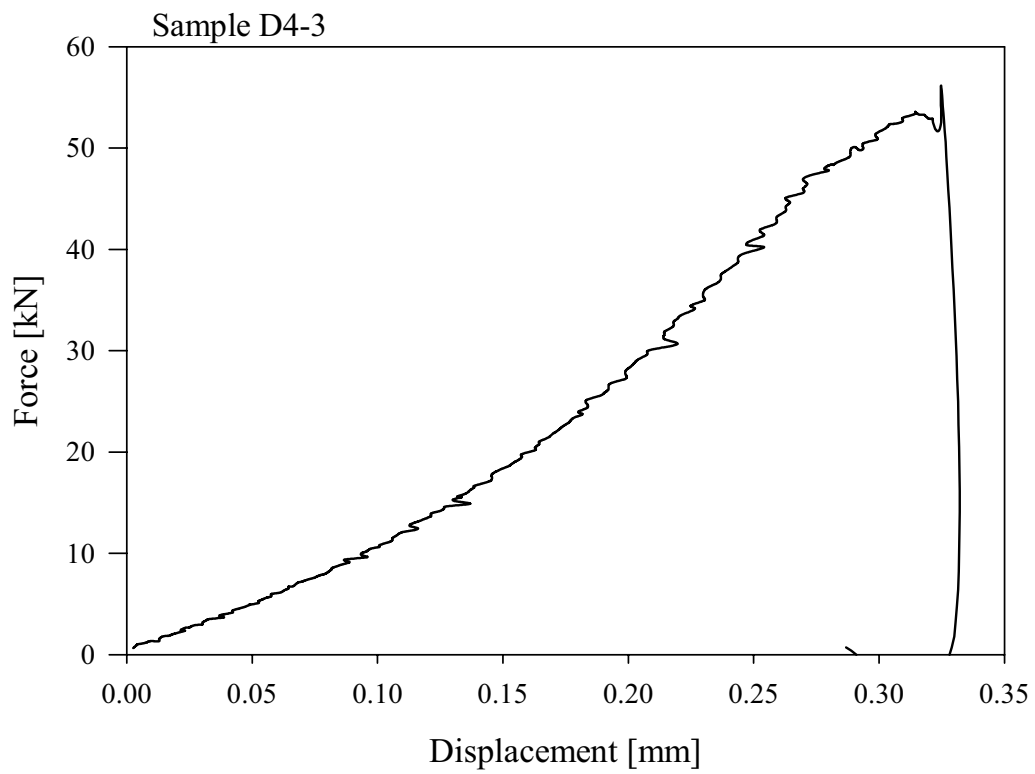
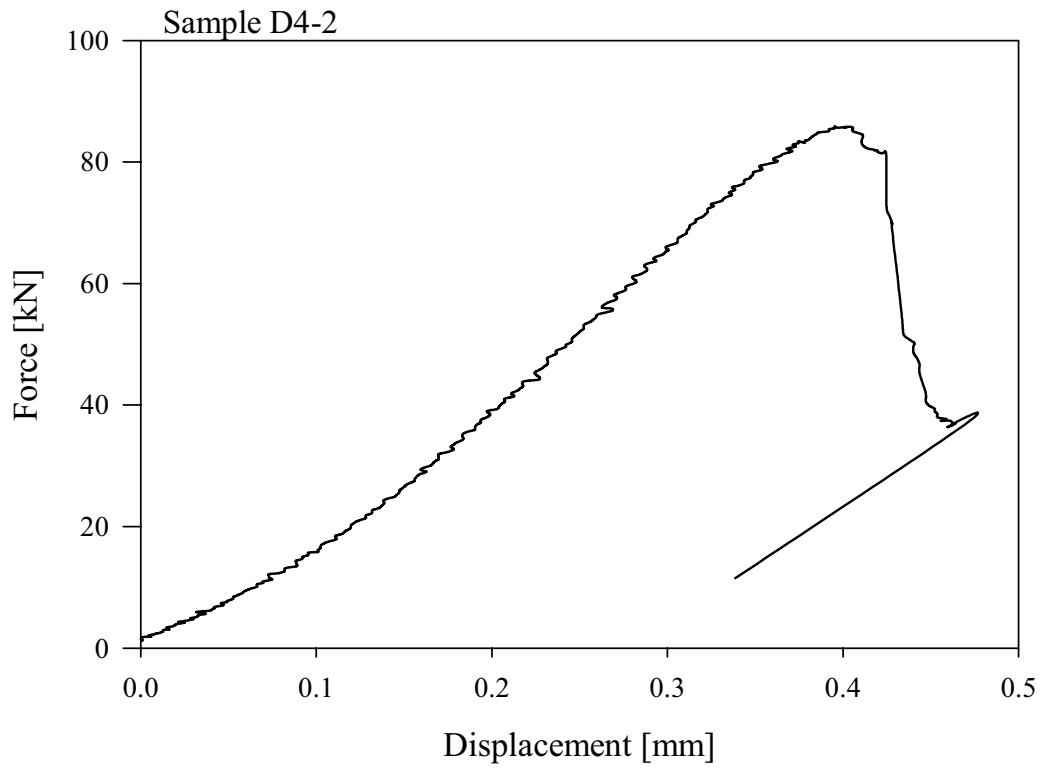
Mode II fracture toughness. Continued (3/6).



Mode II fracture toughness. Continued (4/6).



Mode II fracture toughness. Continued (5/6).



Mode II fracture toughness. Continued (6/6).

Disclaimer

The following conditions for testing of samples apply.

The Mode I testing is carried out according to the ISRM Suggested Method for determination of fracture toughness. Any inaccuracy of the method itself is not subject to our responsibility.

The Mode II testing is carried out according to the method introduced by /Backers et al. 2002a/, Int. J. Rock Mech. Min. Sci. The method is under development. The determined values are strictly valid for the given boundary conditions. Influence of other factors on the values are not known and not considered in the determination of the results.

The fracture normal stiffness is determined according to the method proposed by /Donath, 2002/. The method is under development. The determined values are strictly valid for the given boundary conditions. Influence of other factors on the values are not known and not considered in the determination of the results.

It is stated that the selection of the testing samples is subject of the customer. Any work done or values determined represent the specific rock samples delivered. Variation of properties as to variation of the rock is not considered. The values are strictly valid for the given samples at given boundary conditions.

Any alteration of the rock samples due to transport or handling by the customer or third parties is subject to responsibility of the customer.

Any information delivered by the customer or third parties are taken as is without consideration. Problems or misinterpretations due to these information or values are subject to responsibility of the customer.

Measurement report for sonic velocity in the pilot holes

Äspö Pillar Stability Experiment
Sonic velocity in pilot hole cores

Panayiotis Chryssanthakis, Lloyd Tunbridge
Norwegian Geotechnical Institute, Oslo

September 2003

Summary

The Norwegian Geotechnical Institute has carried out P-wave measurements on drill cores from boreholes KQ0048G01, KQ0064G01 and KQ0066G01 at Simpevarp in September 2003. Twenty four P-wave velocity measurements have been carried out.

The results from the P-wave velocity measurements show a consistent pattern over the three boreholes with maximum velocities generally between 5,500–6,000 m/s and a low anisotropy ratio of generally between 1 to 1.04. There is no apparent trend with depth over the 6 m length of the boreholes, although the higher density of data in the upper part of the borehole makes it look like there is a greater variation in both velocity and anisotropy in the upper part of the borehole. There is a slightly lower value of maximum measured velocity, 5,484 m/s, at the top, 0.15 m depth, of borehole KQ0066G01, which might reflect damage due to excavation, but this is not found in the other two boreholes.

The foliation is not identifiable over most of the core and the orientation of the principal velocities could not be identified relative to the foliation.

Contents

1	Introduction	178
2	General information	179
2.1	Description of the test specimens	179
2.2	Equipment	179
2.3	Test method	180
3	Results	183
3.1	Summary of results	183
3.2	Discussion	183
	References	190

1 Introduction

The Norwegian Geotechnical Institute (NGI) has carried out P-wave velocity measurements on cores from boreholes KQ0048G01, KQ0064G01 and KQ0066G01 at Simpevarp in Sweden in accordance with SKB Aktivitetsplan AP 400-03-049 dated 2003-08-26

The work was carried out by Panayiotis Chryssanthakis and Paweł Jankowski during the period 8th to 9th September 2003 in accordance with SKB's method description MD 190.002 version 1.0 /Janson, 2002/.

2 General information

2.1 Description of the test specimens

Twenty four core specimens of length c 200–500 mm and diameter about 50 mm were selected from boreholes KQ0048G01, KQ0064G01 and KQ0066G01 while the complete length of these boreholes was displayed on the racks in the core shed at Simpevarp. The specimens were selected together by NGI and Thomas Janson representing SKB.

The depths used to describe the location are those marked on the core and core boxes at the time. Detailed description of the specimens is available from the detailed core log by SKB. At the time of sampling, the core had been exposed to the atmosphere at room temperature for an extended period and may be presumed to be air-dried, though no measurements of the moisture content were made.

2.2 Equipment

The measurements were conducted using Panametrics Videoscan transducers with a natural frequency of 0.5 MHz. These were mounted in a special frame to hold them in contact with the core. Special wave guides, metal shoes with a concave radius similar to the core, were installed between the transducers and the core. The equipment was designed and constructed specially for this contract by NGI, based on the information presented in SKB report entitled Detection of Anisotropy by Diametral Measurements of Longitudinal Wave Velocities on Rock Cores by /Eitzenberger, 2002/. The equipment set up is shown in Figure G-1. The appartus for measuring acoustic P-wave travel time is shown in Figure G-2.



Figure G-1. NGI's equipment set up for measuring acoustic P-wave travel time transverse borehole core



Figure G-2. Detail of NGI's apparatus for measuring acoustic P-wave travel time transverse borehole core. The aluminium cylinder for calibration of the device is on the left.

A strong sine-wave pulse at the natural frequency of the transducers was used as the acoustic signal source. The arrival of the signals was measured using a PC with a high speed data acquisition board and software to emulate an oscilloscope (see Figure G-3 and previous work by /Chryssanthakis and Tunbridge, 2003a,b,c,d/). The time pick for the first break was taken as the beginning of the first transition, i.e. the point where the received signal first diverges from the zero volts line. In order to provide consistent interpretation of the time pick, one operator made all the interpretations. The time pick could be measured with a precision better than $0.01\mu\text{s}$. The instrumentation was calibrated using a cylinder of aluminium of known acoustic velocity of the same diameter as the core. Several measurements were taken each day on the calibration piece to check operation of the system.

A thick honey was used as a coupling medium as this proved to be one of the most effective medium and was easily removed by washing without damaging or contaminating the cores.

2.3 Test method

Tests were made at 30° intervals around the core, starting at 0° parallel with the foliation. However, the foliation was generally not identifiable and the tests were thus made at random orientations. The cores were all oriented such that successive measurements were made clockwise looking down the borehole (see Figure G-4). The cores were marked by attaching a piece of self-adhesive tape that had been previously cut to the appropriate length and marked up with the locations for the tests.

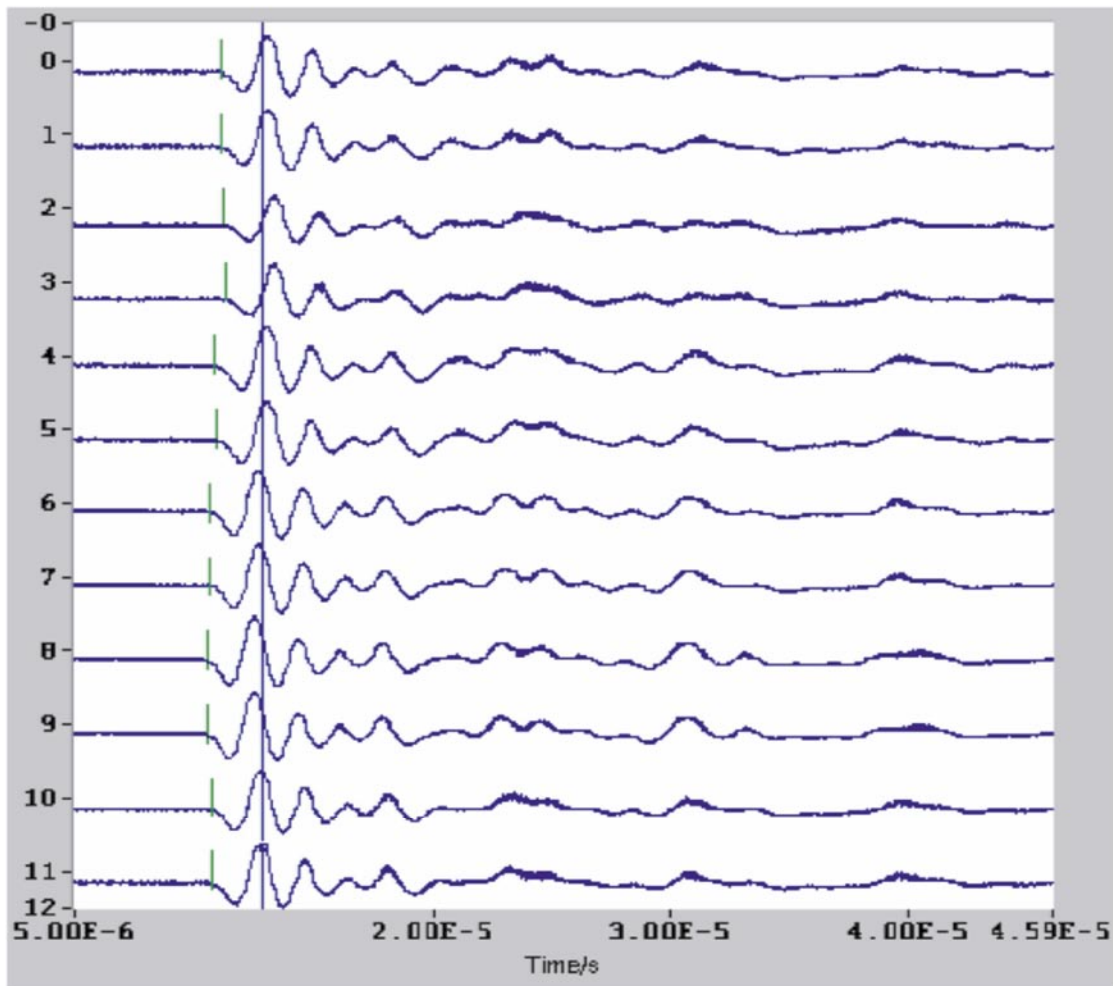


Figure G-3. Example traces from 12 measurements of P-wave travel time transverse borehole core (two from each orientation). Time picks marked with green lines. Picture captured from NGI's oscilloscope emulation software

Each test sample comprised a minimum of two consecutive determinations of acoustic pulse travel time at each of six locations around the core (at 0°, 30°, 60°, 90°, 120° and 150°) at one cross section. The seating of the transducers and application of the coupling medium was adjusted in cases where there was a significant difference between the time picks, and additional measurements were made until two similar time picks were obtained. The average of the two measured time picks was recorded.

As the travel time includes a number of other factors such as travel through the wave guides, time pick method, and delay due to the oscilloscope triggering on the rising part of the sine-wave, the determination of the true travel time was calibrated using an aluminium cylinder with known P-wave velocity. The correction factor determined in the calibration tests was subtracted from all the measurements on the rock cores.

The diameter of the core was measured and the P-wave velocity determined by dividing the diameter (in mm) by the travel time (in μs) and multiplying by 1,000 to obtain the velocity in m/s.

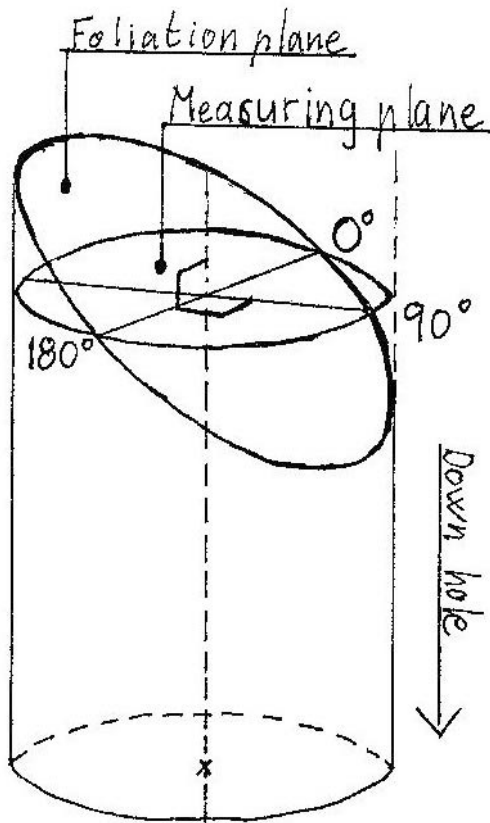


Figure G-4. Orientation of measurements.

Analysis

Since the acoustic velocity is dependant on the elastic properties of the material the results were analysed similarly to determining the stress or strain tensor in the material. In this case the velocity in the orientation θ is given by:

$$V_{\theta} = V_x \cos^2 \theta + V_y \sin^2 \theta + 2 \cdot V_{xy} \sin \theta \cos \theta \quad (1)$$

A simple regression analysis of the six measurements was used to determine the values of V_x , V_y , & V_{xy} (where the X-axis is parallel with the foliation where identifiable).

These values were used to model the complete velocity profile around the core.

The magnitude and orientation of the principal velocities was determined from the Eigen values and vectors of the 2D tensor matrix:

$$\begin{vmatrix} V_x & V_{xy} \\ V_{xy} & V_y \end{vmatrix} \quad (2)$$

3 Results

3.1 Summary of results

The results of measured values of travel time and velocity for all the tests are presented Table G-1, and the velocity and anisotropy are shown diagrammatically against depth in Figures G-5 and G-6.

The results of calculated principal velocities and anisotropy are shown diagrammatically against depth in Figures G-7 to G-9. Since the cores did not exhibit any identifiable foliation the orientation of the principal velocities is not reported.

3.2 Discussion

Accuracy and repeatability

Calibration tests on an aluminium cylinder indicated a variation of $\pm 0.03 \mu\text{s}$ in determination of the time pick. Some of this variation may be explained by temperature variations, thickness of coupling medium and seating of the shoes. Similar variations may be expected from the measurements on the cores.

Generally there is a good fit between the measurements and the best fit line which suggests that random type errors are relatively small. Typically in the whole series of tests the deviation between the measured value and the model fit is about 0.4%, with a maximum average error of 1.6%

Previous work /Chryssanthakis and Tunbridge, 2003a,b,c,d/ concluded that:

- the repeatability of the reported results for velocities is probably in the region of $\pm 100\text{--}200 \text{ m/s}$,
- the error in the orientation of the principal velocities is probably in the region of $\pm 10^\circ\text{--}20^\circ$ where the anisotropy ratio is greater than 1.1 with greater errors below this limit,
- errors in determining the anisotropy ratio and orientation are partly mitigated by the redundant data and regression analysis and it is considered that the error in the anisotropy ratio is in the region of $\pm 0.02\text{--}0.05$,
- the magnitude of the anisotropy suggests that errors of this magnitude will not have a large effect on the determination of the anisotropy ratio and orientation, and this appears to be confirmed by the generally consistent results obtained.

The deviation between the model fitted to the data and the measured data is similar to the previous work. The results are also very consistent. It is therefore concluded that the measurement errors are probably similar to those determined in the previous work. More work needs to be done to quantify the accuracy and repeatability of errors in the measurements.

Conclusions

The results from the P-wave velocity measurements show a consistent pattern over the three boreholes with maximum velocities generally between 5,500–6,000 m/s and a low anisotropy ratio of generally between 1 to 1.04. There is no apparent trend with depth over the 6 m length of the boreholes, although the higher density of data in the upper part of the borehole makes it look like there is a greater variation in both velocity and anisotropy in the

upper part of the borehole. There is a slightly lower value of maximum measured velocity, 5,484 m/s, at the top, 0.15 m depth, of borehole KQ0066G01, which might reflect damage due to excavation, but this is not found in the other two boreholes.

The variation in the results can be explained by measurement error and natural variation of velocity in the rock. However, the variation in the results is slightly greater than seen in more consistent sections of the boreholes previously examined /Chryssanthakis and Tunbridge, 2003a,b,c,d/.

The foliation is not identifiable over most of the core and the orientation of the principal velocities could not be identified relative to the foliation. The orientation of the principal velocities are therefore not reported.

The limited number of data points make any interpretation of trends unreliable. It is considered that a much greater number of measurements would be required to determine trends with a resolution of about 200 m/s.

Table G-1. Measurements of acoustic velocity, transverse core in boreholes KQ0048G01, KQ0064G01 and KQ0066G01, Simpevarp (orientation clockwise looking down hole, 0° is parallel with foliation where identified).

Depth m	Diameter mm	Corrected time, mS						Velocity m/S						Anisotropy ratio
		Parallel foliation			Perpendicular foliation			Parallel foliation			Perpendicular foliation			
		0°	30°	60°	90°	120°	150°	0°	30°	60°	90°	120°	150°	
KQ0048G01														
0.06	50.82	9.14	9.04	8.99	8.98	9.10	9.19	5,558	5,619	5,651	5,657	5,582	5,528	1.02
0.15	50.82	8.56	8.51	8.58	8.65	8.41	8.54	5,934	5,969	5,920	5,873	6,040	5,948	1.03
0.98	50.81	9.03	9.13	9.32	9.56	9.36	9.23	5,624	5,563	5,449	5,313	5,426	5,503	1.06
1.32	50.83	8.98	9.12	8.94	8.86	8.85	8.93	5,658	5,571	5,683	5,735	5,741	5,690	1.03
2.00	50.77	8.61	8.44	8.49	8.43	8.57	8.54	5,894	6,013	5,977	6,020	5,922	5,942	1.02
3.90	50.77	8.58	8.74	8.59	8.62	8.65	8.62	5,915	5,806	5,908	5,887	5,867	5,887	1.02
4.70	50.81	8.40	8.40	8.42	8.43	8.47	8.40	6,046	6,046	6,032	6,025	5,996	6,046	1.01
KQ0064G01														
0.13	50.75	8.69	8.68	8.61	8.49	8.47	8.61	5,837	5,844	5,892	5,975	5,989	5,892	1.03
0.26	50.74	8.82	8.45	8.61	8.64	8.74	8.83	5,750	6,002	5,891	5,870	5,803	5,744	1.04
0.47	50.79	8.56	8.42	8.31	8.44	8.55	8.54	5,931	6,029	6,109	6,015	5,938	5,945	1.03
0.99	50.80	8.75	8.54	8.72	8.86	8.63	8.79	5,803	5,946	5,823	5,731	5,884	5,777	1.04
1.73	50.89	8.95	8.95	8.96	8.95	9.06	9.08	5,684	5,684	5,677	5,684	5,615	5,602	1.01
2.80	50.82	8.73	8.66	8.80	8.89	8.87	8.77	5,819	5,866	5,773	5,714	5,727	5,792	1.03
4.11	50.82	8.63	8.68	8.72	8.84	8.87	8.75	5,886	5,852	5,825	5,746	5,727	5,805	1.03
5.20	50.78	9.16	9.10	9.01	9.11	9.03	9.05	5,541	5,578	5,634	5,572	5,621	5,609	1.02
KQ0066G01														
0.15	50.86	9.58	9.55	9.27	9.42	9.80	9.61	5,307	5,324	5,484	5,397	5,188	5,290	1.06
0.27	50.86	8.95	8.80	8.74	8.81	8.92	9.24	5,680	5,777	5,817	5,770	5,699	5,502	1.06
0.45	50.87	8.54	8.46	8.48	8.55	8.39	8.38	5,954	6,010	5,996	5,947	6,060	6,068	1.02
0.70	50.77	8.93	8.95	8.97	8.90	8.77	8.86	5,683	5,670	5,658	5,702	5,787	5,728	1.02
1.08	50.78	9.18	8.84	8.83	8.91	8.93	9.01	5,529	5,742	5,748	5,697	5,684	5,634	1.04
1.77	50.74	8.39	8.42	8.44	8.42	8.40	8.42	6,045	6,023	6,009	6,023	6,038	6,023	1.01
2.17	50.85	8.60	8.63	8.88	8.70	8.53	8.47	5,910	5,890	5,724	5,842	5,959	6,001	1.05
2.92	50.85	8.60	8.49	8.48	8.55	8.60	8.55	5,910	5,987	5,994	5,945	5,910	5,945	1.01
5.93	50.85	8.76	8.82	8.67	8.52	8.55	8.60	5,802	5,763	5,862	5,966	5,945	5,910	1.04

Acoustic velocity (maximum and minimum of measured data)

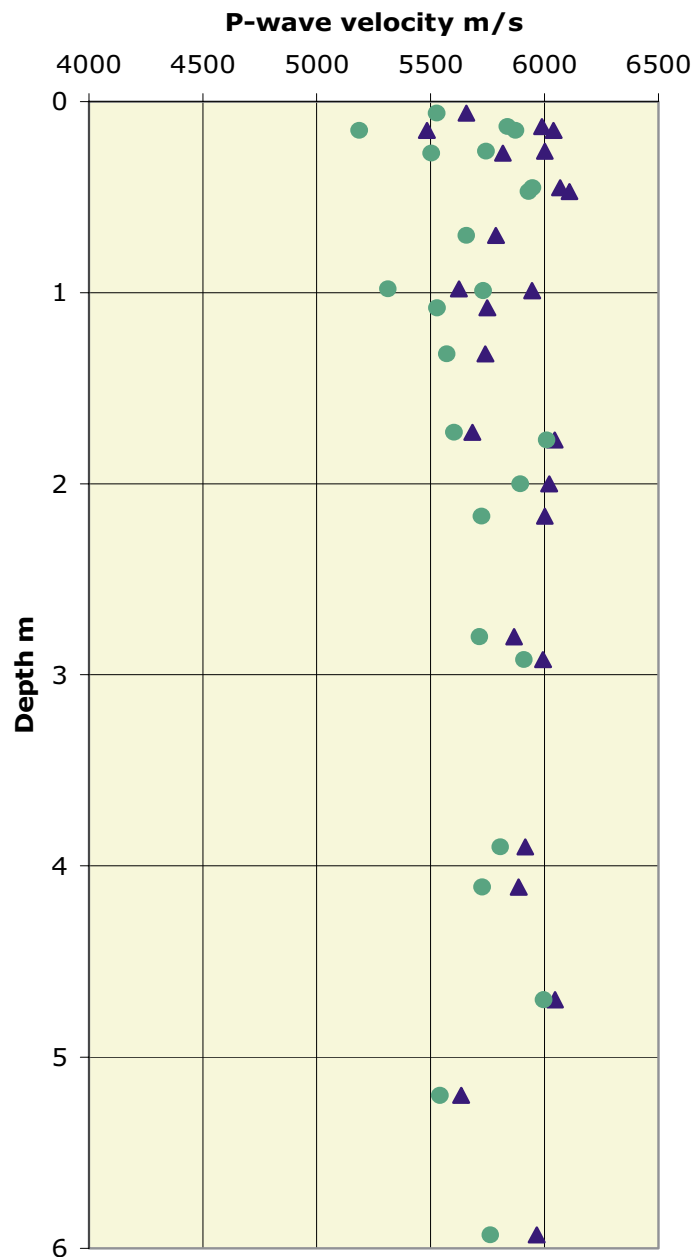


Figure G-5. Measured values of maximum and minimum acoustic velocities plotted against depth down boreholes KQ0048G01, KQ0064G01 and KQ0066G01.

Anisotropy (maximum/minimum - measured data)

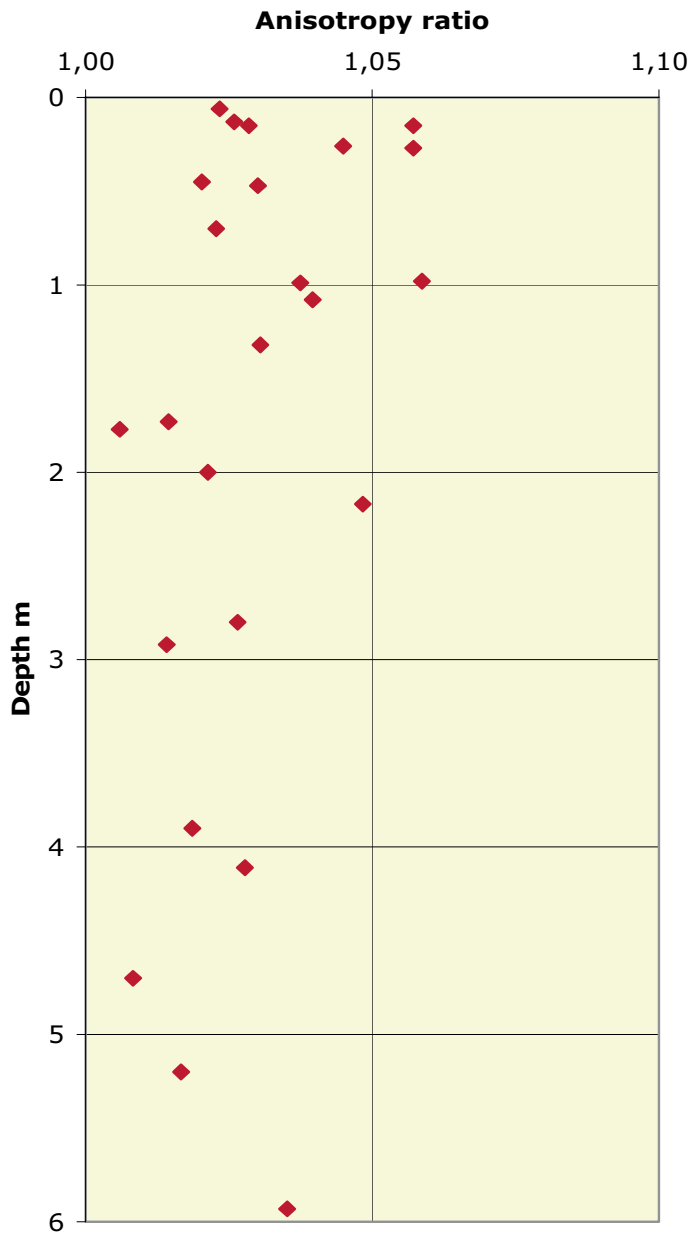


Figure G-6. Measured values of acoustic velocity anisotropy plotted against depth down boreholes KQ0048G01, KQ0064G01 and KQ0066G01.

Acoustic velocity (principal velocities)

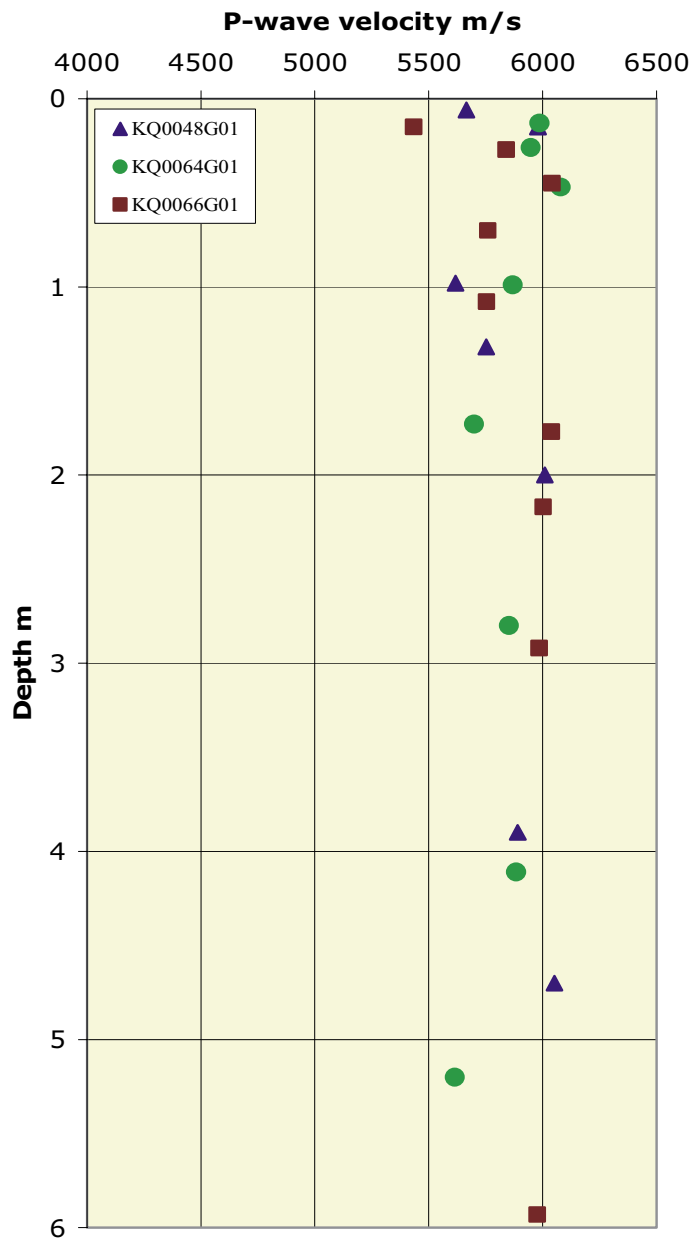


Figure G-7. Calculated values of maximum principal acoustic velocities plotted against depth down boreholes KQ0048G01, KQ0064G01 and KQ0066G01.

Anisotropy (principal velocities)

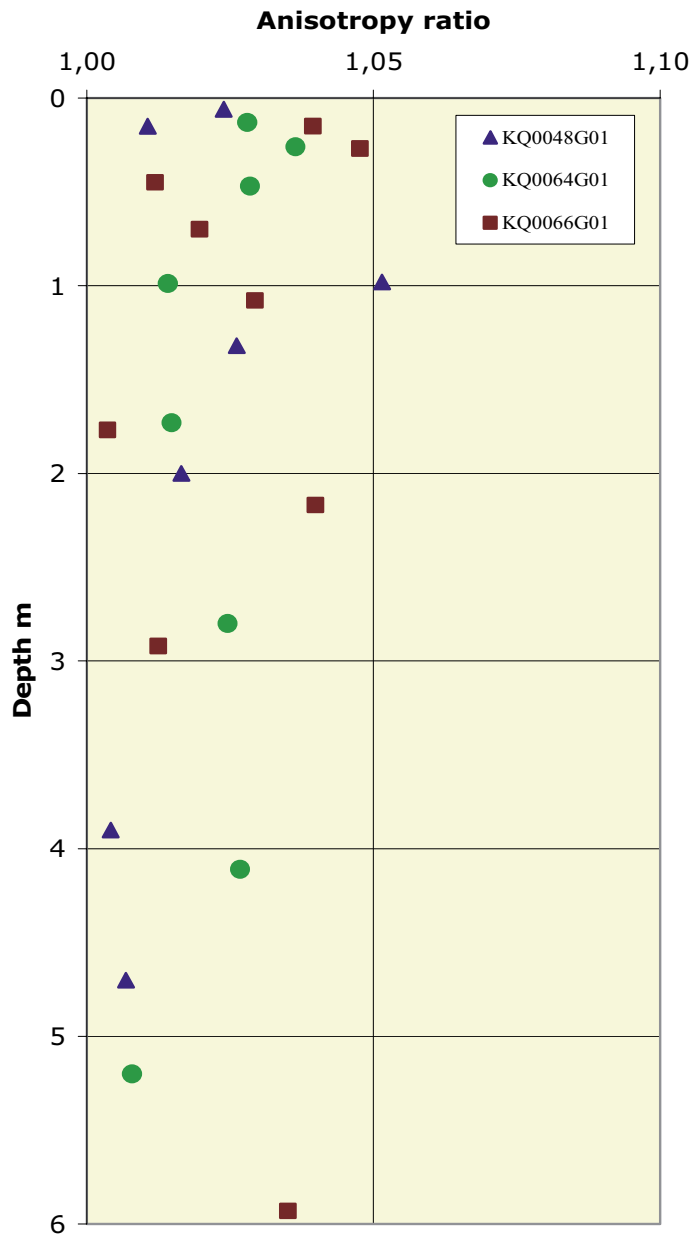


Figure G-8. Calculated values of maximum and minimum principal acoustic velocity anisotropy plotted against depth down boreholes KQ0048G01, KQ0064G01 and KQ0066G01.

Acoustic velocity (principal velocities)

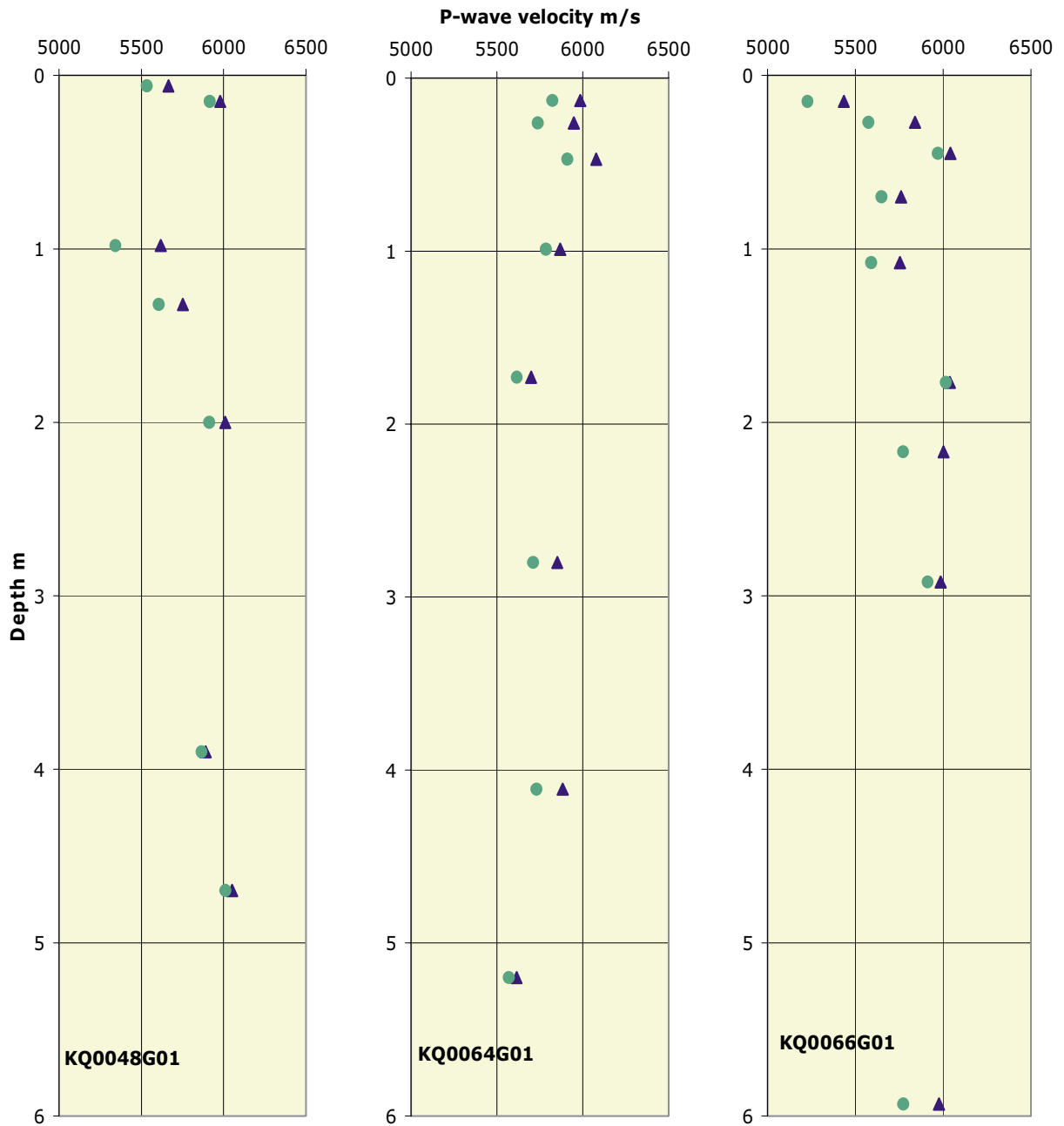


Figure G-9. Calculated values of maximum and minimum principal acoustic velocities plotted against depth down boreholes KQ0048G01, KQ0064G01 and KQ0066G01.

4 References

Chryssanthakis P, Tunbridge L, 2003a. Site investigation, Forsmark. Borehole: KFM01A. Determination of P-wave velocity, transverse borehole core, NGI.

Chryssanthakis P, Tunbridge L, 2003b. Site investigation, Simpevarp. Borehole: KSH01A. Determination of P-wave velocity, transverse borehole core, NGI.

Chryssanthakis P, Tunbridge L, 2003c. Site investigation, Forsmark. Borehole: KFM02A. Determination of P-wave velocity, transverse borehole core, NGI

Chryssanthakis P, Tunbridge L, 2003d. Site investigation, Simpevarp. Borehole: KSH01A. Determination of P-wave velocity, transverse borehole core, NGI.

Eitzenberger A, 2002. Detection of Anisotropy by Diametral Measurements of Longitudinal Wave Velocities on Rock Cores, SKB report in press.

Janson T, 2002. Metodebeskriving för: bestämning av p-vågens hastighet. SKB report MD 190.002 ver 1.0.

Borehole Velocity Profile Survey – report

**Borehole Velocity Profile Survey in
the APSE Tunnel between boreholes
KQ0064G03 and KQ0064G02**

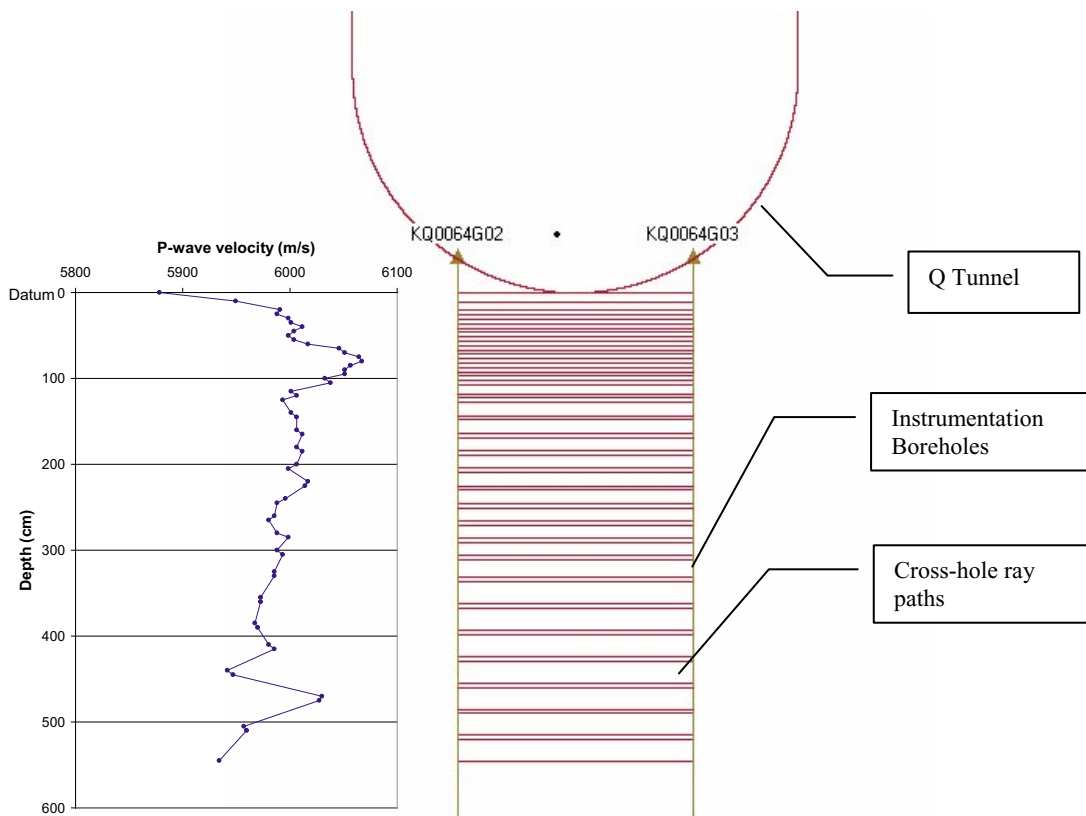
W S Pettitt, D S Collins, J Haycox, R P Young
Applied Seismology Consultants Ltd

November 2003

Executive summary

An ultrasonic velocity survey has been conducted in the Q-tunnel as part of the Äspö Pillar Stability Experiment (APSE). The survey has used two of the acoustic emission instrumentation boreholes excavated vertically from the floor of the tunnel, and was conducted as an additional investigation during the equipment installation. The principal motivation for the survey was to investigate the depth of the Excavation Damaged Zone beneath the tunnel floor.

Two ultrasonic sensors, a receiver and a transmitter, have been inserted into each of the instrumentation boreholes (KQ0064G03 and KQ0064G02) and measurements have been taken at various depths below the sensor datum. The datum represents the lowest level of the tunnel floor. The boreholes were positioned either side of the tunnel axis, so the survey has resulted in ray paths that travel orthogonal to the tunnel axis immediately beneath the tunnel floor (called the 'Cross-hole Profile'). The volume of rock that has been investigated is in the immediate vicinity of the future position of deposition hole DQ0063G01.



The velocity results show an increasing trend in the first 40 cm below the tunnel floor, up to a 'background' level of approximately $6,010 \text{ m}\cdot\text{s}^{-1}$. The background velocity includes a gradual decay down to a P-wave velocity of approximately $5,950 \text{ m}\cdot\text{s}^{-1}$ at 6 m depth. This is believed to be a response to a decaying induced compressive stress beneath the tunnel floor. Between 50 and 125 cm below the floor there is an anomalously high velocity zone (peak velocity of $6,070 \text{ m}\cdot\text{s}^{-1}$) that could also be a stress response, but is more likely to be the result of a lithological change such as the position of a quartz-rich band.

The increasing velocity immediately beneath the tunnel floor will include both a damage and stress-relaxation effect from the tunnel void. The data has been interpreted as a damaged zone that includes the first two data points at 0 and 10 cm depth as these are significantly lower than the background level. This zone is likely to include fractures induced by blast damage from tunnel excavation, but these may be sporadically distributed as the ray path samples a 2.76 m length, and is therefore a summation of variability across the tunnel floor. Measurements between 20 and 40 cm are close to the background level and are believed to be a stress relaxation response. When compared to borehole core measurements the observed in situ velocities are all systematically higher, including those interpreted as being in the tunnel damaged zone. The core measurements show much higher variability, which is likely due to the shorter ray paths (5 cm compared to 2.76 m in situ) causing increased measurement uncertainties. It is therefore difficult to provide a more detailed comparison between the core and in situ measurements.

Signal amplitude changes have also been measured along the Cross-hole Profile. These show a gradual increase in amplitude to 1.5–2 m depth. It should be noted that ultrasonic amplitudes are strongly dependent on the coupling of the sensors. This is observed as variations in the amplitude measured between adjacent depth positions. The overall systematic increase in amplitudes with depth is likely to be a real response in the rock mass and may indicate the extent of a stress-disturbed zone (rather than damaged zone) that the measured velocities are less sensitive to.

The sensor configuration that has been used has also provided two ‘Borehole Profiles’, that include ray paths that travel parallel to the borehole. In this case, there is little effect on the profiles that can be attributed to a tunnel damage zone. As the profiles began at the sensor datum (a few tens of centimetres down each borehole) then this is a consistent result to that observed in the Cross-hole Profile as the damaged zone must therefore be above this. The amplitude result observed in the Cross-hole Profile is also reproduced in the Borehole Profiles, with amplitudes increasing to 1.5–2 m depth. The borehole velocities are consistently greater for KQ0064G02, possibly due to a small difference in lithology across the tunnel.

Contents

1	Introduction	194
2	Instrumentation	195
3	Survey method	196
4	Processing method and estimated uncertainties	199
5	Results and interpretation	200
5.1	Cross-hole Profile	200
5.2	Borehole Profiles	204
6	Conclusions and discussion	208
	Appendix A	209

1 Introduction

This report outlines the procedures and results obtained for the Borehole Velocity Profile Survey (BVPS) between boreholes KQ0064G03 and KQ0064G02 used in the Äspö Pillar Stability Experiment (APSE). Figure H-1 shows the borehole geometry relative to the future positions of the two deposition holes. By inserting two sensors into each borehole and carrying out measurements at various depths it was possible to obtain velocity and amplitude profiles through the rock between and along the boreholes. This survey was performed to primarily determine the depth of the Excavation Damaged Zone beneath the floor of the tunnel, and in the immediate vicinity of the future position of deposition hole DQ0063G01.

The APSE is being undertaken to demonstrate the current capability to predict spalling in a fractured rock mass using numerical modelling techniques. It is also designed to demonstrate the effect of backfill and confining pressure (up to 1 MPa) on the propagation of micro-cracks in rock adjacent to deposition holes within a repository¹. In order to realise these objectives a pillar of rock between two deposition holes will be monitored using an array of ultrasonic transducers. By monitoring for AE (acoustic emission) activity and undertaking regular, repeated velocity surveys the response of the rock pillar to heating and variations in confinement pressure can be assessed. These results will be compared to those obtained from several numerical modelling studies.

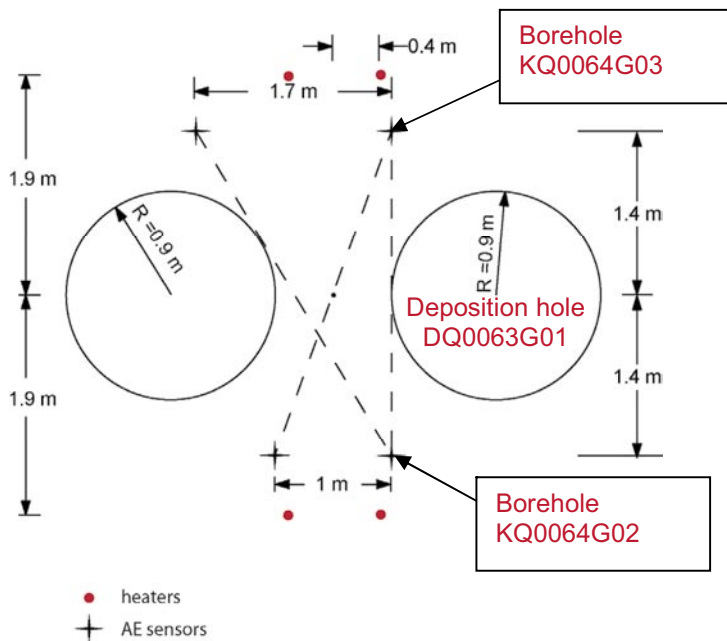


Figure H-1. Plan view of deposition hole geometry showing locations of notable elements for this study; Deposition Hole DQ0063G01 and boreholes KQ0064G03 and KQ0064G02. The two deposition holes shown here were not excavated at the time of the survey.

¹ Christer Andersson, "Äspö Pillar Stability Experiment: Feasibility Study", March 2002. TD-02-07

2 Instrumentation

The BVPS was undertaken prior to the installation of an AE/Ultrasonic System that will monitor the Pillar Stability experiment. The instrumentation was set up with a transmitter and a receiver in each borehole so as to provide a ray path parallel to each borehole and a ray path traversing the rock volume between them.

The sensors used were Physical Acoustics Corporation (PAC) R6UC with a frequency response of approximately 35–350 kHz. This type has a vulcanised surround and a high pressure reinforced cable to protect them from water infiltration. They were fixed at the bottom of two borehole-installation frames manufactured by ASC, as shown in Figure H-2. The frames were assembled as they were inserted into the boreholes allowing measurement at up to 6 m depth. The alternate arrangement of transmitter and receiver enabled two cross-hole ray paths to be measured without moving the frames.

Cables from each borehole were led to junction boxes on each side of the tunnel containing PAC 60dB pre-amplifiers that were temporarily connected to an ESG Hyperion Ultrasonic System (Figure H-3). Channel 1 on the acquisition system corresponded with the receiver in borehole KQ0064G03 and channel 10 with the receiver in borehole KQ0064G02.

Once the experiment had been completed the frames were removed from the boreholes and the system was reconfigured for the Pillar Stability Experiment.

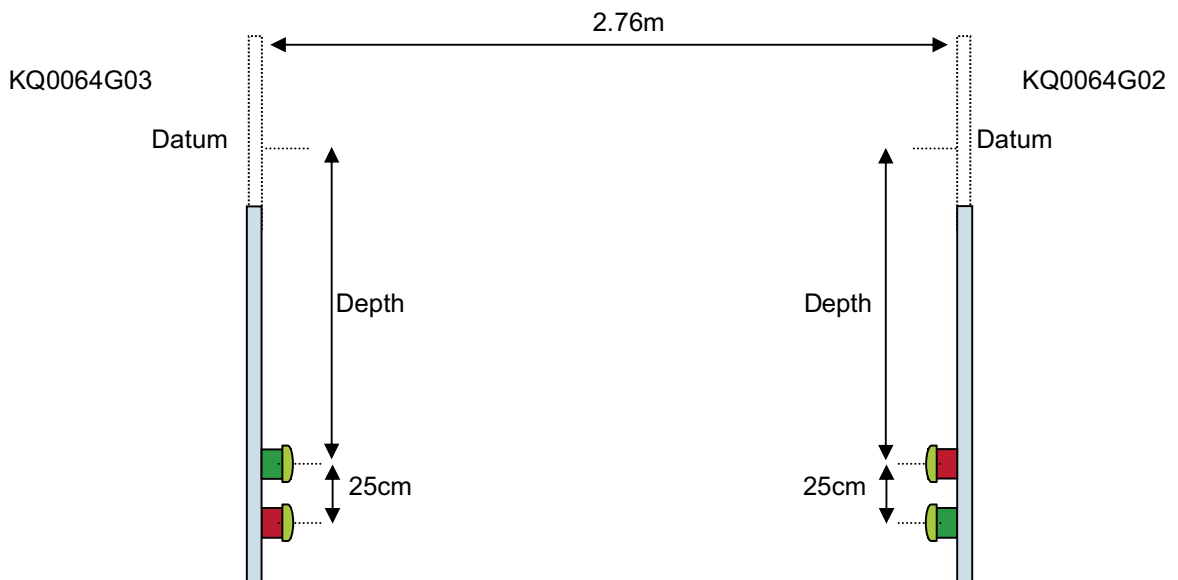


Figure H-2. Arrangement of receivers in boreholes and associated dimensions.

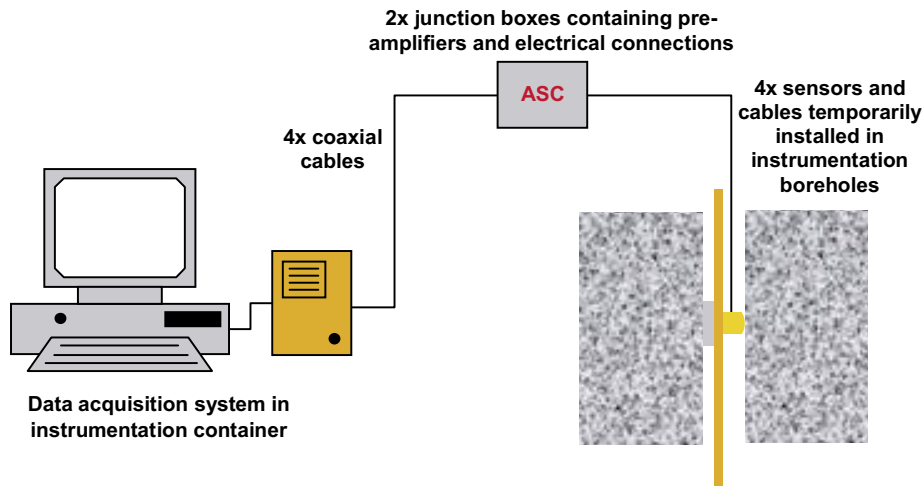


Figure H-3. Schematic diagram of the main components of the temporary instrumentation system.

3 Survey method

The survey was undertaken between boreholes KQ0064G03 and KQ0064G02 (corresponding to ASC 1 and ASC 2 respectively).

The survey consists of two components

- i) A “Cross-hole Profile” where velocity and amplitude measurements are taken between boreholes with ray paths traversing the edge of the future location of deposition hole DQ0063G01.
- ii) Two “Borehole Profiles” where velocity and amplitude measurements are taken along each borehole.

The depth of each ultrasonic measurement was taken from the top sensor to the datum, which corresponds to the lowest level of the tunnel floor. The first measurement was at the datum. In the first 1 m depth measurements were taken every 10 cm. In the next 2 m measurements were taken every 20 cm and a 30 cm gap was used thereafter. The actual density of ray paths is greater than these values because of the use of two sensors per borehole. Figure H-5 gives a representation of the actual coverage appointed by the BVPS.

At each position an ultrasonic measurement was performed. Waveforms were recorded on the two receivers and displayed on two channels in the processing and visualisation software. ASC’s InSite Seismic Processor was used to perform this task. Figure H-6 shows example waveforms.

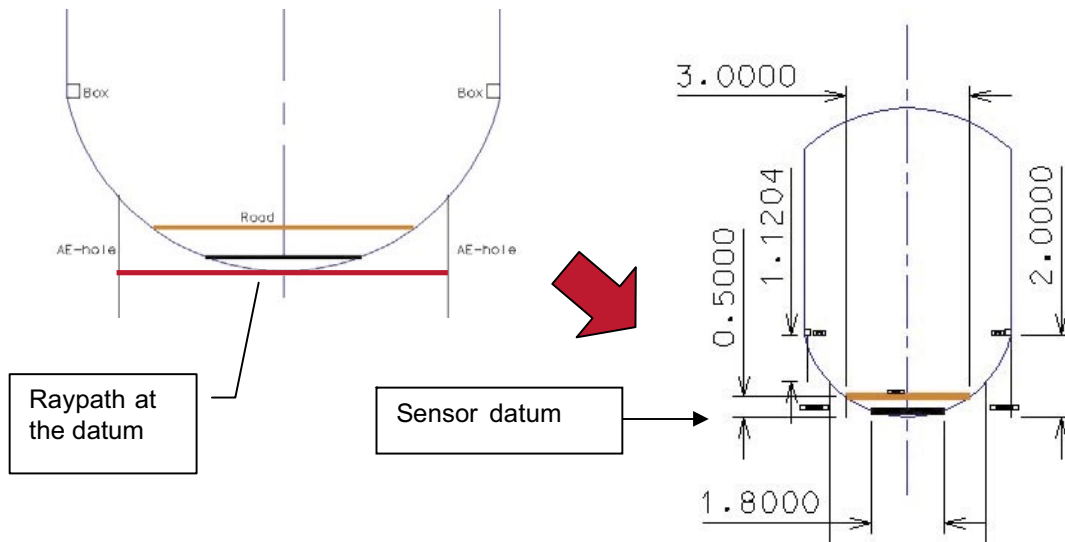


Figure H-4. Illustration of the datum used for positioning the sensors in the instrument boreholes. Table H-1 gives the depths of the sensor datum in each of the boreholes used.

Table H-1. Depth of the datum in each of the instrumentation boreholes used. The depth is measured from the borehole collar.

Borehole	Depth to datum (cm)
KQ0064G03	38
KQ0064G02	26

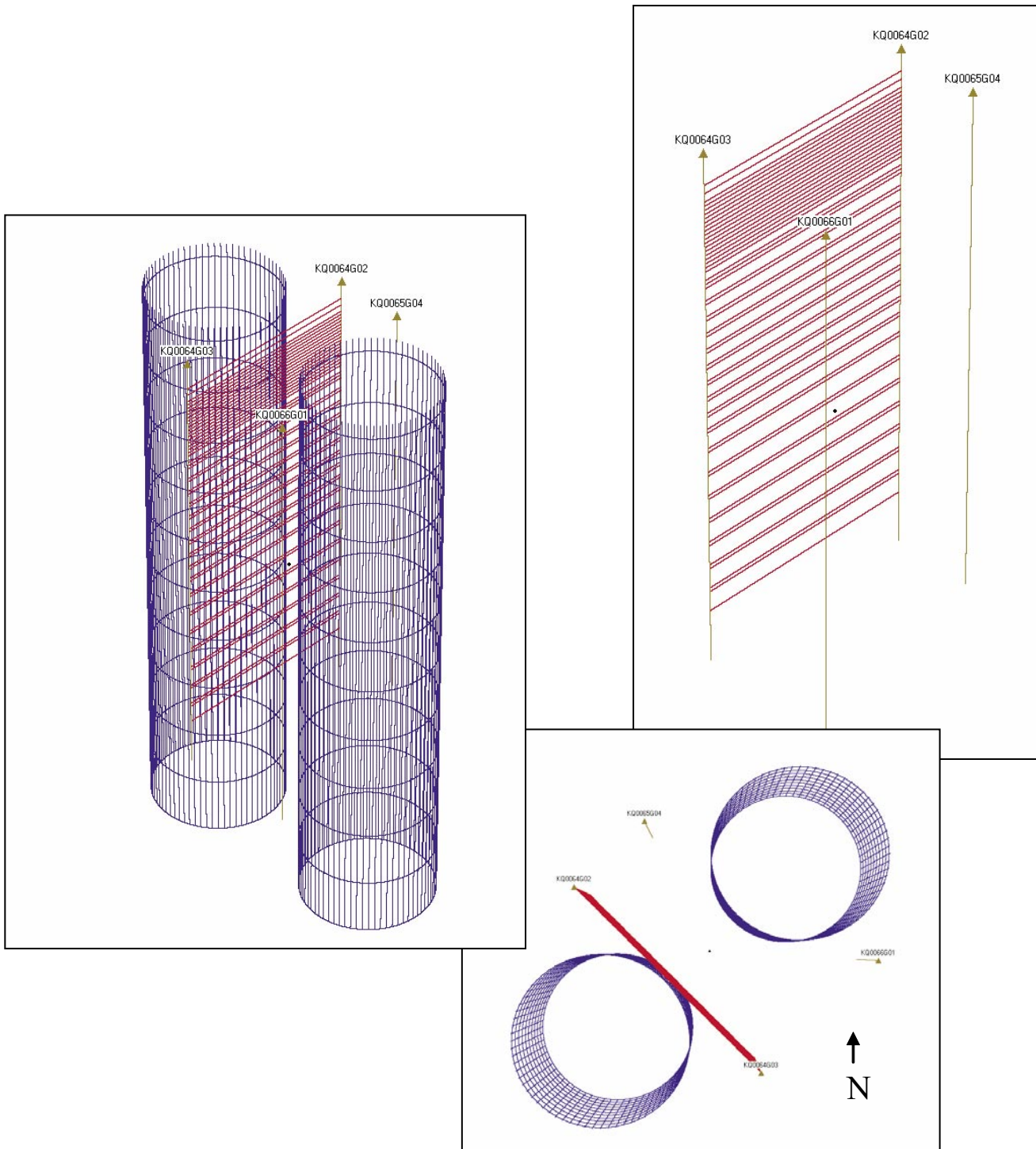


Figure H-5. Location of the boreholes used in the BVPS and coverage through the cross section. All four boreholes and the future position of the deposition holes are displayed.

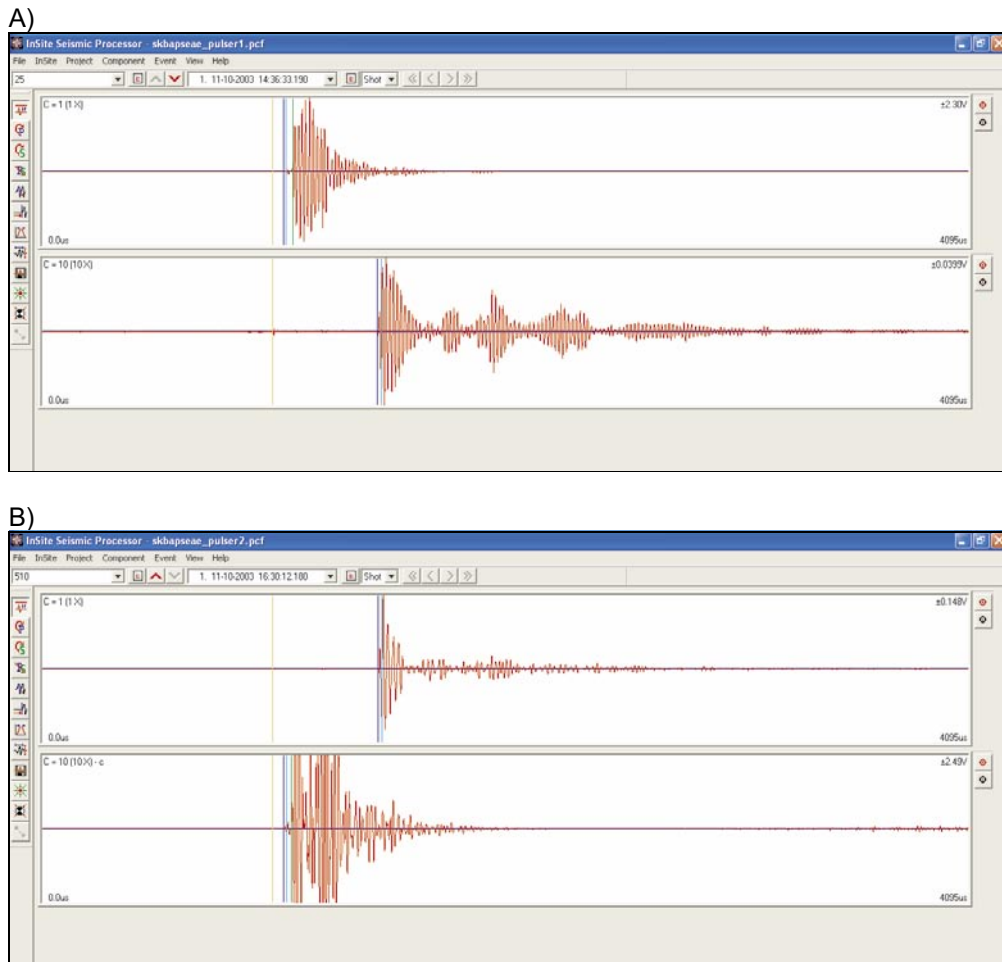


Figure H-6. Examples of waveforms recorded during this study in A) Borehole KQ0064G03 and B) Borehole KQ0064G02. Top waveform recorded after pulse from borehole KQ0064G03 and bottom waveform recorded after pulse from borehole KQ0064G02.

4 Processing method and estimated uncertainties

Waveform signals were all manually picked for phase arrivals and amplitudes. Where possible both P and S waves have been processed. Reference measurements were then chosen on each survey and arrivals from all other measurements were cross-correlated with the reference in order to obtain precise changes in velocity². The software processing parameters are given in Appendix A.

P and S-wave arrivals were manually picked for a ‘reference’ measurement chosen from the start of the survey. Knowing the transmitter and receiver locations the absolute velocity was determined. A cross-correlation procedure was then used to process subsequent measurements to produce a velocity change that was then added to the reference velocity. A 5× oversampling was added to the arrival data using a spline function. This has the effect of smoothing the amplitude functions and results in high-precision measurements of P- and S-wave velocity change. The main reason for the reduction of uncertainty is the dependency

² Pettitt W S, Baker C, Young R P, Dahlström L-O, and Ramqvist G, The assessment of damage around critical engineering structures using induced seismicity and ultrasonic techniques, *Pure and Applied Geophysics*, 159, 179–195, 2002.

of manual picking on the user’s judgement of the point of arrival. This can usually be quite haphazard because of random noise superimposed on the first few data points of the first break.

The Cross-hole Profile has a ray path length of 2.76 m. The absolute velocity calculated on the reference measurement has an estimated uncertainty of $\pm 30 \text{ m.s}^{-1}$ (± 2 data points). The cross-correlation procedure produces changes in velocity between measurements with estimated uncertainties of $\pm 5 \text{ m.s}^{-1}$ (± 2 oversampled data points). This precision can be confirmed by comparing adjacent data points on the survey data. No S-wave information could be obtained from the Cross-hole survey as the transducers were positioned so that they faced each other. In this case the transmission orientation is most optimal for the compressional waves and least optimal for the transverse waves.

The Borehole Profiles have ray path lengths of 25 cm, resulting in an estimated uncertainty of $\pm 250 \text{ m.s}^{-1}$ on the absolute velocity calculated from the reference measurement and $\pm 50 \text{ m.s}^{-1}$ on the cross-correlated velocities. Estimated uncertainties in the S-wave measurements are $\pm 75 \text{ m.s}^{-1}$ and $\pm 15 \text{ m.s}^{-1}$ respectively.

5 Results and interpretation

5.1 Cross-hole Profile

The P-wave velocity profile between the instrumentation boreholes is displayed in Figure H-7. This is a combination plot for ray paths travelling in both directions. The depth is measured with respect to the sensor datum. The datum represents the ray path that passes directly beneath the tunnel floor.

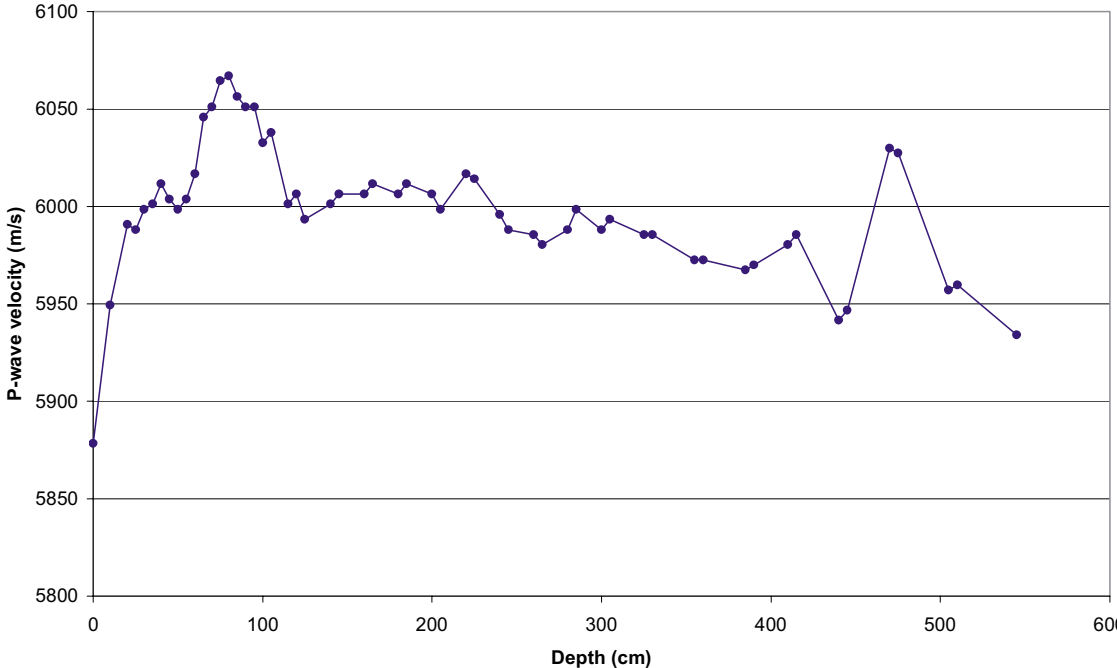


Figure H-7. Combined cross-hole P-wave velocity values between boreholes KQ0064G03 and KQ0064G02.

It should be noted that because the ray paths travel across the tunnel floor, along a 2.76 m ray path, then observed velocity variations are an average of localised variability along the ray path. The velocity increases systematically in the first 40 cm from 5,880 ms⁻¹ to 6,010 ms⁻¹. Between the depths of 50 cm and 125 cm there is a peak in velocity up to a maximum of 6,070 ms⁻¹. This appears to be a significant increase above the background pattern, which is a gradual reduction in velocity down to approximately 5,950 ms⁻¹ at 6 m depth. Another localised variation occurs between 400 cm and 515 cm where a decrease followed by an increase in P-wave velocity occurs.

Figure H-8 shows example P-wave arrivals, used in the cross-correlation algorithm, from two measurement positions. This plot highlights the clear shift in the arrivals associated with the changes in observed velocity.

The extent of the excavation damaged zone can be estimated by determining the depth to where a background velocity level is reached. However, superimposed onto any observations is also the effect of stresses induced by the tunnel void, so it is then a matter of interpretation as to what is related to damage and what is related to stress disturbance. Figure H-9 shows average P-wave velocity data measured through the core from borehole KQ0064G01³. This borehole has been excavated from the floor of the Q tunnel as the pilot hole for deposition hole DQ0063G01 and is positioned close to the cross-hole ray paths. The data is averaged across six different ray paths transmitted at different angles through the core (Figure H-10). The core data shows increased variability from higher measurement uncertainties caused by the much shorter ray path lengths (5 cm compared to 2.76 m). There is a decreasing trend in velocity down the core that appears to be a magnification of the trend observed in situ, but it is uncertain what the significance of this is. There is also a systematically lower velocity than measured in situ, probably due to stress relaxation of the core.

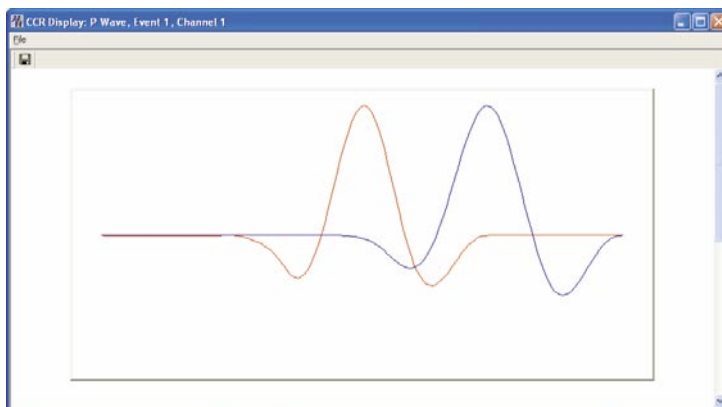


Figure H-8. Comparison of P-wave arrivals measured at two survey points. The red curve is the reference measurement for the cross-correlation algorithm. The example is a pulse from borehole 2 with receiver at 510 cm depth (blue) cross correlated with measurement at 80 cm depth (red).

³ Chyssanthakis and Tunbridge, “Äspö Pillar Stability Experiment: Sonic Velocity in Pilot Hole Cores”, September 2003.

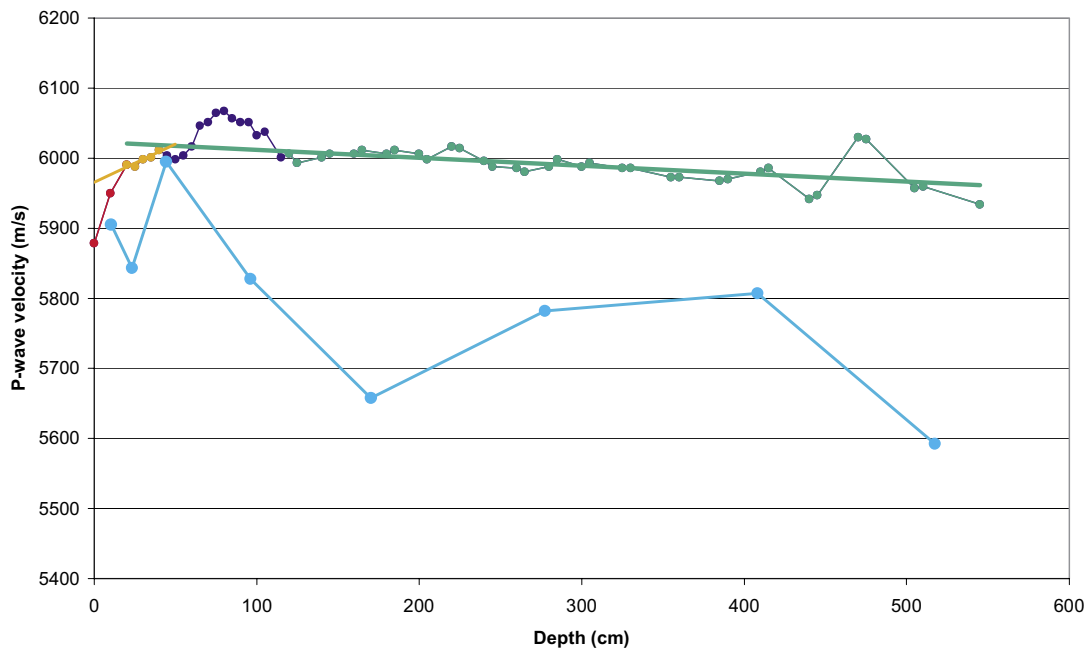


Figure H-9. Average P-wave velocities calculated for the core of borehole KQ0064G01 compared to the cross-hole velocity survey. The latter is split into sections corresponding to interpreted changes.

Also shown on Figure H-9 is the cross-hole velocity survey. This has been interpreted into four sections coloured red, orange, blue and green. The green section is the background velocity trend between 120 and 545 cm. A linear best-fit line has been fit to the data in Microsoft Excel. The gradual reduction of velocity away from the tunnel floor is probably associated with the reduction of compressive stresses away from the void, but may also be a reflection of a gradual change in lithology. The blue section is the high velocity anomaly between approximately 50 and 125 cm depth. This is probably associated with a localised lithological change, perhaps due to quartz rich bands. However, it could also indicate a zone of high compressive stress acting to close existing microfractures. Between 0 and 40 cm depth, the measurements have been split into two sections. The first red section includes two data points at 0 and 10 cm depth. These data points are a significantly lower velocity than the background. Between 20 cm and 40 cm the data points are coloured orange and a best-fit line is given. These data points also show a systematic increase, but at a much reduced rate and have velocities that are similar to those measured at 6 m depth. These variations are interpreted as a damaged zone down to 10–20 cm depth (red) and a zone of stress relaxation extending between approximately 20 and 40 cm. All variations observed here are less than the measurement uncertainties on the cores, and are only observed due to the longer ray paths and higher resolution of the cross-correlation method. Analysis of AE data during the APSE may also provide further evidence of the extent of the damaged zone.

P-wave amplitude measurements across the rock mass are displayed in Figure H-11. It should be noted that there is an effect of sensor coupling differences between measurement positions that are also superimposed on this plot. This explains the variable amplitudes observed between neighbouring measurement positions, particularly at greater depths. However, there is a clear trend of increasing signal amplitudes down to about 1.5 to 2.0 m below the datum. This may indicate that the measured amplitude is sensitive to the excavation stress-disturbed zone and could be associated primarily with rock changes in the immediate vicinity of the measurement boreholes.

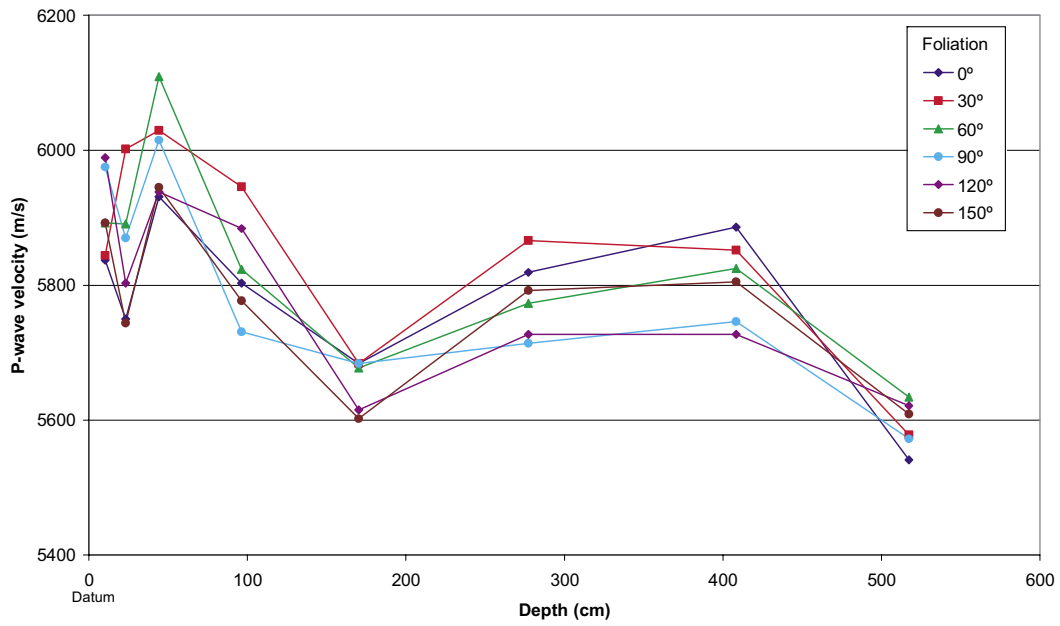


Figure H-10. P-wave velocities measured at different angles around the core from borehole KQ0064G013.

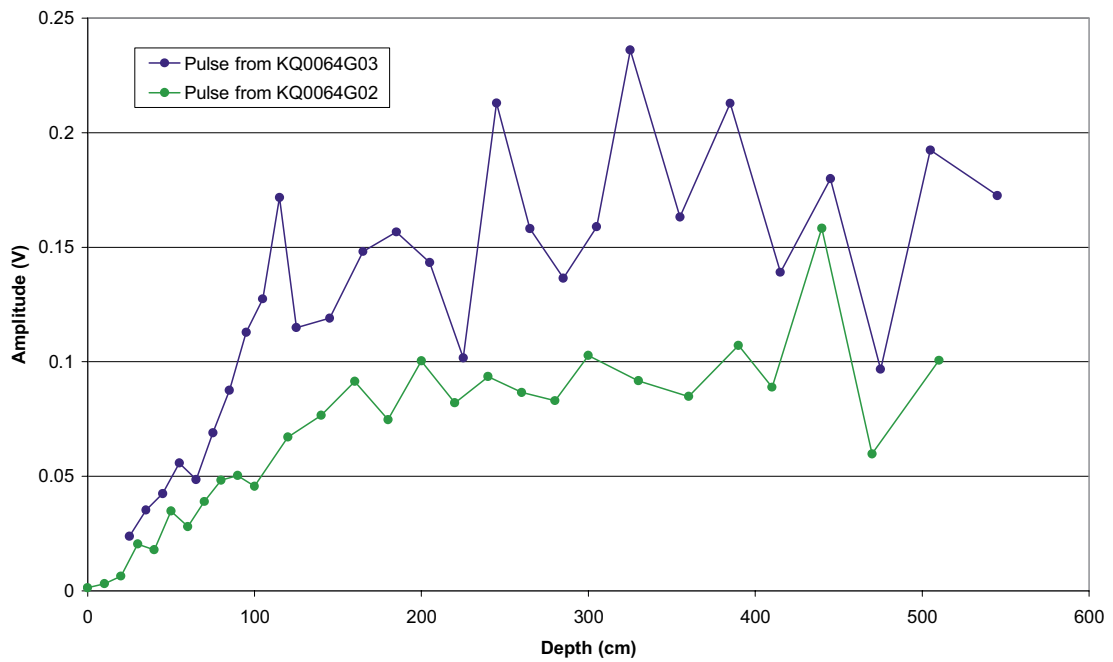


Figure H-11. Cross-borehole P-wave amplitude measurements. The blue line represents pulses from KQ0064G03 received on KQ0064G02. The green line represents pulses from KQ0064G02 received on KQ0064G03.

5.2 Borehole Profiles

The P-wave and S-wave velocity profiles parallel to the instrumentation boreholes are given in Figure H-12 and Figure H-13 respectively. The depth values shown are given by the mid point of the ray path between the transmitter and the receiver. Figure H-14 gives example arrivals used in the cross-correlation algorithm, showing consistent waveform shape between measurement positions.

The profiles start at the sensor datum, 26 and 38 cm from the borehole collars (Table H-1). There is very little effect of a damaged zone indicated on the charts, although the first one or two data points may have reduced velocity. This is consistent with the results measured in the cross-hole profile as the borehole profiles below the edge of the imaged damaged zone (maximum 20 cm depth).

There is greater variation in the velocities obtained along the two instrumentation boreholes than in the cross-hole profile (Figure H-7). This is caused by the higher measurement uncertainty, but can also have an effect of localised inhomogeneities along the borehole over the much shorter ray path length (25 cm). P-wave and S-wave velocities are both consistently greater in borehole KQ0064G03, which might indicate a slight change in lithology across the tunnel. However, this can be explained by the measurement uncertainties in the absolute velocities ($\pm 250 \text{ m.s}^{-1}$ for the P-wave and $\pm 75 \text{ m.s}^{-1}$ for the S-wave). A full explanation may be possible by comparing the logs of the boreholes.

P and S-wave amplitudes are given in Figure H-15 and Figure H-16 respectively. The amplitudes show an increasing trend in the first 1.5 to 2.0 m depth. This is consistent with the cross-hole data, and is interpreted as the extent of the excavation disturbed zone.

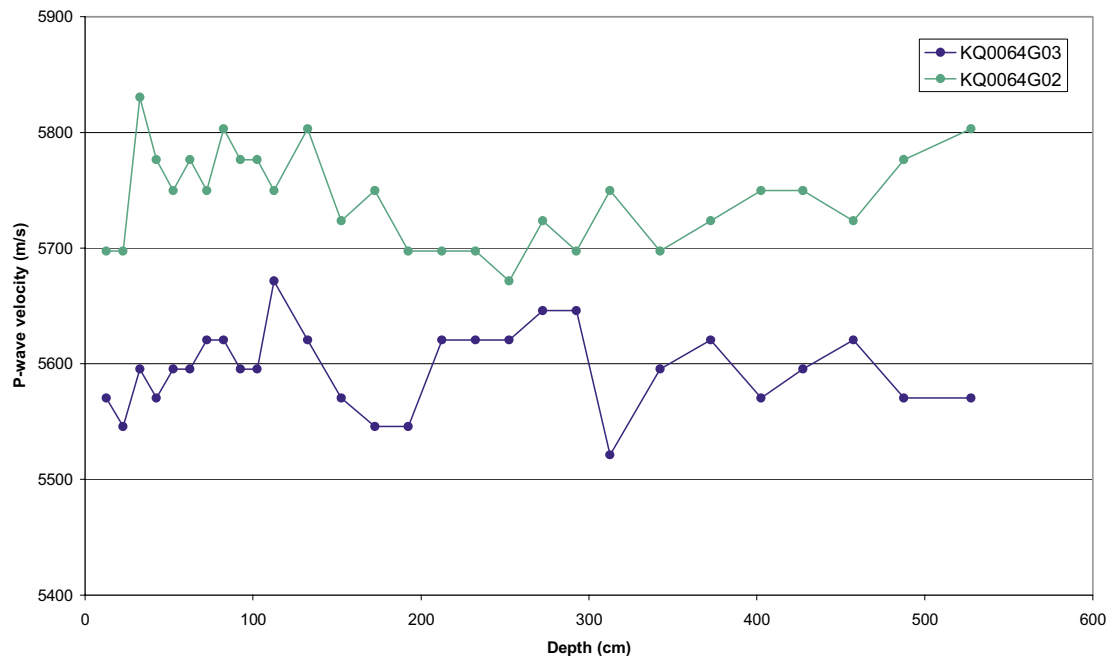


Figure H-12. P-wave velocity along boreholes KQ0064G03 and KQ0064G02. Depth is taken to be the mid-point between transmitter and receiver.

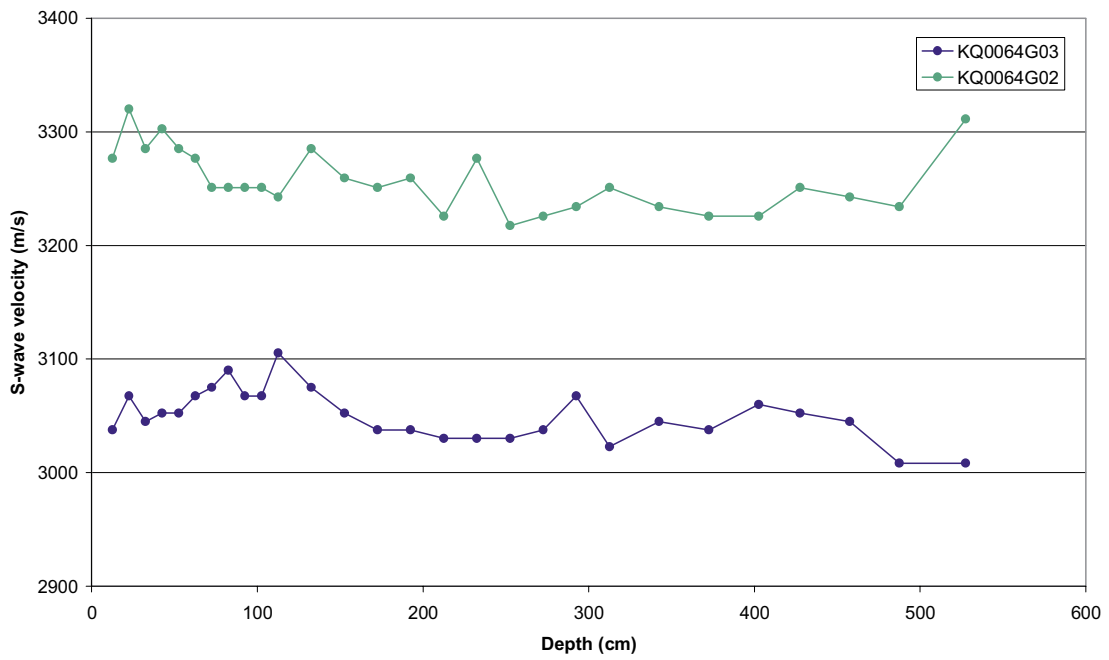


Figure H-13. S-wave velocity along boreholes KQ0064G03 and KQ0064G02. Depth is taken to be the mid-point between transmitter and receiver.

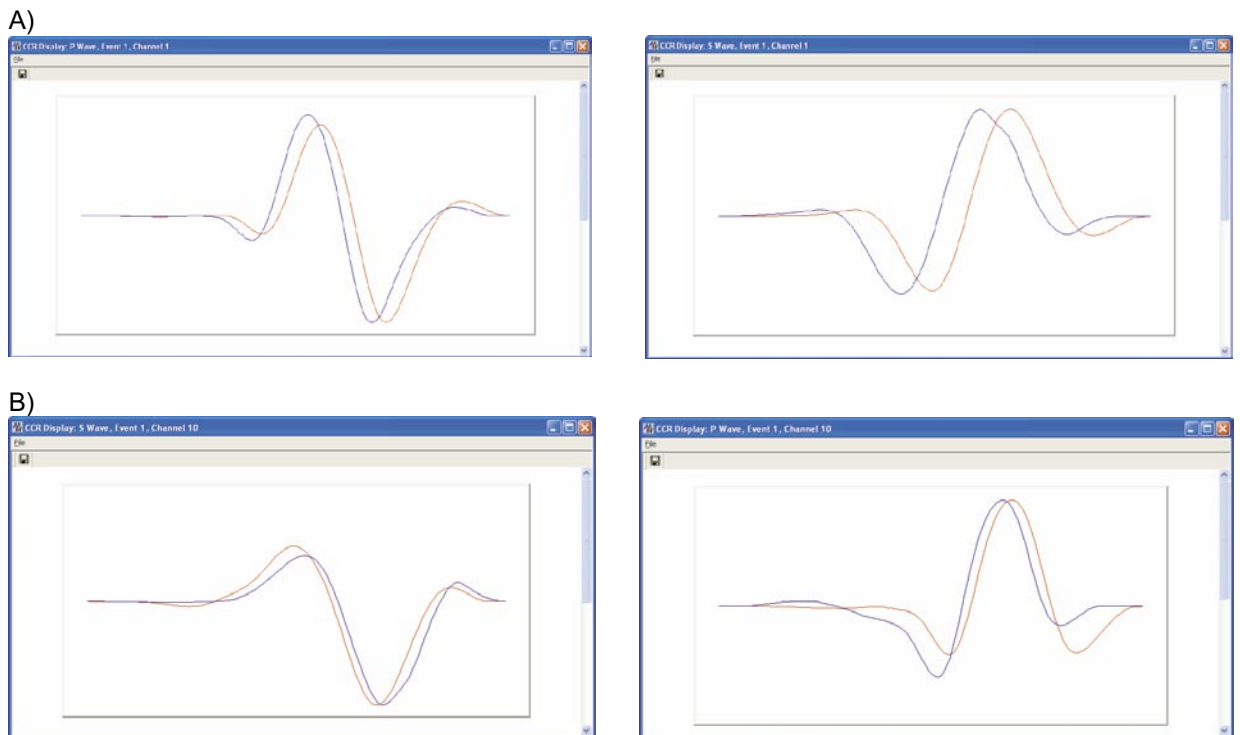


Figure H-14. Comparison of P-wave (left) and S-wave (right) arrivals measured at two survey points. The red curve is the reference measurement for the cross-correlation algorithm. A) Pulse from borehole 1 with the receiver at 125 cm depth cross correlated with the measurement at 25 cm depth. B) Pulse from borehole 2 with the receiver at 510 cm depth cross correlated with the measurement at 0 cm depth.

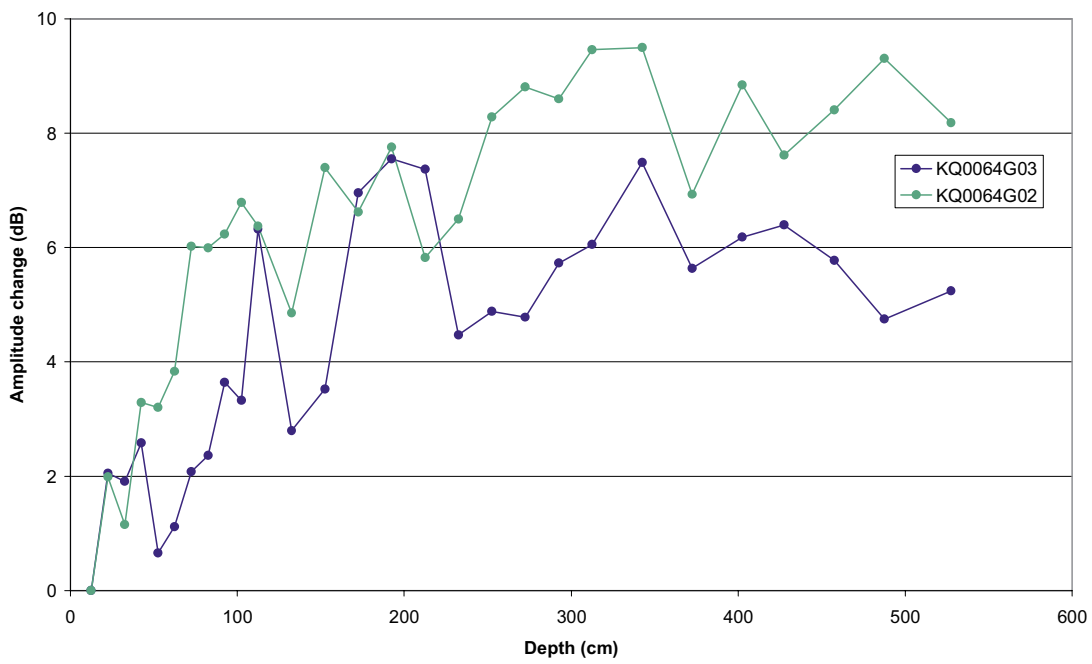
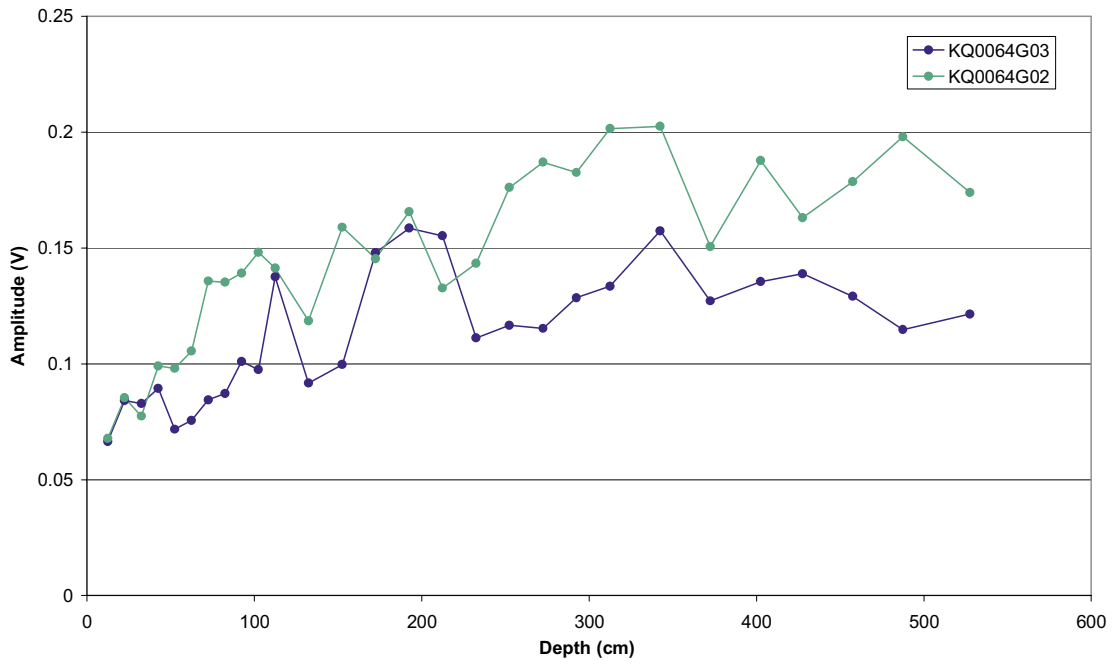


Figure H-15. P-wave amplitude and amplitude change graphs.

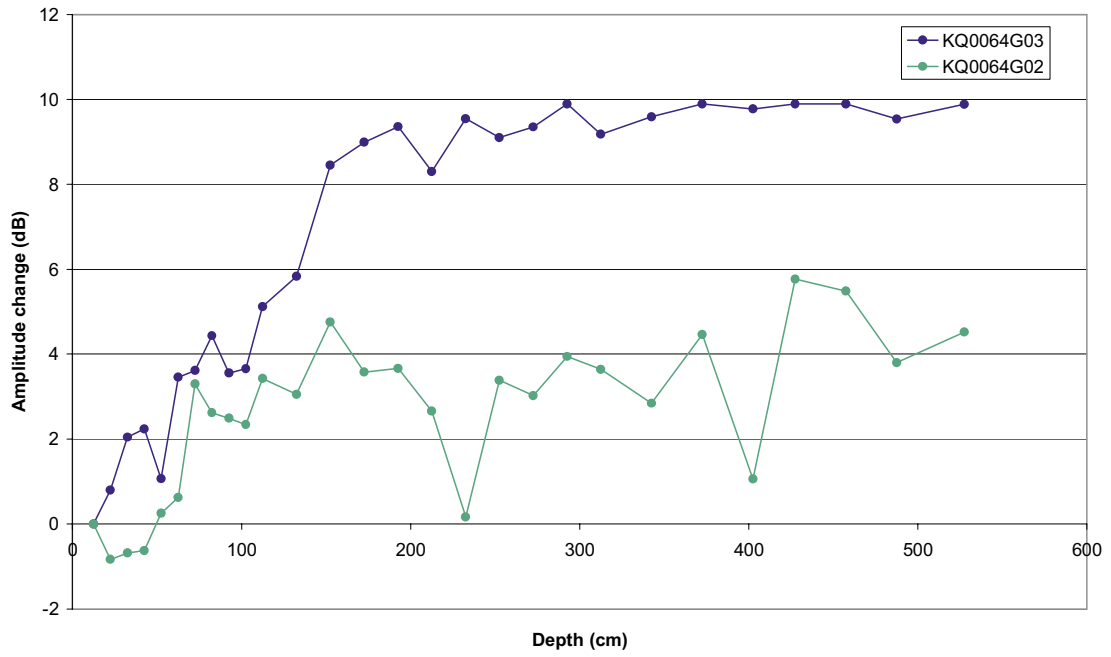
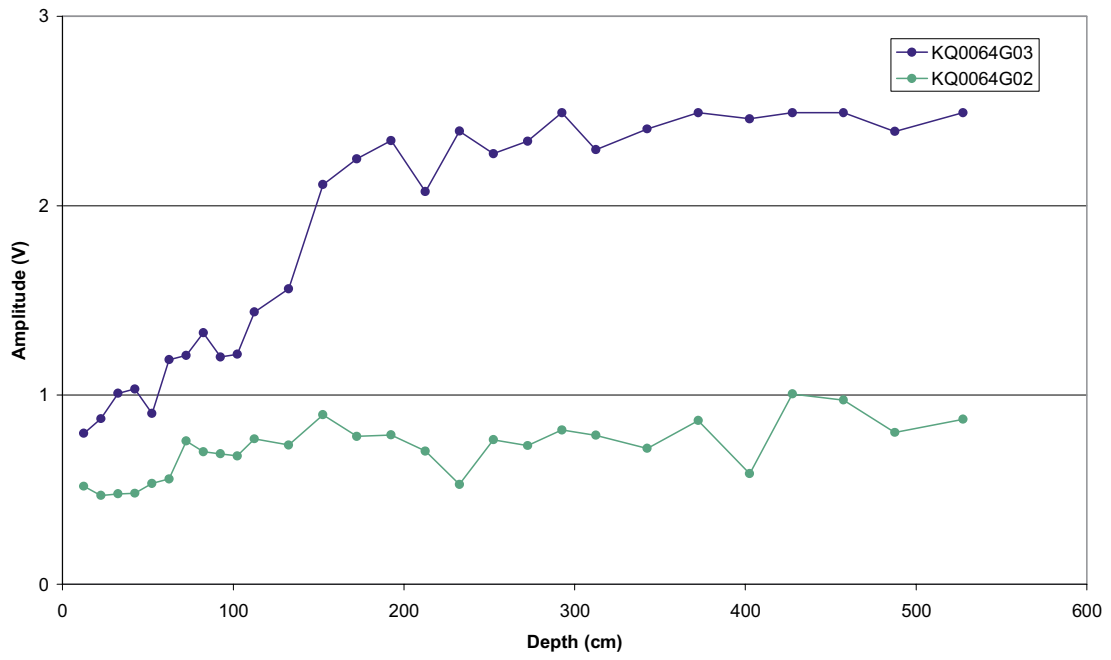


Figure H-16. S-wave amplitude and amplitude change graphs.

6 Conclusions and discussion

- A cross-hole survey has been performed beneath the Q-tunnel in the volume of the Pillar Stability Experiment. The survey was conducted during the installation of acoustic emission and ultrasonic survey instrumentation and utilized boreholes KQ0064G02 and KQ0064G03. The survey consisted of transmitting an ultrasonic signal between the two boreholes at various depths below the sensor datum; the lowest level of the tunnel floor. The boreholes were positioned either side of the tunnel axis, resulting in ray paths that travel orthogonal to the tunnel axis beneath the tunnel floor. The volume of rock that has been investigated is in the immediate vicinity of the future position of deposition hole DQ0063G01.
- The ray paths are 2.76 m long, so observed velocity variations are an average of localised variability along the ray path. The P-wave velocity is shown to increase in the first 40 cm depth from $5,880 \text{ m.s}^{-1}$ to $6,010 \text{ m.s}^{-1}$. Velocity changes have been measured using a cross-correlation procedure with estimated uncertainties of approximately $\pm 5 \text{ m.s}^{-1}$. The largest velocity increase is observed between the first three measurements, at 0 to 20 cm depth. At 20 cm depth the velocity is $5,990 \text{ m.s}^{-1}$. This velocity change has been interpreted as an Excavation Damaged Zone that is likely to be caused by blast-induced fractures along the ray path.
- Between 20 cm and 40 cm depth there is a systematic increase of 20 m.s^{-1} , up to the background velocity level, which then has a general downward trend to approximately $5,950 \text{ m.s}^{-1}$ at 6 m depth. The small increase between 20–40 cm depth is therefore not considered to be significantly below the background and is believed to be a stress-relaxation response. The downward trend of the background velocity is likely to be a response to a decaying induced-compressive stress beneath the tunnel floor.
- Between 50 and 125 cm below the floor there is an anomalously high velocity zone, reaching a peak of $6,070 \text{ m.s}^{-1}$, which could be induced by high compressive stresses, but is more likely to be the result of a lithological change such as the position of a quartz-rich band. It would be interesting to correlate this zone with the core logs from boreholes KQ0064G01, KQ0064G02 and KQ0064G03.
- The cross-hole survey results have been compared with the average P-wave velocity measured through the core from borehole KQ0064G01. This borehole has been excavated from the floor of the Q tunnel as the pilot hole for deposition hole DQ0063G01 and is positioned close to the cross-hole ray paths. The core data shows an increased variability from higher measurement uncertainties, caused by the much shorter ray path lengths (5 cm compared to 2.76 m). There is a decreasing trend in velocity down the core that appears to be a magnification of the trend observed in situ, but it is uncertain what the significance of this is. There is also a systematically lower velocity than measured in situ due to stress relaxation of the core. The uncertainties on the core measurements, and the low density of recordings along the core, make it difficult to provide a more detailed comparison between the core and in situ measurements.
- The sensor configuration that has been used has also provided two ‘Borehole Profiles’, that include ray paths travelling parallel to the borehole. In this case, there is little effect on the profiles that can be attributed to a tunnel damage zone. As the profiles began at the sensor datum (26 and 38 cm down boreholes KQ0064G02 and KQ0064G03 respectively) then this is a consistent result to that observed in the Cross-hole Profile as the damaged zone must therefore be above this.
- Signal amplitude changes on the Borehole and Cross-hole profiles show a systematic increasing trend in the first 1.5 to 2.0 m depth. This may indicate that the measured amplitudes are sensitive to rock changes in the immediate vicinity of the measurement boreholes, and has been interpreted as a response to stress disturbance in the excavation disturbed zone.

Appendix A

Processing parameters

Borehole Velocity Profile Survey

Event initialisation

View/process waveforms by	Channel
Channel-view Width-to-height ratio	6
Waveform Response type	Set from sensor
Sampling time	1
Time units	Microseconds
Pre-signal points	200
Spline sampling time	0.2
Waveform To point	1,023
P-Time correction	0
S-Time correction	0
Automatically update Channel Settings	SET
Project Files	NULL

Auto picking

Allow P-wave-autopicking	YES, Use max peak in the auto-pick function
Back-window length	100
Front-window length	35
Picking Threshold	5
Min Peak-to-Peak amplitude	0
Allow S-wave autopicking	YES, Use first peak in the auto-pick function
Back-window length	100
Front-window length	35
Picking Threshold	5
Min Peak-to-Peak amplitude	0
Allow Automatic Amplitude Picking	NO
Use Velocity Window Picking	YES
P-wave Min Velocity/Max Velocity	4,500, 6,500
S-wave Min Velocity/Max Velocity	2,500, 3,500

Cross-correlation

CCR Events	Referenced to a Survey
Reference Component	Pulser1_Receiver1 25 Pulser1_Receiver10 25 Pulser2_Receiver1 80 Pulser2_Receiver10 0
Reference Event	NULL
Window construction method	Front to Back
Window comparison method	Individual
Window Parameters	Back-window length = 10 Front-window length = 20 Rise-time multiplier = NULL Power to raise waveform = 1 Split to a Spline function = YES Obtain absolute waveform = NOT SET

Locater	<i>(not used in velocity surveys)</i>
Method	SIMPLEX ROUTINE
Method settings	Tolerance = 0.01
Simplex settings	LPNorm = 1 P-wave weighting = 1 S-wave weighting = 1 Use Outlier Identification = NOT SET Arrival error factor = ×3
Geiger settings	Tolerance (Loc. units) = 0.01 Step size (Loc. units) = 0.1 Max Iterations = 100 Conditional No Limit = 10000000000
Velocity Structure	Homogeneous Isotropic
Velocity Structure settings	P-wave velocity (m/s) = 5,872.12 m/s S-wave velocity (m/s) = 3,407.29 m/s Attenuation = 200 Q(S) Value = 100
Data to use	P-wave and S-wave Arrivals
Distance units	Metres
Working time units	Microseconds
Min P-wave arrivals	5
Min S-wave arrivals	0
Min Independent arrivals	7
Max Residual	100
Start point	Start at the centroid of the array
Write report to RPT	NOT SET
Source parameters	Set to calculate automatically